Title

Generating Diversity and Maintaining Stability in the Nervous System, From Synapses to Behavior

Author

Hoagland, Adam Dupaix

Publication Date

2021

Peer reviewed|Thesis/dissertation

Generating Diversity and Maintaining Stability in the Nervous System, From Synapses to Behavior

By

Adam Dupaix Hoagland

A dissertation submitted in partial satisfaction of the

requirements for the degree of

Doctor of Philosophy

in

Molecular and Cell Biology

in the

Graduate Division of the

University of California, Berkeley

Committee in charge:

Professor Ehud Isacoff, Chair
Professor Kristin E. Scott
Professor Helen Bateup
Professor Daniela Kaufer

Fall 2021

Abstract

A central question in neuroscience is how synapses are assembled within neuronal circuits to regulate and maintain complex behaviors. These fundamental nodes of information transfer must be malleable yet maintain stability, all within a nervous system of a developing, learning, and behaving animal. In my thesis work, I have sought to help bridge some of these divides between the many scales of the nervous system and disentangle the overwhelming intricacy that lies between molecules at the synapse and emergent behavior. Behavioral variability in animal populations is thought to increase fitness and aid adaptation to environmental change, yet the underlying neural mechanisms are poorly understood. We found that variation between individuals in neuromodulatory input contributes to individuality in short-term habituation of the zebrafish (Danio Rerio) acoustic startle response (ASR). From here, I studied heterogeneity on a different scale and began researching the synaptic diversity of the model system, the Drosophila neuromuscular junction (NMJ). Most electrophysiological studies of the NMJ have ignored the functional differences between its two distinct motor neuron inputs, the Ib and Is, both of which are comprised of hundreds of synapses of varying vesicular release properties. We found that the Ib and Is inputs generate distinct forms of excitatory drive during crawling and differ in key transmission properties. Finally, after a desire to connect the synaptic level of the NMJ to the behavioral level of the larval zebrafish, my most recent work investigates how circuits increase motor neuron output to maintain normal behavior in response to a reduction in synaptic strength at the NMJ. Although diverse in nature, these model systems provide a unique insight into the complex interplay between generating diversity and maintaining stability in the nervous system.

Dedicated to My Mom and Dad

Acknowledgements

I have been fortunate enough to have a vast support network in my life that has made possible for me to pursue my graduate work. I would first like to thank my parents, who probably could not be more relieved to see me finally finishing school and entering the "real world." I cannot imagine the amount of sacrifice, encouragement, work, and effort they sustained in pushing me along my 30-year journey from preschool to the 23rd grade. My dad, who initially encouraged me to pursue science and loved teaching my brother and me about the science he was most passionate about – geology. He was always pointing out the window on road trips growing up to my brother and me as we drove through the canyon country of Utah, explaining the ways in which its many landscapes came to be. He also helped me land my first research position in a cancer research lab and continues to be a source of inspiration for me in trying to help treat disease. For my mom, who after seven or so years is finally learning how to pronounce "synapses" correctly and has helped me cope through my many late-night crises throughout my education. My brother, who is one of the few people who knows me well-enough to not keep asking me the irritating question about when I'm finally going to finish my dissertation, rather I know he has always had faith in me having it under control. My cousin, Tony, who loved to make fun of me for being a nerd but was always supportive of my career. My godfather, Bob, whose amazing generosity helped support my brother and me through college. And I cannot thank my amazing partner, Katie, enough. She finished graduate school two years earlier than me and thus imparted to me the many wisdoms she learned while paving the way. She helped me through all my moments of stress, listened to countless hours of me gripe, and has provided me with the emotional support when I've felt like giving up. I could not have done this without her.

Much of what made my graduate school experience enjoyable was the amazing environment of our lab. My graduate advisor and mentor, Udi Isacoff, was always available to me when I needed him and offered invaluable advice and guidance. His genuine curiosity and passion for research always served as a source of inspiration for me within my own pursuits. Udi gave me the support, resources, and freedom to pursue whichever questions I wanted to explore – and even if he wasn't necessarily an expert in the area, he would always learn more about the field and offer his support. Udi curated a workplace filled with some of the friendliest, most helpful people with a multitude of different skills and specialties. If it weren't for Beth Carroll, who was the first person to reply to one of my mass emails I sent out to labs as an undergraduate, I probably would have never ended up in the Isacoff Lab. The trust she had in me with programming and building experimental apparatuses gave me the confidence that allowed me to independently succeed in the lab. One of my favorite mentors, Carlos Pantoja, who I worked closely with as a technician, was also a great role model, friend, and someone who I've tried to emulate their style and approach to research. Other mentors in the lab include graduate students Claire Oldfield, Drew Friedmann, and Alden Conner, who I always looked up to as the senior grad students. Zach Newman has been my primary research mentor who never ceases to amaze me in how knowledgeable he is about our model system. He is truly passionate about science and has also been a major role model for me. My office crew in room 215, Irene Grossrubatscher, Krisha Aghi, Amy Winans, Robin Ball, and Victoria Chou, who were always there to bounce ideas off, grab a coffee, or have a spontaneous dance party. My classmate, good friend, and counterpart, Chris Habrian, was one of the main reasons I joined the lab. In addition to providing insightful

advice about my project, he was the person I could truly confide in about anything. And I will never forget the great times we shared in lab, from our afternoon outings at the bowling alley to popping ollies off Terry's lab benches. And finally, how could I forget my "scientific soulmate," Victoria Chou, who was probably the person I was always most excited to see every morning when I got into lab. From helping each other troubleshoot our experiments to her filming me sing all my favorite karaoke songs, I will miss having her sitting next to me, always being there for a laugh and a snack – if I'm lucky.

The teachers who had the biggest impact in my scientific career were from my high school, West High, who always challenged and supported me. I'd like to believe my path in pursuing science was set out this one memorable day in high school when I could have chosen between taking a more difficult chemistry course and an alternative easier class. Mrs. Anderson believed in and encouraged me to stay in her chemistry class and – from a combination of the challenge of the subject, her amazing teaching skills and encouragement, and my cohort, I believe this was the first time when I truly enjoyed learning about science and marked the beginning of my path in research. My biology teacher, Mr. Ekberg, who admittedly was one of the most feared teachers at West, but I know deep down inside he was a total softy and was secretly cared for us greatly. My math teacher, Mr. McGuire – I'll never forget that one day after school when I had to make up a missed test. He could tell I was struggling, so he sat down and surprisingly started helping me with some of the questions. I'll never forget how cool I thought this was that he gave me this attention and support, even though he probably wasn't supposed to. After this moment, I began to excel in his class and further develop my passion for math and science.

I would also like to thank all my best friends outside of the lab. Tanner, Mike, Milo, and John, who even though thought I was a marine biologist, were always encouraging of me finishing my "extended essay" and making sure I was "on-track." All our amazing and memorable trips that we went on, and our weekends just hanging out being buddies, served as a much-needed break from the stressful world of grad school. My friend Andrew, whose discipline, focus, and amazing work ethic in his own academics was always a source of inspiration for me. My friend Annie, for all her helpful mock-up graphs of my zebrafish data, and for her pushing me to graduate. My good friend Adam, who was always genuinely interested in what I was researching and helped motivate me in finishing. And my family friends and dad's best friends, Jack, Tom and Del, all father-figures in my life who always gave me their advice and support.

Table of Contents

Introduction

Neuromodulation generates behavioral diversity

In species ranging from *C. elegans* to humans, individuals exhibit behavior idiosyncrasies despite being genetically identical and raised in indistinguishable environments (Stern 2017; Sanchez-Roige 2018). These behavioral differences are believed to arise from the underlying stochastic processes during development, enabling identical genotypes to give rise to a range of neural phenotypes (Maloney 2021). Yet how these stochastic processes relate to variation in behavior remains unclear, in that they can result in highly stereotyped behavioral outputs as well as variable ones (Johnston 2010). Remarkably, model circuits with varying numbers of neurons, connection, and ion conductances can generate seemingly identical behaviors (Prinz 2004; Daur 2012; Goaillard 2021). It is therefore necessary to understand when and how variations in underlying circuitry lead to divergences in behavior.

Inter-individual differences in behavior are common in animal populations and can increase fitness and aid adaptation to environmental change (Wolf 2012). By having a divergence of behavioral tendencies within a particular species, individuals can hedge against unpredictable environments. This ensures that some proportion of the of the population survives regardless of environmental instabilities (Kain 2015; Xue 2019). Studies showing differing amounts of individuality between isogenic populations with different genetic backgrounds have revealed that genetics plays an important role in shaping behavioral variability (Ayroles 2015; Bruijning 2020), suggesting that intra-genotypic variability is under evolutionary pressure. Yet despite the evidence for a genetic basis of individuality, the underlying neural mechanisms required to generate such variation remain unclear.

One proposed mode of regulation is neuromodulation. As opposed to conventional neurotransmitters, neuromodulators are generally characterized by volume release, broad connectivity, and delayed kinetics (Bargmann 2013). Because they commonly innervate widespread regions, neuromodulators can generate large shifts in behavior (Lee 2012; Taghert 2012). Neuromodulation has been shown to shift animal behavior throughout a variety of contexts, including in response to satiety (Marella 2012), social conflict (Rittschof 2014), arousal (Arnsten 2012), circadian rhythm (Witkovsky 2004), or stress (Rodrigues 2009). Key to neuromodulators' role in the evolution of behavior is their ability to shift behavior without needing to create *de novo* behaviors and circuits in response to evolutionary pressure (Katz 2014). Due to their ability to generate coordinated changes in behavior with relatively few points of variation, neuromodulators are prime candidates to be loci for establishing individuality.

Using larval zebrafish, we pursued this hypothesis using the habituation of the acoustic startle response (ASR) as our model behavior. Habituation is non-associative form of learning where a repeatedly presented stimulus decreases the probability of a behavioral output, while the ASR is an escape behavior characterized by a fast C-bend of the tail, turning the animal away from the startling stimulus (Colwill and Creton, 2011). Integral to the escape circuit are a pair of large reticulospinal hindbrain interneurons, the Mauthner cells, which receive sensory glutamatergic

input from the ears, dopaminergic inputs from the hypothalamus (Mu 2012), and serotonergic inputs from the dorsal raphe nucleus (DRN) (McLean and Fetcho, 2004).

Essential to our study was the ability measure the ASR on a high-throughput behavioral apparatus. Where most variation among individuals is often ignored when behavior is quantified as averages (Geiler-Samerotte 2013), our large sample sizes allowed for a finer dissection of inter-individual variation. Using a combination of calcium-imaging, optogenetics, and pharmacology, we found that higher amounts of serotonin released from the DRN onto the Mauthner cells leads to less habituation within the population, and vise-versa. Furthermore, the degree of DRN activity and extent of habituation within the population is stable and heritable to the next generation. Taken together, these results demonstrate that sensory-evoked responses in a neuromodulatory network can be dynamic and participate in the shaping of individuality in a core behavior in zebrafish.

After researching the circuit and behavioral level components of habituation in zebrafish, a natural question was what were the synaptic mechanisms that gave rise to such diversity in behavior. Since the ability to resolve individual synapses in the larval zebrafish is limited, we turned to the model system, the *Drosophila* larva NMJ. The NMJ is glutamatergic and consists of many synaptic components like those found in central excitatory synapse in vertebrates. It also undergoes activity-dependent changes in synaptic strength, such as short-term plasticity, and is capable of homeostatically responding to deficiencies in synaptic strength (Budnik and Ruiz-Cañada, 2006). Most notably, the NMJ is comprised of two distinct inputs, each capable of distinct forms of plasticity and homeostasis.

Multiple synaptic inputs differentially regulate synaptic strength and homeostasis

In behaving animals, synapses are under the influence of signals that modulate synaptic strength or establish synaptic stability through homeostatic regulation of transmission. Synaptic transmission is further complicated by the fact that individual neurons can receive inputs from many functionally diverse neurons (Atoowd and Karunanithi 2002; O'Rourke 2012). Even synapses formed by only presynaptic neuron onto one or more postsynaptic neurons can vary widely in neurotransmitter release and plasticity (Atoowd and Karunanithi 2002; Branco and Staras 2009; Pelky 2007). Furthermore, the direction of information does not flow one-way from the pre- to postsynpase. Retrograde signals, including homeostatic signals that modulate synaptic release, need to distinguish multiple input neurons (Branco 2008; Paradis 2001). It remains unclear how neurons innervated by more than one input integrate these signals and if these signals are global or specific. Furthermore, how does the postsynapse feedback onto multiple inputs to regulate transmission independently in each? And how do these multiple inputs coordinate in the behaving animal?

To address these questions, we turned to the *Drosophila* larva NMJ. The NMJ represents the final output stage of behavior in its simplest form – a motor neuron contracting a muscle, yet the diversity of synapses that comprise the NMJ could not be more complex. It consists of two morphologically distinct glutamatergic motor neurons – the larger type Ib and smaller type Is, which converge onto most of the larval body wall muscles used for locomotion (Hoang and

Chiba, 2001). At each of the Ib and Is junctions lies hundreds of individual active zones, all displaying significant heterogeneity in their basal release probability (P_r) and the spontaneous release frequency (Peled and Isacoff, 2011, Peled 2014). However, most previous studies on the NMJ have used traditional electrophysiology to simultaneously stimulate both Ib and Is motor neurons and record aggregate postsynaptic currents in the muscle. While these studies have been invaluable in our understanding of NMJ physiology, they fall short in detecting the way hundreds of different active zones across multiple inputs behave to ensure reliable muscle contraction and ultimately behavior. Our approach, however, used a genetically encoded calcium indicator, SynapGCaMP6f, localized to the postsynaptic density in the vicinity of the GluRIIA glutamate receptors. This enabled us to measure calcium influx through the channels representing quantal vesicular release events at individual active zones throughout both Ib and Is NMJs.

Our combination of *in vivo* imaging with optical, quantal analysis in the semi-dissected preparation revealed that the regulation of synaptic strength and homeostasis are shaped in an input specific manner. Local muscle contraction and the associated calcium rise were more associated with Ib than Is inputs in vivo, suggesting that type Ib boutons were primarily accountable for the majority of muscle contraction. Is inputs, on the other hand, likely aid in the intersegmental coordination of the body wall muscles. Furthermore, Ib inputs had lower Pr synapses and facilitated during spike trains. To determine the input specificity of synaptic homeostasis, we examined *GluRIIA* mutant larvae and observed a reduction in the amplitude of spontaneous Ca^{2+} events at both Ib and Is terminals. In this model of homeostasis, the decrease in postsynaptic sensitivity to glutamate is counteracted by an increase in vesicle release, a phenomenon referred to as postsynaptic homeostatic plasticity (PHP) (Petersen 1997; DiAntonio 1999). However, the enhanced probability of release associated was only present at the Ib terminals and not the Is. Taken together, our research revealed how multiple inputs ensure functional diversity and stability in the larval NMJ.

The above results demonstrated that PHP occurs at the Ib synapses and restores postsynaptic response to a single action potential from the motor neuron. Yet muscle contractions necessary for crawling peristalsis require a much higher demand from the motor neurons, where bursts of firing frequencies can reach up upwards of 20Hz and are repeatedly delivered per each bout of muscle contraction (Heckscher 2012). Furthermore, is there a deficit in transmission at the Is inputs that remains unaccounted for due to the lack of PHP occurring its synapses? To answer these questions, I next searched for any potential changes in firing patterns and upstream circuit level activity in the intact larva that may provide evidence for additional forms of homeostatic regulation.

Circuit homeostasis in response to synaptic perturbation ensures robust behavior

Nervous systems are under the constant demand of balancing both flexibility and stability. Throughout development, neurons wire themselves up into complex networks required for the generation of stable patterns activity throughout the life of an organism. These circuits, however, need to maintain their plasticity and be amenable to the changing demands of the animal's environment. The information-storing process of long-term potentiation (LTP), for example, has

been thought by theoreticians to generate destabilizing forces that need to be counterbalanced by homeostatic mechanisms (Miller and MacKay 1994). LTP increases the ability to depolarize a postsynaptic neuron, which increases the probability of further LTP – in turn leading to an uncontrolled amount of synaptic strengthening. Therefore, for an animal's behavior to be both adaptable and coherent, there needs to be a coexistence of counteracting forces that either generate flexibility or sustain stability.

Homeostatic plasticity is broadly defined as a set of neuronal responses that restore activity to a setpoint following a perturbation (Turrigiano 2004; Davis 2013). Such perturbations have been performed across an array of model systems and elicit a variety of neuronal homeostatic mechanisms, including the activity-dependent control of neuronal firing (Marder and Prinz 2003); forms of pre- and postsynaptic plasticity (Turrigiano and Nelson 2004; Davis 2006); the balancing of excitation and inhibition within circuits (Maffei 2004); and homeostatic regulation of intrinsic excitability (Marder and Goaillard 2006). Despite the array of experiments performed across varying models, many of the key mechanisms required in establishing and regulating neuronal homeostasis have yet to be elucidated – particularly in *in vivo* systems (Lee 2019).

Synaptic homeostasis at the NMJ arises from the need for motor neurons to remain capable of sufficiently contracting muscle fibers as they grow throughout development. Although documented as mammalian and *C. elegans* as well (Davis and Bezprozvanny 2001), the dissected *Drosophila* larva preparation has proven to be the most successful model used in gaining insight in homeostasis at the NMJ. The robustness of the fly larva NMJ enables it to maintain a constant gain of transmission to the muscle in response to varying perturbations. Reductions in postsynaptic glutamate receptor function or chronic hyperpolarization of the muscle, for example, lead to a compensatory increase in vesicular glutamate release to restore normal excitatory postsynaptic current (EPSC) amplitudes (Paradis 2001). This compensation can occur rapidly – within the course of ~10 minutes – and is believed to be triggered by a retrograde signal from the muscle to the motor neuron that leads to enhanced transmitter release (Frank 2006). An abundance of different molecular players has been found to serve a role in homeostasis at the NMJ, yet the key signals in determining the target EPSC amplitude, or homeostat, and the primary retrograde messenger remain largely unknown (Frank 2020).

One of the most well understood forms of homeostatic plasticity at mammalian central excitatory synapses is synaptic scaling. First described in cultured neocortical neurons (Turrigiano 1998), whose networks consist of excitatory pyramidal and inhibitory GABAergic neurons that exhibit spontaneous firing activity. When blocking the activity of the GABAergic neurons, there is an initial increase in overall firing rates, but over the course of many hours firing rates return to baseline values. This homeostatic response can also be observed when transfecting cultured hippocampal neurons with an inwardly rectifying potassium channel to hyperpolarize them and reduce firing. Over a similar timescale of hours, baseline firing rates are reestablished despite the continued expression of the channel (Burrone 2002). By recording miniature excitatory postsynaptic currents (mEPSCs) arising from many synapses onto the same neuron, the researchers discovered that modulating network activity increased or decreased the distribution of mEPSCs amplitudes uniformly, thereby scaling synaptic strength up or down (Turrigiano 1998). Several molecular players that influence synaptic scaling have been discovered, including soluble released factors (Rutherford 1998; Kaneko 2008), transsynaptic signaling molecules

(Cingolani 2008; Goddard 2007), and intracellular signaling pathways (Ibata 2008; Thiagarajan 2005). Yet despite the recent advancements surrounding synaptic scaling, the recurring questions surrounding homeostasis persist – such as how the activity "set-point" of a neuron is determined, or how does modulating intracellular signaling molecules lead to a precise homeostatic calibration without overshooting or creating drift in the system.

Synaptic scaling is the most thoroughly studied form of homeostatic plasticity *in vivo* using the mouse visual system. Analogous to blocking activity in neuronal cultures, the standard visual deprivation paradigms in mice can reduce activity in the visual cortex. During the second and third postnatal weeks when synaptogenesis is high, for example, there is an inverse relationship between the frequency and amplitude of mEPSCs onto principal neurons in layer 4 of primary visual cortex. As the frequency of mEPSC rises (signifying an increase in excitatory synapses) and visual input increases, the amplitude of mEPSCs decreases. This homeostatic mechanism appears to be activity-dependent since raising the mice in the dark prevents this developmental decrease in mEPSC amplitude (Desai 2002). Using tetrodotoxin to block activity in the optic nerve scales up mEPSC amplitude in layer 4 neurons and is reversed when optic nerve activity resumes (Desai 2002).

Another model system that sheds light on the many facets of homeostatic plasticity is the lobster stomatogastric ganglion (STG). The STG is a central pattern generator, which generates a characteristic triphasic, or pyloric, firing pattern to control the rhythmic peristaltic contraction of the animal's digestive system (Marder 2006). As the animal develops from juvenile to adult, not only does the intestine of the animal increase ~100-fold, but the neurons that comprise the STG also increase in size, in turn altering membrane capacitances and channel abundances and distributions. Furthermore, over the course of the animal's lifetime, ion channels and receptors within the neurons of the STG turnover in the membrane over the timescale of minutes to weeks, yet the overall triphasic pattern of activity generated by the STG remains constant for digestion. The STG can even be completely decentralized from the animal, with the descending inputs removed, and be sustained *in vitro*. Initially its triphasic activity pattern is abolished, yet amazingly after several days the characteristic pattern is restored (Marder 2006).

When voltage clamping neurons in the STG and measuring K^+ currents followed by real-time quantitative PCR measurements for the K^+-channel in the same cell, current densities are well-correlated with the levels of channel expression. Conversely, when measuring the K^+-current densities and channel copy numbers in the same type of neuron across different animals, there were two-to fourfold variations in these measurements, yet the total inward hyperpolarizing current and the frequency of action potentials remained the same (Schulz 2006). A similar phenomenon has been discovered in voltage-clamped dissociated Purkinje neurons, where different ratios of inward Na^+ and Ca^{2+} currents were found at the same membrane potential in different neurons with virtually identical firing activity profiles (Swensen 2005). Modeling the network of neurons that comprise the STG has revealed that in principle there can be more than 20 million models of varying synaptic strengths and voltage-dependent conductances to create the characteristic pyloric rhythm (Prinz 2004). Taken together, these results demonstrate that there can be various homeostatic solutions in modulating synaptic strength and intrinsic excitability to produce a similar network output. It remains unclear, however, how these

different forms of compensation are recruited, and if model systems employ a combination of solutions in some sort of hierarchical fashion depending on the nature of perturbation.

The *Drosophila* larva presents an ideal model system for studying many of the outstanding questions surrounding homeostatic plasticity. In some regards, it shares striking similarities with the crustacean digestive system: the larva increases rapidly in size – roughly 200-fold in only three days (Robertson 1963) – and uses a CPG to generate the peristaltic contraction of body wall muscles required for crawling. Much like the stomatogastic intestine, the larva needs to maintain consistent peristaltic behavior throughout its lifetime as it both grows rapidly in size and its neurons turnover proteins. In my thesis work, I have found that the normal generation of peristaltic crawling is preserved despite synaptic perturbations – ranging from mild to severe – at the NMJ. The ability to observe this in the intact, behaving animal has revealed upstream, circuit-level compensatory adjustments and the timescale over which they can occur. Furthermore, it is possible that the system is employing several of the previously mentioned homeostatic solutions in combination: that is, increasing glutamate release from the motor neuron, the tuning of the motor neuron's excitability, and modulating activity of the inputs to the motor neuron. Together with the wide-array of genetic tools available to it and its well-characterized connectivity maps (Hoang 2001; Zarin 2019), the larva presents a tractable model system where we can for the first time investigate circuit-level homeostasis occur in real time – in an intact, behaving animal – thereby giving new potential to answering many of the outstanding questions surrounding homeostatic plasticity.

Chapter 1: Neuromodulatory Regulation of Behavioral Individuality in Zebrafish

Pantoja, C., Hoagland, A., Carroll, E. C., Karalis, V., Conner, A., & Isacoff, E. Y. (2016). Neuromodulatory regulation of behavioral individuality in zebrafish. Neuron, 91(3), 587-601.

Abstract

Inter-individual behavioral variation is thought to increase fitness and aid adaptation to environmental change, but the underlying mechanisms are poorly understood. We find that variation between individuals in neuromodulatory input contributes to individuality in short-term habituation of the zebrafish (*Danio Rerio*) acoustic startle response (ASR). ASR habituation varies greatly between individuals, but differences are stable over days and are heritable. Acoustic stimuli that activate ASR-command Mauthner cells also activate dorsal raphe nucleus (DRN) serotonergic neurons, which project to the vicinity of the Mauthner cells and their inputs. DRN neuron activity decreases during habituation in proportion to habituation and a genetic manipulation that reduces serotonin content in DRN neurons increases habituation, whereas serotonergic agonism or DRN activation with ChR2 reduces habituation. Finally, level of rundown of DRN activity co-segregates with extent of behavioral habituation across generations. Thus, variation between individuals in neuromodulatory input contributes to individuality in a core adaptive behavior.

Introduction

One of the most interesting aspects of the study of animal behavior is the wide variation in animal-to-animal behavior. Since neuromodulatory input can act at multiple points in a neural circuit to control output and switch circuit dynamics and behavioral state (Gordus et al., 2015, Lee and Dan, 2012, Marder, 2012), we considered that neuromodulatory variation could contribute to behavioral variation between individuals. We examined this possibility in zebrafish (Danio rerio). Zebrafish display complex behaviors and patterns of neural activity in circuits that receive neuromodulatory input (Brustein et al., 2003, Thirumalai and Cline, 2008, Woods et al., 2014). Zebrafish populations are outbred, highly polymorphic, and could therefore have behavioral variation more similar to wild animal populations and humans than do the inbred genetic models that are commonly used in behavioral studies (Brown et al., 2012, Howe et al., 2013).

We examined two types of locomotor behavior that are easily quantifiable in hundreds of animals: the habituation of the zebrafish acoustic startle response (ASR) (Burgess and Granato, 2007) and spontaneous swim activity (Lambert et al., 2012). Habituation is a critical adaptive behavior: a non-associative form of learning characterized by decreased probability of a behavioral output when the same stimulus is presented repeatedly. Habituation increases at shorter inter-stimulus interval (ISI) and decreases at higher intensities of the sensory stimulus

(Rankin et al., 2009). During short-term habituation, which occurs in seconds to minutes, the motor output changes dramatically due to changes in sensory processing that may occur at multiple levels of a circuit and involve several neural mechanisms, while circuit anatomy remains unchanged (Ramaswami, 2014).

The ASR is evolutionarily conserved in vertebrates and characterized by a short-latency defensive behavior elicited by strong and sudden acoustic stimuli. In zebrafish, the escape behavior is expressed by a fast unilateral C-bend of the tail, which turns the animal so that it can swim away from the startling stimulus (Colwill and Creton, 2011). This behavioral output is regulated by the balance between sensory excitatory glutamatergic inputs and glycinergic feedforward inhibitory networks that converge on the Mauthner cells (M-cells), a pair of large reticulospinal hindbrain interneurons. A single action potential in one M-cell suffices to elicit the C-bend escape behavior in the contralateral direction (Korn and Faber, 2005). Intriguingly, differences in ASR habituation levels have been associated with different personality types and behavioral disorders in humans, including schizophrenia and anxiety disorders (Blanch et al., 2014, Braff et al., 1992).

The neuronal populations that comprise the ASR circuit are extensively modulated by neuromodulatory inputs. First, vestibulo-auditory (eighth nerve) afferents and the M-cell are subject to synaptic modulation by hypothalamic dopaminergic projections (Mu et al., 2012). Second, serotonergic varicosities are present in the vicinity of M-cell dendrites (McLean and Fetcho, 2004a) and axon cap, two locations in the M-cell where serotonin receptors are present (Curtin et al., 2013, Whitaker et al., 2011).

We tested the hypothesis that larval zebrafish display stable inter-individual differences in core adaptive behaviors that depend on differences in neuromodulatory activity. We find that inter-individual differences in ASR habituation, unlike differences in the spontaneous swim behavior, are stable over days and heritable. These differences are associated with differences in the rate at which M-cell firing drops off in response to repeated sound stimulation. DRN serotonergic neurons, which project into the vicinity of the M-cells, are also activated by acoustic stimuli and lower habituation is associated with individuals that sustain sound-evoked activity in larger number of serotonergic neurons for longer times during the repeated stimuli or are activated with channelrhodopsin-2 (ChR2) during sound stimulation. This suggests that serotonergic input to the M-cells and/or their inputs acts to blunt ASR habituation. Consistent with this interpretation, a serotonergic agonist decreases the frequency of individuals with high ASR habituation and a genetic manipulation that reduces the serotonin content of DRN neurons increases ASR habituation. Finally, individual differences in sound-evoked DRN neural activity co-segregate with heritable individual differences in ASR habituation. We propose that inter-individual differences in sensory-evoked behaviors are shaped by differences in neuromodulatory activation by sensory inputs.

Results

Large Variation between Individuals in ASR Habituation Behavior

To characterize ASR short-term habituation in zebrafish, we used a high-throughput behavioral apparatus (Levitz et al., 2013) to monitor many individual larvae simultaneously. Forty-eight wild-type AB strain larval zebrafish placed individually in wells of a multi-well plate were imaged simultaneously at 30 frames per second (fps) under infrared illumination from an LED array and stimulated with brief, precisely timed acoustic-vibration stimuli (3 ms, 900 Hz, ~95 dB) from speakers that were coupled to the plate (Figure 1A). Behavioral movies were analyzed with custom-written software that automatically detects the C bend behavior (Levitz et al., 2013). First, we characterized the naive responsiveness of healthy larvae under the minimally habituating inter-stimulus interval (ISI) of 90 s (Figure S1A). The majority of individuals (56%–90%) obtained from independent crosses and tested on multiple experimental days responded to at least nine out of the first ten stimuli, ($P_{initial} \geq 0.9$), while a small minority (2.5%) responded to fewer than three stimuli. Habituation was examined only in the stably responsive $P_{initial} \geq 0.9$ group when the stimulation was switched to the much shorter ISI of 5 s (Figures 1B and 1C).

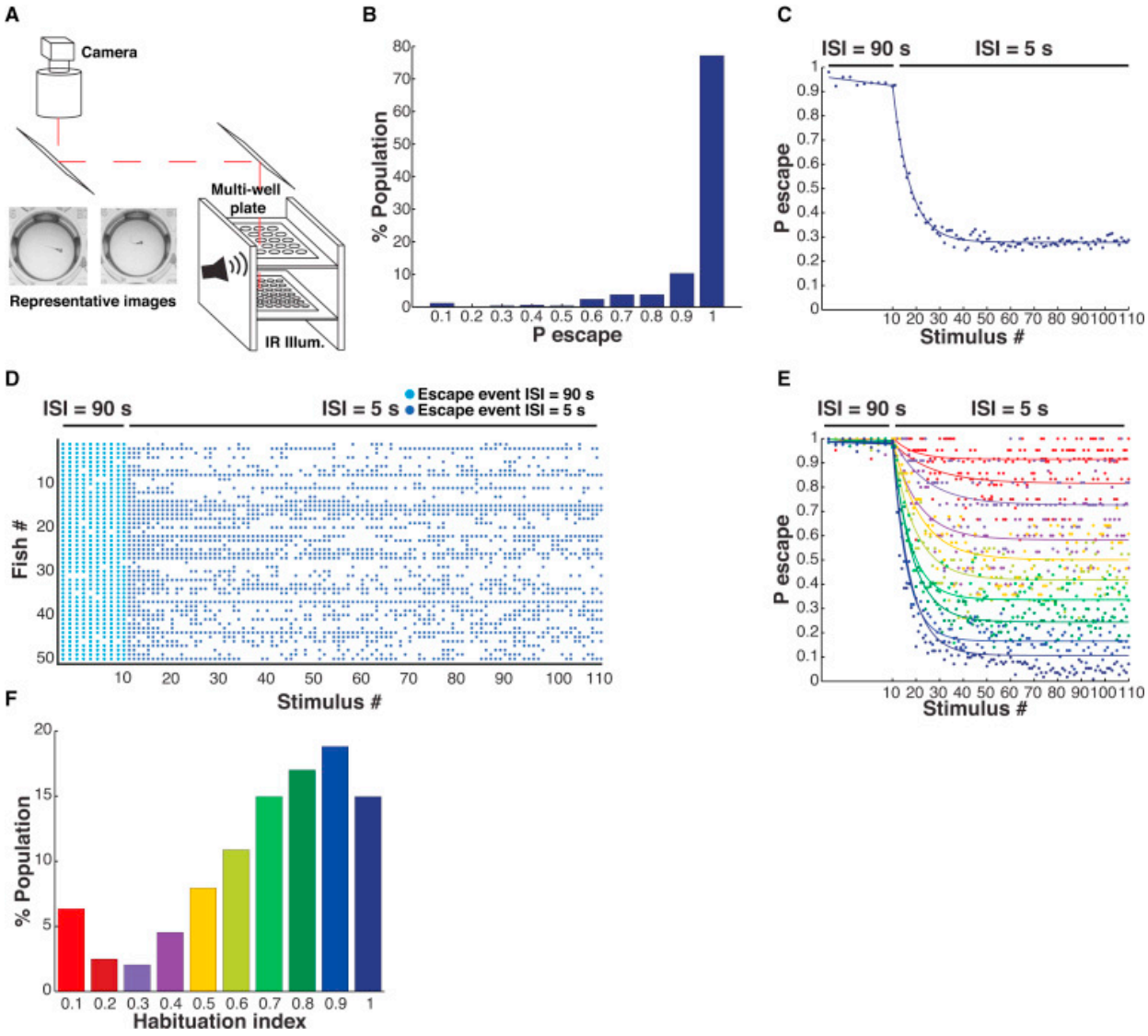

Figure 1. High-Throughput Analysis of Larval Zebrafish Startle Behavior (A) Multi-well behavioral apparatus. (B) Frequency distribution of probability of escape values during the first 10 stimuli (ISI = 90 s) of habituation series. (C) Population average of the probability of sound-induced escapes during acoustic startle response (ASR) habituation (Stimuli #1–10, inter-stimulus interval (ISI) = 90 s; stimuli #11–110, ISI = 5 s; n = 441). (D) Representative acoustic startle responses of 50 individual larvae ordered in the y axis with each dot representing a sound-induced escape. (E) Average ASR probability curves for population in (B) binned by habituation index (HI). (F) Frequency distribution of HIs of same population as in (C).

We quantified the habituation index (HI), which we defined as the steady-state probability of response at the end of a series of stimuli at the 5 s ISI (Pafter) divided by the initial probability (Pinitial) at the minimally habituating ISI of 90 s (HI = 1 – Pafter/Pinitial). HI values close to 1

indicate strong habituation, while values close to 0 indicate weak habituation. At 6 days post-fertilization (dpf), the average population behavior showed strong habituation at the 5 s ISI (HI ~0.7) (Figure 1C). However, the behavior varied considerably between individuals (Figure 1D), with approximately 10% of fish showing little or no habituation (HI ≤ 0.2) (Figures 1E and 1F), and approximately 45% showing strong habituation (HI ≥ 0.8) (Figures 1E and 1F).

Degree of ASR Habituation Behavior Is Stable over Days and Is Heritable

To determine whether the level of behavioral habituation is a stable characteristic of each fish or varies over time, we tested larval zebrafish daily at 5, 6, and 7 dpf. Fish with intermediate and high HIs at 5 dpf converged in behavior and remained statistically indistinguishable 2 days later (Figure 2A). In contrast, fish with low HIs (<0.2) at 5 dpf retained a significantly lower HI, when

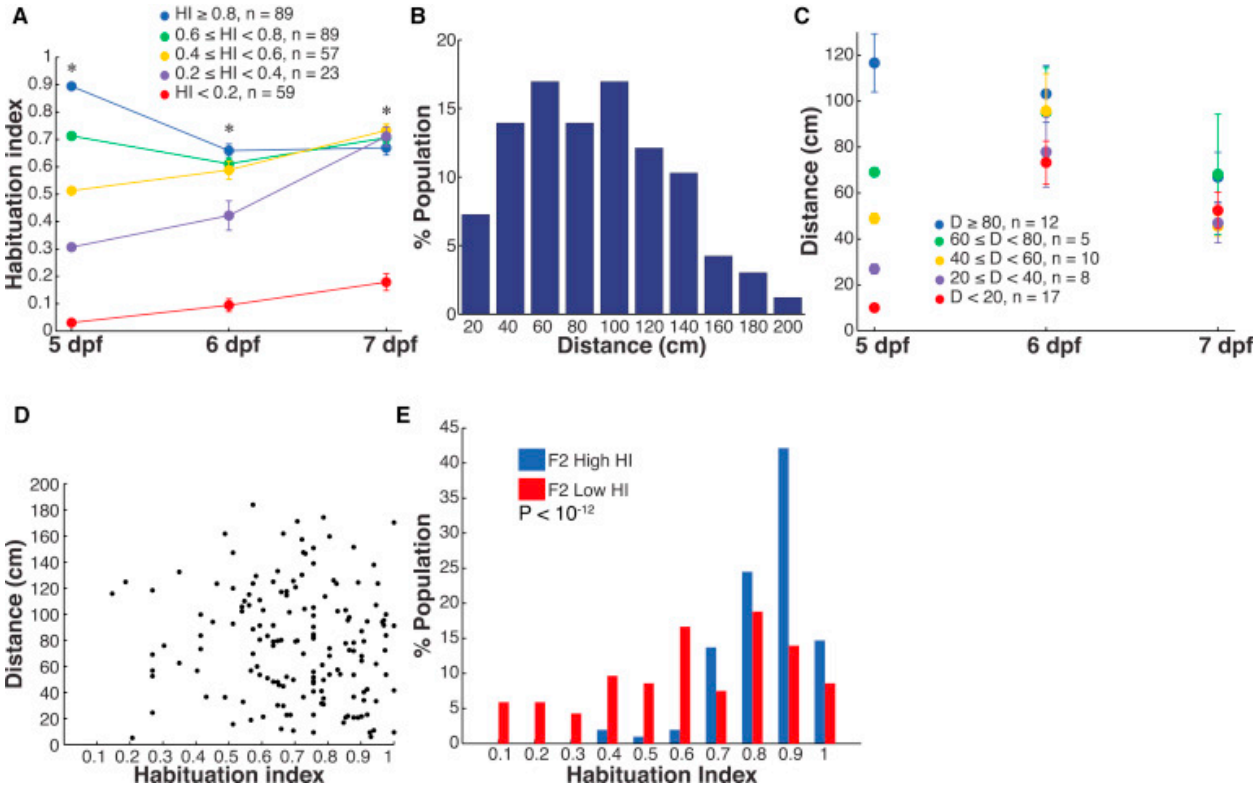

Figure 2. Longitudinal Analysis of ASR Habituation and Spontaneous Swim Behavior (A) Repeated measurement of HI over 3 days. The HI value measured on 5 dpf was used to group larvae. HI value of HI < 0.2 group is significantly smaller than all groups at all time points; remaining groups are not significantly different in comparison to one another on 7 dpf (∗p < 10−9; two-tailed Mann-Whitney test, nHI < 0.2 = 59, n0.2 ≤ HI < 0.4 = 23, n0.4 ≤ HI < 0.6 = 57, n0.6 ≤ HI < 0.8 = 89, nHI ≥ 0.8 = 89; error bars, SEM). (B) Frequency distribution values for individual larvae for total displacement in 10 min (n = 165). (C) Repeated-measurement of distance swum over 3 days. Mean values for displacement of individual larvae. The distance value measured on day 5 was used to group larvae. The difference between groups on 7 dpf is not statistically significant (p > 0.1; two-tailed Mann-Whitney test, nD < 20 = 17, n20 ≤ D < 40 = 8, n40 ≤ D < 60 = 10, n60 ≤ D < 80 = 5, nD ≥ 80 = 12; error bars, SEM). (D) Graph shows habituation index value versus total displacement values for individual larvae (6 dpf, n = 110). Pearson's correlation coefficient, r = −0.0285, p = 0.71. (E) Highly responsive F2 Low HI, 6 dpf larvae have significantly lower HI than highly responsive F2 High HI larvae (z = 7.08, p < 10−12; two-tailed Mann-Whitney test; nF2 High HI = 102, nF2 Low HI = 186).

compared to the rest of the population, at both day 6 and day 7 (Figure 2A). This result shows that diversity between individuals at the high and low ends of ASR habituation is stable over days.

We wondered whether persistent differences between individuals also characterize other larval zebrafish behaviors. We addressed this by examining spontaneous swimming behavior. As with ASR habituation, the level of spontaneous activity was widely distributed across the population (Figure 2B), yet differences in spontaneous activity were not stable from one day to the next (Figure 2C). We found no correlation (Pearson's correlation coefficient, $r = -0.0285$, $p = 0.71$) between levels of spontaneous activity and ASR habituation in experiments in which the behaviors were measured sequentially (Figure 2D). Thus, individual constancy and diversity between individuals appear to be properties of ASR habituation and not of spontaneous swimming.

To assess whether HI differences between individuals are heritable, we raised siblings from one parental cross that we split into two groups: one group selected for having a stably low HI ($HI \leq 0.4$), as measured over 2 days, and the other group for having a stably high HI ($HI \geq 0.9$). Both groups were also selected for high responsiveness, with $Pinitial \geq 0.9$ under non-habituating conditions (ISI = 90 s). Six sets of F1 progeny were obtained by F0 inbreeding of two low HI group couples (F1Low HI) and four high HI couples (F1High HI). These sets of progeny were then assayed at 6 dpf. The progeny of the low and high HI crosses were both shifted toward higher initial responsiveness, consistent with their common selection from the subset of parentals that were highly responsive ($Pinitial \geq 0.9$) (Figure S2A). We observed both increased frequency of individuals with $Pinitial \geq 0.9$ and decreased frequency of individuals with $Pinitial \leq 0.1$ in the low HI crosses, but only decreased frequency of individuals with $Pinitial \leq 0.1$ in the high HI crosses (Figure S2A), which suggests an association between basal ASR and ASR habituation. F1s of low HI F0 couples had substantially lower HI than did F1s of the high HI F0 couples (Figure S2B). Moreover, the F1s were also shifted lower and higher in HI, respectively, compared to the parental distribution, although this difference was only statistically significantly for the low HI crosses (Figure S2B). We found that the difference in HI was maintained, and indeed made more extreme, after a second round of selection in the F2 generation of F1 couples selected for high or low HI (low HI couple #2 and high HI couple #3 [Figure S2]) (Median F2 Low HI = 0.63, Median F2 High HI = 0.86, $p < 10^{-12}$) (Figure 2E). Thus, the short-term habituation of the ASR is a heritable quantitative trait.

Mauthner Cell Activity during ASR Habituation

To investigate whether neural mechanisms participate in shaping the broad diversity in ASR habituation behavior, we constructed a two-headed microscope for simultaneous and synchronized high-speed behavioral measurement (1,000 fps) and neuronal calcium imaging (20–40 fps) in a single head-fixed larva (Figures 3A–3F). Acoustic stimuli were presented by two speakers resting on the imaging stage. The high speed of the behavioral camera and short duration of the acoustic stimulus (1,000 Hz, 1–10 ms) allowed precise determination of zebrafish scape behavior latency and kinematics.

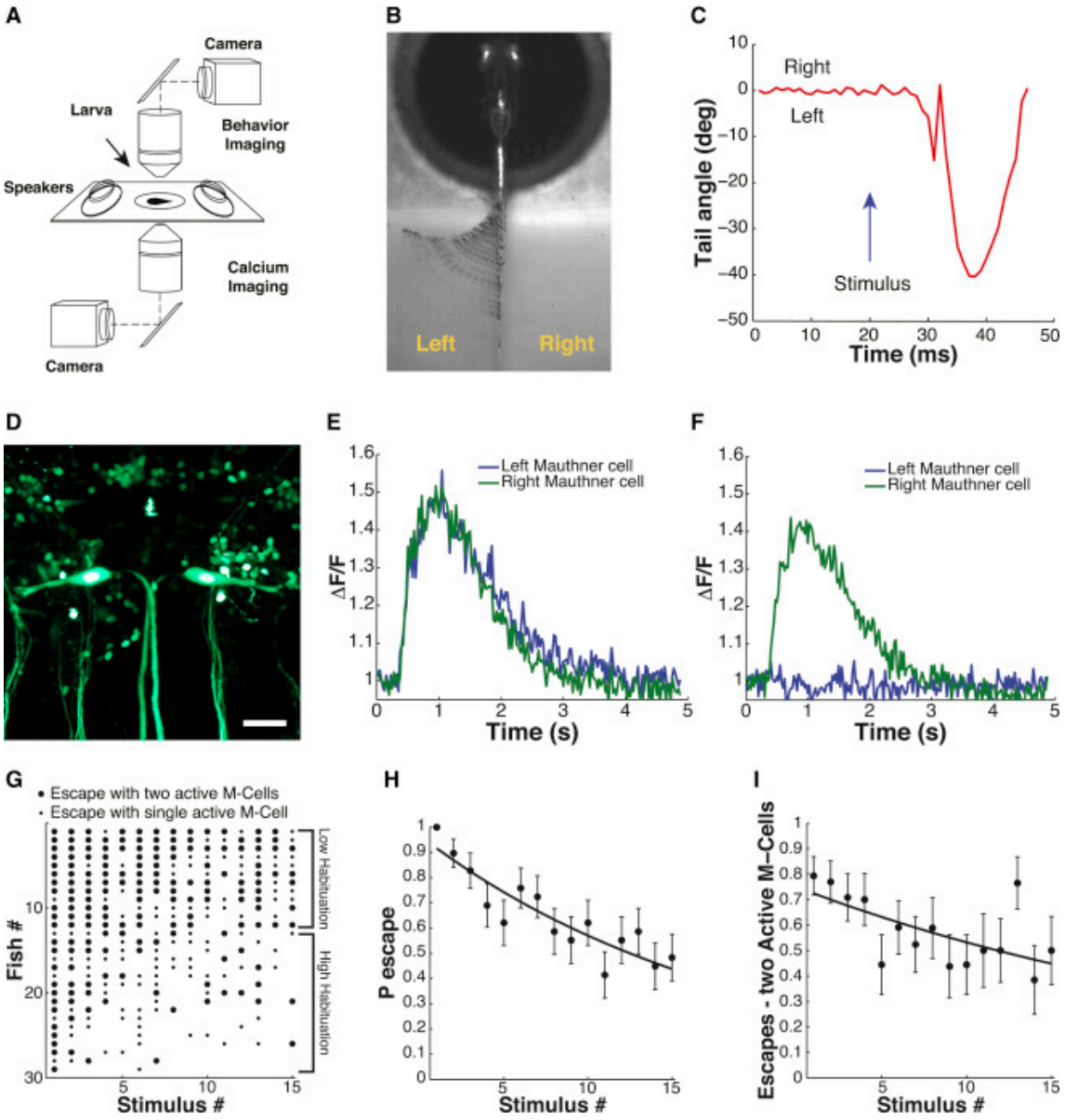

Figure 3. Simultaneous Analysis of Escape Behavior and M-Cell Calcium Signals during ASR Habituation in 6 dpf Zebrafish Larvae (A) Simultaneous behavior (2.5× objective, 1,000 fps) and GCaMP5 calcium imaging of M-cells (40× objective, 40 fps) with two independent light paths. (B) Representative image of time-series projection (ventral view) of sound-induced escape behavior. (C) Tracking of tail movement during response to acoustic stimulus at t = 20 ms. (D) Representative image (dorsal view) of tg(s1181t:Gal4;UAS:kaede) transgenic zebrafish line. Scale bar, 25 μm. (E and F) GCaMP5 calcium activity traces from M-cells in response to acoustic stimulus at 400 ms. (G) Acoustic startle responses of individual larvae ordered along y axis by probability of escape over the stimulus series. Each dot represents a sound-induced escape event: large dot represents escape with two M-cells active; small dot represents escape with one M-cell active. (H) Decrease in ASR probability during stimulus series (F-statistic versus constant model: 41.5, $p < 10^{-9}$, adjusted R-squared = 0.085). (I) ASR habituation accompanied by significant decrease in the fraction of escapes with two active M-cells (F-statistic versus constant model: 9.15, $p < 0.01$, adjusted R-squared = 0.028). Statistics: linear regression model analysis. N larvae = 29. Error bars, SEM.

M-cells are the command-like neurons for the ASR network and receive multiple inputs that control the properties of the ASR behavior. We hypothesized that the firing properties of M-cells might differ between individuals with different levels of ASR habituation. To test this hypothesis, we combined detection of ASR escape behavior with calcium imaging in M-cells using the tg(s1181t:Gal4;UAS:GCaMP5) transgenic line, to drive expression of the genetically encoded calcium indicator GCaMP5 in M-cells and only a few other hindbrain and spinal neurons (Akerboom et al., 2012, Scott et al., 2007) (Figure 3D). A larva was embedded in agar, which was cut away to free the tail to obtain a head-fixed preparation where tail motion could be observed (Figure 3B). Head-fixed zebrafish are generally less responsive to sensory stimuli when compared to freely swimming fish. To maximize the number of behavioral responses obtained from each larva, and to minimize photobleaching of GCaMP5 during the extended habituation assay, we tested zebrafish at an ISI of 90 s, enabling use of short (5 s) bouts of fluorescence excitation, separated by longer periods (85 s) of time for diffusion-based recovery of the GCaMP5 signal. Acoustic-vibration stimuli were given at a fixed intensity that reliably elicited short-latency C-bend responses that are characteristic of the ASR (Figures 3B and 3C). In trials in which sound stimuli elicited escapes, we observed large M-cell calcium transients, sometimes in only one M-cell and sometimes concurrently in both (Figures 3E and 3F).

Head-fixed larval zebrafish exposed to a series of 15 sound stimuli at an ISI of 90 s showed high diversity in ASR habituation (Figures 3G and 3H), resembling the diverse behavior seen under the free swimming conditions (Figures 1B–1F). ASR latency duration was characteristic of M-cell-dependent short latency ASR (in 332 out 334 of escapes, latency < 14 ms) and did not significantly change during the stimulus series (Figure S3A). Analysis of sound-induced M-cell calcium fluorescence signals showed a decrease in peak calcium amplitudes in individual M-cells (Figure S3B), no significant changes in calcium decay times (Figure S3C), and an overall decrease in the integral of sound-evoked M-cell calcium signals during habituation (Figure S3D). Despite the fact that firing of one M-cell is sufficient to produce the escape behavior and occurred in 100% of escapes, in 54% of escapes two M-cells fired (Figures 3E–3G). Notably, the frequency of escapes with two M-cells firing was higher during the early stimuli of the habituation series and decreased later in the series, trending with the behavioral habituation (Figures 3H and 3I). Fish with sustained behavioral responses (low habituation) sustained a high probability of response in each of the M-cells and a higher frequency of dual M-cell responses when compared to high habituation individuals (Figure 3G, compare fish #1–12 with fish #13–29). The kinematics of escapes with two M-cells active did not differ significantly from those of escapes with one M-cell active (Figure S3E). This result agrees with the extensive cross-inhibition between the M-cells (Satou et al., 2009). Thus, the probability of sound-evoked calcium responses in each M-cell decreases in parallel to the habituation of the ASR behavior.

Dorsal Raphe Nucleus Activity during ASR Habituation

The individual differences in the loss of all-or-none M-cell responses during ASR habituation led us to wonder whether the excitatory drive to the M-cells, or their excitability, is subject to regulation by neuromodulatory inputs, and, if so, whether differences in neuromodulation between individuals could contribute to ASR habituation diversity. Serotonergic dorsal raphe

nucleus (DRN) neurons project axons near the M-cell dendrites (McLean and Fetcho, 2004a) (Figure 4A; Movies S1 and S2), raising the possibility that serotonin may either act directly on the M-cells or on their inputs to modulate M-cell activity and ASR habituation. We therefore set out to measure the activity of the DRN neurons during the ASR. To perform calcium imaging in serotonergic DRN neurons, we used the tg(tph2:Gal4ff)y228 line, which expresses Gal4 under the control of a fragment of the promoter of the tryptophan hydroxylase 2 gene that drives expression in serotonergic neurons in the DRN and a few spinal neurons tg(tph2:Gal4ff)y228 (Yokogawa et al., 2012). We crossed this driver line to a UAS:GCaMP5 line (Figure 4B). Transgenic head-fixed larvae were subjected to the ASR habituation protocol, as described above.

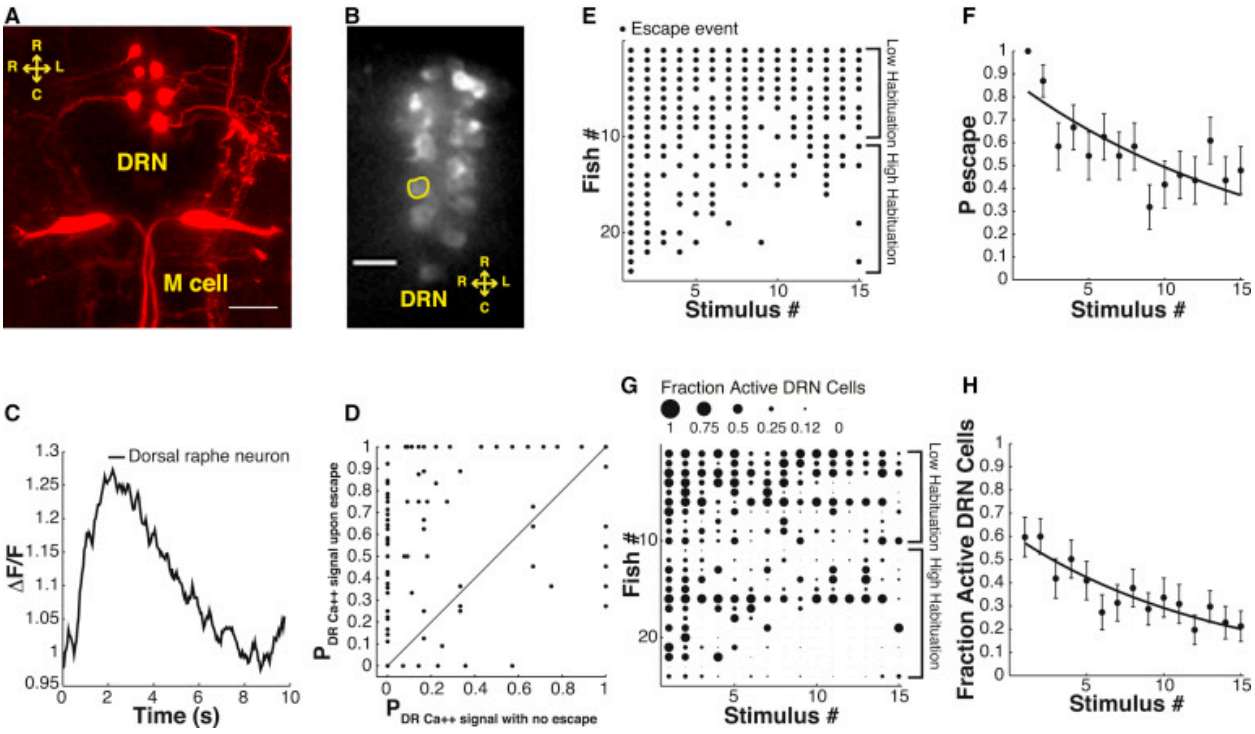

Figure 4. Simultaneous Analysis of ASR Behavior and Dorsal Raphe Nucleus Neuron Calcium Signals in 6 dpf Zebrafish Larvae (A) Image shows varicosities projecting from the dorsal raphe nucleus (DRN) toward the Mauthner cell dendrites (maximum projection of a z stack of confocal images, variegated individual shown for ease of demonstration). (B) Representative image of a confocal slice of DRN serotonergic neurons expressing GCaMP5. (C) Representative trace shows ROI normalized fluorescence in a single DRN neuron. (D) Probability of sound-evoked calcium responses for individual DRN neurons. Graph shows probability of sound-induced responses for individual cells during sound stimuli that did not induce escapes versus stimuli followed by escapes. (E) Acoustic startle responses of individual larvae ordered along y axis by probability of escape over the stimulus series. Each dot represents a sound-induced escape. (F) Significant decrease in ASR probability (F-statistic versus constant model: 23, $p < 10{-}5$, adjusted R-squared = 0.06). (G) Fractional activation of DRN neurons in individual larvae ordered in the y axis by probability of escape during stimulus series. The size of each dot is proportional to the number of cells activated by acoustic stimuli as a fraction of total number of analyzed individual neurons/fish. (H) Decrease in number of sound-activated DRN neurons as fraction of total number of analyzed individual neurons/fish during habituation (F-statistic versus constant model: 29.2, $p < 10{-}6$, adjusted R-squared = 0.073). Statistics: linear regression model analysis. 8–14 neurons/fish, nDRN neurons = 244, nlarvae = 24. Error bars, SEM. Scale bar, 25 μm.

Acoustic-vibration stimuli activated calcium signals in the DRN neurons (Figures 4B and 4C) with a similar temporal profile to responses that were shown earlier to be induced in these cells by water flow on the tail in another behavior paradigm (Yokogawa et al., 2012). Next, we asked whether this line of fish retained the variability in ASR habituation that we described above. We found similar diversity in ASR behavior habituation in larvae expressing GCaMP5 in tph2 serotonergic neurons when compared to animals expressing GCaMP5 in the M-cells and that ASR latency did not change significantly during habituation (Figures 4E and 4F; Figure S4A). Sound-induced calcium signals in individual tph2 DRN neurons were longer lasting than those of the M-cells (compare Figure 3E and Figure S3C to Figure 4C and Figure S4C). As ASR habituation progressed, single DRN neuron calcium fluorescence peak amplitude and integral decreased, but calcium decay times did not significantly change (Figures S4B–S4D).

Responses to acoustic stimulation of the DRN neuron groups within each fish revealed great diversity between individuals. Most animals responded to early sound stimuli with DRN activity and the fraction of DRN cells that responded declined as the stimulus series progressed (Figures 4G and 4H; Figure S4E). Overall, individuals with low habituation showed sound-evoked activity in a larger number of DRN neurons than did individuals with high habituation (Figures 4E and 4G, compare fish #1–10 with #11–24). Indeed, DRN neuron calcium responses were evoked much more frequently when the sound stimulus also induced the ASR behavior (Figure 4D), suggesting a causal link. However, behavioral output was not required for sound-induced activity in the DRN neurons (Figure 4D).

Together, these results suggest that the sound-evoked activity of DRN neurons suppresses ASR habituation and that variability between individuals in this activity contributes to the diversity of habituation behavior.

Serotonin and Dopamine Regulate ASR Habituation in Opposite Ways

The previous results suggest that serotonin released by DRN neurons modulates ASR circuit function and escape behavior. We tested this pharmacologically first for serotonin and then for a second major neuromodulator, dopamine, which often works either in tandem with or in opposition to serotonin (Boureau and Dayan, 2011). Consistent with the observation that individuals with low habituation display high activity in serotonergic DRN neurons, we found that although treatment with the broad serotonergic agonist quipazine did not affect the initial probability of escape under non-habituating conditions (ISI = 90 s) (Figure 5A), it strongly reduced habituation of stably responsive larvae, $P_{initial} > 0.9$, shifting the population distribution of HI values to lower levels (Median $_{HI\ Control} = 0.76$, Median $_{HI\ Quipazine} = 0.56$, $p < 10{-}16$) (Figure 5B). Strikingly, treatment with the broad dopaminergic agonist apomorphine increased the initial probability of escape (Figure 5D), but had the opposite effect of serotonin signaling, and strongly increased ASR habituation (Median $_{HI\ Control} = 0.76$, Median $_{HI\ Apomorphine} = 0.91$, $p < 10{-}12$) (Figure 5E). Thus, it appears that the distribution of individual ASR habituation phenotypes in a population is controlled in opposite ways by serotonin and dopamine. In contrast to the pronounced effect on ASR habituation at the population level, serotonergic agonism only

slightly decreased spontaneous activity levels at the population level (Figure 5C) (Median $_{\text{Distance Control}}$ = 44.3 cm, Median $_{\text{Distance Quipazine}}$ = 38.4 cm, $p < 0.015$). Similarly to previous findings, dopaminergic agonism strongly decreased spontaneous activity (Figure 5F) (Median $_{\text{Distance Control}}$ = 44.3 cm, Median $_{\text{Distance Apomorphine}}$ = 0 cm, $p < 10{-}6$) (Thirumalai and Cline, 2008).

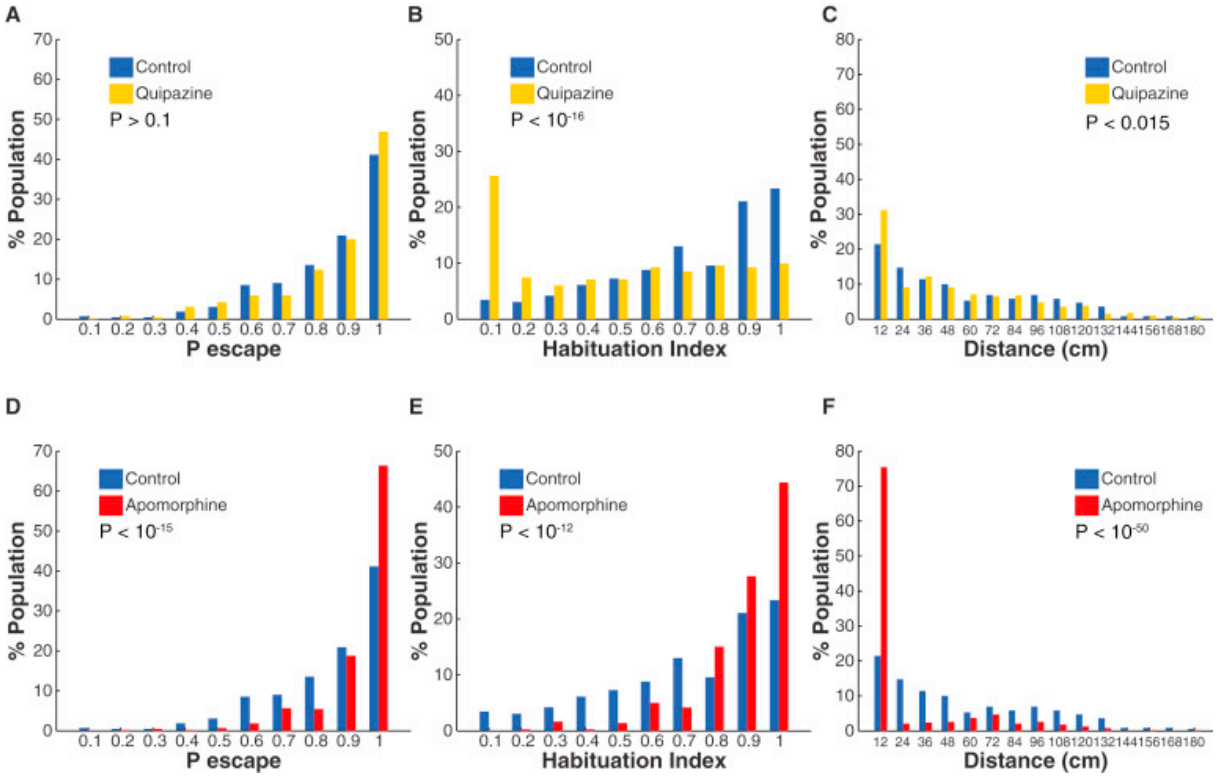

Figure 5. Effect of Serotonin and Dopamine Agonists on ASR Habituation and Spontaneous Swim Behavior (A–C) Treatment with serotonin receptor agonist (quipazine 50 µM). (A) Quipazine treatment does not significantly affect ASR probability under non-habituating conditions (nControl = 420, nQuipazine = 420, z = 1.53, $p > 0.1$). (B) Quipazine treatment shifts the habituation index (HI) frequency distribution to lower values (less habituation) (n_{Control} = 261, $n_{\text{Quipazine}}$ = 281, z = 8.4, $p < 10{-}16$). (C) Quipazine treatment shifts the frequency distribution of total displacement during 10 min to lower values when compared to control group (n_{Control} = 359, $n_{\text{Quipazine}}$ = 394, z = 2.5, $p < 0.015$). (D–F) Treatment with dopamine receptor agonist (apomorphine 15 µM). (D) Apomorphine treatment increases initial ASR probability (n_{Control} = 420, $n_{\text{Apomorphine}}$ = 420, z = 8.2, $p < 10{-}15$). (E) Apomorphine treatment shifts HI frequency distribution to higher values (greater habituation) (n_{Control} = 261, $n_{\text{Apomorphine}}$ = 358, z = 7.38, $p < 10{-}12$). (F) Apomorphine treatment significantly shifts the frequency distribution of total displacement values during 10 min to lower values when compared to control group (n_{Control} = 359, $n_{\text{apomorphine}}$ = 383, z = 15.12, $p < 10{-}50$). Two-tailed Mann-Whitney test.

Reduction in DRN Serotonin Increases ASR Habituation

Our findings so far suggest a model in which serotonergic neuromodulation of the ASR circuit suppresses habituation of the ASR behavior and that differences between individuals in neuromodulation are associated with differences in ASR habituation. To test this model, we sought to disrupt the serotonergic DRN neurons and ask whether this would result in greater habituation. Previous studies in rat cell cultures implicated the cAMP signaling pathway in regulating the development of serotonergic neurons (Rumajogee et al., 2005). We therefore set out to manipulate cAMP signaling in DRN serotonergic neurons. To accomplish this goal, we built a transgenic line in which expression of a dominant-negative peptide for the Gαi subunit of the heterotrimeric G protein complex (DNGαi) (Dell et al., 2013) is controlled by UAS sequences tg(tph2:Gal4ff;UAS:DNGαi,gap43-citrine). We crossed these with the transgenic line tg(tph2:Gal4ff)y228 to induce DNGαi expression in DRN neurons (Yokogawa et al., 2012). Immunofluorescence analysis of the tg(tph2:Gal4ff;UAS:DNGαi,gap43-citrine) line using an antibody directed against serotonin and intrinsic fluorescence of membrane-targeted citrine fluorescent protein revealed that the DNGαi peptide is expressed specifically in serotonergic DRN neurons, but not in adjacent hypothalamic serotonergic neurons (Yokogawa et al., 2012) (Figures 6A and 6B). Expression of DNGαi was detected in ∼20%–50% of DRN neurons and occasionally in isolated cells in the spinal cord, consistent with earlier work (Yokogawa et al., 2012). In contrast to previously reported results in primary neuronal cultures (Rumajogee et al., 2005), DNGαi expression in the DRN did not affect the number of serotonergic neurons in the DRN (Figure 6C). Moreover, hypothalamic serotonergic neurons, which do not express the DNGαi peptide, were also not affected in number (Figure 6C). However, the fraction of DRN neurons that expressed the DNGαi peptide, which were marked green by the co-expressed citrine fluorescent protein, had lower amounts of serotonin than did neurons in the same DRN that were unmarked and did not express the DNGαi peptide (Movie S3). DNGαi expression significantly reduced serotonin content in DRN neurons in 12 out of 12 individual larvae examined by an average of ∼30% ($p < 0.001$) (Figure 6D). Importantly, animals expressing DNGαi in DRN cells had similar serotonin levels in the hypothalamus when compared to control animals (Figure S5A).

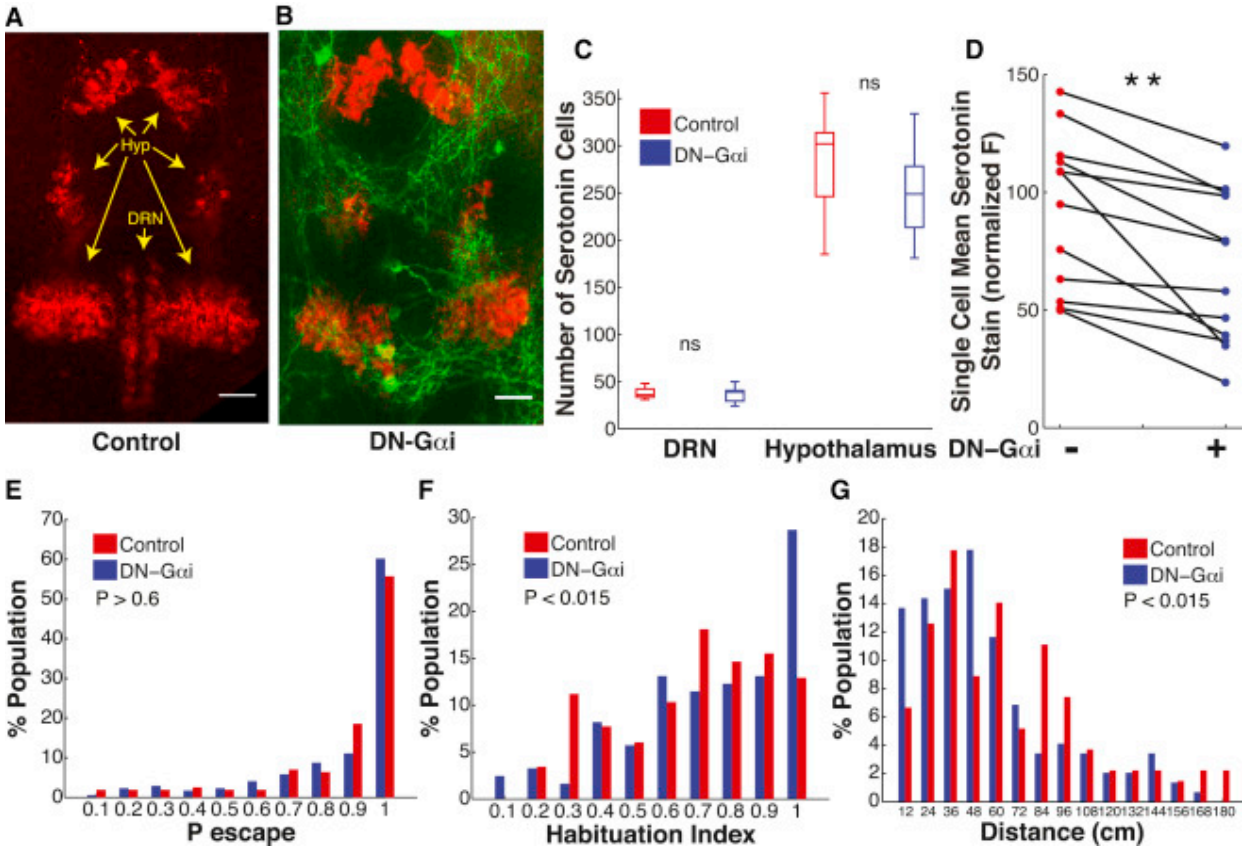

Figure 6. Effect on ASR Habituation of Reduced Serotonin Content in DRN Serotonergic Neurons (A-B) Representative images of labeling with serotonin antibody (red) in control larva (A) and in tg(Tph2:Gal4ff;UAS:DNGαi,gap43-citrine) larva that co-expresses DN-Gαi and citrine fluorescent protein (green) in DRN serotonergic neurons (B). Scale bars, 25 μm. (C) DRN DNGαi expressing larvae do not have significantly different numbers of serotonergic neurons in the DRN or hypothalamic serotonergic nuclei (nDN-Gαi = 11, nControl = 11, $p > 0.9$). Central mark of box plots is the median value, vertical edges are the 25th and 75th percentiles and whiskers are the extreme values of distribution of numbers of serotonergic neurons for each group. (D) DRN neurons co-expressing DN-Gαi and citrine fluorescent protein (green) have significantly lower mean serotonin content than neurons in the same DRN that do not express (n = 12 larvae, $**p < 0.001$). (E) ASR probability under non-habituating conditions in DN-Gαi expressing larvae compared to control sibling larvae (nDN-Gαi = 171, nControl = 156, $z = 0.43$, $p > 0.06$). (F) DN-Gαi larvae habituation index frequency distribution is shifted to higher values (more habituation) compared to control larvae (nDN-Gαi = 122, nControl = 116, $z = 2.28$, $p = 0.011$). (G) Frequency distribution of total displacement during 10 min in DN-Gαi larvae is shifted toward decreased displacement compared to control larvae (nDN-Gαi = 146, nControl = 106, $z = 2.46$, $p = 0.014$). Statistics: unpaired, two-tailed Student's t test (C), paired, two-tailed Student's t test (D), two-tailed Mann-Whitney test (E–G).

Consistent with our findings above, we found that decreased serotonin content in DRN serotonergic neurons did not affect ASR probability under non-habituating conditions (Figure 6E), but significantly increased the frequency of individuals with high ASR habituation when compared to a population of control sibling larvae with no DNGαi expression (Median HI Control = 0.76, Median HI DN-Gαi = 0.83, $p < 0.015$) (Figure 6F).

Tg(tph2:Gal4ff;UAS:DNGαi,gap43-citrine) transgenic larvae developed normally and were morphologically indistinguishable from control sibling larvae with no DNGαi expression (Figure S5B). Larvae with DNGαi expression were slightly decreased in median spontaneous swim activity levels compared to control sibling larvae (Median D Control = 58.2 cm, Median D DN-Gαi = 46.7 cm, $p < 0.015$) (Figure 6G). Similarly to our previous observation (Figure 2D), we did not observe significant correlation between spontaneous swim activity levels and HI in control larvae or in larvae expressing DNGαi under control of the tph2 promoter (Pearson's correlation coefficient Distance versus HI Control, $r = 0.0948$, $p = 0.23$, Distance versus HI DN-Gαi, $r = -0.0104$, $p = 0.89$).

DRN Activation with Channelrhodopsin-2 Suppresses ASR Habituation

Having seen that reduction of the serotonin content of DRN neurons increased the fraction of individuals with high ASR habituation, we asked whether stimulating these cells to promote serotonin release would have the opposite effect and reduce habituation. To do this, we generated zebrafish larvae expressing YFP-tagged ChR2 (Lacoste et al., 2015) specifically in the DRN neurons. In tg(tph2:Gal4ff; 14xUAS-E1b:hChR2(H134R)-EYFP) larvae, ChR2 expression was restricted to the DRN and did not include other serotonergic populations (Figure 7A). We examined whether DRN activation with ChR2 modified ASR habituation in the head-fixed larval preparation, as above (Figures 3 and 4). ChR2-expressing DRN neurons and neuronal processes were illuminated with laser light (488 nm, 1 s, 14 mW/mm2) administered through the microscope objective (40×/1.1), which yielded minimal light scattering to the eyes (Figure 7A). To mimic the pattern of DRN activation induced by acoustic stimuli, which activate DRN neurons at the same time as they activate the M-cell circuit, we paired the sound stimulus with optical activation of ChR2 in DRNs (Figure 7B).

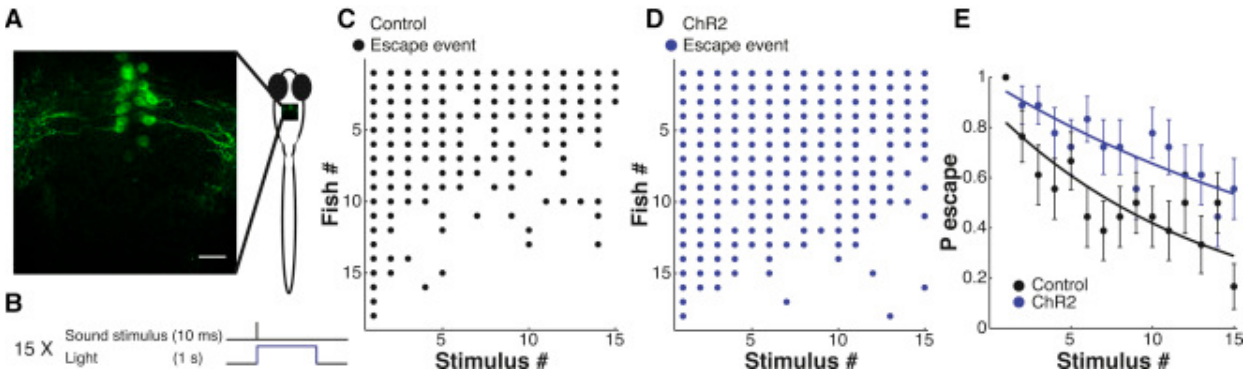

Figure 7. Effect on ASR Habituation of DRN Activation with Channelrhodopsin-2 (A) Representative image showing channelrhodopsin-2 (ChR2)-YFP expression in cell bodies and processes of DRN neurons in tg(tph2:Gal4ff; 14xUAS-E1b:hChR2(H134R)-EYFP) in 6 dpf larva. (B) Protocol showing single stimulus from habituation series, pairing illumination at 488 nm (to activate ChR2 in DRN neurons) with sound stimulation (to elicit the ASR). (C and D) Acoustic startle responses of all of the individual larvae ordered in the y axis by probability of escape during the stimulus series, separated into two groups from the sibling larvae: not expressing ChR2-YFP (C, Control) and those expressing ChR2-YFP (D, ChR2). Each dot represents a sound-induced escape. (E) Plots of mean ± SEM of data shown in (C) and (D) showing less habituation in siblings with ChR2 in DRN neurons (nChR2 = 18, nControl = 18, analysis of covariance, F-statistic: 28.24, $p < 10^{-6}$).

We measured ASR habituation in individual larvae expressing ChR2 in DRN neurons and in sibling larvae that did not express ChR2 but which were exposed to the same light stimuli. We found that the ChR2-expressing fish showed lower habituation compared to their non-expressing sibling controls (analysis of covariance, F-statistic: 28.24, $p < 10^{-6}$) (Figures 7C–7E). Thus, as shown in the previous section, ASR habituation is increased by reduction of DRN neuron serotonin content (and presumably release) and, as shown here, decreased by optogenetic stimulation of the DRN neurons (and presumably promotion of serotonin release).

Differences in DRN Activity Co-segregate with Behavioral Differences

Having observed heritability in high versus low ASR behavioral habituation and having observed that the higher the behavioral habituation, the faster the rundown of activity in serotonergic DRN neurons, we wondered whether behavioral habituation and DRN neuron rundown would co-segregate between generations. To test this, we measured DRN neuron activity during ASR habituation, as above (Figure 4), in the F1 progeny of F0 animals that had been selected in our high-throughput apparatus (Figure S2, F0 Low HI couple 2 or F0 High HI couple 3).

We found that although the behavioral selection was done in freely swimming fish and subsequent testing in head-fixed fish, F1 Low HI fish had significantly lower habituation rates than F1 High HI fish (Figures 8A–8C). This result confirms that habituation is heritable, as shown above (Figure 2E and Figure S2), and suggests that the regulation of ASR habituation is similar in freely swimming and head-fixed preparations. Next, we compared DRN activity in the high and low habituation F1 groups. Consistent with the above evidence that DRN serotonergic

neuronal activity suppresses ASR habituation, we found that sound-evoked activation of DRN serotonergic neurons was stronger and showed less rundown in F1 Low HI larvae than in F1 High HI larvae (Figures 8D–8F). This amounted to an ∼180% higher integrated area under the response curves during habituation (Figure 8F) in the low habituation group. Behavioral latencies were slightly increased in low HI larvae as a group when compared to high HI larvae at the end of the stimulus series (Figure S6A). Single DRN neuron mean calcium peak values decreased during ASR habituation in both high and low HI groups but were significantly higher in the low HI group (Figure S6B). Single neuron mean calcium decay values did not change significantly during habituation and were not significantly different between groups (Figure S6C). The mean values of the integral of the calcium flux in DRN neurons also decreased during ASR habituation and were significantly higher in F1 low HI larvae (Figure S6D). In summary, differences in sound-evoked activation of DR serotonergic neurons co-segregate with heritable individual differences in ASR habituation (Figure 8G).

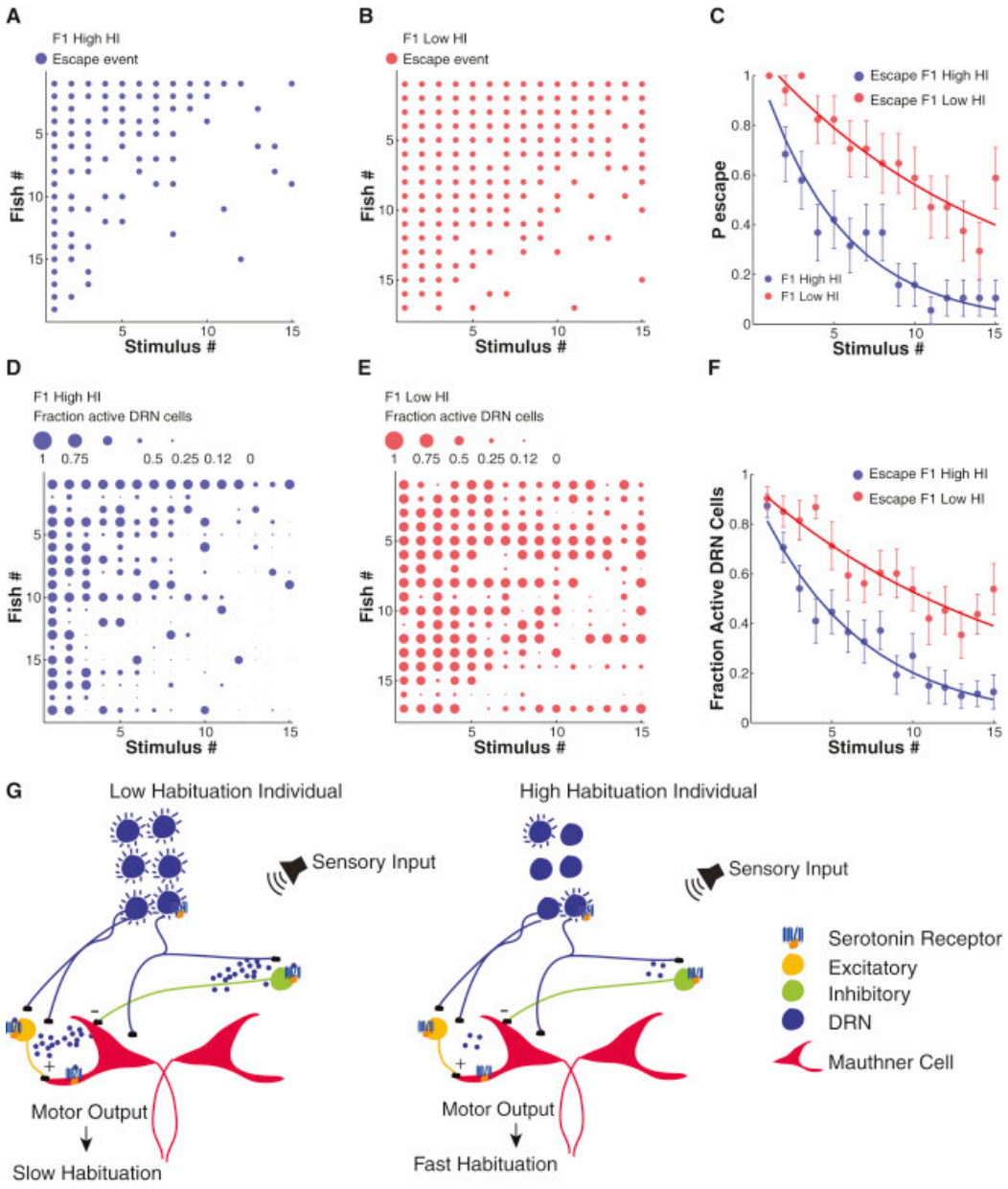

Figure 8. ASR Habituation Behavior and DRN Neuronal Activity in F1 Progeny of Zebrafish Selected for High or Low Habituation (A and B) Acoustic startle responses of individual larvae ordered in the y axis by probability of escape during stimulus series. Each dot represents a sound-induced escape. (C) Slower habituation in F1 Low HI zebrafish larvae compared to F1 High HI group (F-statistic: 90.51, $p < 10{-}19$). (D and E) Fractional activation of DRN neurons in individual larvae ordered in the y axis by probability of escape during stimulus series. The size of each dot is proportional to the number of cells activated by acoustic stimuli as a fraction of total number of analyzed individual neurons/fish. (F) Larger number of sound-activated DRN neurons as fraction of total number of analyzed individual neurons/fish in F1 Low HI zebrafish larvae compared to F1 High HI group (F-statistic: 86.45, $p < 10{-}18$). Statistics: analysis of covariance. 12–16 neurons/fish. n Low HI DRN neurons = 248, n High HI DRN neurons = 268, n Low HI larvae = 17, n High HI larvae = 19. Error bars, SEM. (G) Model illustrating how differential activation of DRN serotonergic neurons by acoustic stimuli contributes to differential habituation in the ASR circuit.

Discussion

ASR Habituation Is Diverse, Stable, and Heritable

Inter-individual differences in behavior are common in animal populations and underlie the related concepts of animal individuality and personality (Wolf and Weissing, 2012). Behavioral variability in individuals is due to genetic, developmental, pharmacological, environmental, and social processes (Kappeler and Anthes, 2010, Laskowski and Bell, 2014). Inter-individual behavioral variation is widely observed across animal phyla and might be under selective pressure during animal evolution (Ayroles et al., 2015, Laurila et al., 2008). However, variation among individuals is often ignored when behavior is quantified as averages with associated dispersions (Geiler-Samerotte et al., 2013). In vertebrates, it has been challenging to study the extent of behavioral variation in outbred populations and the associated neural mechanisms that underlie behavioral variation at the individual level. In the present study, we used zebrafish in an effort to identify properties of a neural circuit that determine behavioral individuality and generate behavior diversity at the population level.

Our high-throughput behavioral analysis revealed a large diversity in the rate of ASR habituation between individual wild-type larval zebrafish. Interestingly, this large inter-individual behavioral diversity was present in laboratory conditions, where the role of environmental factors in determining behavioral differences is minimized. In fact, we found that differences in the rate of habituation between individuals are maintained over days and are heritable, indicating that ASR habituation has a genetic or epigenetic component. The genetic implications are consistent with recent findings from a forward genetic screen in larval zebrafish, which identified several mutants that affect ASR habituation without affecting startle performance (Wolman et al., 2015). Two of these genes were identified: one encoding the metabolic enzyme pyruvate carboxylase and the other the pregnancy-associated plasma protein A, a secreted metalloprotease. Although the mechanisms through which these genes affect ASR habituation are unclear, it is possible that polymorphisms in them contribute to the diversity of ASR habituation in wild-type populations.

In humans, differences in behavior are also heritable and variations in genes involved in dopamine and serotonin signaling are associated with differences in personality and heritable psychiatric conditions (Kishi et al., 2013, Ptácek et al., 2011). Furthermore, patients with a diagnosis of schizophrenia have ASR habituation deficits (Braff et al., 1992). Because the ASR habituation behavior is an example of an animal personality trait that is present at the zebrafish larval stage it represents an attractive vertebrate paradigm to investigate the neural bases of behavioral individuality.

In contrast to the properties of ASR habituation, which show stable differences between individuals, quantitation of the spontaneous swim locomotor behavior showed diversity among individuals but lack of stability over a period of days. Intriguingly, a recent study found that differences in spontaneous locomotor behavior were stable over days in adult zebrafish and more robust in female zebrafish than in males (Tran and Gerlai, 2013). Zebrafish sex-specific gonadal differentiation begins around 1 month post-fertilization (Takahashi, 1977). It is possible that the circuits controlling spontaneous locomotor behavior are subject to developmental control and

that differences between individuals that are unstable early in life are crystalized as animals reach full sexual maturity. Comparison of the two behaviors in young and older adult zebrafish will be useful to address the mechanisms that lead to stability in behavioral parameters during development.

Inter-individual Differences in ASR Circuit Properties

To determine whether differences between individuals in properties of the ASR neural circuit account for variation in ASR habituation in a population, we monitored ASR-inducing M-cell calcium signals during a series of sound pulses that produced ASR habituation. During habituation, M-cell calcium fluxes decreased as the stimulus series progressed. Typically, the two M-cells were activated simultaneously early in the stimulus series and more than half of escapes in the entire series involved their simultaneous activity, as recently reported and found to be blocked by strychnine or MK-801, suggesting that change in glutamatergic and/or glycinergic input to M-cells or their inputs participates in ASR habituation (Marsden and Granato, 2015).

But what is the cause of the inter-individual difference in M-cell ability to follow repeated stimulation? Both dopamine and serotonin containing neurons have processes near the M-cells and these neuromodulators have been shown to influence the startle behavior (Lillesaar et al., 2009, McLean and Fetcho, 2004a, McLean and Fetcho, 2004b, Mu et al., 2012, Wolman et al., 2011). Previous studies in adult goldfish showed that serotonin inhibits M-cell activity pre- and post-synaptically (Mintz and Korn, 1991) and that in adult cichlid fish, serotonergic inputs modulate activity of M-cells and their inhibitory glycinergic inputs, while the 5-HT2R antagonist ketanserin increases startle probability (Whitaker et al., 2011). In contrast to what was reported in cichlid fish, the 5-HT2R antagonists ritanserin and pirenperone enhance ASR habituation in larval zebrafish (Wolman et al., 2011). We found that treatment with quipazine does not affect ASR probability under non-habituating conditions, but strongly suppresses habituation under strongly habituating conditions. The results of Wolman et al. are consistent with our observation that treatment with quipazine decreases ASR habituation (Figure 5B), while the discrepancy between these results and those of Mintz et al. and Whitaker et al. might be due to experimental differences in ISI, and/or developmental or species differences. In our study, we sought to determine whether the activity of DRN serotonergic neurons is involved in the ASR individuality.

Differences in Neuromodulatory Input between Individuals

Differences in neuromodulation have been previously shown to be associated with differences in behavioral state in mouse (Tereshchenko et al., 2008, Zalocusky et al., 2016), Caenorhabditis elegans (Mersha et al., 2013), honeybee (Müller and Hildebrandt, 2002), and Aplysia californica (Glanzman et al., 1989). Moreover, studies in the sea slug Pleurobranchaea californica, in Drosophila, and in C. elegans suggest that serotonergic modulation of behavior variability seems to be conserved during evolution (Flavell et al., 2013, Kain et al., 2012, Lillvis and Katz, 2013). We found that the sound stimulus that triggers the ASR also triggers activity in serotonergic DRN neurons whose nerve terminals project widely in the larval zebrafish brain and traverse the hindbrain in close proximity to M-cell dendrites and, hence, to their inputs (Lillesaar et al., 2009,

Yokogawa et al., 2012). Animals in which a larger number of DRN neurons responded to the sound stimulus and dropped out more slowly during repeated sound stimulation had lower habituation. Consistent with this, ASR habituation was decreased by either application of a serotonin agonist or optogenetic stimulation of DRN neurons. In further support, a genetic manipulation that reduced the serotonin content of the DRN serotonergic neurons had the opposite effect and increased habituation. Thus, variability between individuals in the ability of DRN neurons to respond to and follow repeated bouts of startling sensory input appears to contribute to diversity of habituation rates.

The identity of the neuronal populations that are the targets of DRN inputs and mediate the behavioral impact of differential DRN activation by sensory stimuli remains unknown. We speculate that elements of the ASR circuit in the hindbrain mediate these effects (Figure 8G). First, we observed differential drop-off of M-cell activity between individuals during ASR habituation. Second, serotonin modulates M-cells and the inhibitory glycinergic neurons that control ASR circuit gain. Third, the DRN send projections that traverse the hindbrain. These results are consistent with a model in which individual differences in serotonergic signaling to the hindbrain M-cell circuit mediate the behavioral impact of differential DRN activation by sensory stimuli (Figure 8G). It is also possible that individual differences in DRN-dependent serotonergic signaling affecting additional nodes of the ASR circuit located in the mid-brain or forebrain, for example, participate in the control of ASR habituation individuality.

The cause of variability in DRN responses between individuals remains to be determined as does the question of whether it is cell autonomous or due to differences in synaptic input to the DRN neurons. Multiple stimuli activate DRN neurons in larval zebrafish (Cheng et al., 2016, Filosa et al., 2016, Yokogawa et al., 2012); however, the neuroanatomy of the circuits that provide the synaptic inputs that mediate activation of the DRN is unknown. In adult zebrafish it has been proposed that the dorsal interpeduncular nucleus might send projections to the DRN (Agetsuma et al., 2010). In mice, the DRN receives inputs from multiple brain nuclei and multiple sensory modalities affect the properties of DRN neurons (Pollak Dorocic et al., 2014, Ranade and Mainen, 2009, Weissbourd et al., 2014). Moreover, transient activation of serotonergic neurons in the DRN acutely modulates behavioral states in mice and zebrafish (Cheng et al., 2016, Miyazaki et al., 2014, Yokogawa et al., 2012). Thus, it is possible that variation in DRN activation by sensory inputs might also contribute to inter-individual behavioral diversity in mammals. In Aplysia, sensory feedback participates in the control of behavioral variability by increasing intra-individual variability in motor neurons that participate in swallowing behavior control (Cullins et al., 2015). In fact, sensory inputs appear to participate in the control of behavioral variability at the population level and may increase or decrease behavioral variability at the individual level. Our work suggests that differential activation of neuromodulatory networks by sensory inputs may be a key mechanism through which sensory systems control behavioral variability (Figure 8G).

After a single round of behavioral selection for animals with low versus high habituation, we obtained F1 animals with significant differences in ASR habituation behavior and the strength and sustainability of serotonergic DRN neuron activity in response to sensory activation. This

observation indicates that differences in the sensory activation of the DRN are heritable and may provide a neural substrate upon which selection could act to shape behavioral diversity at the population level. Observation of behavior and neural activity in single individuals also reveals that some individuals with high levels of DRN activity had high habituation (Figures 4 and 7). Conversely, low DRN activity was not fully correlated with high habituation rates (Figures 4 and 7). Previous studies have shown that dopaminergic inputs modulate several nodes of the ASR network (Mu et al., 2012, Pereda et al., 1992, Toro et al., 2015). Significantly, a dopamine agonist had the opposite effect of the serotonin agonist, and decreased habituation, despite increasing pre-habituation ASR probability, suggesting that individuality in this adaptive behavior may be determined by the operational balance between dopaminergic and serotonergic drive to the escape circuit.

In conclusion, our study shows that sensory-evoked responses in a neuromodulatory network can be dynamic, vary greatly between individuals, and participate in the shaping of individuality in a core adaptive behavior in zebrafish, which may, for its parallels to the startle circuits of other vertebrates and importance of neuromodulation, be relevant to psychiatric disorders.

Methods

Zebrafish Transgenesis and High-Throughput Behavioral Assay

The transgenic lines used in this study were generated with the Tol2 transposase transgenesis system. Detailed description of transgenesis procedures can be found in Supplemental Experimental Procedures. The high-throughput behavioral assay was performed in multi-wells, as described earlier (Levitz et al., 2013).

Immunohistochemistry in Larval Zebrafish

We quantified the number of serotonergic cells and 5-HT content using immunohistochemistry against 5-HT (MAB352, 1:200, Millipore) in embryos obtained from crosses of tg(tph2:Gal4ff) fish to tg(cmlc2:Kal4/cry:Red;UAS:DNGαi) fish. Detailed protocols for immunohistochemistry and image analysis are presented in the Supplemental Experimental Procedures.

Head-Mounted Behavioral Assay with Calcium Imaging and ChR2 Activation

For behavioral experiments with simultaneous calcium imaging and sound stimulus presentation larvae were mounted in a glass well petri dish dorsal side down with free tail in 2% agar E3 solution. ChR2 activation was accomplished with 488 nm laser light (∼14 mW/mm2) administered through a 40×/1.1 Zeiss objective, at a focal plane encompassing DRN neurons cell bodies and processes, and lasted for 1 s. ChR2 activation was initiated simultaneously with sound stimulus. Control fish without ChR2 expression were subjected to the same protocol. Detailed description of the experimental set up is included in the Supplemental Experimental Procedures. Animal experiments were approved by the University of California Animal Care and Use Committee.

Behavioral Analysis

Behavioral analysis was performed using custom MATLAB scripts previously described and modified for the present study (Bianco et al., 2011, Levitz et al., 2013). Scripts are summarized in the Supplemental Experimental Procedures.

The Habituation Index (HI) is defined as the difference in escape probability to the last 40 high-level stimuli under habituating conditions (5 s ISI) with the first 10 high-level stimuli under non-habituating conditions (90 s ISI), divided by the probability of escape to the last 40 stimuli (HI = (Plast40 − Pfirst10)/Plast40). Only fish that responded 90% or more to the initial 10 high-level stimuli were used in calculating the HI.

Calcium Imaging Analysis

Analysis of calcium signals was performed with custom-written MATLAB scripts and is described in the Supplemental Experimental Procedures. All scripts used in this study are freely available upon request.

Statistics and Data Analysis

Data and statistical analysis were performed using MATLAB. Unless noted, all data points reported are mean ± SEM. No statistical methods were used to estimate required sample sizes. Sample sizes used in this study are similar to those reported in similar studies previously published (Brustein et al., 2003, Whitaker et al., 2011, Wolman et al., 2011, Yokogawa et al., 2012). Investigators conducting the experiments were not blind to the groups being tested or analyzed. The one- or two-sided Mann-Whitney U test was used in comparing the nonparametric distributions of HIs among groups. The two-sided Student's t test was used to compare distributions of serotonergic cell numbers and serotonin content in the DRN neurons. Linear regression model was used to determine variation of behavioral or calcium signals during stimulus series. The one-way analysis of covariance with linear fits for each group was used to compare groups with different habituation levels in experiments with head-mounted fish.

Zebrafish transgenesis

Primers 5'- ATATATGGATCCTCACGTTACTAGTATGGGTTCTC -3' and 5'-ATATATGCGGCCGCTCACAAAGATCCTCTAGACTTCG -3' were used to PCR amplify the open reading frame (ORF) of GCaMP5.003. The GCaMP5.003 ORF was inserted into the PME-MCS vector, the middle vector in the Tol2 zebrafish transgenesis Gateway® kit. The PME-MCS-GC5 vector was combined with the p5E-UAS, p3EpolyA and pDestTol2pA2 vectors with the Multisite Gateway® technology to generate the Tol2-UAS:GCaMP5 fish transgenesis vector.

Tg(cmlc2:Kal4/cry:red) AB line embryos, in which a modified version of the transcription factor Gal4 is expressed in the larval zebrafish heart, were injected at the one-cell stage with Tol2-UAS:GCaMP5 or Tol2- UAS:DNGαi1/2;UAS:citrine (gift from the Raper lab, University of Pennsylvania) plasmid DNA (30 ng/ml), RNA for the Tol2 transposase (25 ng/µl) and 0.1% Phenol Red (wt/vol). F0 founder fish that generated tg(cmlc2:Kal4/cry:Red;UAS:GCaMP5) or tg(cmlc2:Kal4/cry:Red;UAS:DNGαi1/2;UAS:citrine) F1 fish, with GCaMP5 or DNGαi1/2-

citrine expression in the heart, were crossed to wild-type fish to create stable lines. The tg(s1181t:Gal4; UAS:GCaMP5) line, in which Gal4 drives expression of GCaMP5 in the Mauthner cells and a few additional hindbrain and spinal neurons, was generated by crossing tg(cmlc2:Kal4/cry:Red; UAS:GCaMP5) fish to tg(s1181t:Gal4) fish (gift from the Baier laboratory, Max Planck Institute for Neurobiology) and phenotypically screening out the cmlc2:Kal4/cry:red insertion. Tg(s1181t:Gal4;UAS:GCaMP5) zebrafish were crossed to tg(tph2:Gal4ff) zebrafish (gift from the Burgess laboratory at the Laboratory of Molecular Genetics, NICHD, National Institutes of Health) to generate line tg(s1181t:Gal4; tph2:Gal4ff; UAS:GCaMP5) in which Gal4 drives expression of GCaMP5 in serotonergic cells and the s1181t expression pattern. The tg(s1181t:Gal4; tph2:Gal4ff; UAS:GCaMP5) line was used to monitor activity in dorsal raphe neurons. Tg(tph2:Gal4ff; UAS:DNGai) larvae and tg(cmlc2:Kal4/cry:Red;UAS:DNGai) larvae were generated by crossing tg(tph2:Gal4ff) fish to tg(cmlc2:Kal4/cry:Red;UAS:DNGai) fish. To generate zebrafish larvae expressing ChR2 specifically in the DRN tg(14xUAS-E1b:hChR2(H134R)-EYFP; 6.7FRhcrtR:gal4VP16) fish were crossed to tg(tph2:Gal4ff) fish. Phenotypical screen was employed to separate tg(tph2:Gal4ff; 14xUAS-E1b:hChR2(H134R)-EYFP) larvae that express ChR2 in the DRN, or sibling larvae with no fluorescence that were used as controls. The tg(6.7FRhcrtR:gal4VP16; 14xUAS-E1b:hChR2(H134R)-EYFP) line was a gift of Alex Schier's laboratory, Department of Molecular and Cellular Biology, Harvard University.

High-throughput behavioral assay

AB line larval zebrafish were raised in petri dishes (Corning) at low densities (~2 fish per mL) at 28.5 °C in E3 medium. In order to ensure intact ASRs as well as minimize developmental variation, fish without inflated swim bladders and that did not respond to a light tap on the dish were removed at 4 dpf. For the high-throughput microplate experiments the zebrafish larvae submitted to different treatments were randomly transferred with a pipette from the incubation petri dish to the 48-well multi-well plate (Corning) in 300 µL of E3 zebrafish embryo medium. Zebrafish larvae exposed to different treatments were evenly distributed in the plate, to minimize the possibility of spatial bias in the acoustic-vibration stimulus, and were tested simultaneously. Larvae used in singleday experiments were 6 dpf, whereas those used in the three-day long experiments were 5-7 dpf. For the three-day experiments, the fish were kept in the microplates with 1300 µL E3 overnight at 28.5 °C between measurements. The medium was refreshed the next day and then readjusted to 300 µL for the next habituation trial.

During experiments 48-well microplates were housed within a plexiglass box kept inside an isolated dark chamber. The environment was controlled and constant diffuse white light was supplied by a 60W bulb. Behavioral activity within the microplate was recorded with CCD camera (fire-i 780b, Unibrain, 30 fps), which was backlit by an array of infrared LEDs. Sound stimuli were administered by two speakers (Visaton SC 5.9) mounted to the same platform as the microplate. The speakers were powered by a 15W amplifier and delivered 900Hz square waves of ~ 3 ms duration. Stimuli were delivered via a Native Instruments PCI-6229 DAQ controlled by MATLAB.

The behavioral assay in multi-wells consisted of 15 min of acclimation to the high-throughput apparatus, followed by 10 min of spontaneous activity recording, and then the habituation protocol. The habituation protocol consisted of 10 low-voltage (0.025 V, ~ 75 dB) stimuli at 90 s ISI, 10 high-voltage (0.4 V, ~ 95 dB) stimuli at 90 s ISI, and then 100 high-voltage (0.4 V, ~ 95 dB) stimuli at 5 s ISI. In the experiments involving pharmacological treatments, the fish were incubated in a given drug for 1 h. The last 15 min of incubation took place during the acclimation period; thus, spontaneous activity recording started 1 h after treatment began. All behavioral experiments were performed in a controlled environment at 22 °C. For each behavior experiment, data was analyzed from randomly sampled larval zebrafish derived from multiple clutches obtained in different days. For the selection experiments, selected low or high HI fish were each raised in separate tanks at low density (~2 fish/L). The transgenic lines used in this study (Figures 2E, 3,4,6, 7 and 8) were obtained by crossing transgenic fish obtained from other labs or generated in our own lab. For those experiments, it was not possible to standardize the genetic background. Because different zebrafish strains vary in average locomotor behavior (de Esch et al., 2012), it is possible that differences in ASR probability and ASR habituation among the control groups in different figures reflect differences in strain background. To get around this source of variation, our experiments always compared siblings from the same cross that were randomly sampled and measured simultaneously in the same multi-well plate.

The pharmacological agents used in this study were supplied by TOCRIS bioscience and were diluted according to supplier instructions; control groups were exposed to the solvent recommended for each agent at concentrations not higher than 0.1 %. Drugs used in this study: (R)-(-)-Apomorphine hydrochloride (Cat. No. 2073), quipazine (Cat. No. 0629).

Immunohistochemistry in larval zebrafish

Larvae were anesthetized with tricaine and then fixed in 4% paraformaldehyde O/N, followed by methanol fixation. Larvae were treated with 1 mg/ml collagenase for 1 h at room temperature before incubation with primary antibody. Alexa Fluor 594-conjugated secondary antibodies (1:200; Invitrogen) were used to detect primary antibody. 5-HT immunofluorescence (excitation laser 594 nm, emission 599-734 nm) or gap43-citrine intrinsic fluorescence (excitation laser 514 nm, emission 519-589 nm) signals were independently detected in whole-mounted larvae with confocal imaging on a Zeiss LSM 880 NLO AxioExaminer confocal microscope with a 20x/1.0 water objective (Carl Zeiss). Image stacks were pre-processed by applying a 3-dimensional Gaussian filter of 2 um, and rotating each z-stack so that DRN and hypothalamus regions were easily separable by z-plane. Cell counts and mean 5-HT content were subsequently determined from sum projections of the set of z-planes corresponding to either DRN or hypothalamus. Cells were detected semi-automatically based on regional maxima using the Fiji distribution of ImageJ. Cells expressing 5-HT were counted with the cell counter plugin in ImageJ. ROIs for individual cells were manually drawn for determination of 5-HT content, which was estimated by calculating mean fluorescence intensity of the Alexa Fluor 594 fluorescence in individual cells (total fluorescence intensity ROI/ROI area). Cells expressing the DNGai peptide were determined by intrinsic fluorescence of the gap43-citrine marker. Data normalization was

performed independently for each individual larva by dividing the mean fluorescence intensity of individual cells by the average fluorescence of all cells in the DRN.

Head-mounted behavioral assay with simultaneous calcium imaging and channelrhodopsin-2 activation

Agar was removed from a region caudal to the fish anus. All experimental larvae used in experiments had an intact ASR, as determined by a light tap in the dish containing the larvae. Illumination and behavioral set up were mounted on a 3i Marianas system (Intelligent imaging innovation (3i), Inc.) with a spinning disk confocal (Yokogawa) mounted on a Zeiss microscope. For behavior imaging, tail-free mounted fish were illuminated from the side with far red light provided by a custom-built red LED light source and were imaged from above. Images were captured with a 2.5x/0.06 air objective (Carl Zeiss, Inc.) at 1000 fps and 800 x 600 pixel resolution with a CMOS camera (Mikrotron Eosens 1362). Simultaneous confocal fluorescent calcium imaging with the GCaMP5 sensor was from below through a 40x/1.1 Zeiss objective at 20-40 fps. For calcium imaging of M-cells or DRN neurons, GCaMP5 fluorescence excitation and detection were performed with continuous 488 nm laser light at low intensity and detection through BP 488-568 nm and BP 520-535 nm to block red light used for behavior imaging. Sound stimuli were administered by two speakers (Visaton SC 5.9) resting on the imaging stage with the cone side down. A sinusoidal wave (1000 Hz, 1-10 ms, 0.4 V) stimulus was generated by a function waveform generator (Agilent, 33220A) connected to the speakers. The behavior set up was controlled and synchronized by the software controlling the behavior camera (Piper, Stanford Photonics). The confocal imaging microscope was controlled with Slidebook software (Intelligent imaging innovation (3i), Inc.) and was triggered by Piper. The sound stimulus was presented 400 ms after initiation of simultaneous behavior and calcium imaging.

Behavioral analysis

The latencies of sound/vibration-induced escapes in head-mounted fish were determined by visual observation in behavioral movies of characteristic C bends induced by sound/vibration stimulus. For tail tracking of mounted zebrafish, the point along the tail that lied on the agar-water boundary was chosen as rotational axis. Angular displacement about the axis was measured using the midpoint of the free region of the tail. The analysis of behavior in freely swimming larvae was performed using a background subtraction method for detecting the fish. The centroid of the fish was then used as the reference point for tracking. Escapes were detected using changes in pixel values between frames. An escape was counted if the difference of the integrated pixel values from the two frames immediately following the stimulus was statistically higher ($P < 0.01$, 2-sample t-test) than the distribution of pixelchange values taken from the non-escape portion spontaneous activity taken across all 120 movies (720 frames). The accuracy of this method was verified by visual inspection of the movies. Calcium imaging analysis For each sound stimulus, a series of single confocal plane slices of the DRN (20 fps) or the M-cells (40 fps) was acquired, starting 400 ms before sound-vibration stimulus and lasting a total of 5 s (M-cell) or 10 s (DR). Regions of interest (ROI) were manually drawn around cells. ROIs were drawn and analyzed only when cell bodies were clearly identifiable and did not overlap with adjacent cells. We estimate that between 10-20% of the total number of DRN cells were

analyzed in each animal. Images were motion-corrected and visually inspected to assure automatic correction did not produce artifacts. Minimal bleaching was observed during stimulus series. For detection of soundevoked calcium signals, the average integrated ROI fluorescence values in the 400 ms before stimulation were used to generate DF traces. DF peaks after sound stimulus were automatically detected with the peakdet peak detection MATLAB script. Minimum threshold for peak detection was determined based on the variance of the basal fluorescence signal before sound stimulus (400 ms basal recording) and visually verified for each stimulus. Singleexponential fit was used to determine calcium transient decay (tau). The integral of DF values were generated by the integral of DF traces encompassing the epoch spanning 7 s or 4 s after sound stimulus, the duration of a typical sound-induced calcium signal for DRN or M-cell neurons, respectively.

Supplemental Figures

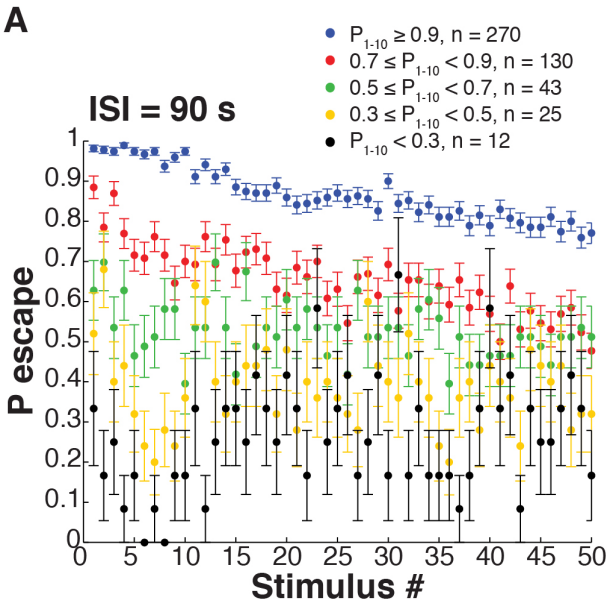

Figure S1 related to Figure 1. Probability of acoustic startle response at long inter-stimulus interval. Average probability of escape during 50 stimuli with 90 s inter-stimulus interval. Probability of escape values during the first 10 stimuli were used to group larvae.

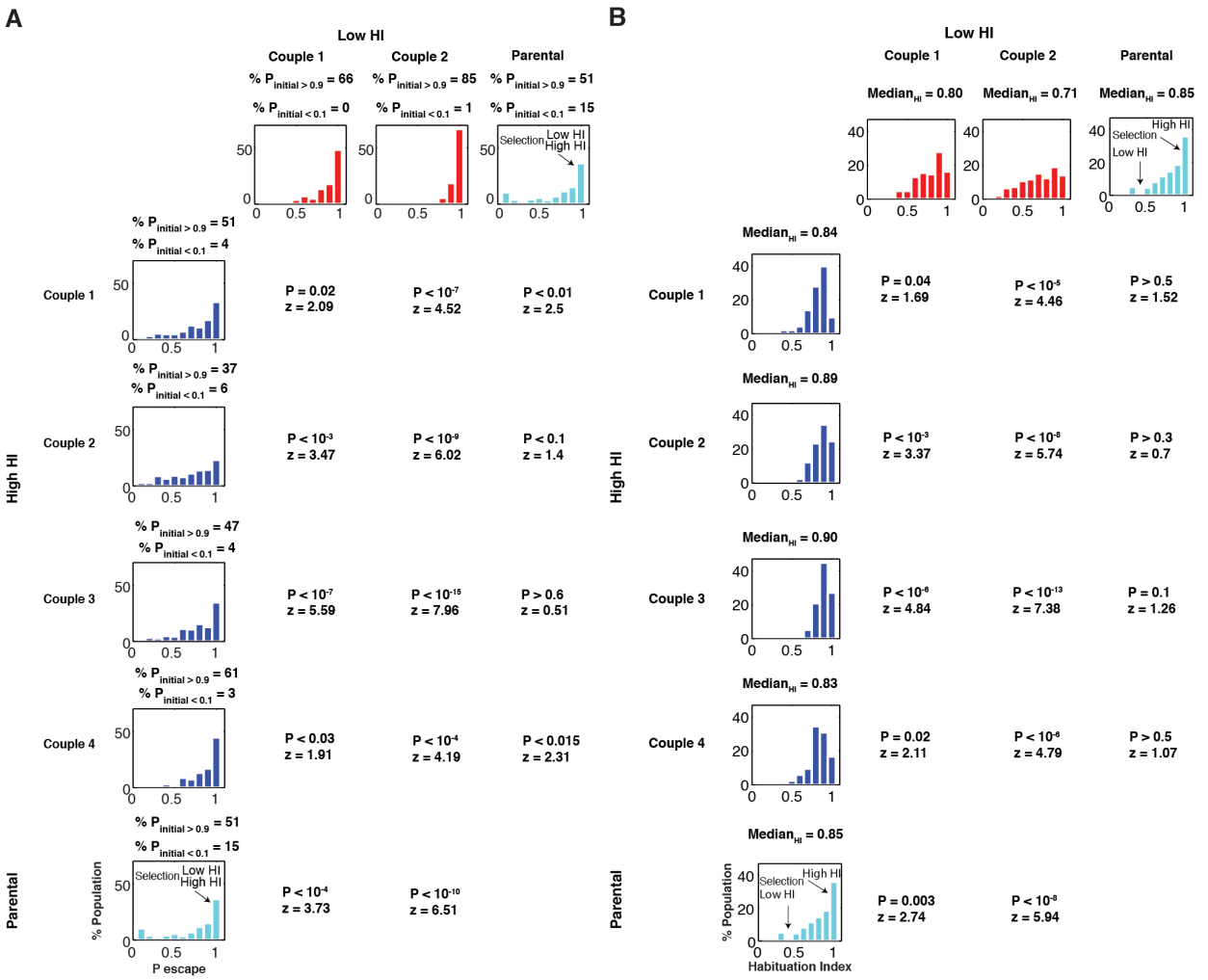

Figure S2 related to Figure 2. Acoustic startle response habituation differences between the F1 progeny of larvae selected for low or high habituation. (A) Pairwise comparisons of probability of escape frequency distributions of the progeny of couples selected for low or high habituation and the parental population used for selection. N Low HI couple1 = 184, n Low HI couple2 = 379, n High HI couple1 = 183, n High HI couple2 = 217, n High HI couple3 = 210, nHigh HI couple4 = 275, n Parental = 336. (B) Pairwise comparisons of habituation index frequency distributions of the progeny of couples selected for low or high habituation and the parental population used for selection. N Low HI couple1= 122, n Low HI couple2 = 289, n High HI couple1 = 93, n High HI couple2 = 81, n High HI couple3 = 96, n High HI couple4 = 84, n Parental =173. Statistics: one-tailed Mann-Whitney test.

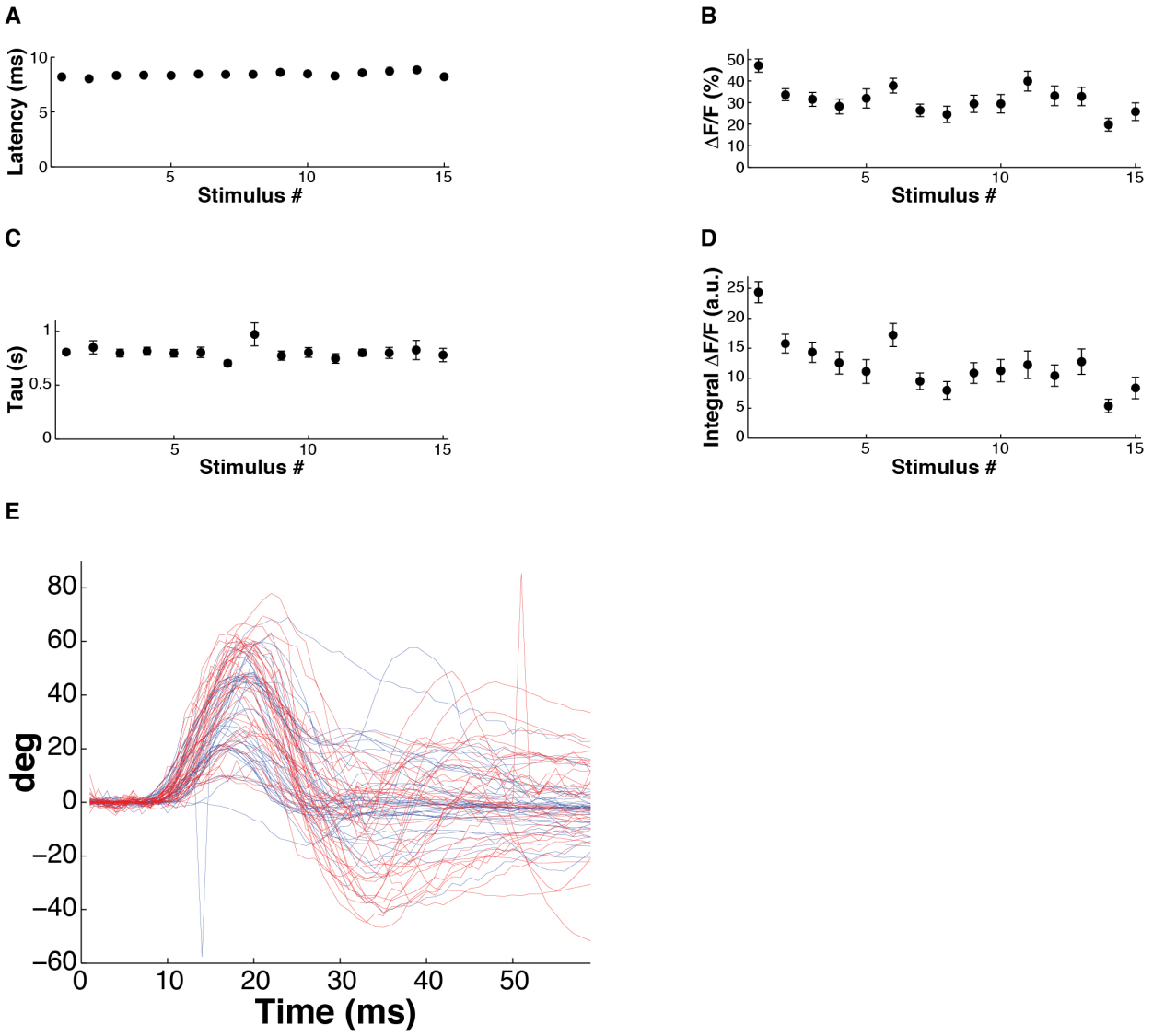

Figure S3 related to Figure 3. Simultaneous analysis of escape behavior and M-cell calcium signals during ASR habituation in 6 dpf in tg(s1181t:Gal4;UAS:GCaMP5) transgenic zebrafish larvae. (A) Mean latency from acoustic stimulus to escape behavior does not change significantly during the stimulus series (F-statistic vs. constant model: 2.97, $P > 0.08$, adjusted R-squared = 0.01). (B-D) GCaMP imaging of M-cell activity over stimulus series shows significant decrease in peak calcium ΔF (F-statistic vs. constant model: 12.8, $P < 0.001$, adjusted R-squared = 0.025) (B), no significant change in calcium transient decay (tau) (F-statistic vs. constant model: 0.32, $P > 0.5$, adjusted R-squared = 0.001) (C), and a significant decrease in the calcium ΔF integral (F-statistic vs. constant model: 57.4, $P < 10\text{-}12$, adjusted R-squared = 0.068) (D). Statistics: linear regression model analysis. Nlarvae = 29. Error bars, s.e.m. (E) Tail-tracking traces for escapes in which one Mauthner cell fired (blue trace) superimposed on traces in which two Mauthner cells fired (red traces).

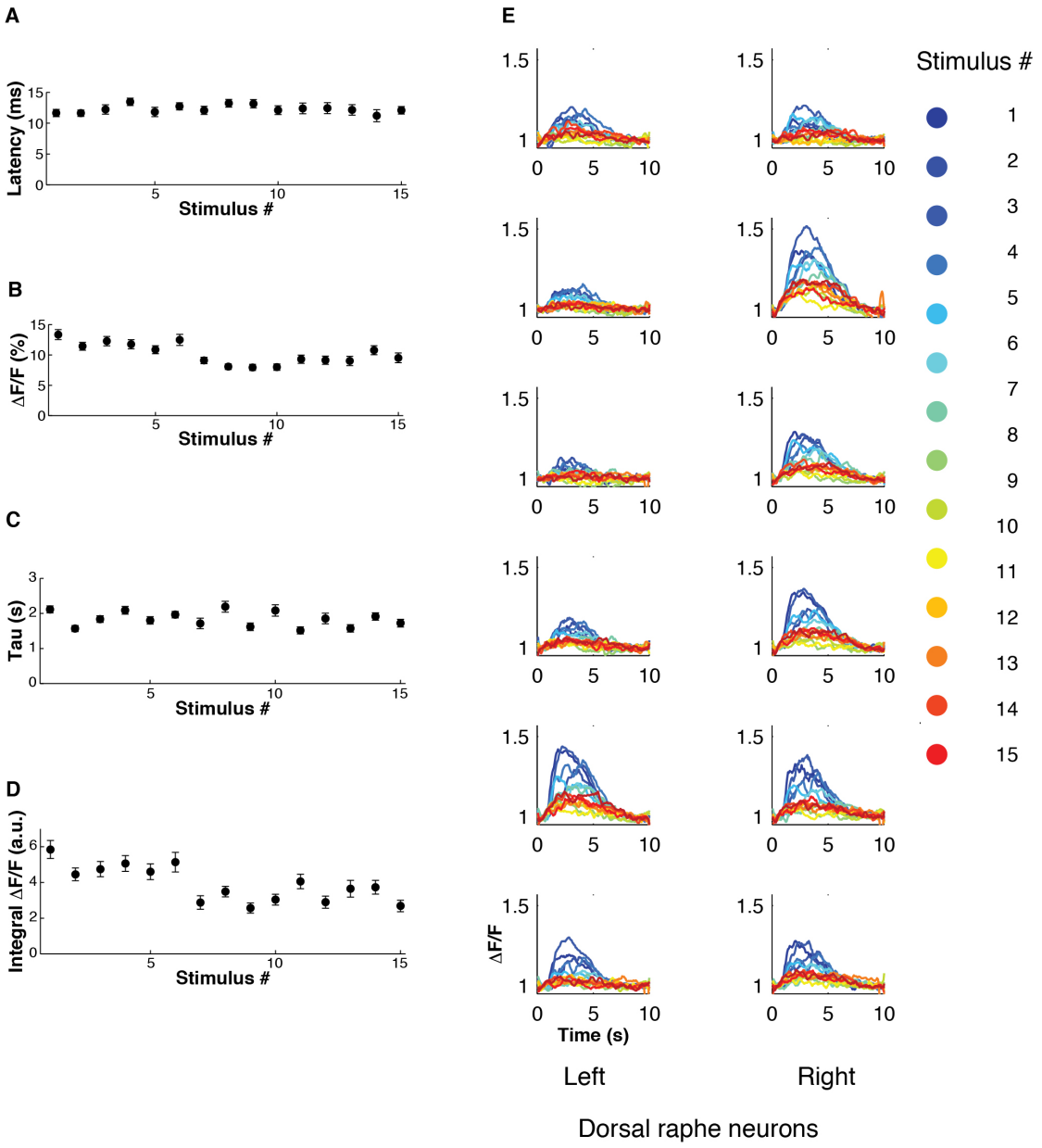

Figure S4 related to Figure 4. Simultaneous analysis of ASR behavior and dorsal raphe nucleus (DRN) neuron calcium signals in 6 dpf zebrafish larvae. (A-D) Measures of behavior and DRN calcium responses during the habituating sound stimulus series. (A) Mean ASR behavior latency does not significantly change (F-statistic vs. constant model: 0.06, P > 0.7, adjusted R-squared = 10-3). (B) Decrease in mean peak calcium ΔF (F-statistic vs. constant model: 45.8, P < 10-10, adjusted R-squared = 0.033). (C) No significant change in mean DRN neuron calcium transient decay (tau) during habituation (F-statistic vs. constant model: 3.63, P > 0.05, adjusted R-squared = 0.002). (D) Decrease in integral of calcium signal ΔF (F-statistic vs. constant model: 47.4, P < 10-11, adjusted Rsquared = 0.031). Statistics: linear regression model analysis. 8-14 neurons/fish, nDR neurons = 244, nlarvae = 24. Error bars = s.e.m. (E) Single-DRN neuron activity responses (ΔF/F traces) to a series of 15 sounds stimuli (ISI = 90 s) in 12 neurons (6 on the right and 6 on the left of the DRN) of a representative larva.

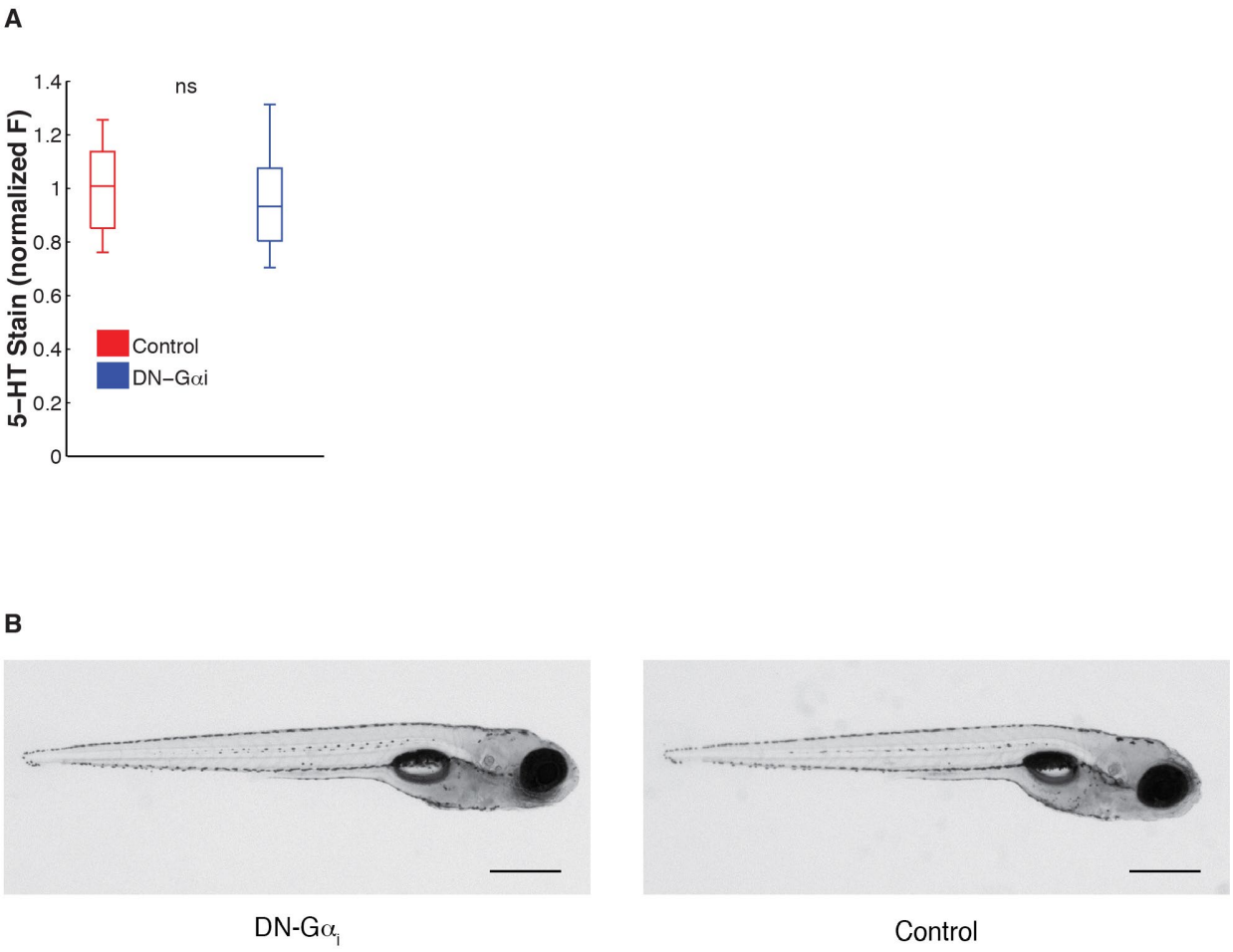

Figure S5 related to Figure 6. No effect on serotonin content in hypothalamus or on zebrafish morphology of expression of dominant-negative αi G-protein signaling peptide. (A) DRN DNGαi expressing larvae do not have significantly different serotonin content in the hypothalamus (normalized serotonin stain: control = 1.004 ± 0.063; DN-Gαi = 0.996 ± 0.080, P = 0.14, 2-sided student's T-test). (B) Representative image of tg(Tph2:Gal4ff;UAS:DNGai) (DN-Gαi) or control 6 dpf transgenic zebrafish larva. Scale bars 500 μm

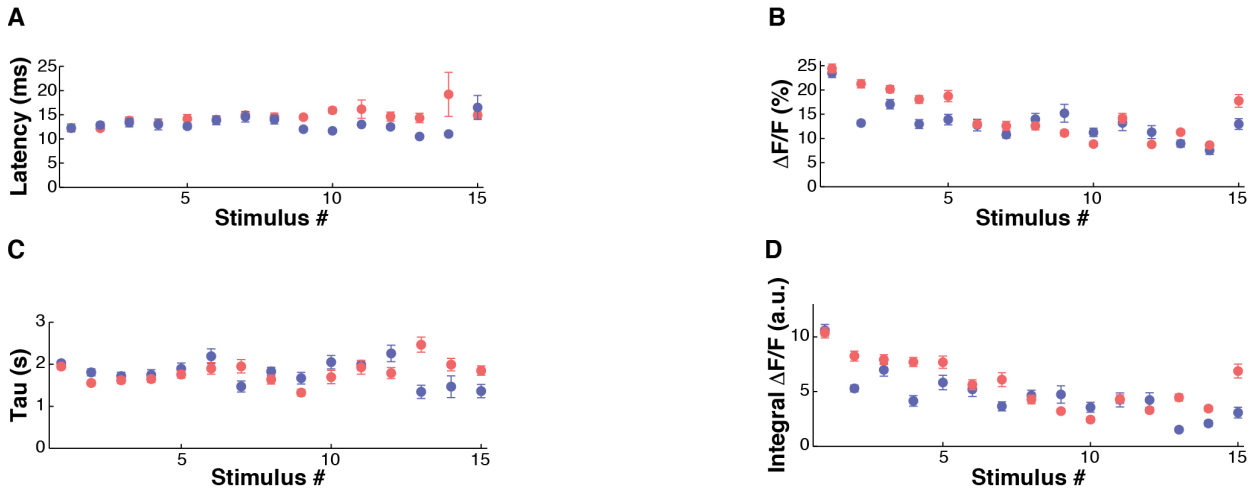

Figure S6 related to Figure 8. ASR habituation behavior and DRN neurons activity in F1 progeny of zebrafish selected for high or low habituation. (A) Longer ASR latency in F1 Low HI zebrafish larvae compared to F1 High HI group (F-statistic: 5.09, P = 0.025). (B) Larger mean peak calcium ΔF of DRN neurons during habituation in F1 Low HI zebrafish larvae compared to F1 High HI group (F-statistic: 31.29, P < 10-7). (C) Mean DRN neuron calcium transient decay (tau) does not significantly change during habituation or between groups (Fstatistic: 3.07, P > 0.08). (D) Larger integral of calcium signal ΔF of DRN neurons during habituation in F1 Low HI zebrafish larvae compared to F1 High HI group (F-statistic: 35.28, P < 10-8). Statistics: analysis of covariance. 12-16 neurons/fish. N Low HI DRN neurons = 248, n High HI DRN neurons = 268, n Low HI larvae = 17, n High HI larvae = 19. Error bars, s.e.m..

Chapter II: Input-Specific Plasticity and Homeostasis at the Drosophila Larval Neuromuscular Junction

Newman, Z. L., Hoagland, A., Aghi, K., Worden, K., Levy, S. L., Son, J. H., ... & Isacoff, E. Y. (2017). Input-specific plasticity and homeostasis at the Drosophila larval neuromuscular junction. Neuron, 93(6), 1388-1404.

Abstract

Synaptic connections undergo activity-dependent plasticity during development and learning, as well as homeostatic re-adjustment to ensure stability. Little is known about the relationship between these processes, particularly in vivo. We addressed this with novel quantal resolution imaging of transmission during locomotive behavior at glutamatergic synapses of the *Drosophila* larval neuromuscular junction. We find that two motor input types, Ib and Is, provide distinct forms of excitatory drive during crawling and differ in key transmission properties. Although both inputs vary in transmission probability, active Is synapses are more reliable. High-frequency firing "wakes up" silent Ib synapses and depresses Is synapses. Strikingly, homeostatic compensation in presynaptic strength only occurs at Ib synapses. This specialization is associated with distinct regulation of postsynaptic CaMKII. Thus, basal synaptic strength, short-term plasticity, and homeostasis are determined input-specifically, generating a functional diversity that sculpts excitatory transmission and behavioral function.

Introduction

The transfer of information between neurons throughout the nervous system relies on communication across inherently unreliable chemical synapses. Synaptic communication is further complicated by the fact that individual neurons can receive inputs from many functionally diverse neurons (Atwood and Karunanithi, 2002, O'Rourke et al., 2012). Even synapses formed by one presynaptic neuron and one or more postsynaptic target neurons can vary greatly in neurotransmitter release, postsynaptic sensitivity, and plasticity (Atwood and Karunanithi, 2002, Branco and Staras, 2009, Pelkey and McBain, 2007). Additionally, postsynaptic cells are not passive receivers of information but can produce retrograde signals, including homeostatic signals that modulate synaptic release (Branco et al., 2008, Frank et al., 2006, Jakawich et al., 2010, Paradis et al., 2001, Petersen et al., 1997). The mechanisms that regulate diversity in transmission at individual synapses are not well understood, nor are their relationships to the plasticity and homeostatic mechanisms that adjust synaptic strength. In particular, it is unclear whether retrograde signaling is input or synapse specific and able to maintain input context among diverse convergent synapses (Branco and Staras, 2009, Turrigiano, 2012).

The Drosophila larval neuromuscular junction (NMJ) is a model system for studying glutamatergic transmission, with pre- and postsynaptic molecular machinery similar to that of central excitatory synapses in vertebrates, while also possessing activity-dependent adjustments in synaptic strength, including short- and long-term plasticity, as well as homeostatic plasticity (Budnik and Ruiz-Cañada, 2006). Two morphologically distinct glutamatergic motor neurons, larger type Ib and smaller type Is, converge onto most of the larval body wall muscles used for

locomotion (Atwood et al., 1993, Hoang and Chiba, 2001, Jia et al., 1993, Kurdyak et al., 1994, Lnenicka and Keshishian, 2000). There is evidence that the transmission properties of these inputs differ (Kurdyak et al., 1994, Lnenicka and Keshishian, 2000, Lu et al., 2016), thus providing a powerful system for investigating the role of input and synapse specificity in the regulation of basal synaptic strength, plasticity, and homeostasis. In addition, there is great heterogeneity, in that both the basal release probability (Pr) of evoked release and the frequency of spontaneous release differ greatly between synapses of the same Ib axon (Peled and Isacoff, 2011, Peled et al., 2014). We set out to understand how plasticity and homeostasis function in a diverse pool of synapses and to determine whether synaptic homeostasis operates globally or has input specificity.

To address these questions requires high-resolution, high-speed analysis of function at many synapses simultaneously. Quantal resolution measurements of excitatory transmission through Ca2+-permeant glutamate receptors (GluRs) has been achieved by imaging chemical or genetically encoded Ca2+ indicators (GECIs) in the postsynaptic cell (Cho et al., 2015, Guerrero et al., 2005, Lin and Schnitzer, 2016, Melom et al., 2013, Muhammad et al., 2015, Peled and Isacoff, 2011, Peled et al., 2014, Reese and Kavalali, 2015, Reese and Kavalali, 2016, Siegel and Lohmann, 2013). We generated a vastly improved postsynaptically targeted GECI based on GCaMP6f. When expressed in Drosophila larval muscle, “SynapGCaMP6f” enables quantal imaging without voltage clamping. We combined SynapGCaMP6f with an optical platform that immobilizes larvae without anesthetics to measure synaptic transmission simultaneously at hundreds of Ib and Is synapses in the intact, behaving animal.

Our quantal imaging makes it possible to connect the elementary properties of transmission at single synapses, to the synaptic drive that is generated by convergent synaptic inputs, to the operation of muscle groups in large parts of the animal, and finally to behavior. Our observations show that basal synaptic strength, short-term plasticity, and, most strikingly, synaptic homeostasis are input specific, diversifying excitatory transmission and behavioral output.

Results

Distinct Synaptic Activity at Ib and Is Synapses during Locomotion

Most muscles in Drosophila larvae are innervated by two glutamatergic motor neurons (MNs), the morphologically distinct type Ib (big) and Is (small) MNs (Atwood et al., 1993). Patch clamp recordings in the ventral nerve cord (VNC) suggest that these MNs have different firing patterns and intrinsic electrophysiological properties (Choi et al., 2004, Schaefer et al., 2010). However, MN activity and synaptic release dynamics in the behaving animal are not known. To understand these differences, we constructed a new postsynaptically targeted GECI, SynapGCaMP6f (MHC-CD8-GCaMP6f-Sh), on the basis of GCaMP6f (Chen et al., 2013). We generated transgenic animals that express SynapGCaMP6f in all body wall muscles throughout development, where it is targeted to the plasma membrane and postsynaptic density, as done earlier (Guerrero et al., 2005, Peled and Isacoff, 2011, Peled et al., 2014). Similar to the previous postsynaptically targeted GECIs, SynapGCaMP6f does not affect NMJ health or function, as determined by the muscle resting membrane potential (w1118 −64.3 ± 3.6 mV, n = 4; w1118;+;SynapGCaMP6f/+

−68.1 ± 2.4 mV, n = 5; p = 0.45, Student's t test), muscle input resistance (w1118 6.47 ± 0.36 MΩ, n = 4; w1118;+;SynapGCaMP6f/+ 5.36 ± 0.47 MΩ, n = 5; p = 0.16, Student's t test), excitatory postsynaptic potential (EPSP) amplitude (0.1 Hz; w1118 35.3 ± 2.5 mV, n = 4; w1118;+;SynapGCaMP6f/+ 40.0 ± 2.0 mV, n = 5; p = 0.23, Student's t test), or excitatory postsynaptic current (EPSC) amplitude (0.1 Hz; w1118 87.4 ± 5.4 nA, n = 4; w1118;+;SynapGCaMP6f/+ 95.9 ± 8.2 nA, n = 5; p = 0.43, Student's t test).

To measure synaptic transmission in vivo, we designed a transparent polydimethylsiloxane (PDMS) microchip that allows restricted crawling motion of unanesthetized wild-type (WT) SynapGCaMP6f-expressing larvae (Figures 1A, 1B, and S1A). Under wide-field epifluorescence imaging, we observed repeated bouts of increased SynapGCaMP6f fluorescence associated with bidirectional, peristaltic waves of body wall muscle contraction in the postsynaptic surround of the Ib and Is axon terminals and throughout the surface of the muscle (Figures 1C and 1D; Movie S1). The waves of muscle contraction were similar to those documented previously in freely moving larvae (Heckscher et al., 2012), although in our case the restrictive chamber prevents larvae from translating, thus allowing extended observations of individual NMJs. We focused on dorsal muscles 1, 2, 9, and 10 in the anterior segments (Figure 1E), each of which receives input from a distinct Ib MN (MN-1b, MN-2b, MN-9b, and MN-10b, respectively) and a common Is MN (MNISN-Is) (Hoang and Chiba, 2001). SynapGCaMP6f imaging unambiguously differentiates Ib and Is NMJs by activity patterns and respectively high and low basal fluorescence (Figures 1F and S1B–S1D; Movie S2), as Is postsynapses have significantly less subsynaptic reticulum (SSR) and less postsynaptic density protein disks-large (Dlg) (Atwood et al., 1993, Lahey et al., 1994), a protein that clusters SynapGCaMP6f to the postsynaptic density. Consistent with previous electrophysiological data in dissected larvae, with the CNS intact (Knodel et al., 2014, Kurdyak et al., 1994, Lu et al., 2016, Schaefer et al., 2010), both Ib and Is synapses were active during muscle contraction (Figure 1G). This fluorescence activity resembled that seen in the dissected preparation in response to electrical stimulation of the motor nerve, which triggers an action potential (AP) and evokes synchronous transmitter release (and postsynaptic Ca2+ rise) along the length of the Ib NMJ (Guerrero et al., 2005, Melom et al., 2013, Peled and Isacoff, 2011, Peled et al., 2014) (Movie S2). As expected for a single common presynaptic MN (MNISN-Is), the Is synapses in this muscle group had a high degree of correlation, whereas the four Ib NMJs were more weakly correlated, suggesting coordination in upstream input to the dorsally projecting Ib MNs (Figure S1E).

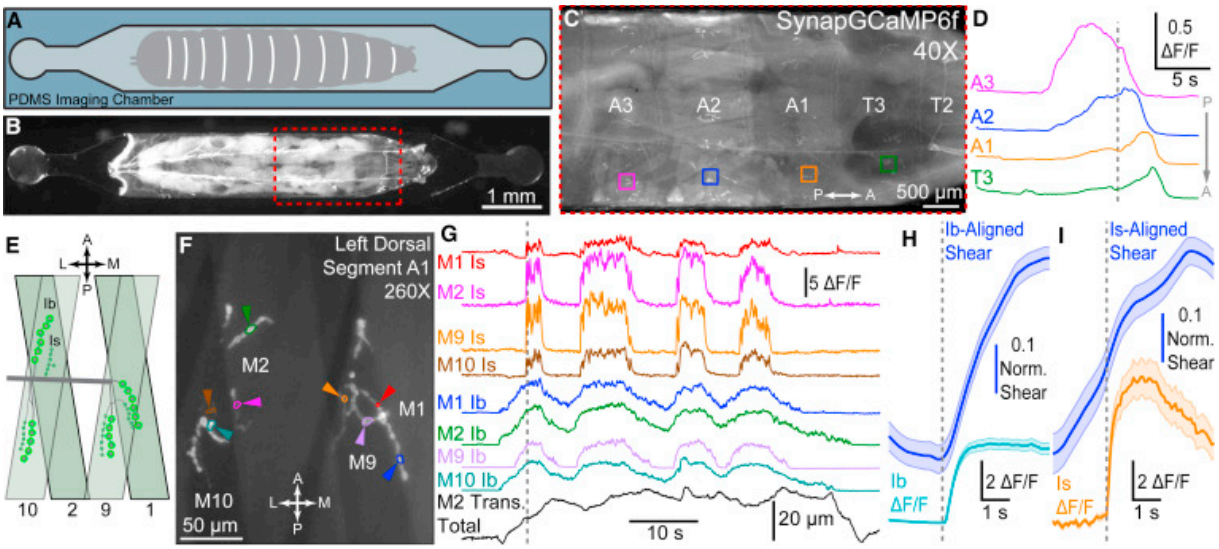

Figure 1 In Vivo SynapGCaMP6f Synaptic Imaging at Ib and Is NMJs during Restrained Locomotion (A) Schematic of live larval imaging chamber. (B) Wandering third-instar larva mounted in imaging chamber.(C) SynapGCaMP6f fluorescence increases at synapses as a contraction wave propagates along the body (A, anterior; P, posterior). (D) ΔF/F traces during P-A wave in four segments of larva in (C). Gray dotted line indicates frame in (C). (E) Schematic of NMJs on dorsal muscles of the larva (L, lateral; M, medial). (F) Higher magnification dorsal Ib and Is NMJs. (G) Single bouton ΔF/F traces and translation data (for muscle 10) for example in (F). Dotted line indicates frame in (F). (H and I) Mean ΔF/F (±SEM) and mean time-locked shearing (±SEM) at onset of synaptic activity in Ib (H) and Is (I) NMJs, respectively. Vertical gray dashed line indicates alignment time (Ib: n = 157 activity bouts from 51 NMJs; Is: n = 80 bouts from 42 NMJs; data from 14 larvae).

Although both motor inputs were engaged during crawling, Ib synaptic activity was more closely associated with muscle translation (Figures 1G and S1B–S1D) and initiation of local muscle contraction (Figure 1H). Additionally, Ib synaptic activity was more tightly correlated with the muscle-wide fluorescence increases triggered by Ca2+ elevation during the contraction of the muscle (Figure S1F) (see STAR Methods). Ib synaptic transmission rose more gradually than did Is (Figure 2A), which engaged later in contraction bouts (Figure 2B), with maximal activity occurring concurrently (Figure 2C). The spatially (Figures 2D and 2E) and temporally integrated Ib ΔF/F activity (Figure 2F) was ~6-fold greater than Is activity at the same target muscle (Figures 2F and 2G), partially because of ~2.5-fold longer active times of Ib synapses (Figure 2H). These observations indicate that Ib synaptic inputs drive larger rises in local postsynaptic Ca2+ and are primarily responsible for generating muscle contraction.

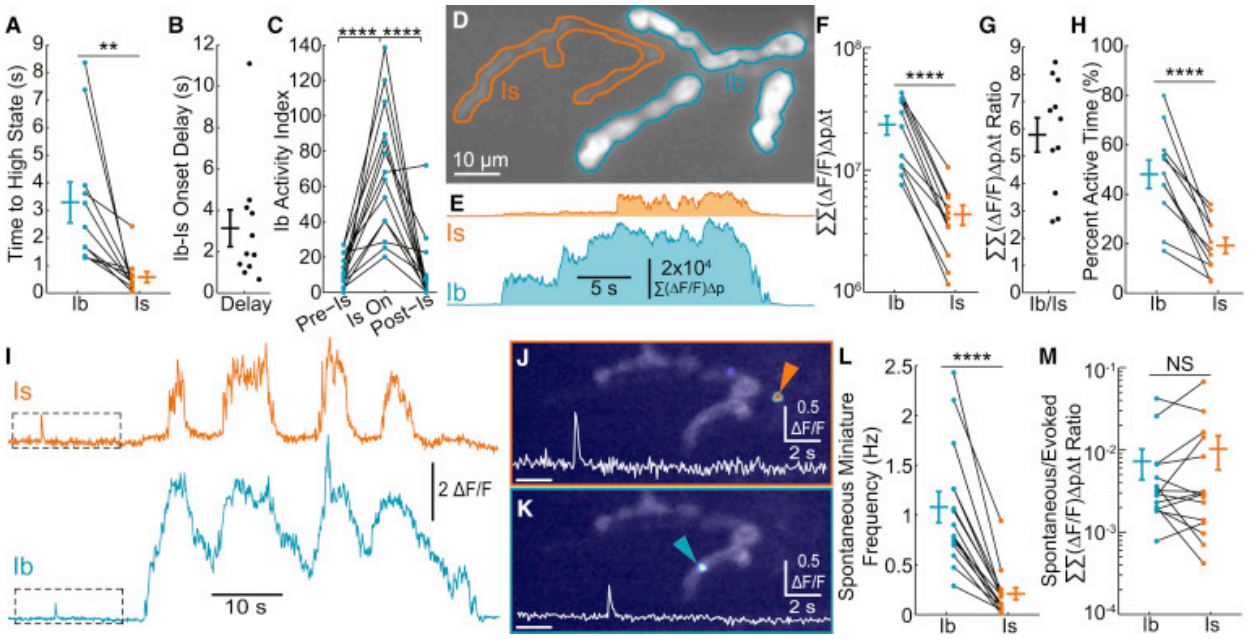

Figure 2 MN Drive during Restrained Locomotion Is Dominated by the Ib Input (A) Mean delay between initiation of synaptic activity and the high-activity state during multiple independent activity bouts. Each point represents the average delay for a single larva (n = 11 larvae). (B) Ratio of the delay between the start of Ib activity and Is activity for each of the larvae in (A). (C) Activity index for individual Ib NMJs before, during, and after synchronous activity at the convergent Is NMJ (n = 14 Ib NMJs from 13 larvae). (D) Example of in vivo SynapGCaMP6f fluorescence for a Ib-Is pair (Ib, blue; Is, orange). (E) Summated ΔF/F over entire NMJ (Σ[ΔF/F]Δp) versus time, where p indicates each pixel. (F) Total synaptic transmission (ΣΣ[ΔF/F]ΔpΔt) for Ib and Is pairs (n = 11 Ib-Is pairs from 11 larvae). (G) Total synaptic transmission (ΣΣ[ΔF/F]ΔpΔt) ratio for each of the Ib-Is pairs in (F). (H) Percentage of total time in active state (synchronous activity at multiple synapses). (I) Mean ΔF/F activity for single release sites (same as Figure 1G). Example spontaneous release events locations and traces are highlighted in (J) and (K). (J and K) Peak ΔF/F image superimposed on baseline fluorescence for spontaneous quantal event examples in (I). An event from the Is input is indicated in (J) and an example from the Ib input is provided in (K). For both panels, insets are higher resolution mean ΔF/F traces. (L) In vivo spontaneous event frequency (n = 15 NMJs from 6 larvae). (M) Total synaptic transmission (ΣΣ[ΔF/F]ΔpΔt) ratio of all spontaneous events versus MN-active periods (n = 15 NMJs from 6 larvae).
Values are mean ± SEM. Comparisons made with Mann-Whitney test (F and M) Student's t test (A, H, and L), or one-way ANOVA with Tukey's post hoc test (C). **p < 0.01; ****p < 0.0001; NS, not significant.

In addition to the long-lasting, axon-wide bouts of activity at Ib and Is synapses, similar to burst stimulation in the dissected preparation (Peled et al., 2014), we also detected small, brief, asynchronous, low-frequency fluorescent events in both NMJs during periods of muscle relaxation (Figures 2I–2K and S2A–S2H; Movie S3). These are consistent with spontaneous quantal "miniature" events detected at the dissected larva in macropatch recordings (Karunanithi et al., 2002, Nguyen and Stewart, 2016) or imaging (Cho et al., 2015, Melom et al., 2013,

Muhammad et al., 2015, Peled and Isacoff, 2011, Peled et al., 2014) as well as imaging in cultured neurons (Reese and Kavalali, 2015, Reese and Kavalali, 2016). These spontaneous events had larger amplitudes at Is synapses (Figures S2C–S2H) but were more frequent at Ib synapses (Figures 2L, S2C, and S2F). Spontaneous release has been proposed to play a role in synapse regulation and development (Choi et al., 2014, Frank et al., 2006, Kavalali, 2015, Saitoe et al., 2001) and may represent a substantial fraction of total synaptic release, especially at low-Pr central synapses (Chadderton et al., 2004). However, by comparing the total activity integral ($\Sigma[\Delta F/F]\Delta p\Delta t$) of spontaneous events with that of synchronous MN-driven events, we find that spontaneous transmission at both inputs represents a very small fraction (<1%) of the total postsynaptic Ca2+ signal (Figures 2M and S2I). These calculations may miss some low-amplitude spontaneous events, but their small size would mean a minimal impact compared with the large and sustained evoked events. This suggests that spontaneous transmission may have a larger role in development and plasticity at synapses with low evoked transmission.
Taken together, these results demonstrate that SynapGCaMP6f enables quantal resolution, quantitative imaging of synaptic activity in vivo and that during restrained behavior, AP-evoked synchronous release represents the vast majority of synaptic transmission. In addition, Ib and Is synapses provide distinct forms of synaptic input, with Ib synaptic activity being the dominant, muscle-contracting input during crawling behavior.

Spontaneous Quantal Transmission at Ib and Is Synapses

To understand the physiological differences between transmission at Ib and Is synapses, we performed high-resolution optical quantal analysis in the semi-dissected larval fillet preparation, in which we removed the brain and imposed AP firing patterns by electrical stimulation of the nerve containing the Ib and Is axons. Despite the large difference in SynapGCaMP6f baseline fluorescence (Figures 3A and S3A), confocal imaging of SynapGCaMP6f at muscle 4 provided a robust readout of spontaneous, quantal synaptic transmission in the absence of nerve stimulation at both Ib and Is synapses (Figures 3B–3E; Movie S4). As in the intact preparation (Figures S2C–S2H), spontaneous events were larger in amplitude at Is postsynapses (Figures 3F, 3G, and S3B–S3E) but had nearly identical kinetics (Figures S3E and S3F), consistent with the kinetics observed in neurons in response to single APs (Chen et al., 2013). Imaging combined with electrophysiology (Movie S5) enabled identification of the site of origin of the miniature EPSP (mEPSP) electrical events (Figures 3H and S3B–S3D). These measurements demonstrated that, just as they produce larger fluorescent events (Ib mean: 0.57 ± 0.01 $\Delta F/F$; Is mean: 0.95 ± 0.02 $\Delta F/F$), mEPSPs are also 56% larger at Is synapses (Ib mean: 0.42 ± 0.008 mV; Is mean: 0.66 ± 0.002 mV) (Figures 3I, 3J, and S3D), in agreement with focal extracellular electrode studies and the finding that Is terminals have larger synaptic vesicles (Karunanithi et al., 2002, Nguyen and Stewart, 2016). Optical quantal amplitudes at both inputs showed identical and linear sensitivities to extracellular Ca2+ (Figure S3G). Additionally, SynapGCaMP6f responses could be attributed to GluRs, as depletion of Ca2+ stores with thapsigargin had no effect on spontaneous event amplitudes (Figures S3H and S3I), and voltage steps to activate voltage-gated Ca2+ channels failed to produce any change in SynpGCaMP6f fluorescence (Figures S3J–S3M). Together, these data indicate that SynapGCaMP6f provides a robust, quantitative, report of glutamate release at the NMJ.

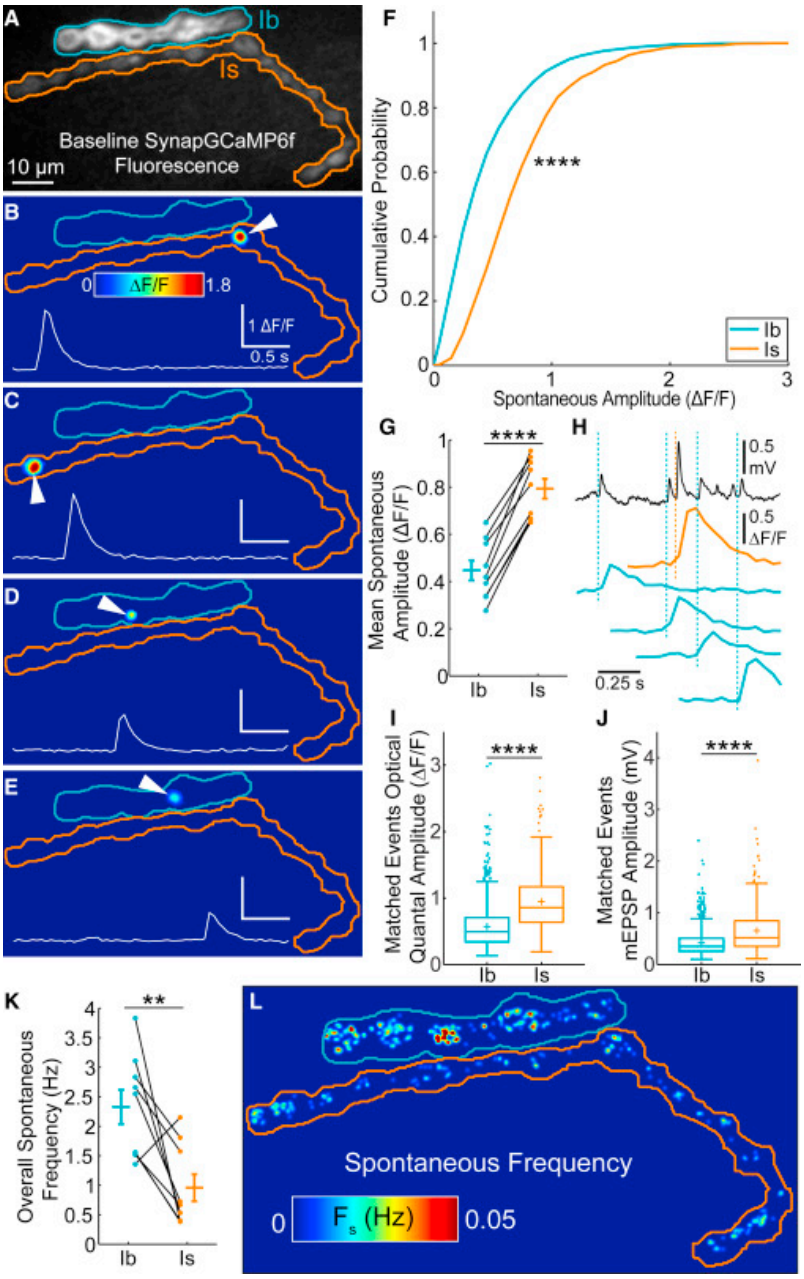

Figure 3 Ib and Is Synapses Differ in Optical Quantal Size and Spontaneous Release Rate (A) Baseline SynapGCaMP6f fluorescence in fillet preparation at a WT NMJ with Ib (blue) and Is (orange) NMJ borders highlighted. (B–E) Example spontaneous events at Ib and Is NMJs. Individual examples correspond to time 0.35 s (B), 0.65 s (C), 1.20 s (D), and 2.10 s (E) in Movie S4. Insets indicate mean ΔF/F for synapses indicated with white arrowheads. (F) Cumulative probability for pooled spontaneous event maximum amplitudes from multiple NMJs (Ib n = 9 NMJs, 2,515 pooled events; Is n = 9 NMJs, 1,035 pooled events; no electrophysiology). (G) Mean spontaneous event peak amplitude. Each point is average for one NMJ (n = 9 NMJ pairs; no electrophysiology). (H) Electrical mEPSPs (top, black trace) with matched optical quantal events at Ib (blue) and Is (orange) NMJs. (I) Boxplot for pooled optical quantal amplitudes with matched mEPSPs (different data from [F] and [G]) (+ indicates mean). (J) Boxplot for pooled mEPSP amplitudes of all the matched events in (I) (+ indicates mean). (K) Overall total spontaneous release frequencies by NMJ (n = 9 NMJ pairs). (L) Locations of spontaneous quantal events during 120 s of imaging without motor neuron stimulation. Color scale is local spontaneous frequency (Fs). Values are mean ± SEM except in (I) and (J), where error bars indicate the ± 1.5 inner quartile range. Comparisons made with Kolmogorov-Smirnov test (F), Student's t test (G and K), or Mann-Whitney test (I and J). **p < 0.01; ****p < 0.0001.

In further agreement with our in vivo analysis (Figure 2L), the global frequency of spontaneous transmission was lower at the Is input (Figures 3K and S3N). We have previously demonstrated that at single Ib synapses, the local spontaneous release frequency (Fs) is highly variable (Peled et al., 2014). We observed heterogeneous Fs at both Ib and Is synapses (Figure 3L), with similar average values for individual animals (Figure S3O) but slightly different distributions when single synapses were pooled from multiple larvae (Figure S3P). Thus, the difference in global spontaneous release between these two inputs is due to the significantly smaller number of spontaneously active synapses in the Is axon (Figure S3Q). Following optical recording of transmission, we immunostained for Bruchpilot (Brp), a Drosophila ELKS/CAST homolog, which forms the central T-bar structure of the motor axon active zone cytomatrix (Kittel et al., 2006). We found Is axon terminals to have significantly lower Brp puncta densities (Figures S3R–S3T) (Paul et al., 2015), consistent with their lower global Fs. Additionally, the amount of Brp was similar at Is and Ib synapses (Figures S3U and S3V), consistent with recent super-resolution microscopy measurements (Ehmann et al., 2014), and the portion of Brp-containing synapses that participated in spontaneous release was similar (Figure S3W).

Thus, spontaneous release occurs at similar rates in individual Is and Ib synapses, evokes larger responses at Is synapses, and, because of the higher synapse density and larger area of Ib terminal axons, is considerably more frequent overall at Ib inputs.

Ib and Is Synapses Differ in Basal Evoked Transmission

To measure basal evoked release, we performed optical quantal analysis simultaneously at Ib and Is inputs during low-frequency (0.1 Hz) stimulation of the nerve containing both Ib and Is axons (Figures S4A–S4E; Movie S6). This enabled us to construct cumulative activity maps of the Pr throughout both NMJs (Figures 4A and 4B). We matched these maps to presynaptic Brp puncta from post hoc immunostaining (Figures 4C–4F) and found that AP-responsive sites were more numerous at Ib synapses (Figure S4F) yet only accounted for approximately half of the Brp puncta in both axons (Figure S4G). This indicates that a large fraction of synapses at both inputs are either silent or have very low P_r.

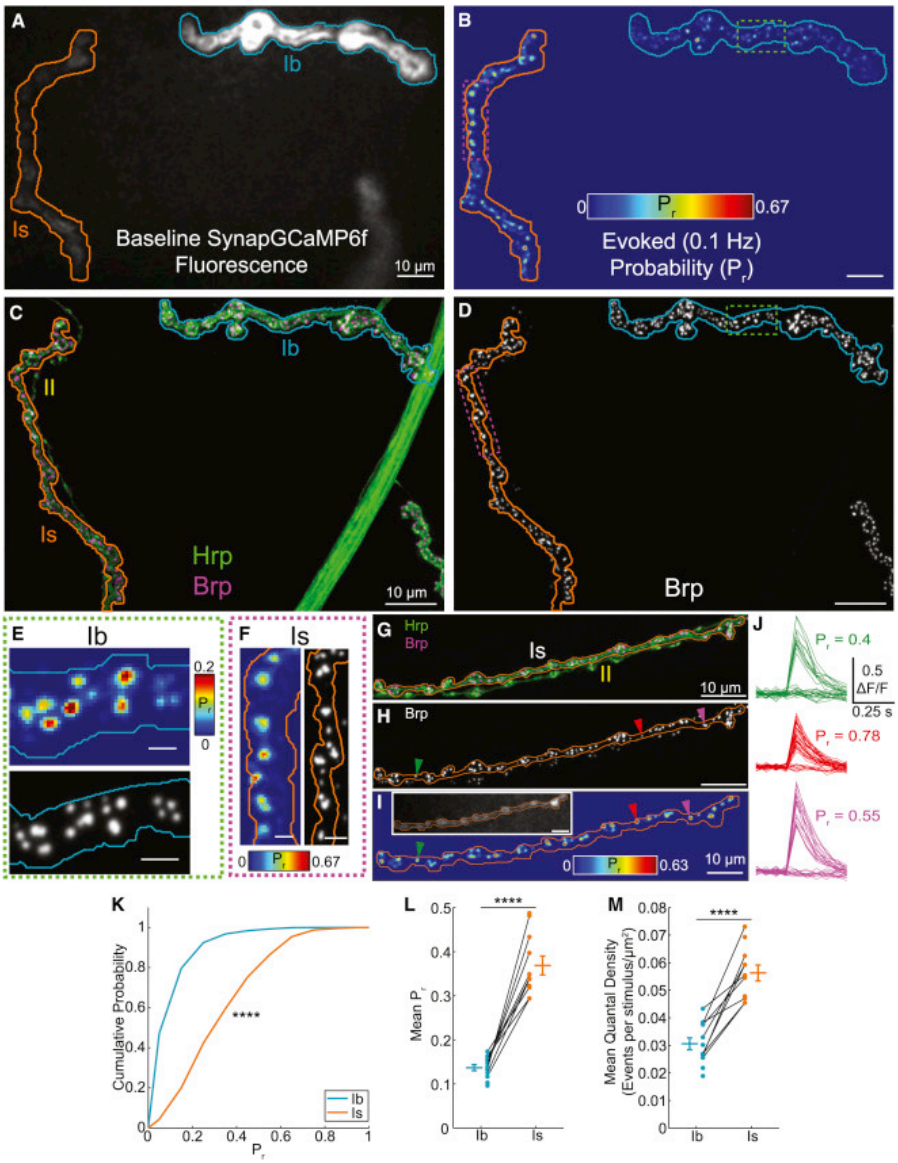

Figure 4 Basal Transmission Is More Reliable at Is Synapses (A) Baseline SynapGCaMP6f fluorescence at a WT NMJ (Ib, blue; Is, orange). (B) Cumulative AP-evoked quantal release location heatmap (200 trials at 0.1 Hz). Color scale is local Pr. (C) Maximum-intensity projection for neuron (Hrp, green) and Brp (magenta) immunofluorescence (Ib, blue; Is, orange; regions correspond to imaged areas A and B). (D) Isolated maximum intensity projection for Brp immunofluorescence. (E and F) High-magnification comparison of quantal activity spatial distribution and Brp puncta for a Ib region (E) (green boxes indicated in B and D) and a Is region (F) (magenta boxes indicated in B and D). The scale bars represent 2 µm. (G–J) AP-evoked quantal behavior of single synapses. (G) Example Is NMJ (Hrp, green; Brp, magenta; axon border, orange; type II axon, yellow). (H) Brp image corresponding to (G). (I) Cumulative AP-evoked quantal release location heatmap (200 trials at 0.1 Hz) from (G) and (H). Inset shows baseline SynapGCaMP6f fluorescence. Color scale is local Pr. (J) ΔF/F traces for synapses indicated with arrows in (H) and (J) during 40 stimulation trials. Pr = number of responses/number of trials at individual sites. (K) Pooled cumulative probability distribution for 0.1 Hz evoked Pr at all active synapses (Ib n = 995 and Is n = 413 sites). (L) Mean 0.1 Hz evoked Pr by NMJ (Ib n = 12 and Is n = 11 NMJs with 9 NMJ pairs). (M) Mean quantal density for NMJs in (L) (quantal content normalized to imaged NMJ area).
Values are mean ± SEM. Comparisons made with Kolmogorov-Smirnov test (K) and Student's t test (L and M). ****p < 0.0001.

Transmission at single synapses was all or none, alternating between failures and responses that were similar in amplitude to spontaneous quantal events (Figures 4G–4J). Therefore, this method provides a direct readout of single release site Pr from the fraction of APs that evoke release at a given active site (Figure 4J). Active synapses of both Ib and Is axons were broadly distributed in basal Pr (Figures 4B and 4K), although Is variability was lower at individual NMJs (Figure S4H) and average Pr was significantly higher (Figures 4K and 4L). Average Pr values at both inputs are consistent with recent electrophysiological estimates (Lu et al., 2016). Despite the lower synaptic density at Is NMJs (Figure S4F), the high Pr resulted in a higher quantal density (imaged area-normalized quantal content) (Figure 4M), a metric that we chose because of its ability to accurately distinguish differences in release at low Pr synapses (see STAR Methods). As with spontaneous transmission, AP-evoked events were larger at Is synapses (Figures S4I–S4O; see also STAR Methods). Finally, cross-correlation comparisons between maps of evoked and spontaneous release sites (Figures S4P–S4V) revealed a low spatial correlation at both Ib and Is synapses (Ib: 0.31 ± 0.03, n = 7 NMJs; Is: 0.33 ± 0.3, n = 9 NMJs; p = 0.79, Student's t test), indicating that synapses are specialized for either spontaneous or evoked release in both axons, as found earlier at Ib synapses (Peled et al., 2014).

Thus, while active synapses of both Ib and Is inputs are broadly heterogeneous and specialized for either spontaneous or evoked release, and both contain a large fraction of silent synapses, Is active synapses have an ∼2- to 3-fold higher Pr. This difference in release exists despite the fact that Brp, whose level is correlated to Pr within the Ib input (Peled et al., 2014), is present in similar amounts at Is and Ib synapses. This suggests that an additional mechanism of regulation differentiates between basal glutamate release reliability at Is and Ib inputs.

Homeostatic Plasticity Is Input Specific

Homeostatic plasticity at the fly NMJ stabilizes synaptic strength over a wide range of timescales (Davis and Müller, 2015). Removal of the GluRIIA subunit with a GluRIIA null mutation (GluRIIASP16) reduces mEPSP amplitudes (quantal size), but EPSP amplitudes remain constant, indicating a retrograde homeostatic signal that increases presynaptic release to compensate for the decreased sensitivity to glutamate (Petersen et al., 1997). Given the striking differences during in vivo and basal transmission between Ib and Is inputs, we next asked whether homeostatic compensation occurs similarly at the two inputs.

GluRIIA larvae expressing SynapGCaMP6f had no detectable GluRIIA expression at either Ib or Is postsynapses (Figures S5A and S5B), but baseline SynapGCaMP6f fluorescence was unchanged (Figure S5C), consistent with normal postsynaptic development. Electrophysiological analysis of mEPSPs and compound EPSCs indicated that presynaptic homeostatic compensation is intact in the presence of SynapGCaMP6f (Figures S5D–S5H). As expected, the GluRIIA mutation reduced the amplitude of spontaneous optical events at both Ib and Is NMJs (Figures 5A–5D). We performed optical quantal analysis of basal transmission under low-frequency (0.1 Hz) MN stimulation (Figures S5I–S5L). Analysis of both inputs showed that there was no difference between GluRIIA and WT in terms of the normalized variability of Pr (Figure S5M), the density of active synapses (Figure S5N), or the density of Brp puncta (Figure S5O).

However, GluRIIA had a significantly higher quantal density per stimulus and single-synapse Pr in the Ib input (Figures 5E–5H). In striking contrast, there was no difference in quantal density or Pr in the Is input (Figures 5E–5H). We found no relationship between the Pr of Is synapses and that synapse's distance to the nearest Ib synapse (Figures S5Q and S5R), suggesting that the retrograde homeostatic signal was highly specific for the Ib input and did not affect Is synapses, even when they were located nearby on the surface of the muscle. Furthermore, even when we reduced the Pr of Is synapses to WT Ib levels by reducing extracellular Ca2+, we observed no compensation in presynaptic strength at Is synapses (Figures S5S–S5V). Thus, the homeostatic increase in evoked release is mediated by an increase in transmission reliability, which takes place selectively at Ib synapses.

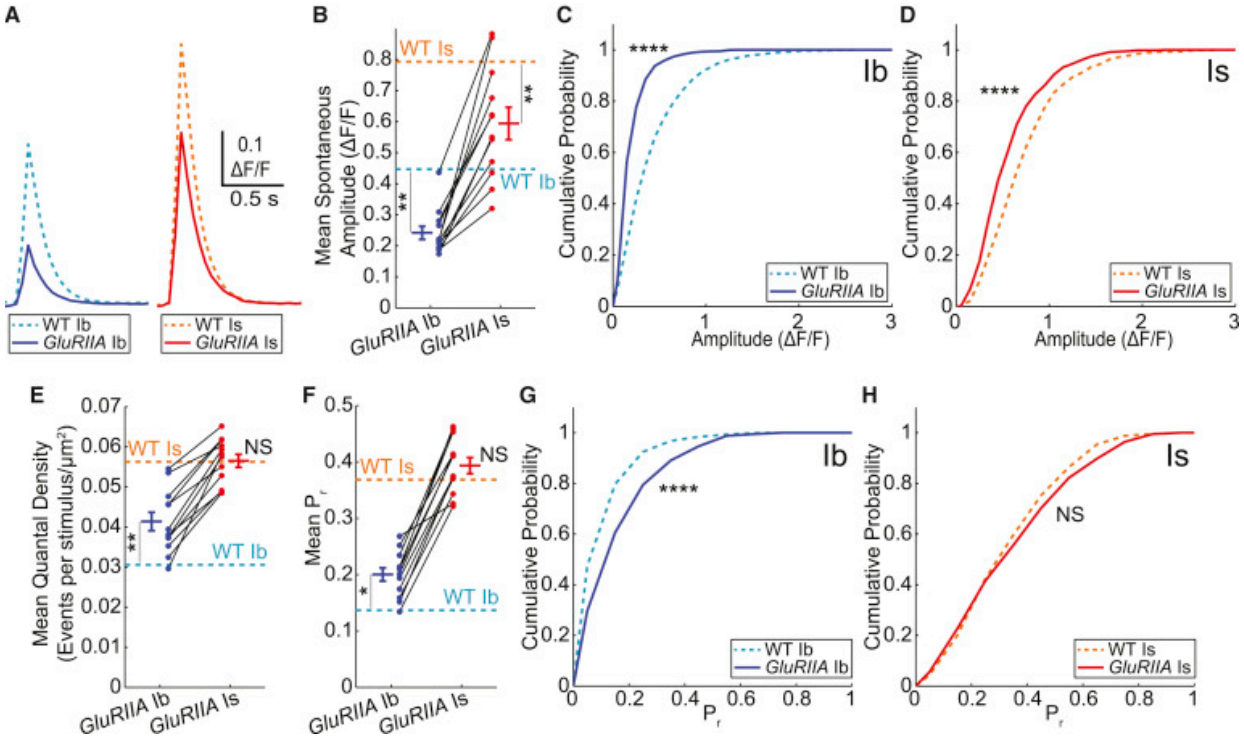

Figure 5 Homeostatic Plasticity Is Input Specific (A) Mean ΔF/F waveforms for pooled and aligned spontaneous events in WT and GluRIIA animals (WT Ib n = 9 NMJs, 2,515 events; WT Is n = 9 NMJs, 1,035 events; GluRIIA Ib n = 12 NMJs, 1,470 events; GluRIIA Is n = 12 NMJs, 590 events). (B) Mean spontaneous event amplitudes at each NMJ (****GluRIIA Ib versus GluRIIA Is). (C and D) Cumulative probability for pooled spontaneous event maximum amplitudes at WT and GluRIIA Ib NMJs (C) and Is NMJs (D). (E) GluRIIA quantal density by NMJ (GluRIIA n = 12 NMJ pairs; ***GluRIIA Ib versus GluRIIA Is). (F) GluRIIA mean 0.1 Hz evoked Pr by NMJ (****GluRIIA Ib versus GluRIIA Is). (G and H) Cumulative probability for pooled 0.1 Hz evoked single synapse Pr at WT and GluRIIA Ib NMJs (G) and Is NMJs (H). (GluRIIA Ib n = 1,146 sites; GluRIIA Is n = 585 sites).
Data in (B) to (H) are from Figures 3 and 4 and are presented here for comparison. Values are mean ± SEM. Comparisons made with Kolmogorov-Smirnov test (C, D, G, and H) and one-way ANOVA with Tukey's post hoc test (B, E, and F). *p < 0.05; **p < 0.01; ***p < 0.001; ****p < 0.0001.

Relationship between Homeostasis and Input-Specific Short-Term Plasticity

Having seen that homeostatic compensation in basal transmission strength occurs exclusively at Ib synapses, we asked how compensation affects short-term plasticity during the kind of AP bursts in MNs that occur during fictive locomotion (Knodel et al., 2014, Lu et al., 2016). Two-electrode voltage-clamp recording, during simultaneous stimulation of WT, SynapGCaMP6f-expressing Ib and Is MNs at 1–20 Hz with 1.5 mM Ca^{2+} saline (HL3, with 25 mM Mg^{2+}) to simulate native hemolymph (Stewart et al., 1994), showed a depression in compound EPSC amplitude (Figure 6A), which was identical to the extent of depression observed in the absence of SynapGCaMP6f expression (Figure S6A). Although quantal density per stimulus was stable at 0.1 Hz (Figure S6B), global $\Delta F/F$ optical analysis during stimulation at 1–10 Hz showed depression at Is NMJs, and stimulation at ≥5 Hz showed facilitation at Ib NMJs (Figures 6B and S6C–S6E; Movie S7). Analysis of the $\Delta F/F$ signals at individual synapses during a 5 Hz stimulation showed that it is possible to identify quantal events despite the stimulus interval being shorter than the complete decay of the SynapGCaMP6f signal because of the low single-synapse Pr (Figure S6F). To quantify the overall changes in synaptic activity during stimulus trains, we calculated the change in quantal density per stimulus during the bursts (Figures S6G–S6I and S6K). At 5 Hz, the Ib input facilitated by nearly 100%, while the Is input depressed by ~20% (Figures 6C–6E).

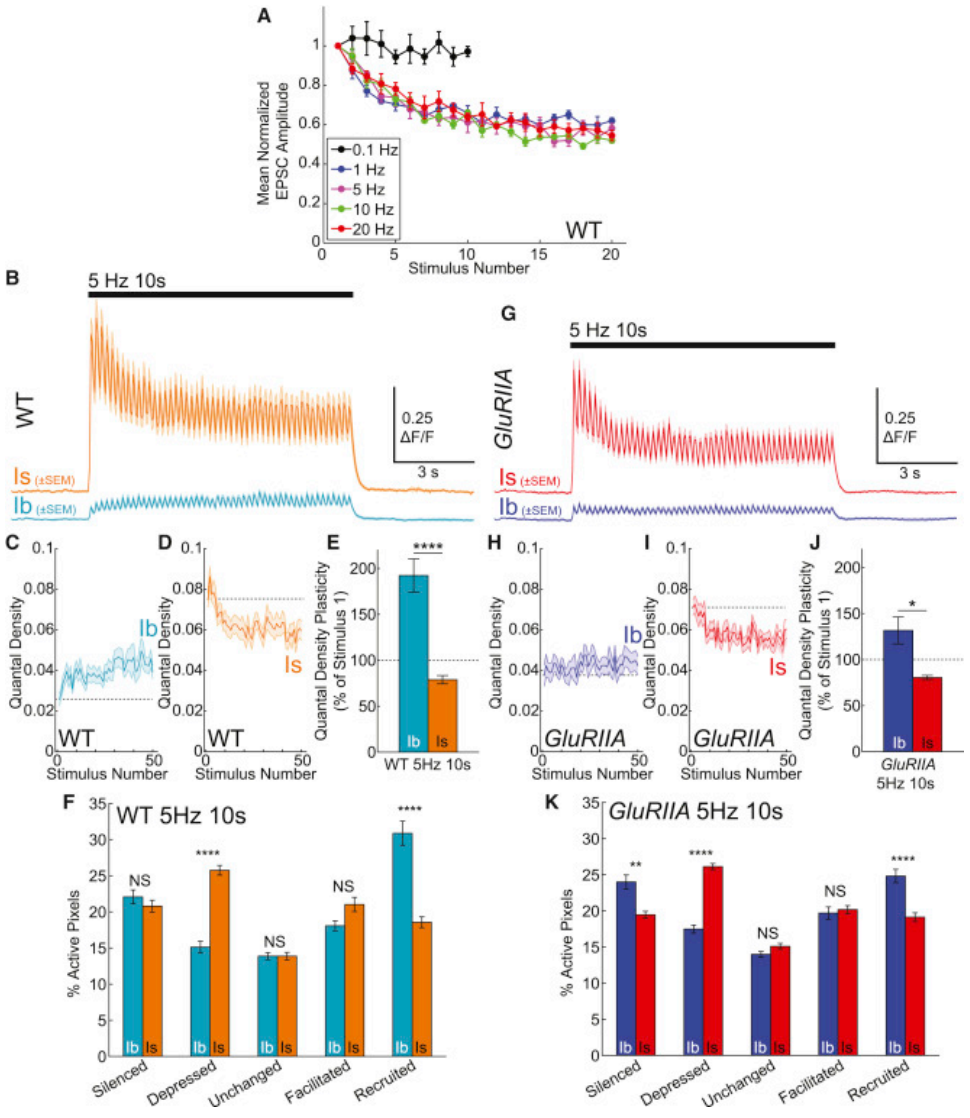

Figure 6 Short-Term Synaptic Plasticity and Influence of Homeostatic Signaling on Plasticity Are Input Specific (A) Mean normalized (to stimulus 1) EPSC amplitudes for WT larvae at several frequencies and aligned by stimulus number (0.1 Hz n = 5, 1 Hz n = 5, 5 Hz n = 4, 10 Hz n = 5, 20 Hz n = 5 muscles). (B) WT mean ΔF/F for entire NMJ areas during a 10 s, 5 Hz train (Ib, blue; Is, orange; n = 13 NMJ pairs). (C and D) WT mean quantal density (area normalized quantal content in events per stimulus per square micrometer) at Ib (C) and Is (D) NMJs during a 10 s, 5Hz stimulus from (B). Dotted line aligned to value at first stimulus. (E) Mean quantal density plasticity (mean of final five responses divided by first response during 10 s 5 Hz train) for WT NMJs in (B). (F) Single-pixel plasticity WT NMJs in (B). Values are percentages of active pixels. Pixels classified by difference in activity between first 25 and last 25 stimuli. (G) GluRIIA mean ΔF/F trace for entire NMJ area during a 10 s, 5 Hz train (GluRIIA Ib, dark blue; GluRIIA Is, red; n = 11 NMJ pairs). (H and I) GluRIIA mean quantal density at Ib (H) and Is (I) NMJs during a 10 s, 5Hz train from (G). Dotted line is aligned to the value at the first stimulus. (J) Mean quantal density plasticity for GluRIIA NMJs during 10 s at 5 Hz in (G) (**WT Ib versus GluRIIA Ib; NS WT Is versus GluRIIA Is). (K) Single-pixel plasticity for GluRIIA NMJs in (G) (**WT Ib versus GluRIIA Ib recruited, otherwise all same class, cross-genotype comparisons NS). Mean ± SEM indicated. Comparisons made with one-way ANOVA with Tukey's post hoc test (E and J) and also one-way ANOVA with Tukey's post hoc test within each classification group but between NMJ class and genotype (F and K). **$p < 0.01$; ****$p < 0.0001$.

Given the heterogeneity in Pr between synapses at both Ib and Is NMJs (Figures 4K and S4H), we wondered whether the basal properties of a synapse (e.g., whether it has high or low Pr or is silent) determine its tendency to depress or facilitate. To address this, we categorized quantal responses for each pixel within Is and Ib NMJs during trains of stimulation at 5 Hz. By comparing the second half of a train to the first half, we identified pixels as either unchanged, facilitated, depressed, silenced, or recruited (Figures 6F and S6K–S6M). Reflecting the overlapping basal Pr distributions (Figure 4K), Ib and Is inputs had similar percentages of pixels that were silenced, facilitated, or unchanged during the train, but pixels that were recruited from a silent state were ~70% more abundant at Ib inputs, whereas pixels that were depressed (but not silenced) were ~70% more abundant at Is inputs (Figure 6F). The sites that fell into the different categories were highly intermingled spatially (Figure S6L). These results suggest that depression at Is inputs is primarily an outcome of a tendency of synapses to decline in Pr but remain active, while facilitation at Ib inputs is primarily an outcome of the recruitment of silent synapses.

Having identified different classes of synapses on the basis of basal transmission and short-term plasticity in WT larvae, we next asked how these synapse subtypes contribute to Ib-specific homeostatic compensation in GluRIIA larvae. First, we observed that quantal density depression at the Is input was normal in GluRIIA (WT Is depresses to 78.9% ± 5% and GluRIIA Is depresses to 80.5% ± 2%; $p = 0.996$) (compare Figures 6G, 6I, and 6J with Figures 6B, 6D, and 6E). However, Ib inputs in GluRIIA showed significantly less global facilitation in quantal density during stimulation at 5 Hz compared with WT (WT Ib facilitated to 192.3% ± 18% and GluRIIA Ib facilitated to 131.6% ± 15%; $p = 0.006$). This reduction in global facilitation was due to a reduction in the number of silent sites that were recruited during the 5 Hz train (WT Ib 30.9% ± 1.7% versus GluRIIA Ib 24.8% ± 0.92%; $p = 0.004$). These data, coupled with higher single-synapse basal Pr (Figures 5F and 5G), similar basally active synapse densities (Figure S5N) and similar active zone densities (Figure S5O), suggest that homeostatic signaling at Ib inputs compensates for decreased postsynaptic sensitivity by both increasing the reliability of active synapses and reducing recruitment of silent sites during high-frequency activity.

Input-Specific Homeostasis at Ib Synapses Is Independent of Is Release

We have shown above that, during locomotor behavior, the Is input provides a relatively small percentage of the total synaptic drive (Figures 2F and 2G). However, its larger quantal size (Figures 3F and 3G) and higher Pr (Figures 4K and 4L) means that the Is input can still provide a significant depolarization and influx of Ca^{2+} into the muscle over a range of AP frequencies (see Figures 6B and S6C–S6E). We therefore asked whether loss of Is transmission would trigger homeostatic compensation at the Ib input that innervates the same muscle. Because we could not selectively block GluRs at Is postsynapses, we turned to presynaptic disruption of transmission by expressing the tetanus toxin light chain (TeTxLC), which blocks AP-evoked transmitter release through proteolysis of synaptobrevin 2 (Sweeney et al., 1995). We targeted UAS-TeTxLC expression specifically to Is inputs using either RN2-Gal4 (Fujioka et al., 2003) that drives expression in a single Is MN (MNISN-Is), a single Ib MN (MN1-Ib) (Figures 7A and 7B) and a single interneuron in each hemisegment or ShakB-Gal4 to drive expression primarily in Is MNs (data not shown) (Takizawa et al., 2007).

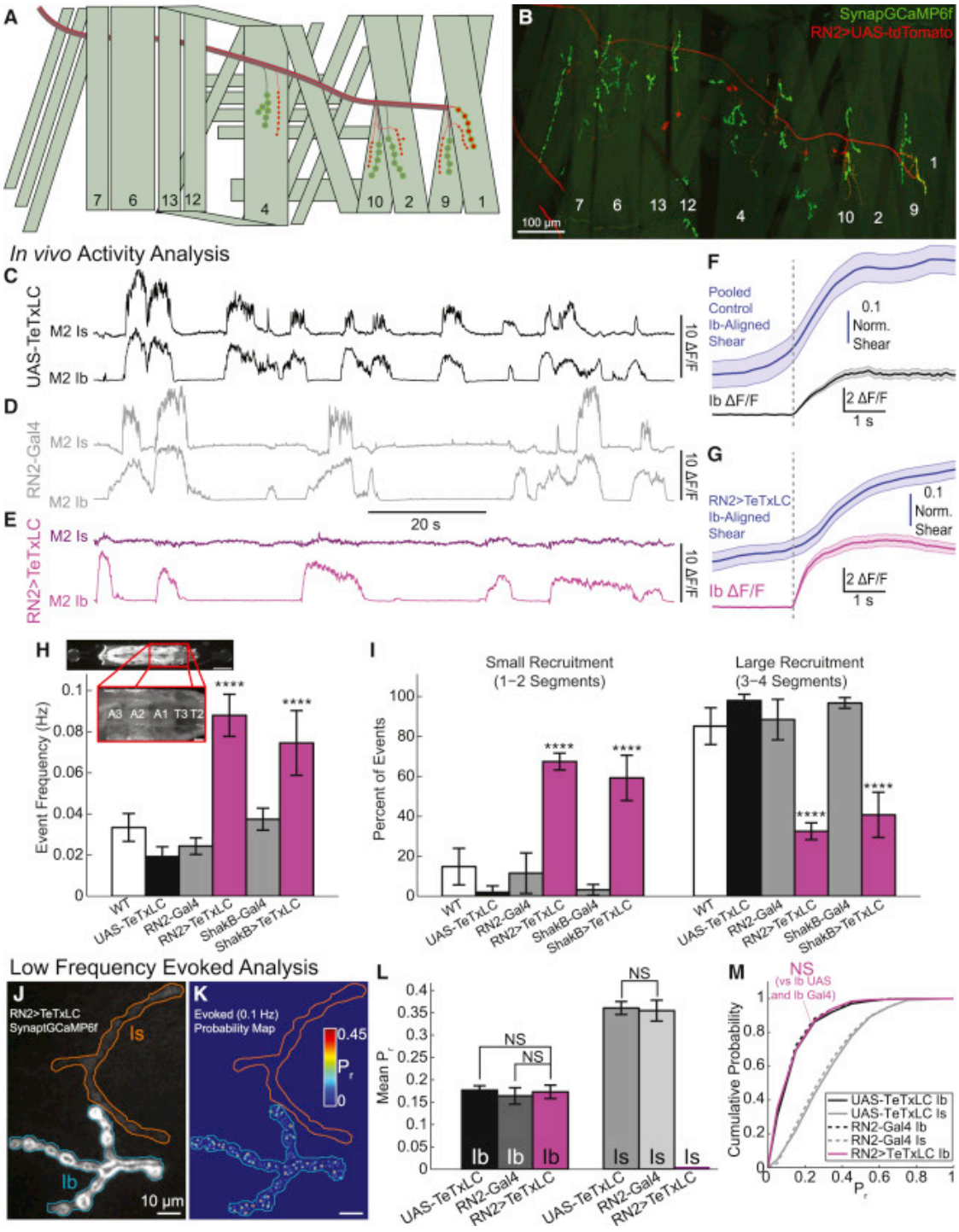
A
7 6 13 12 4 10 2 9 1
B
SynapGCaMP6f
RN2>UAS-tdTomato
100 µm
7 6 13 12 4 10 2 9 1
In vivo Activity Analysis
C
UAS-TeTxLC
M2 Is
M2 Ib
10 ΔF/F
D
RN2-Gal4
M2 Is
M2 Ib
10 ΔF/F
20 s
E
RN2>TeTxLC
M2 Is
M2 Ib
10 ΔF/F
F
Pooled Control Ib-Aligned Shear
0.1 Norm. Shear
Ib ΔF/F
2 ΔF/F
1 s
G
RN2>TeTxLC Ib-Aligned Shear
0.1 Norm. Shear
Ib ΔF/F
2 ΔF/F
1 s
H
A3 A2 A1 T3 T2
Event Frequency (Hz)
0 0.02 0.04 0.06 0.08 0.1
****
****
WT
UAS-TeTxLC
RN2-Gal4
RN2>TeTxLC
ShakB-Gal4
ShakB>TeTxLC
I
Small Recruitment (1–2 Segments)
Large Recruitment (3–4 Segments)
Percent of Events
0 20 40 60 80 100
****
****
****
****
WT
UAS-TeTxLC
RN2-Gal4
RN2>TeTxLC
ShakB-Gal4
ShakB>TeTxLC
Low Frequency Evoked Analysis
J
RN2>TeTxLC
SynaptGCaMP6f
Is
Ib
10 µm
K
Evoked (0.1 Hz)
Probability Map
0.45
Pr
0
L
Mean Pr
0 0.05 0.1 0.15 0.2 0.25 0.3 0.35 0.4
NS
NS
NS
Ib Ib Ib Is Is Is
UAS-TeTxLC
RN2-Gal4
RN2>TeTxLC
M
NS (vs Ib UAS and Ib Gal4)
Cumulative Probability
0 0.2 0.4 0.6 0.8 1
0 0.2 0.4 0.6 0.8 1
Pr
UAS-TeTxLC Ib
UAS-TeTxLC Is
RN2-Gal4 Ib
RN2-Gal4 Is
RN2>TeTxLC Ib

Figure 7 Homeostatic Plasticity Is Input Autonomous (A) Schematic showing expression pattern of RN2-Gal4 (red). (B) Multiple stitched maximum-intensity projections of SynapGCaMP6f and RN2 > UAS-tdTomato. (C–E) Representative in vivo activity at M2 Ib and Is NMJs in a UAS-TeTxLC larva (C) (black; also Figure S7A), a RN2-Gal4 larva (D) (gray; also Figure S7B), and a RN2 > TeTxLC larva (E) (magenta; also Figure S7C). (F and G) Ib NMJ mean ΔF/F (±SEM) and mean time-locked NMJ shearing associated with the onset of Ib synaptic activity in control (F) (UAS-TeTxLC and RN2-Gal4 were pooled) or RN2 > TeTxLC (G) NMJs. The activity start time used for alignment is indicated by the vertical gray dashed line. M1-Ib NMJ data were excluded from this analysis in the RN2 > TeTxLC animals because of their expression of TeTxLC (pooled control, n = 46 activity bouts from 38 NMJs, 9 larvae; RN2 > TeTxLC, n = 125 bouts from 84 NMJs, 14 larvae). (H) Frequency of segment-wide SynapGCaMP6f activity within segments T2-A3 in WT (n = 10 larvae), UAS-TeTxLC (n = 10 larvae), RN2-Gal4 (n = 10 larvae), and RN2 > TeTxLC (n = 10 larvae), ShakB-Gal4 (n = 10 larvae), and ShakB > TeTxLC (n = 10 larvae). Inset illustrates the imaged area. Significance (∗∗∗∗) was found between either RN2 > TeTxLC or ShakB > TeTxLC and all controls but not between TeTxLC expressing groups. (I) Percentage of continuous activity in (H) that spanned either one or two segments (left) or three or four segments (right). Similarly, in both sets, significance (∗∗∗∗) was found between either RN2 > TeTxLC or ShakB > TeTxLC and all controls but not between TeTxLC expressing groups. (J) Baseline fluorescence of RN2 > TeTxLC larva (Ib, blue; Is, orange). (K) RN2 > TeTxLC cumulative AP-evoked quantal release location heatmap (200 trials at 0.1 Hz) Color scale corresponds the local Pr. (L) Mean 0.1 Hz evoked Pr by NMJ for UAS-TeTxLC (Ib n = 6; Is n = 6 NMJs), RN2-Gal4 (Ib n = 6; Is n = 6 NMJs), and RN2 > TeTxLC (Ib n = 6; Is n = 6 NMJs; no AP-responsive Is sites). (M) Cumulative probability for 0.1 Hz evoked Pr at pooled synapses for UAS-TeTxLC (Ib n = 667; Is n = 242 sites), RN2-Gal4 (Ib n = 642; Is n = 377 sites), and RN2-Gal4 > TeTxLC (Ib n = 653 sites).
Mean ± SEM indicated. Comparisons were made using one-way ANOVA with Tukey's post hoc test (H, I, and L) or Kruskal-Wallis with Tukey's post hoc tests for pooled data (M). ∗∗∗∗$p < 0.0001$.

As expected, in vivo SynapGCaMP6f imaging of dorsal muscles 1, 2, 9, and 10 showed that larvae expressing UAS-TeTxLC under RN2-Gal4 had a complete lack of Is activity, while Ib activity remained intact (Figures 7C–7E and S7A-D; Movie S8). In the semi-dissected preparation, low-frequency MN stimulation failed to evoke transmission from MNISN-Is and MN1-Ib but not MNSNb/d-Is (a ventral projecting Is MN that does not express the Gal4) or any other Ib synapse (Figures S7E–S7G). SynapGCaMP6f fluorescence and optical quantal sizes were unaffected by Is-TeTxLC expression at either input (Figures S7H and S7I), with only a subtle decrease in spontaneous transmission rate being observed in the TeTxLC-expressing Is NMJ (Figure S7J). Thus, expression of TeTxLC specifically eliminates evoked transmitter release from Is inputs. Interestingly, although loss of Is evoked activity left muscle contraction intact (Figures 7F and 7G), intersegmental wave activity was elevated using both selective MN Gal4 lines (Figure 7H), and an increased number of waves failed to propagate through multiple segments (Figure 7I), suggesting a role for Is transmission in large-scale muscle coordination during locomotion.

Having found a driver for TeTxLC that selectively eliminates evoked transmission at Is inputs, we could now turn to muscles whose Is evoked activity was eliminated and examine the basal transmission properties of its paired Ib input. Strikingly, we found no change in Ib basal single-synapse Pr or quantal density in the Is-specific TeTxLC larvae (Figures 7J–7M and S7K). In addition, high-frequency stimulation also revealed normal Ib plasticity in the absence of Is transmission (Figures S7L–S7O). Thus, there is no change of transmission at Ib synapses when the excitatory drive to a muscle is reduced by elimination of transmission from the nearby convergent Is input. In other words, homeostatic upregulation at Ib synapses is specifically responsive only to loss of postsynaptic glutamate sensitivity at its own Ib postsynapse.

Reduction in Postsynaptic CaMKII Activity Selectively Enhances Ib Presynaptic Release

Reduction in postsynaptic CaMKII activity has been shown to boost transmitter release, suggesting that homeostatic signaling is triggered by reduced activation of CaMKII following a reduction in Ca2+ influx when GluRIIA-containing GluRs are removed (Haghighi et al., 2003). This led us to ask whether homeostatic compensation occurs exclusively at Ib presynapses because Ib postsynapses reach much higher internal Ca2+ levels during locomotion (Figures 2E and 2F). As a first test of this idea, we asked whether Ib and Is postsynapses differ in levels of activated CaMKII by staining WT SynapGCaMP6f NMJs with an antibody against the active (phosphorylated) form of CaMKII (pCaMKII) (Figures S8A–S8E). Consistent with earlier work, which showed that is CaMKII enriched at postsynapses (Koh et al., 1999), we observed strong staining surrounding both Ib and Is axons, which overlapped with GluRIIA puncta more closely than it did with presynaptic Brp puncta (Figures 8A–8C and S8B–S8E). These observations indicate strong postsynaptic localization of active CaMKII at both inputs, near the site of transmission-evoked Ca2+ influx. Interestingly, the total integrated pCaMKII values were 2.5- to 6-fold higher at Ib inputs compared with Is inputs that innervated the same muscle (Figures 8G and 8H). This difference in pCaMKII is similar to the difference we observed in integrated Ca2+ influx in vivo (Figure 2G). Consistent with the proposed relationship between GluRIIA and postsynaptic CaMKII, total pCaMKII levels were lower in GluRIIA, but only at Ib postsynapses (Figures 8D–8H).

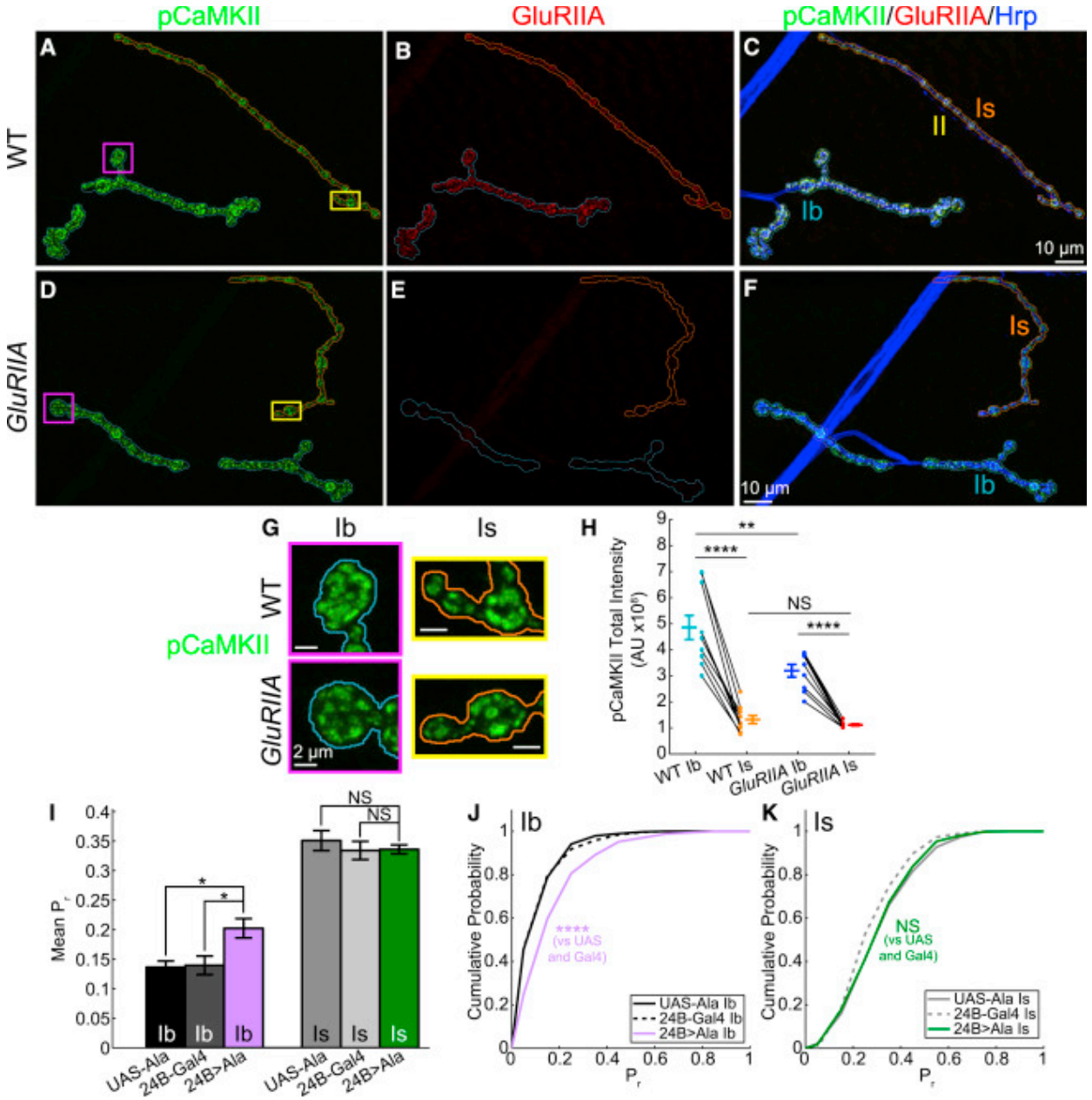

Figure 8 Inhibition of Postsynaptic CaMKII Only Increases Ib Release (A–F) Maximum-intensity projections of pCaMKII (A and D), GluRIIA (B and E), and Hrp (merged images of all three channels in C and F) antibody labeling for WT (A–C) and GluRIIA (D–F) larvae (Ib, blue; Is, orange). (G) Representative bouton maximum-intensity projections of pCaMKII labeling for Ib (magenta) and Is (yellow) NMJs in WT (top) and GluRIIA (bottom) from (A–F). (H) Total integrated pCaMKII intensity for WT and GluRIIA Ib and Is maximum intensity projections. (I) Mean 0.1 Hz evoked Pr by NMJ for UAS-Ala (Ib, n = 8; Is n = 8 NMJs), 24B-Gal4 (Ib, n = 8; Is n = 8 NMJs), and 24B > Ala (Ib, n = 9; Is n = 9 NMJs). (J and K) Cumulative probability for pooled 0.1 Hz evoked single synapse Pr for UAS-Ala (Ib, n = 869; Is, n = 414 sites), 24B-Gal4 (Ib, n = 792; Is, n = 339 sites), and 24B > Ala (Ib, n = 717; Is, n = 427 sites) for Ib (J) and Is (K) NMJs. Mean ± SEM indicated. Comparisons made with one-way ANOVA with Tukey's post hoc test (H and I) or Kruskal-Wallis with Tukey's post hoc tests for pooled data (J and K). ∗p < 0.05; ∗∗p < 0.01; ∗∗∗∗p < 0.0001.

The above observations suggest that homeostatic compensation only occurs at the Ib input because GluRIIA only reduces CaMKII activity at Ib postsynapses. This selectivity may reflect a nonlinear relationship between the spatiotemporal rise in internal Ca2+ and CaMKII activation (Stratton et al., 2013). The experiments left unresolved whether Is postsynapses would be capable of generating the homeostatic signal if CaMKII activity was reduced. To address this, we turned to a method for inhibiting CaMKII activity throughout the postsynaptic muscle using the CaMKII inhibitory peptide, UAS-Ala (Griffith et al., 1993), under the control of the muscle-specific 24B-Gal4 (Luo et al., 1994). The CaMKII inhibitory peptide had no effect on baseline SynapGCaMP6f fluorescence (Figure S8F) or evoked fluorescent event amplitudes (Figure S8G). Additionally, similar to GluRIIA, there was no change the density of active synapses (Figure S8H) or the variability in Pr (Figure S8I) at either input. Thus, most aspects of synaptic function were normal, putting us in position to ask how CaMKII inhibition affects transmitter release. We found that postsynaptic expression of the CaMKII inhibitory peptide increased both the single-synapse Pr (Figures 8I and 8J) and quantal density per stimulus at Ib synapses (Figure S8J), similar to the effect of the GluRIIA mutation. In striking contrast, the CaMKII inhibitory peptide had no effect on either Pr or quantal density at Is synapses (Figures 8I, 8K, and S8J).

Together, these observations indicate that the Ib postsynapse signals more strongly to the homeostatic machinery in response to reduced CaMKII activity and, moreover, reacts with a larger decline in CaMKII activity in response to loss of excitatory drive. The upshot is that homeostatic compensation occurs exclusively at the Ib input that dominates locomotor drive (see Figures 1 and 2).

Discussion

The relationship between in vivo synaptic activity and the homeostatic mechanisms that stabilize synaptic function has remained unclear. In this report, we present a new optical reporter of excitatory synaptic transmission, combined with novel imaging of a live, intact, and behaving organism that enables us to relate synaptic activity at multiple targets simultaneously throughout an animal in vivo, to synaptic activity at synapses formed on a common postsynaptic cell by two convergent input types, Ib and Is. These techniques are sensitive enough to detect single quantal events, while tracking neurotransmitter release from hundreds of synapses simultaneously. Moreover, we are able to obtain a direct measure of the Pr at individual synapses of both inputs from optical failure analysis. Using these methods, we have investigated short-term plasticity and the homeostatic regulation of synaptic reliability. We find that both activity-dependent forms of synapse regulation as well as basal synaptic transmission are controlled differentially in the two input types (see Figure S8K), reflecting the discrete physiological roles of these inputs in the behaving animal.

Input-Specific Synaptic Physiology and Behavior

The Ib and Is inputs to the Drosophila larval muscle respectively resemble tonic (low Pr, facilitating) and phasic (high Pr, depressing) inputs seen at neuro-muscular and neuro-neuronal connections in other organisms (Atwood and Karunanithi, 2002). Given these differences, the Is input has been proposed to initiate strong, phasic muscle contractions (Schaefer et al., 2010).

However, we find that the primary excitatory drive and main cause of muscle contraction in larval Drosophila is actually the Ib input. This is despite the fact that Is synapses have a higher basal Pr and larger quantal sizes. These functional differences likely reflect the relatively short duration of the Is bursts of activity and the relatively small number of active zones of the Is terminal. Whereas elimination of transmission from Is inputs had little or no effect on muscle contraction during restrained locomotion, just as it had earlier been shown to have negligible effect on general behavior (Suster et al., 2003), we find that the Is input is needed for normal intersegmental coordination of contraction waves. This is consistent with the broad, multi-muscle Is innervation pattern (Hoang and Chiba, 2001).

Ib synaptic activity begins before and ends after Is activity, consistent with their common presynaptic inputs and different intrinsic excitabilities (Choi et al., 2004, Schaefer et al., 2010). Recent work has shown that excitatory and inhibitory interneurons regulate the differential recruitment of MNs between hemisegments and within hemisegments, respectively (Heckscher et al., 2015, Zwart et al., 2016). While Ib inputs ramp up their synaptic drive during locomotor bursts, Is inputs abruptly reach a maximum, which they often sustain for the duration of the shorter burst. Given their substantial depression during high-frequency stimulation, the ability of the Is input to sustain a fixed output level during locomotion suggests that it increases the firing frequency during the bursts. The common interneuron drive within the VNC suggests that the progressive increase in synaptic drive during the Ib burst may also be partly due to an increase in frequency during the burst, in addition to the recruitment of silent synapses and increase in Pr of active synapses, which we observe during facilitating high-frequency trains. Thus, a combination of circuit-level and cell-autonomous differences combine to generate the complex behavioral output of the larva from a limited number MNs and muscles.

Diversity in Basal Transmission and Short-Term Plasticity

Spontaneous glutamate release has been shown to play a role in synapse development (Choi et al., 2014). However, we find that spontaneous release in vivo represents only ∼1% of total release, suggesting that evoked release would drown out the influence of spontaneous release. One possible explanation is that in late third-instar larvae, spontaneous release may represent a larger fraction of total synaptic transmission than earlier in development when the developmental influences are exerted. An intriguing alternative explanation derives from our finding that, at both inputs, synapses preferentially participate in either evoked or spontaneous release. This suggests that developmental signals could occur at a subset synapses that are dominated by spontaneous release.

We find that synapses of both inputs differ in key properties, with Is synapses having larger quantal sizes, less total spontaneous release, higher Pr, and short-term depression (as opposed to facilitation in Ib synapses) during high-frequency trains. The difference in short-term plasticity between the inputs is consistent with electrophysiological analysis of responses to separate stimulation of Is or Ib axons (Lnenicka and Keshishian, 2000, Lu et al., 2016), as well as modeling (Knodel et al., 2014). These resemble input-specific differences seen in the mammalian brain, such as between parallel and climbing fibers converging on Purkinje cells (Dittman et al., 2000, Mapelli et al., 2015) or interneurons in the cortex (Gupta et al., 2000). The tendency to facilitate or depress is shaped by basal Pr, where high Pr results in greater depletion

of immediately releasable vesicles leading to depression (Zucker and Regehr, 2002). Although overall this agrees with our observation that Is synapses have higher Pr and depress, we find that despite overlapping distributions of single-synapse Pr, overall release tended to depress in Is and facilitate in Ib, suggesting additional differences in regulation. This greater complexity comes into stark relief when we examine the behavior of hundreds of individual synapses during high-frequency trains of presynaptic firing. We find that the heterogeneity of short-term plasticity within an input is much greater than was previously appreciated. We categorize local plasticity dynamics by how transmission changed during a stimulus train and find that the inputs differ only in two categories, Is inputs having a larger number of active sites that depress and Ib having a larger number of silent sites that are recruited to a releasing state. These observations reveal a previously unknown level of specialization in basal release and plasticity between neighboring synapses of a common input.

Input-Specific and Input-Autonomous Homeostatic Plasticity

The Drosophila larval NMJ has proven to be a powerful system for studying synaptic homeostasis. The mechanism of this homeostasis is that reduction in quantal size (because of reduced GluR conductance that results from either mutation of a GluR subunit or partial pharmacological block) triggers a retrograde signal that leads to increased transmitter release, restoring the normal the normal level of excitatory drive (Davis and Müller, 2015). Our results reveal a new aspect to homeostatic plasticity by showing that it is specific to input and acts primarily at synapses with certain properties of basal transmission, short-term plasticity and physiological function. We find that only glutamate release from the Ib input is boosted during homeostatic compensation. We attribute this to the fact that despite the smaller quantal size and unitary Ca2+ influx at Ib synapses, Ib inputs have longer bouts of activity, resulting in much larger aggregate Ca2+ elevation in the Ib postsynapse during locomotion. The larger Ca2+ influx drives a higher activation of CaMKII in the Ib postsynapse. Critically, mutation of the GluR subunit to reduce quantal size at both Ib and Is synapses exclusively reduces activated CaMKII at the Ib postsynapse. Why there is no reduction in activated CaMKII at the Is postsynapse is not clear, though nonlinearity in the relationship between the Ca2+ concentration profile and CaMKII activation (Stratton et al., 2013) and differences in GluR subunit composition that influence Ca2+ influx (Marrus et al., 2004) may contribute.

A second mechanistic difference ensures exclusivity for homeostatic signaling to the Ib input: even when CaMKII activity is inhibited throughout the muscle, only Ib presynapses are boosted in Pr. This could mean that Is presynapses are not responsive to the homeostatic signal. Alternatively, it could mean that Is postsynapses are incapable of generating the homeostatic signal, an idea that would be consistent with our finding that elimination of release from Is axons does not induce homeostatic compensation at Ib synapses. However, this would also require that the retrograde homeostatic signal act very locally so that it could not travel even a few microns from signaling-capable Ib postsynapses to Is boutons that are often located very close by. Another possibility is that basal Pr is high at Is synapses partly due to lower levels of activity in vivo resulting in greater homeostatic enhancement in presynaptic release, which in turn could occlude further increases in synaptic reliability following changes in GluR composition or global postsynaptic CaMKII inhibition.

Evidence for signaling compartmentalization can be seen in the structural differences between Ib and Is NMJs, particularly on the postsynaptic side. Ib axons are surrounded by a significantly thicker and more elaborate SSR (Atwood et al., 1993, Jia et al., 1993). There are also substantial differences in the localization of key organizing postsynaptic proteins such as Dlg which is present at higher levels in Ib postsynapses (Lahey et al., 1994). CaMKII activity has also been shown to affect SSR structure and Dlg localization (Koh et al., 1999). Thus, the different activity patterns during native behaviors may also directly regulate postsynaptic properties other than presynaptic release to maintain functional diversity.

The presynaptic changes that mediate homeostatic compensation in Pr are only partly known. Homeostasis has been shown to be accompanied by an increase in presynaptic AP-evoked Ca2+ elevation in Ib boutons (Müller and Davis, 2012). Although a number of molecules have been demonstrated to play a role in mediating presynaptic homeostatic compensation (Davis and Müller, 2015), it remains to be determined how these mechanisms interact with input-specific differences in strength and plasticity.

Although homeostasis has been generally thought to be a global mechanism to regulate synaptic strength, evidence has emerged that homeostasis can be regulated with variable degrees of specificity (Davis and Müller, 2015, Turrigiano, 2012). We have now demonstrated that homeostatic changes can also propagate retrogradely to the presynaptic neuron in an input-specific and synapse-autonomous manner. Given the divergent innervation of multiple muscles by Is inputs and unique innervation by Ib inputs, a Ib-specific homeostatic mechanism can provide greater functional flexibility.

Conclusions

By combining in vivo, physiological measurements of glutamate release with high-resolution quantal analysis at single synapses in the semi-dissected preparation, we have clarified the relative properties of convergent glutamatergic inputs in the larva during native behaviors. Importantly, we have demonstrated that the regulation of basal synaptic strength, short-term plasticity, and homeostasis are shaped in a precise input-specific manner. The Ib input has higher levels of in vivo activity, lower Pr synapses, and a propensity for facilitation by recruiting silent synapses during spike trains. Furthermore, the Ib input is the primary determinant for contraction dynamics in the behaving animal. Consistent with its dominant role, when postsynaptic sensitivity to glutamate is altered at both inputs, there is a selective homeostatic adjustment in the amount of neurotransmitter released from Ib input. CaMKII, localized to the postsynaptic density, is ideally placed to detect local changes in postsynaptic activity at both inputs, and postsynaptic inhibition of CaMKII activity is sufficient to enhance release at the Ib input, demonstrating a high degree of signaling compartmentalization within a single muscle cell. Together, these results demonstrate how synaptic activity at the Drosophila larval NMJ is precisely regulated to ensure both functional diversity and stability.

Methods

Experimental Model and Subject Details

Transgenic flies were made using standard germline transformation by embryo injection (BestGene, Chino Hills CA). UAS-tdTomato flies were generated by Einat Peled. 24B-Gal4 (Luo et al., 1994), UAS-Ala (Griffith et al., 1993), GluRIIASP16 and Df(2L)clh4 (Petersen et al., 1997) flies were from Corey Goodman (UC Berkeley). UAS-TeTxLC (Sweeney et al., 1995) was from Kristen Scott (UC Berkeley). RN2-Gal4 (#7473) and ShakB-Gal4 (#51633) lines were from Bloomington Drosophila Stock Center (Bloomington, IN). Flies were raised on standard corn meal and molasses media at 25°C. Both male and female wandering third instar larvae were used in all experiments. When required, third instar larvae were screened using an Axio Zoom.V16 microscope (Carl Zeiss, Oberkochen, Germany) through the use of balancers with larval markers including CyOGFP (3xP3-EGFP variant) and TM6B. Only actively crawling larvae were used for experiments.

Unless otherwise noted, all larvae contained a single copy of SynapGCaMP6f. The following genotypes were used: wild-type control (w1118;+;+), wild-type SynapGCaMP6f (WT; w1118;+/+;SynapGCaMP6f/+), GluRIIA (GluRIIASP16/Df(2L)clh4;SynapGCaMP6f/+), UAS-Ala (w1118;UAS-Ala/+;SynapGCaMP6f/+), 24B-Gal4 (w1118;+/+;SynapGCaMP6f/24B-Gal4), 24B > Ala (w1118;UAS-Ala/+;SynapGCaMP6f/24B-Gal4), UAS-TeTxLC (w1118;UAS-TeTxLC/+;SynapGCaMP6f/+), RN2-Gal4 (w1118;RN2-Gal4/+;SynapGCaMP6f/+), RN2 > TeTxLC (w1118;UAS-TeTxLC/RN2-Gal4;SynapGCaMP6f/+), RN2-Gal4 > UAS-tdTomato (w1118;RN2-Gal4/UAS-tdTomato;SynapGCaMP6f/+), ShakB-Gal4 (w1118;ShakB-Gal4/+;SynapGCaMP6f/+), and ShakB > TeTxLC (w1118;UAS-TeTxLC/ShakB-Gal4;SynapGCaMP6f/+).

SynapGCaMP6f Construct

The Ca2+ sensor GCaMP6f (Chen et al., 2013) was targeted to the muscle as done previously (Peled and Isacoff, 2011, Peled et al., 2014) starting with the SynapGCaMP3 DNA construct (MHC-CD8-GCaMP3-Sh), which includes the myosin heavy chain (MHC) promoter, CD8 transmembrane domain and 154 amino acids from the C-terminal tail of the D. melanogaster shaker (Sh) potassium channel. GCaMP6f (#40755, Addgene, Cambridge, MA) was amplified with SpeI containing primers and inserted into the SpeI site of the SynapGCaMP3 construct, exchanging GCaMP3 for GCaMP6f to generate the SynapGCaMP6f construct MHC-CD8-GCaMP6f-Sh.

In vivo Imaging Chambers

For all in vivo imaging, third instar larvae were mounted in a custom-built gas-permeable poly(dimethylsiloxane) (PDMS) imaging chamber. The PDMS chambers were fabricated using standard soft lithography replica molding techniques. A 500 μm-thick mold for the PDMS chambers was fabricated with SU8-2150 (Microchem, Westborough, MA) on a silicon wafer, followed by the silanization of SU8 mold in a vacuum desiccator to aid release from PDMS. PDMS (Sylgard 184, Dow Corning, Auburn, MI) was prepared with a 10:1 mass ratio (base to

cross-linker), degassed in a vacuum chamber for 30 min, poured on the SU8 mold, cured in an oven at 60°C for at least 2 hr. The PDMS was then carefully peeled off the mold and individual chambers were cut to shape.

In vivo Intact Larval SynapGCaMP6f Imaging

Imaging was performed in a PDMS chamber with an internal depth of 500 μm and an internal width of 1 mm (Figures 1A and S1A). Larvae were oriented with the dorsal surface up in the chamber and gently sealed in the chamber using standard coverslip glass. Larvae were imaged using an Axio Zoom.V16 microscope (Zeiss) with a 2.3x 0.57 NA objective, a FS 38 HE filter set (Zeiss, excitation BP 470/40nm HE; emission 525/50nm HE) and an AxioCam Hr R3 camera. Image acquisition was performed by Zen 2 (Zeiss). Anterior half of the whole larva or dorsal muscles 1, 2, 9 and 10 from segments T3, A1 or A2 were used. Anterior segments provided the cleanest images without significant contamination from the often autofluorescent gut and light scattering fat tissue; however, this technique was able to detect synaptic activity at nearly all body-wall muscles from all segments. For image acquisition, 50 ms images were acquired at frequencies between 14-20 Hz continuously for 1-2 min with a final magnification of either 40x or 260x and a 2 μm depth of field (aperture fully opened). The large depth of field prevents the NMJs from moving out of focus during small movements. All MN activity was endogenous and data were only used from larvae that exhibited sustained activity following the mounting and imaging process. Recordings or NMJs where there was too much movement or NMJs that moved completely out of focus were excluded from the analysis.

SynapGCaMP6f Optical Quantal Imaging

For high-resolution quantal analysis, third instar larvae were first dissected in HL3 solution containing, in mM: 70 NaCl, 5 KCl, 0.45 CaCl2·2H2O, 20 MgCl2·6H2O, 10 NaHCO3, 5 trehalose, 115 sucrose, 5 HEPES, and with pH adjusted to 7.2. Following removal of the brain, larval fillets were washed and imaged in HL3 containing 1.5 mM Ca2+ and 25 mM Mg2+, unless otherwise noted (see Figures S3G and S5S–S5V). Fluorescence images were acquired with a Vivo Spinning Disk Confocal microscope (3i Intelligent Imaging Innovations, Denver, CO), which included a 63x 1.0NA water immersion objective (Zeiss), LaserStack 488nm (50 mW) laser, Yokogawa CSU-X1 A1 spinning disk (Tokyo, Japan), standard GFP filter, and EMCCD camera (Photometrics Evolve, Tucson, AZ). Unless otherwise noted (see Figure S7F and S7G, where 20x water objective was used), all fillet recordings were done on ventral longitudinal abdominal muscle 4 at segments A2-A5 of third instar larvae. Fields of view were first selected to maximize the area of both Ib and Is terminals that could be imaged within a single focal plane. The imaging area was then cropped to just the NMJ area.

Nerve stimulation was performed with a suction electrode attached to a Stimulus Isolation Unit (SIU, ISO-Flex, A.M.P.I Jerusalem, Israel) with a 75-100 μs stimulus duration. Stimulation intensity was adjusted to recruit both Ib and Is axons as verified during the imaging. Nerve stimulation and imaging were synchronized using custom-written MATLAB (MATLAB Version R2015b and Image Processing Toolbox Release R2015b, MathWorks, Natick, MA) scripts used to control the SIU and trigger imaging episodes within SlideBook (v6.0.9, 3i Intelligent Imaging Innovations).

Episodic stimulation and imaging protocols (only possible at stimulation frequencies between 0.1 - 1 Hz) involved acquiring images as a series of 10 images (50 ms exposures). Each episode had at least 3-4 baseline frames prior to nerve stimulation. In most cases, 200 stimulus trials at 0.1 Hz were used for analysis to minimize the effects of statistical fluctuations on the calculation of Pr at individual synapses (see below). Spontaneous release was measured by imaging continuously at 20 Hz (50 ms exposures in streaming capture mode) for 2 min total separated into four 30 s imaging blocks to allow for the manual correction of any drift. For the simultaneous analysis of spontaneous and evoked quantal amplitudes (only Figure S4K), images were similarly acquired at 20 Hz continuously for 100 s with 10 stimulation trials at 0.1 Hz. High-frequency stimulation experiments involved imaging continuously (50 ms exposures in streaming capture mode) at 20 Hz and waiting 3 s before stimulating at the indicated frequencies and durations (Figures 6 and S6). Stimuli were time-locked to the start of the recording to register stimuli.

Data collection and subsequent analysis were not performed blind; however, care was taken to ensure that the animals received the same treatment before and during the recordings. Data were then analyzed with the same parameters for all relevant automatic detection thresholds when possible. In all cases, due to the length of individual recording sessions for a given experiment, genotypes were randomly rotated on each day to ensure that data for each genotype were generated on multiple days. However, all replicates for a particular experiment were performed by the same person to remove any source of variability in the preparation of animals. Similar numbers of replicates were used for each genotype within a given experiment.

Electrophysiology

Third instar larvae were dissected as described above and all recordings were performed on muscle 4 from segment A3 in HL3 containing 1.5 mM Ca^{2+} and 25 mM Mg^{2+}. Recording electrodes contained 3 M KCl and had resistances in the range 15-35 MΩ. Only muscles with a resting membrane potential (Vm) below −60 mV and a membrane resistance above 4 MΩ were used for the analysis. For two-electrode voltage clamp experiments, the membrane was held at −80 mV. All data were recorded at 5 kHz, with an AxoClamp-2A amplifier and Digidata 1322A interface and Clampex 8.0 software (Molecular Devices, Sunnyvale, CA). The motor neuron was stimulated as described above. For simultaneous spontaneous mEPSP measurements with imaging, the image acquisition was triggered by the Digidata so that the imaging was time-locked to the start of the electrophysiology recording. During these recordings we are unable to account for all mEPSP events during our optical analysis. This is due to several technical factors. The combination of spinning disk confocal microscope and high-magnification objective (63x) mean that we can only image from a fairly limited Z section of the muscle surface. We are able to reliably identify events around a single bouton, but if other boutons are located at a different Z position along the curved muscle surface, we may not be able to image those SynapGCaMP6f signals. Similarly, the branching patterns of both Ib and Is axons may prevent us from imaging the entire Ib and Is NMJs simultaneously. Thus, as many as about 50% of either input may not be imaged at a given time, while the electrical mEPSP measurements should be detectable from the entire muscle. However, we should also note that it is possible that mEPSPs may also be missing, as has recently been reported (Nguyen and Stewart, 2016). Given these concerns, we

find that nearly all optical events have a corresponding mEPSP but not vice-versa, with many mEPSPs not having an observed optical event.

For simultaneous two-electrode voltage clamp and imaging experiments (see Figures S3J–S3M), image acquisition was similarly triggered by the Digidata and brief voltage steps were applied to determine whether voltage-gated channels contributed to the SynapGCaMP6f response. We find that voltage steps, even to a membrane potential of 0 mV from −80 mV, failed to produce a detectable fluorescence change.

Antibody Labeling

Larvae were fixed in Bouin's fixative (Ricca Chemical Company, Arlington, TX) for 5 min, permeabilized in PBS with 0.1% Triton X-100 (PBT) and blocked in PBS with 0.1% Triton X-100, 5% normal goat serum, and 0.02% NaAzide (PBN). All antibody incubations were performed in PBN and washes were performed in PBT. Mouse anti-Brp (nc82) and mouse anti-GluRIIA (8B4D2) primary antibodies were used at 1:100 (Developmental Studies Hybridoma Bank, Iowa City, IA). Polyclonal rabbit anti-pT286 CaMKII (PA5-17755, Thermo Fisher Scientific, Waltham, MA) antibody was used at 1:200. Rabbit anti-GFP antibody (A21311; Thermo Fisher Scientific) was used at 1:1000 to label SynapGCaMP6f following fixation. Alexa Fluor 488 (123-545-021) and Cy3-conjugated (123-165-021) goat anti-Hrp antibodies (Jackson ImmunoResearch Laboratories, West Grove, PA) were used at 1:100. Alexa Fluor 488 goat anti-rabbit (A11008), Alexa Fluor 532 goat anti-mouse (A11002), and Alexa Fluor 647 goat anti-mouse (A21235) secondary antibodies (Invitrogen) were used at 1:1000. Following antibody incubations and washes, larval fillets were mounted in Vectashield (Vector Laboratories, Burlingame, CA). Antibodies obtained from the Developmental Studies Hybridoma Bank were developed under the auspices of the National Institute of Child Health and Human Development of the National Institutes of Health and maintained by the Department of Biological Sciences of the University of Iowa, Iowa City, IA.

Immunofluorescence Imaging

NMJ images of antibody labeled fillets were acquired with a LSM 780 or LSM 880 microscope and a 63x/1.4 DIC oil immersion objective using Zen software (Zeiss). For comparisons of pCaMKII levels between different genotypes all antibody labeling and imaging were performed on the same day under identical conditions. Z stacks were acquired with between 0.5 µm to 0.25 µm z axis spacing except for images of the larval central nervous system and ventral nerve cord, which used a 5x objective and 2 µm spacing.

Quantification and Statistical Analysis

In vivo Image Analysis

All image analysis was performed using custom-written MATLAB routines. Images were first converted using the Bio-Formats MATLAB Toolbox from the Open Microscopy Environment (Linkert et al., 2010). To stabilize the moving and contracting NMJs in vivo, movies were run through a series of successive image registration steps. Individual recordings often contained

several Ib and Is NMJ pairs that were processed separately. Coarse, rigid translational movements of the NMJ pairs were removed by computing the x- and y-displacements to arrive at the maximum 2D cross-correlation between successive frames. These corrections eliminated the movement from neighboring hemisegments and large local contractions. The individual NMJs within the tracked areas were then registered using affine and diffeomorphic nonlinear (Demon) transformations (MATLAB Image Processing Toolbox Release R2015b), where a high intensity frame (with both Ib and Is NMJs showing activity) was used as reference. The combination of these methods corrected for the shape changes that occurred during contraction of the muscle locally. Fluorescence data were calculated using regions of interest (ROIs) that were manually drawn around either 1 to 2 boutons or the entire NMJ depending on the type of analysis performed. Absolute fluorescence from both Ib and Is NMJs was always contaminated by a combination of internal larval autofluorescence, residual out of focus SynapGCaMP6f fluorescence, and broad SynapGCaMP6f fluorescence within the muscle. This later fluorescence was present at lower levels and therefore capable of measuring Ca2+ activity more broadly throughout the muscle near the membrane. Muscle contractions gave rise to slower and spatially uniform fluorescence signals, which remained tightly correlated with high levels of synapse activity (see Figure S1F). These fluorescence changes were consistent with what one would expect from the rapid conduction of the EPSP voltage along the large diameter muscle fiber, coupling of Ca2+ influx through voltage-gated channels to Ca2+-induced Ca2+ release from internal stores. These spatially uniform muscle fluorescence signals (Fm), along with any corresponding background fluorescence changes were therefore always subtracted from the absolute fluorescence prior to calculating Ib and Is ΔF/F by calculating the mean fluorescence intensity from an area adjacent to both types of NMJs but not containing any synapses. Bleaching under these imaging conditions was minor but Fm subtraction often also corrected for any slow bleach during long recordings. This process allowed the synaptic component of the SynapGCaMP6f fluorescence changes to be cleanly isolated in the complex in vivo environment of a behaving larva.

In order to quantify the degree of synchronicity between Ib and Is NMJs, Pearson's correlation coefficients were calculated between ΔF/F traces averaged across single boutons (Figure S1E). Similar correlation analysis was performed between ΔF/F traces and Fm (Figure S1F). Total NMJ translation magnitude was calculated as the summed magnitudes of all of the motion correction steps for an individual bouton including the coarse translation correction and affine translation magnitudes (see Figure 1G, black trace and Figures S1B–S1D). Muscle contraction dynamics were quantified using the shear values from the 2D affine transformation matrices for each frame, which were computed during the registration process. Thus the normalized shear metric (Figures 1H and 1I and 7F and 7G) was computed by taking the square root of the sum of squared x-shear and y-shear values, sh_x and sh_y, respectively:

$$Affine\ transformation\ matrix = \begin{bmatrix} 1 & sh_y & 0 \\ sh_x & 1 & 0 \\ 0 & 0 & 1 \end{bmatrix}$$

$$Shear\ magnitude = \sqrt{sh_x^2 + sh_y^2}$$

This shear magnitude was then normalized from 0 to 1 for each of the individual traces. These normalized shear values were aligned to the start of Ib or Is ΔF/F activity and then averaged for multiple NMJs and animals.

To define distinct periods of activity, time to high-state, and mean onset delay (Figures 2A, S2B and 2H), we binned ΔF/F values into 100 equally spaced bins based on their magnitudes. The relaxed, low-state was defined when the ΔF/F signal was in the lower 25 bins. Since the high-state was more variable, it was defined when the ΔF/F signal surpassed the 50th bin. Percent active time was calculated by dividing the period when ΔF/F signals were in this high-state by the total duration of the movie. The time to high-state was defined when ΔF/F surpassed 10% of the low-state level, which represented the start time, and reached to within at least 10% of the high-state level, representing the end time. This 10% tolerance was used to minimize false positive start and end times due to the noisiness of the ΔF/F signals. Delays between Ib and Is bouts of activity were calculated using these aforementioned start times. All onset periods were then verified manually to guarantee that none were false positives.

To classify Ib NMJ activity states relative to the paired Is activity (Figure 2C) we first took the raw fluorescence traces from Ib regions, normalized to the baseline and peak normalized, and then divided by the maximum peak value to obtain activity values from 0 to 1. The activity index value was obtained by taking the integral underneath this new normalized activity trace. We divided Ib synaptic activity into distinct phases by looking at the temporal correlates of Is activity. Since Ib activity occurred before, during, and after Is activity, our activity index values were therefore divided into three distinct phases: a pre-Is phase, an on-Is phase, and a post-Is phase.

A metric reflecting the total integrated Ca2+ influx, or total synaptic transmission, at Ib and Is NMJs was achieved by summating ΔF/F values spanning the majority of the SynapGCaMP6f area corresponding to each NMJ subtype as well as the entire duration of the recording (Figures 2D–2G). For a given frame, we first subtracted Fm. We then calculated the ΔF/F at each pixel (p) of the NMJ region, where F0 was calculated for each pixel during a silent period. These ΔF/F values were then summated within the entire NMJ region (m pixels) for each frame (t), and finally summated across all movie frames (n) to give us a final total synaptic transmission value for a given movie and NMJ:

$$Total\ synaptic\ transmission \equiv \sum_j^{n\ frames} \sum_i^{m\ pixels} \frac{F(p_i\ , t_j) - F_o(p_i)}{F_o(p_i)} \Delta p \Delta t$$

There are several caveats to this analysis. The inactive in vivo baseline fluorescence (F0) at Is NMJs is usually quite low. Therefore, the Is F0 following subtraction of the Fm often became very small, likely leading to an overestimation of the ΔF/F. Care was taken to use ROIs to calculate Fm that permitted the retention of accurate information about Is activity. As the background, Fm, subtraction is necessary to isolate the Is activity, the calculation of the total synaptic transmission in Is NMJs is also likely overcorrected. However, we found that the total

integrated activity at Ib is always larger than the Is total synaptic transmission despite this, so overcorrection does not change the results (Figures 2E–2H). Additionally, we cannot account for the nonlinearities in the SynapGCaMP6f responses under persistent high levels of synaptic activity or the nonlinear summation (see below) in the membrane voltage during simultaneous Ib and Is activity in vivo, which may also affect the apparent Ca2+ activity.

Fluorescent events representing quantal, spontaneous vesicular release were detected during periods of muscle relaxation and the absence of motor neuron activity (Figures 2I–2K and Figure S2). These events were automatically detected within the affine registered data for each NMJ using the same method as described in more detail below. All automatically detected events were further filtered by their amplitude, size, and roundness and were subsequently verified manually. The frequency of spontaneous release was calculated by selecting ROIs over the majority of the Ib or Is NMJ areas, counting the number of events occurring in either area and dividing by the total relaxed, inactive time (Figure 2L). The spontaneous/evoked total synaptic transmission ratio was calculated using the suprathreshold pixels associated with each spontaneous quantal event (Figures 2M and S2I). The ΔF/F after background subtraction was summated for these pixels in the same manner as described above. This method increased the signal-to-noise by ensuring that only spontaneous, quantal events made up our total activity integral during relaxed periods rather than background or movement-associated ΔF/F artifacts. The total MN-evoked activity was calculated in a similar manner as above, using the whole Ib or Is NMJ area, except only the MN-active frames were included in the total synaptic transmission calculation, excluding those time points that were spontaneously active. These spontaneous quantal summated values were then divided by the active state to calculate the spontaneous/evoked ratio.

To analyze intersegmental wave propagation dynamics (Figures 7H and 7I) we manually analyzed 40x magnification movies (see Movie S1), where at least four segments between T2 and A3 were visible and in focus. We classified large-scale activity based on the number of segments that individual wave events propagated through. The maximum value was four segments, and the minimum value was one segment. Single segment events were defined based on asynchronous firing patterns between segments, indicating uncoordinated large-scale activity.

Optical Quantal Image Analysis

Quantal image analysis was performed using techniques similar to previous work (Peled and Isacoff, 2011, Peled et al., 2014), using custom-written MATLAB routines. All images were initially filtered (Gaussian low-pass filter), to reduce high-frequency noise. Images were then separated into Ib and Is regions based on their baseline SynapGCaMP6f fluorescence, which was 2- to 3-fold lower at Is synapses compared to their Ib counterparts on the same muscle (Figure S3A). Individual stimulus trial episodes were motion corrected by maximizing the 2D cross-correlation for the whole NMJ region of the first frame of each episode to a reference frame. This was repeated again separately for smaller portions of the NMJ to account for minor shape changes that often occurred during long recordings. Images were then bleach corrected (with SynapGCaMP6f and spinning disk confocal imaging, bleaching is very minor) using a double exponential fit to the baseline and post-activity fluorescence data for each trial separately. Individual stimulus trials were excluded if the NMJ was out of focus, moving during the acquisition period, or the stimulus failed to recruit one of the axons.

For automatic detection of MN stimulation-evoked ΔF spots, in the episodic imaging mode, we first manually identified several (> 20) ΔF spots (across > 10 release sites and several stimulation trials). These were used for generating ΔF traces. The average of these ΔF traces was used to generate a template response. A separate template response trace was used for different image intervals and recording conditions. Pixel-by-pixel ΔF values were then used to generate ΔF response images, and ΔF images were divided by basal-fluorescence (t = 0) images to obtain the normalized ΔF/F values. Participating pixels were identified if they had a high degree of correlation with the template response, as determined by the maximum cross-covariance as well as ΔF/F amplitudes that were above a threshold (typically between 0.04 - 0.05 ΔF/F) and at least 1.5 to 2 times larger than the standard deviation of the values at that pixel. Active pixels were grouped together and we applied additional size and amplitude thresholds to eliminate any false positive quantal spots (Figures S4B–S4E).

To construct release probability maps we applied an additional filter (Gaussian) to smooth the edges of the thresholded quantal spots. We then identified the centers of ΔF spots in response images by searching for well-isolated 2D local maxima, and counted how many times out of all stimulation trials each pixel was identified as a spot center. The probability maps are color coded to show the percentage of times each pixel was identified as a ΔF spot center (Figure 4B). The probability scale for these images was set so that its maximum reports the maximal release-site Pr in the image. Probability maps were filtered (Gaussian) for display purposes. Reported probability values were not affected by this filtering because they were determined using unfiltered data (see below).

To determine Pr of individual release sites, each site was manually identified as a spatially distinct local maximum in the filtered Pr map. For Ib release sites, a 4x4 square area was assigned to each site and the number of ΔF spots that were centered in that area during all stimulation trials was counted. For Is release sites a 5x5 pixel area was used because of the greater uncertainty in the spot center locations due to the larger evoked quantal spot sizes and amplitudes. To obtain Pr values for each site, the total number of ΔF spot centers was divided by the number of stimulation trials. To determine evoked transmission amplitudes within individual release sites, the maximum ΔF/F within the release site box was measured each time a response was counted within that site.

To avoid any bias due to the need for manual identification of release site locations as well as the possibility of low probability sites near high Pr sites that would not otherwise be identified, we also included an unbiased metric of the quantal density for all of the recordings. Quantal density is calculated as the area-normalized quantal content. This metric used the total number of ΔF spot centers identified for each stimulus trial and averaged over the total 200 stimulus trials and divided by the total area of the imaged Ib or Is NMJ. We normalized this to the total imaged area because, due to the shape of the muscle and the branching patterns of both NMJs, it was often impossible to image the entire NMJ (something that was not a problem in vivo). The quantal density metric is relatively stable over 200 trials, > 30 min of episodic imaging (see Figure S6B), even though some slow bleaching was noted in the average ΔF/F amplitudes during long recordings. This decay during 0.1 Hz stimulation experiments occurred slowly and similarly at both NMJs (data not shown). This metric is unbiased and more sensitive to changes in release at

the low Pr synapses as it does not require any synapse detection in the cumulative activity maps prior to calculation. However, it is not equivalent to the classic quantal content metric as we were not always able to image the entire Ib and Is NMJ areas simultaneously.

Automatic detection of spontaneous activity was accomplished with a technique similar to the method described above for the episodic acquisition mode. Motion correction for these recordings was accomplished using a customized subpixel registration algorithm (Guizar-Sicairos et al., 2008) in order to allow for ΔF/F analysis over extended periods of time without any edge pixel jitter artifacts (i.e., when single pixel translations cause artifacts on edges of the NMJ). Correlation of ΔF traces with a template trace was evaluated over the entire imaging time, to allow detection of miniature events at any time point during the 30 s window except for several initial frames and the last few frames where a complete template match could not be obtained. This was done as described above for evoked quantal analysis. All automatically detected events were verified manually, using unfiltered ΔF/F images and ΔF/F traces to confirm that the events had characteristic shapes and ΔF/F profiles.

Spontaneous event local maxima were identified similarly to the evoked responses. Spontaneous frequency maps were then generated by counting the number of times each pixel had a spontaneous event center and these maps were filtered (Gaussian) for display purposes (Figure 3L). Spontaneous event amplitudes were measured as the maximum ΔF/F amplitude at the event local maxima. Local spontaneous frequencies were calculated using the same methods as the single release site Pr values. Using the maps of cumulative spontaneous activity, 3x3 pixel areas were assigned at both NMJs at any non-overlapping spontaneously active location. Fs was then calculated as the number of events within each of these regions divided by the total time of the recording (2 min) (Figures S3F and S3G).

In most conditions in the filleted larvae, quantal responses, either spontaneous or evoked, were easily distinguished from noise (Figures 3B–3E). However, the smaller amplitude of unitary events in the GluRIIA mutant posed a potential problem. We noted that this was especially true GluRIIA Ib synapses where events profiles were much closer to the noise level of our recordings (Figure S5P), something that did not pose such a problem at GluRIIA Is synapses. However, given the increases in both Pr and quantal density observed in GluRIIA Ib NMJs, this would suggest that we are likely underestimating the degree of compensation at those Ib synapses, while the Is synapses should be unaffected by any detection issues (Figure S5P). When the extracellular Ca2+ concentration was further reduced (see Figure S3G for quantification of the effects on optical quantal amplitudes) the responses at the Ib NMJs became more difficult to detect (data not shown). This prevented the accurate quantification of presynaptic GluRIIA synaptic strength at 1.0 mM Ca2+, although the GluRIIA Is responses remained strong enough to detect accurately under these conditions (see Figures S5S–S5V).

Simultaneous spontaneous and evoked amplitude measurements (Figure S4K) were performed similarly to the spontaneous event measurements. All events were identified through the entire continuous 100 s imaging window, which included both spontaneous and evoked responses using the same template. Events were then binned into spontaneous and evoked response windows according to their peak time relative to the nerve stimulation (a 1 s window surrounding the nerve stimulation was used for all evoked trials). Events were then processed in

the same way as the spontaneous measurements above to calculate the relative evoked and spontaneous quantal event amplitudes. For these calculations only spontaneous and evoked events with exact same peak location were used for comparisons of amplitudes.
Unlike the low-frequency episodic imaging or spontaneous event imaging protocols, stimulating at frequencies above 2 Hz makes it difficult to perform unambiguous template matching to identify quantal events. This is largely due to the quantal SynapGCaMP6f decay time (spontaneous quantal event decay times were Ib: t1/2 = 149.0 ± 2.8 ms and Is: t1/2 = 152.6 ± 1.6 ms, see Figures S3E and S3F). However, due to the low-to-moderate basal Pr at either Ib or Is synapses, local quantal activity is not expected to summate significantly during repetitive stimulation. For example, during a 10 s, 5 Hz stimulus a ∼0.2 Pr synapse would only be predicted to release a vesicle 10 times, with, on average, 1 s between responses, much longer than the decay time required for full decay of the SynapGCaMP6f signal. Similarly, a higher Pr synapse of 0.5, such as what we tend to observe at Is NMJs or a transiently facilitated low Pr Ib synapse, would, on average, have 400 ms between responses, long enough to for SynapGCaMP6f to mostly decay back to baseline. This quantal separation is indeed what we observed during 5 Hz stimulation with individual quantal responses clearly identifiable during the train without substantial summation occurring (Figure S6F). Nevertheless, in order to identify when, where, and how strong these quantal responses are during repetitive stimulation, we developed an alternative detection technique that did not require template fitting. These recordings were analyzed by first performing the same subpixel registration as used above for the spontaneous event detection. We then thresholded the ΔF data to remove any low amplitude, high-frequency noise and searched for local maxima within in x-y-t space (MinimaMaxima3D, MathWorks File Exchange). These event locations were then used to identify peak timing and ΔF/F amplitudes. Stimulus timing was used to bin the recordings into individual stimuli to calculate the quantal density per stimulus. Spontaneous events occurring before or after the stimulus period were excluded.

For the local plasticity analysis (Figures 6F and 6K and S6L–S6M) all response timings were collected for overlapping 3x3 pixel regions centered at every pixel within the Ib or Is NMJ area. Only pixel regions that had at least one MN-evoked response were included in the analysis. All responsive pixels were then sorted based on the number of responses in the first half of the recording compared to the second half of the recording. The categories included active regions that increased the number of responses (facilitated), decreased the number of responses (depressed), had the exact same number of responses (unchanged), went from no responses to some responses (recruited), or went from some responses to no responses (silenced).

Optical Quantal Amplitude Comparisons

In our comparisons between spontaneous and evoked transmission separately, we noted a larger difference in the evoked response amplitudes at Is sites compared to Ib sites than we would have predicted from optical mini amplitudes alone (compare Figures 3F and 3G and Figures S4I and S4J). Several factors could contribute to this discrepancy. First, due to the high basal Pr at Is synapses, it was possible that a large percentage of Is evoked responses were multiquantal from the same synapse. Second, we could have been observing evoked quantal release from neighboring synapses that were located too close to reliably identify separate peak responses. The density of active release sites was found to be lower than the density of Brp puncta (i.e.,

approximately the number of active zones) (Figure S4G). Third, evoked and spontaneous release events at Is NMJs could be restricted at spatially separate synapses with significantly different quantal sizes (either different vesicle sizes or different postsynaptic glutamate sensitivities). Finally, neighboring synapse postsynaptic responses could be slightly overlapping enough raise the peak amplitude at neighboring sites.

In order to differentiate between these interpretations, we first measured spontaneous and evoked response amplitudes simultaneously from the same NMJs and at the same locations using the same detection settings (see above). Consistent with measurements for these two transmission modes taken separately, we observed larger evoked responses at Is synapses compared to the spontaneous events at the same sites. We found that the ratio of evoked to spontaneous release amplitudes at single Is synapses were distributed between 1 and 3 (Figure S4K) confirming our suspicion from separate recordings of either evoked or spontaneous activity.

To determine whether quantal response crosstalk was a factor, we next isolated functional release sites at both NMJs that had only a single matching and spatially isolated Brp punctum in the post hoc Brp structural data (Figures S4L and S4M). We then compared mean evoked response amplitudes and evoked Pr at these sites to the pooled data for all release sites. When we compared single-Brp site mean evoked amplitudes at Ib NMJs we did not observe any differences (Figure S4N). However, we found that single-Brp Is response amplitudes were significantly smaller than the pooled data (Figure S4N). Importantly, these isolated Is sites had average amplitudes that were the same size as spontaneous quantal responses at Is NMJs (Figure 3G). Because these sites likely only had a single active zone we concluded that spontaneous-evoked site quantal size differences and single-site multiquantal release likely did not contribute to this discrepancy in amplitude. Rather the differences were likely due to the interaction between neighboring synapses leading to the boosting of the amplitude of neighboring responses.

The evoked quantal amplitude boosting/crosstalk when neighboring synapses were both present and active, necessitated that we confirm that our Pr measurements weren't skewed by the high quantal density at Is NMJs. We found that the single-Brp release sites had similarly large distributions of Pr compared to the pooled data at both NMJs, with a nearly identical mean and median Prs (Figure S4O). This confirmed that our Pr data were representative of the population of active synapses despite the lower resolution of the activity data relative to the density of Brp-containing AZs and the high Is quantal density. Furthermore, these data would suggest that the large numbers of Brp puncta that do not have a corresponding active release site are very weakly active or completely inactive during low-frequency stimulation as has been noted previously (Peled and Isacoff, 2011).

Our high-frequency quantal data also supports this idea as along with a decreasing quantal content at Is NMJs during stimulus trains (Figure 6D) we noted decreases in the amplitude of the quantal responses (see Figures S6I and S6J). This occurs because with fewer active synapses as the Is NMJ depresses, there is a reduced probability of overlap of quantal responses during repetitive stimulation. However, we were still able to isolate neighboring active synapses, as single sites are only active for a small portion of action potentials during repetitive stimulation (Figure S6F). Taken together, we conclude that discrepancies between spontaneous and evoked response amplitudes, at least at WT Is NMJs, are largely due to either glutamate spillover or

postsynaptic Ca2+ signal contamination from neighboring and simultaneously active synapses. Smaller SSR surrounding Is axons may allow for this quantal crosstalk between synapses more readily than at Ib NMJs (Atwood et al., 1993).

Our comparisons of evoked and spontaneous event amplitudes also unveiled another complication to the analysis of evoked response amplitudes. Ib evoked quantal responses were generally slightly smaller than spontaneous event amplitudes (Figure S4K). This suggests that not only are most Ib responses single quantal events, but that there may be some reduction in amplitude due to nonlinear summation during simultaneous motor neuron activity. With such a large quantal content and large quantal sizes, the Is axon, when co-active with the Ib axon, could interact in the non-voltage clamped muscle to alter the Ca2+ driving force into the muscle (Wolf et al., 1998). Supporting this conclusion, we were able to demonstrate that the Ca2+-dependence of our SynapGCaMP6f responses are linear through a large range of extracellular Ca2+ concentrations (Figure S3G) so any differences are likely consistent with changes in Ca2+ entry.

Nonlinear summation-based decreases in Ib quantal amplitudes were confirmed with our Is-specific TeTxLC expression quantal analysis data where, in the absence of synchronous MN-evoked Is activity, we noted somewhat larger evoked quantal responses at the corresponding Ib synapses (UAS-TeTxLC control Ib $\Delta F/F$ mean = 0.43 ± 0.03 n = 6 NMJs; RN2-Gal4 control Ib $\Delta F/F$ mean = 0.39 ± 0.03 n = 6 NMJs; RN2 > TeTxLC Ib $\Delta F/F$ mean = 0.61 ± 0.03 n = 6 NMJs; $p = 0.13$ RN2 > TeTxLC versus UAS control and $p = 0.038$ RN2 > TeTxLC versus Gal4 control using ANOVA with post hoc Tukey's test). Though it is important to note that this effect has no effect on our quantal density or Pr measurements as despite the increase evoked amplitudes in the Is-TeTxLC expression case, no differences were noted in either metric (Figures 7L and S7K). However, we should note that in light of these issues, widely implemented quantal content corrections to compound EPSP measurements (Martin, 1955) that try to account for nonlinear summation should be used carefully as the effects of nonlinear summation may be non-uniform with convergent inputs in fly larvae.

Electrophysiology Analysis

All electrophysiological recordings were analyzed with custom-written MATLAB routines. Briefly, all data were filtered offline at 1 kHz. EPSP and EPSCs were calculated as the difference between the peak response to the average baseline immediately prior to MN stimulation. At least 20 evoked responses were acquired at 0.1 Hz and then averaged to calculate the mean compound response. Spontaneous mEPSP events were automatically identified using the same template correlation method described above for detection of spontaneous optical quantal events. All mEPSPs were validated manually as having characteristic rise and decay profiles. Quantal content was calculated as the mean EPSP amplitude divided by the mean mEPSP amplitude. For simultaneous mEPSP and optical recordings verified optical events and mEPSPs were paired manually and we only included events where optical and electrophysiological event pairs were unambiguously matched.

Immunofluorescence Image Analysis

Unless otherwise noted all images are maximum intensity projections that were generated using custom-written MATLAB routines. For post hoc analysis of Brp puncta, maximum intensity projections of Brp and Hrp images were first filtered (Gaussian). Then axonal regions were identified using the Hrp maximum intensity projection image corresponding to the live SynapGCaMP6f imaged region (see below). Pixels within their respective Hrp areas were then intensity thresholded to remove any pixels that were not part of a Brp punctum. Using these thresholded images, local maxima were identified and all maxima were validated manually. False puncta were removed and any puncta that were missed by the automatic detection were added manually. These locations were then used to identify the number of Brp puncta, their density (relative to the total Hrp area), and their maximum intensity. Because the post hoc Brp analysis was not all performed at the same time and under the exact same labeling and imaging conditions we found that the Ib-Is internally compared differences in the intensity of Brp labeling were more reliable (Figures S3T and S3U versus S3V).

For quantitative analysis of the total integrated pCaMKII levels, we similarly used maximum intensity projections of pCaMKII and Hrp labels that were filtered (Gaussian). Ib and Is regions were identified using both the pCaMKII and Hrp signals. We then excluded any pixels below a common intensity threshold for all preps and genotypes and NMJ types. Finally, we summated the remaining pixel intensity values for the respective Ib or Is NMJ. The pCaMKII integrated intensities were likely underestimated because maximum intensity projections were used; however, this would likely bias the Ib NMJ which always has a much larger z-axis profile compared to the Is NMJs.

In contrast to a recent report (Nesler et al., 2016), we noted robust postsynaptic pCaMKII labeling. These differences could be due to different antibodies and the presence of potentially many splice isoforms of CaMKII in flies (GuptaRoy et al., 2000), which have been shown to have large functional diversity. We did find that the pCaMKII antibody used in this study (PA5-17755, Thermo Fisher), also provided robust staining of the neuropil of the larval central nervous system, approximately overlapping with Brp (Figure S8A). This would suggest that the strong postsynaptic labeling at the NMJ is not limited to glutamatergic synapses. pCaMKII labeling was also present in non-SynapGCaMP6f expressing animals (w1118;+;+ data not shown), so labeling was not an artifact of overexpressing SynapGCaMP6f, a sensor that contains calmodulin. Furthermore, we noted similar but less specific labeling (data not shown) with another rabbit polyclonal anti-pT286 CaMKIIα antibody (sc12886, Santa Cruz Biotechnology, Dallas, TX).

Statistics

The calculation of Pr at individual sites required special consideration given the stochastic and all-or-none nature of release at each synapse. First, the number of stimulation trials at each NMJ will define the theoretical detection threshold of the very low Pr synapses. Second, in a binomial system, the relationship between the number of measurements, the Pr of a single site, and the expected coefficient of variation (CV) can be calculated with the following formula:

$$CV\ P_r = \frac{\sqrt{nP_r(1-P_r)}}{nP_r}$$

where n is the number of stimulus trials and Pr is the likelihood that an individual synapse will release a single vesicle of glutamate, assuming it does not change over the course of the experiment. With this relationship, the normalized variance will increase as Pr decreases or the number of trials decreases. Thus, care was taken to acquire enough single action potential stimuli at a low (0.1 Hz) frequency to provide an accurate Pr calculation even at very low Pr synapses. Thus, 200 trials were used for these experiments, as this would provide a theoretical detection limit of synapses with a Pr of 0.01 since multiple release events were required to define an evoked active synapse. More importantly, this would bring the predicted CV for all synapses with a Pr of ≥ 0.02 below 0.5 and all synapses with a Pr of > 0.1 around or below 0.2. In this way, we increased the confidence in our single-synapse Pr measurements for a large range of basal synaptic strengths.

Unpaired Student's t tests were used for average NMJ data Ib-Is comparisons. Paired Student's t tests were used to compare spontaneous and evoked amplitudes within the same NMJ. Mann-Whitney Rank Sum test was used to compare in vivo activity integral groups and average imaging-electrophysiology matched amplitudes. Two-sample Kolmogorov-Smirnov tests were used to compare pooled data Ib-Is frequency distributions. One-way ANOVAs with Tukey-Kramer post hoc tests were used to compare mean NMJ Ib-Is properties for different genotypes. Kruskal-Wallis with Tukey-Kramer post hoc tests were used to compare pooled data frequency distributions for different genotypes. One dimensional Pearson's correlation coefficients (r) were used to compare ΔF/F traces with motion traces or Fm or optical quantal amplitudes with mEPSP amplitudes, and two dimensional Pearson's correlation coefficients were used to compare spontaneous and evoked response maps. Reported values are mean ± SEM unless otherwise stated. The specific statistical tests as well as number of replicates including numbers of animals, activity bouts, NMJs, synapses or quantal events, are provided in the corresponding figure legends. For all figures significance corresponds to $*$ $p < 0.05$, $**$ $p < 0.01$, $***$ $p < 0.001$, $****$ $p < 0.0001$ or NS not significant for the comparisons indicated in the figure or figure legend.

Supplementary Figures

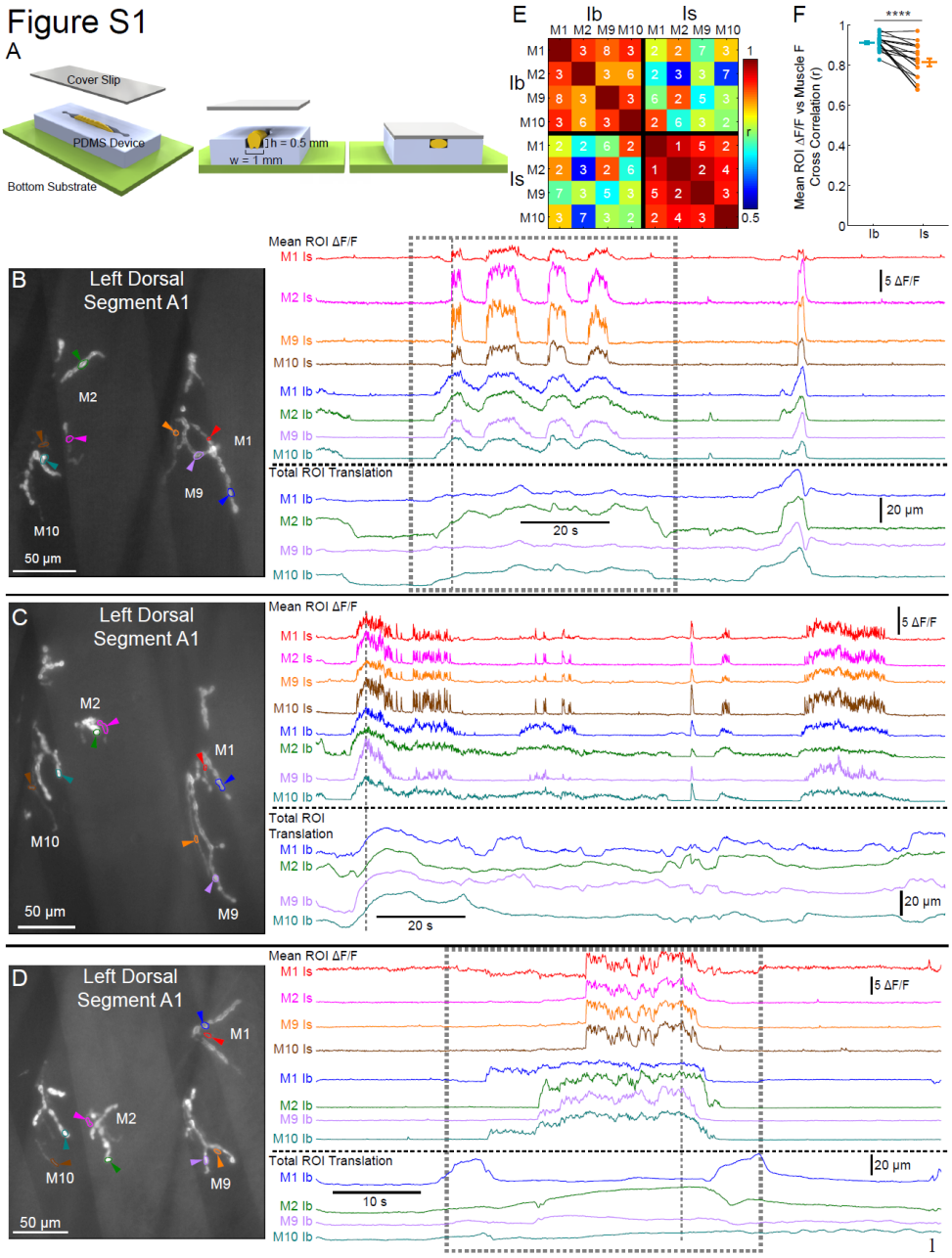

Figure S1. Additional in vivo SynapGCaMP6f analysis (Related to Figure 1) (A) 3D rendering of the in vivo PDMS imaging chamber. (B-D) (Left) Reference image and ROIs used for ΔF/F and translation calculations. (Right) In vivo ΔF/F recording data and translation data. Vertical gray dashed line indicates the frame corresponding to the reference image. Data in (B) corresponds to the example in Figure 1F-1G (gray dashed box region) as well as Figure 2I-2K, Figure S2 and Supplemental Movie 2. Data in (D) corresponds to the M10 data in Figure 2D and 2E (gray dashed box region). (E) Pearson's cross-correlation matrix between M1-Ib, M2-Ib, M9-Ib, M10-Ib, M1-Is, M2-Is, M9-Is, M10-Is. Numbers indicate the number of comparisons. (F) Cross-correlations between ΔF/F traces and the background muscle fluorescence (Fm). (n = 17 animals, 21 Ib NMJs and 21 Is NMJs)
Mean ± SEM indicated in relevant panels. Comparison made with Student's t-test (F). **** $p < 0.0001$.

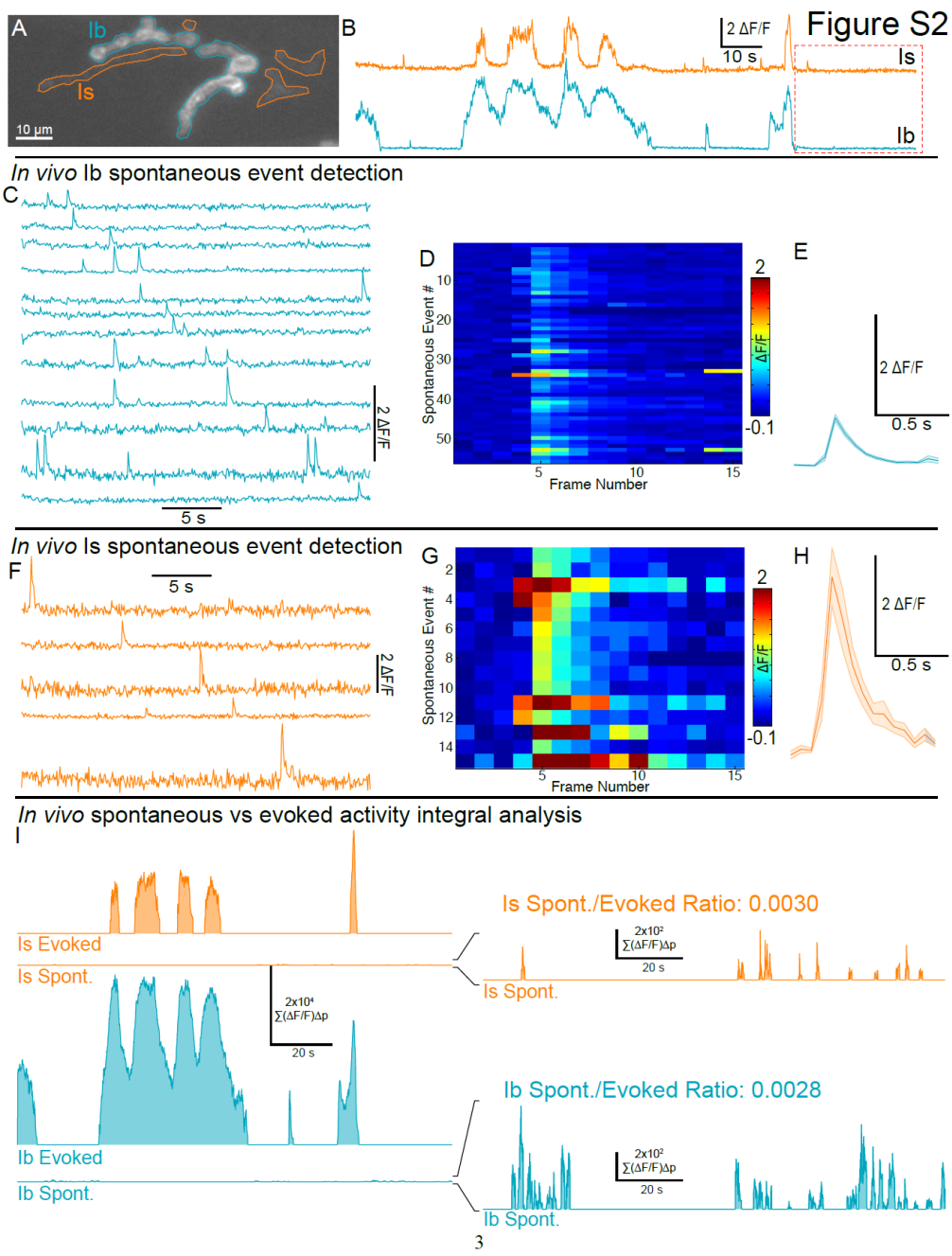
A
Ib
Is
10 µm
B
2 ΔF/F
10 s
Is
Ib
Figure S2
In vivo Ib spontaneous event detection
C
2 ΔF/F
5 s
D
Spontaneous Event #
10
20
30
40
50
5
10
15
Frame Number
2
ΔF/F
-0.1
E
2 ΔF/F
0.5 s
In vivo Is spontaneous event detection
F
5 s
2 ΔF/F
G
Spontaneous Event #
2
4
6
8
10
12
14
5
10
15
Frame Number
2
ΔF/F
-0.1
H
2 ΔF/F
0.5 s
In vivo spontaneous vs evoked activity integral analysis
I
Is Evoked
Is Spont.
2x10⁴
∑(ΔF/F)Δp
20 s
Is Spont./Evoked Ratio: 0.0030
2x10²
∑(ΔF/F)Δp
20 s
Is Spont.
Ib Evoked
Ib Spont.
Ib Spont./Evoked Ratio: 0.0028
2x10²
∑(ΔF/F)Δp
20 s
Ib Spont.

3

Figure S2. Additional illustration of in vivo spontaneous quantal release analysis (Related to Figure 2) (A) In vivo analysis regions for Ib (blue) and Is (orange) NMJs (B) Full single synapse ΔF/F traces corresponding to Figure 2I. Red box indicates the time window displayed in Figures S2C-S2H. Data matches example in Supplemental Movie 3. (C-H) Examples of in vivo spontaneous quantal release analysis for Ib (C-E) and Is NMJs (F-H). Includes single synapse ΔF/F examples showing examples of spontaneous quantal events (C and F), heatmaps showing the aligned spontaneous ΔF/F amplitude data for all identified spontaneous quantal events (D and G) for this recording period (B), and mean ΔF/F waveforms (E and H) (± SEM). (I) Example calculation of the spatial ΔF/F integral, Σ(ΔF/F)Δp at all time points for the example in Figure S2A and S2B. Traces are separated by evoked and spontaneous Σ(ΔF/F)Δp for Is (orange) and Ib (blue) NMJs. Expanded view on right shows more detailed spontaneous Σ(ΔF/F)Δp traces as well as the corresponding spontaneous/evoked total synaptic transmission (ΣΣ(ΔF/F)ΔpΔt) ratio.

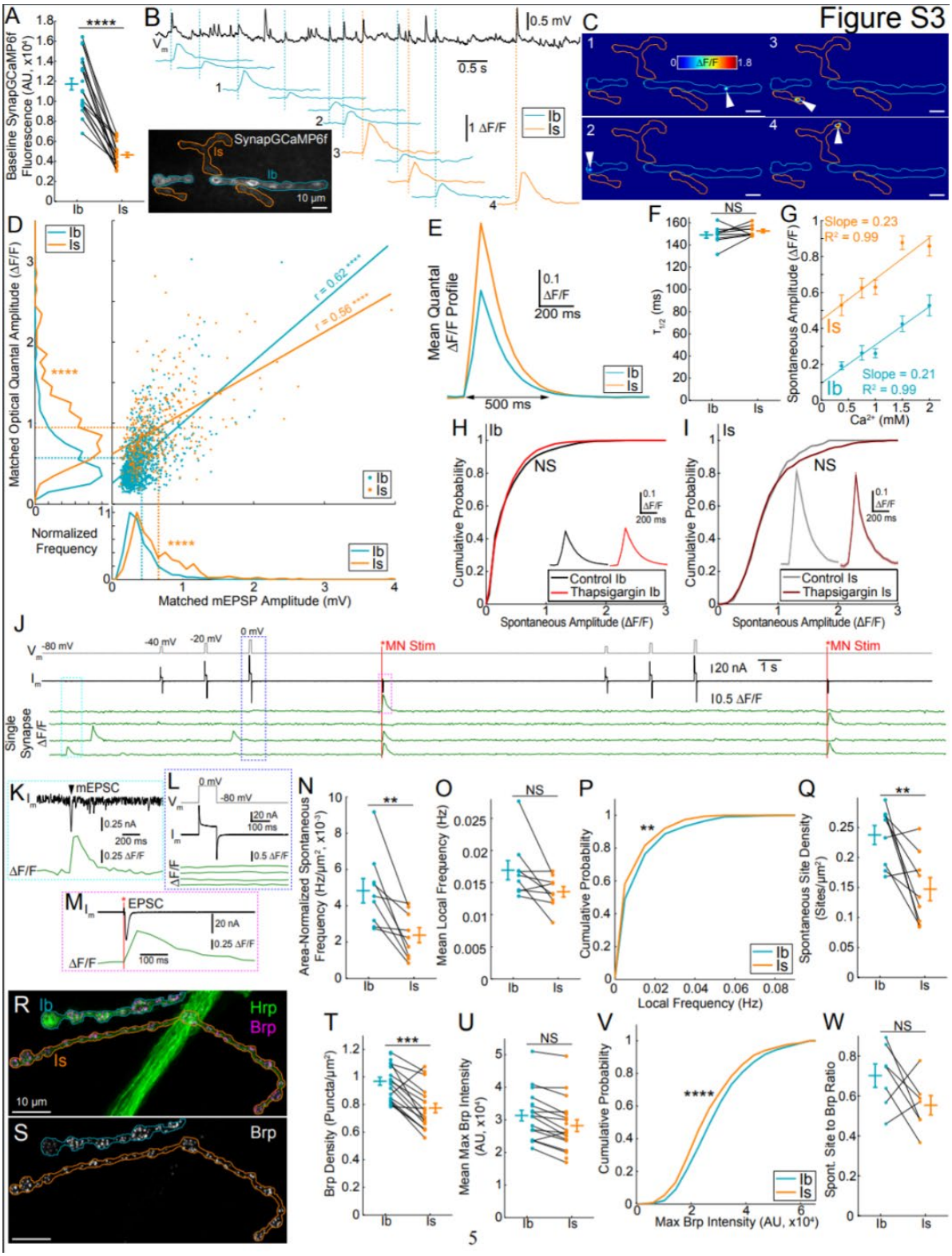
Figure S3
A
Baseline SynapGCaMP6f Fluorescence (AU, x10⁴)
****
Ib
Is
B
0.5 mV
Vm
0.5 s
1 ΔF/F
SynapGCaMP6f
10 μm
C
ΔF/F
1.8
D
Matched Optical Quantal Amplitude (ΔF/F)
r = 0.62 ****
r = 0.56 ****
Normalized Frequency
Matched mEPSP Amplitude (mV)
E
Mean Quantal ΔF/F Profile
0.1 ΔF/F
200 ms
500 ms
F
NS
τ1/2 (ms)
G
Slope = 0.23
R² = 0.99
Slope = 0.21
R² = 0.99
Spontaneous Amplitude (ΔF/F)
Ca²⁺ (mM)
H
Cumulative Probability
NS
Control Ib
Thapsigargin Ib
Spontaneous Amplitude (ΔF/F)
I
Control Is
Thapsigargin Is
J
-80 mV
-40 mV
-20 mV
0 mV
*MN Stim
20 nA
1 s
0.5 ΔF/F
Single Synapse ΔF/F
K
mEPSC
0.25 nA
200 ms
0.25 ΔF/F
L
20 nA
100 ms
M
EPSC
N
Area-Normalized Spontaneous Frequency (Hz/μm², x10⁻³)
O
Mean Local Frequency (Hz)
P
Local Frequency (Hz)
Q
Spontaneous Site Density (Sites/μm²)
R
Hrp
Brp
10 μm
S
T
Brp Density (Puncta/μm²)
U
Mean Max Brp Intensity (AU, x10⁴)
V
Max Brp Intensity (AU, x10⁴)
W
Spont. Site to Brp Ratio

Figure S3. Additional characterization of WT Ib and Is spontaneous release (Related to Figure 3) (A) Mean NMJ baseline SynapGCaMP6f fluorescence. (Ib n = 21 NMJs; Is n = 20 NMJs; 18 NMJ pairs) (B) Vm trace with matched mEPSP and ΔF/F traces for identified spontaneous quantal events at the Ib (blue) or Is (orange) NMJ. Inset shows the baseline SynapGCaMP6f fluorescence with Ib (blue) and Is (orange) NMJ borders highlighted. Note that not all mEPSPs will have a corresponding fluorescence response, as the whole Ib and Is NMJs are not in the imaging field of view. (C) Images corresponding to four of the events indicated in Figure S3B. White arrows highlight the event locations. Example is also presented in Supplemental Movie 5. (D) Matched mEPSP amplitudes (mV) versus optical amplitudes (ΔF/F) along with the normalized histograms for both mEPSP amplitudes and optical amplitudes. Dotted lines correspond to mean mEPSPs amplitudes (Ib = 0.419 mV and Is = 0.654 mV) and mean optical amplitudes (ΔF/F: Ib = 0.367 and Is = 0.6219). Plots include data from 31, 30s recordings at 11 different NMJs including n = 1084 matched Ib events (blue) n = 325 matched Is events (orange). Linear regression line for Ib is y=0.53x+0.2 and for Is is y=0.34x+0.4 with r values indicated on the plot. (E) Mean spontaneous quantal ΔF/F time course for all pooled events at Ib and Is NMJs. All identified events were aligned according to their peak time and then averaged. (Ib n = 9 NMJs, 2515 pooled events; Is n = 9 NMJs, 1035 pooled events) (F) Half decay time kinetics for spontaneous quantal responses. Spontaneous quantal ΔF/F events were first averaged for each Ib or Is NMJ. The decay phase of these average traces was then fit to a double exponential curve to calculate the mean half decay time for each NMJ. (G) Optical quantal ΔF/F responses at multiple Ca2+ concentrations in WT SynapGCaMP6f larvae. In all cases the Mg2+ concentration was 25 mM. Each data point represents the average of the NMJ mean optical quantal amplitude. The mean amplitude at each concentration was then fit with a linear regression with the indicated slopes and R2 values (Pearson's tests Ib: r = 0.982, p = 0.003 and Is: r = 0.936, p = 0.02). (0.375 mM Ca2+ Ib n=7 NMJs, 847 events; 0.375 mM Ca2+ Is n=7 NMJs, 126 events; 0.75 mM Ca2+ Ib n=6 NMJs, 1714 events; 0.75 mM Ca2+ Is n=6 NMJs, 364 events; 1.0 mM Ca2+ Ib n=9 NMJs, 3318 events; 1.0 mM Ca2+ Is n=9 NMJs, 445 events; 1.5 mM Ca2+ Ib n=7 NMJs, 2729 events; 1.5 mM Ca2+ Is n=7 NMJs, 250 events; 2.0 mM Ca2+ Ib n=4 NMJs, 1645 events; 2.0 mM Ca2+ Is n=4 NMJs, 155 events) (H-I) Thapsigargin has no effect on spontaneous optical quantal ΔF/F amplitudes. Animals were treated with 2 μM thapsigargin (or 0.2 % ethanol for the vehicle control) for 10 min with the brain intact to allow for muscle contractions in the presence of thapsigargin. Spontaneous events were recorded following removal of the brain in the continued presence of thapsigargin. (H) Cumulative probability for all Ib pooled spontaneous event maximum amplitudes (EtOH Ib: n = 6 NMJs, 1848 pooled events; thapsigargin Ib n = 12 NMJs, 3243 pooled events). (I) Cumulative probability for all Is pooled spontaneous event maximum amplitudes (EtOH Is: n = 6 NMJs, 205 pooled events; thapsigargin Is n = 12 NMJs, 509 pooled events). Insets show the mean (± SEM) spontaneous quantal ΔF/F time course for all pooled events. (J-M) Simultaneous two-electrode voltage clamp and SynapGCaMP6f imaging shows that SynapGCaMP6f does not respond to membrane depolarization alone. (J) Representative example of the voltage clamp and imaging. Top trace (gray) shows the command voltage for the voltage clamp. 100 ms steps to the indicated voltages were then repeated at 2 s intervals before the axon was stimulated to produce evoked release. Motor neuron (MN) stimulation is indicated (red). Below the voltage is the current (black, Im) during the whole recording showing the responses to the voltage steps and the EPSCs. The bottom four traces (green) are individual Ib synapse mean ΔF/F profiles that have been aligned to the voltage clamp recording. Spontaneous events are not time-locked to the motor neuron stimulation. (K) Higher resolution view of a spontaneous mEPSC example and the corresponding ΔF/F response (indicated in J, cyan box). (L) Higher resolution view of a depolarization, the corresponding current, and the fluorescence response at each synapse (indicated in J, blue box). (M) Higher resolution view of an EPSC and a corresponding quantal ΔF/F response (indicated in J, magenta box). (N) NMJ area normalized spontaneous frequencies. Areas calculated using the total imaged Ib and Is SynapGCaMP6f baseline fluorescence regions. (Ib n = 9 NMJs; Is n = 9 NMJs; 9 NMJ pairs) (O) Mean NMJ local spontaneous release frequencies. (Ib n = 9 NMJs; Is n = 9 NMJs; 9 NMJ pairs) (P) Pooled cumulative probability distributions for the local spontaneous frequencies. (Ib n = 1070 spontaneously active sites; Is = 525 sites) (Q) Spontaneously active site densities. Sites include all locations where there was at least one spontaneous event. Areas calculated as in (E). (Ib n = 9 NMJs; Is n = 9 NMJs; 9 NMJ pairs) (R-S) Example of post hoc staining for Hrp and Brp following live SynapGCaMP6f imaging, specifically the example presented in Figures 3A-3E. (R) Maximum intensity projection for Hrp (green) and Brp (magenta) with Ib (blue) and Is (orange) axon borders indicated. (S) Isolated maximum intensity projection for Brp staining with Ib (blue) and Is (orange) axon borders. (T) Mean Brp puncta density by NMJ. Areas were calculated using the corresponding Hrp motor neuron area. (Ib n= 21 NMJs; Is n = 20 NMJs; 18 NMJ pairs) (U) Mean Brp puncta maximal intensity by NMJ. (Ib n = 21 NMJs; Is n = 20 NMJs; 18 NMJ pairs) (V) Pooled cumulative probability distributions for the maximal intensity of all Brp puncta. (Ib n = 3461 puncta; Is = 1609 puncta). (W) Ratio of spontaneously active sites to Brp puncta within the corresponding NMJ and MN areas. (Ib n = 7 NMJs; Is n = 7 NMJs; 7 NMJ pairs) Mean ± SEM indicated in relevant panels. Comparisons made with Pearsons's test (D, G), Student's t-test (A, F, N, O, Q, T, U, W), Kolmogorov-Smirnov test (D, P, V), or Kruskal-Wallis with Tukey's post hoc test (H, I). ** $p < 0.01$, *** $p < 0.001$, **** $p < 0.0001$ or NS not significant.

Figure S4

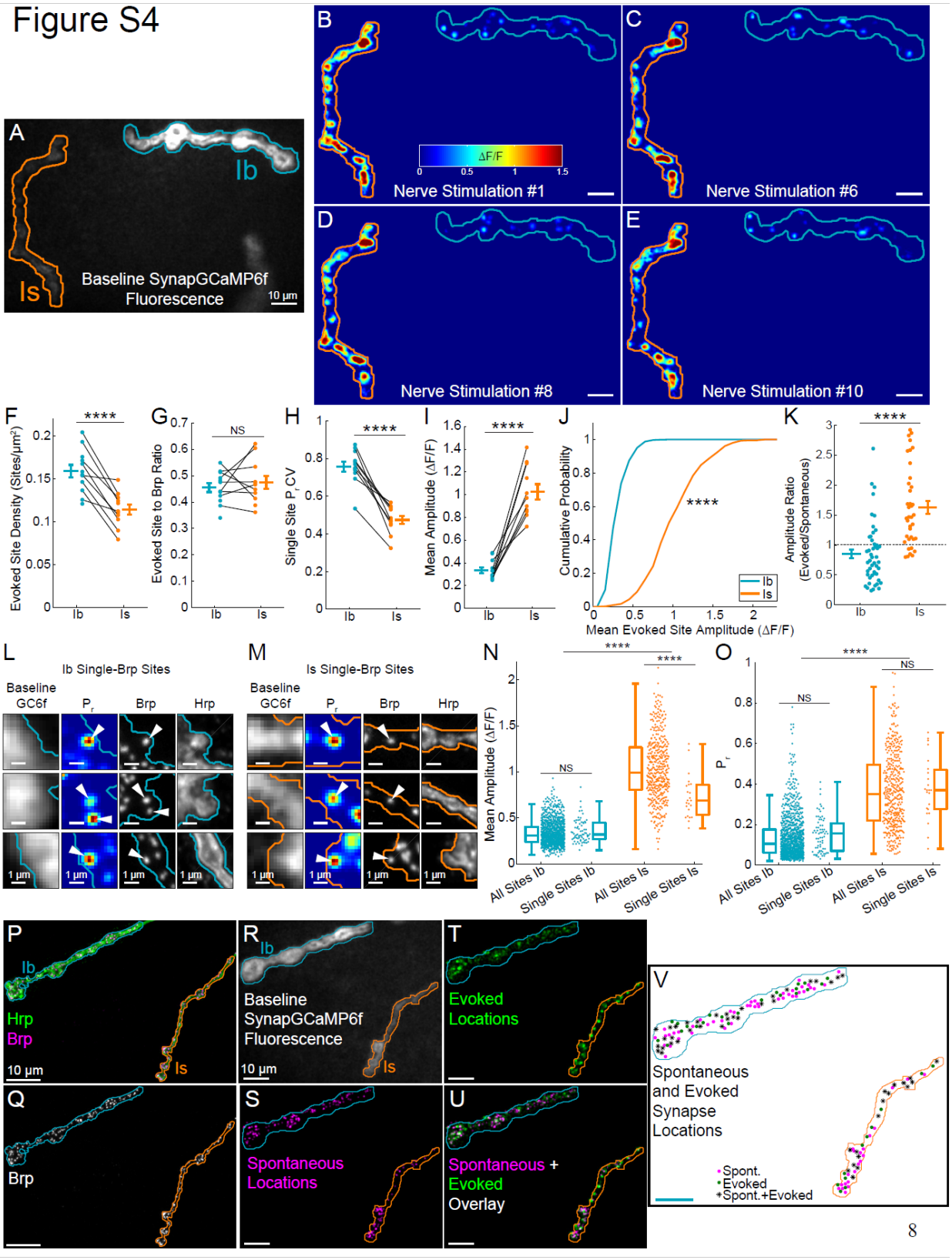
A
Ib
Is
Baseline SynapGCaMP6f Fluorescence
10 µm
B
ΔF/F
0
0.5
1
1.5
Nerve Stimulation #1
C
Nerve Stimulation #6
D
Nerve Stimulation #8
E
Nerve Stimulation #10
F
Evoked Site Density (Sites/µm²)
****
Ib
Is
G
Evoked Site to Brp Ratio
NS
H
Single Site Pr CV
I
Mean Amplitude (ΔF/F)
J
Cumulative Probability
Mean Evoked Site Amplitude (ΔF/F)
K
Amplitude Ratio (Evoked/Spontaneous)
L
Ib Single-Brp Sites
Baseline GC6f
Pr
Brp
Hrp
1 µm
M
Is Single-Brp Sites
N
Mean Amplitude (ΔF/F)
All Sites Ib
Single Sites Ib
All Sites Is
Single Sites Is
O
Pr
P
Hrp
Brp
R
Baseline SynapGCaMP6f Fluorescence
T
Evoked Locations
Q
S
Spontaneous Locations
U
Spontaneous + Evoked Overlay
V
Spontaneous and Evoked Synapse Locations
Spont.
Evoked
Spont.+Evoked

Figure S4. Additional characterization of wild-type Ib and Is low frequency evoked activity (Related to Figure 4) (A) Baseline SynapGCaMP6f fluorescence with Ib (blue) and Is (orange) NMJ borders highlighted. Example is the same as in Figure 4. (B-E) Examples of identified quantal ΔF/F locations for individual APs in Ib (blue) and Is (orange) NMJs. Examples correspond to single trials #1 (B), #6 (C), #8 (D), and #10 (E) in the recording presented in Supplemental Movie 6 as well as the activity map presented in Figure 4. (F) Mean MN-evoked active site density by NMJ. Active sites were defined as any isolatable active site used for the single-synapse Pr calculations. Areas were calculated using the area corresponding to the analyzed baseline SynapGCaMP6f fluorescence region. (Ib n = 12 NMJs; Is n = 11 NMJs; 9 NMJ pairs) (G) Ratio of evoked sites to Brp puncta within the corresponding NMJ and MN areas. (Ib n = 12 NMJs; Is n = 11 NMJs; 9 NMJ pairs) (H) Coefficient of variation for individual NMJ single-site Pr distributions. (Ib n = 12 NMJs; Is n = 11 NMJs; 9 NMJ pairs) (I) Mean evoked site response amplitudes (ΔF/F) by NMJ for low frequency stimulation (200 trials 0.1 Hz; Ib n = 12 NMJs; Is n = 11 NMJs; 9 NMJ pairs). (J) Pooled cumulative probability distributions for all mean evoked release site amplitudes (ΔF/F; 200 trials 0.1 Hz; Ib n = 995 sites; Is n = 413 sites). (K) Spontaneous versus evoked release response amplitude (ΔF/F) ratio during simultaneous recordings. Spontaneous quantal responses were recorded simultaneously during 100s seconds of continuous imaging during which 10 stimuli were also delivered at 0.1 Hz. Quantal responses were identified using the exact same detection settings and separated by their timing relative to the MN stimulation. Only synapses that had at least one spontaneous and one evoked event were included in the analysis. Ratios were calculated using the average response amplitudes for either evoked or spontaneous transmission at each of these sites (Ib n = 5 NMJs with n = 48 sites; Is n = 5 NMJs n = 38 sites). (L and M) Examples of single-Brp evoked sites at Ib NMJs (L) and Is NMJs (M). Showing the baseline SynapGCaMP6f (GC6f) fluorescence (far left), probability map (middle left), Brp (middle right), and Hrp (far right) along with the analysis borders. All evoked sites used for the analysis (N and O) had an unambiguous and wellisolated Brp punctum in the corresponding post hoc antibody labeled image indicated with an arrowhead in these examples. (N) Comparison of all pooled Ib and Is mean evoked release site amplitudes (ΔF/F) with the subset of single-Brp evoked sites and the corresponding box plots to indicate the median and distribution of the respective populations (ΔF/F; Ib n = 995 sites total with n = 71 single-Brp sites; Is n = 413 sites total with n = 23 single-Brp sites). (O) Comparison of all pooled Ib and Is evoked release site Pr values along with the subset of single-Brp evoked sites and the corresponding box plots to indicate the median and distribution of the respective populations (Ib n = 995 sites total with n = 71 single-Brp sites; Is n = 413 sites total with n = 23 single-Brp sites). (P) Maximum intensity projection for Hrp (green) and Brp (magenta) with Ib (blue) and Is (orange) axon borders. (Q) Isolated maximum intensity projection for Brp staining with Ib (blue) and Is (orange) axon borders. (R) Baseline SynapGCaMP6f fluorescence with Ib (blue) and Is (orange) NMJ borders highlighted. (S) Cumulative spontaneous quantal release location heatmap (120s continuous imaging; magenta) (T) Cumulative AP-evoked quantal release location heatmap (200 trials at 0.1 Hz; green). Recording of evoked release occurred after analysis of spontaneous release in (U). (U) Merged image showing spontaneous (magenta) and evoked (green) release locations. White regions indicate areas participating in both forms of glutamate release. 2D cross-correlations were performed on the spontaneous versus evoked images to calculate the degree of overlap (see main text). (V) Locations of all spontaneously active synapses (magenta dots, any isolated site with at least one spontaneous event), all evoked active synapses (green dots, any site that participated at least 3 times during 200 stimulus trials), and dual sites (*) where spontaneous and evoked synapses were located within less than 1 pixel (approx. 0.25 μm) of one another. Mean ± SEM indicated in relevant panels except in (N, O) where error bars indicate the ± 1.5 inner quartile range. Comparisons made with Student's t-test (F, G, H, I), Kolmogorov-Smirnov test (J, K), or Kruskal-Wallis with Tukey's post hoc test (N, O). **** $p < 0.0001$ or NS not significant.

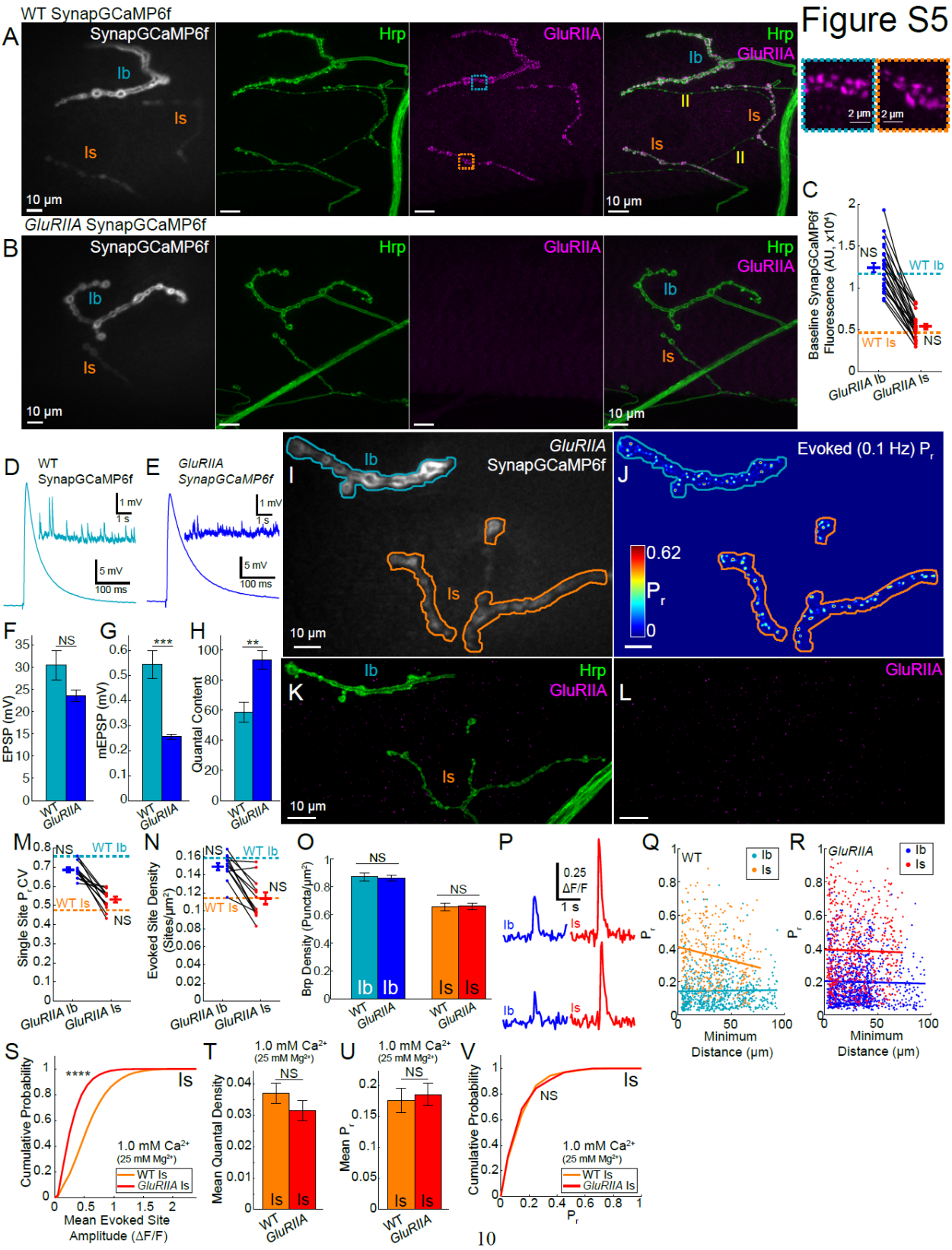
Figure S5
WT SynapGCaMP6f
A
SynapGCaMP6f
Hrp
GluRIIA
Hrp GluRIIA
Ib
Is
II
10 µm
2 µm
GluRIIA SynapGCaMP6f
B
C
Baseline SynapGCaMP6f Fluorescence (AU, x10⁴)
NS
WT Ib
WT Is
GluRIIA Ib
GluRIIA Is
D
WT SynapGCaMP6f
1 mV
1 s
5 mV
100 ms
E
GluRIIA SynapGCaMP6f
I
J
Evoked (0.1 Hz) Pr
0.62
Pr
0
K
L
F
EPSP (mV)
G
mEPSP (mV)
H
Quantal Content
WT
GluRIIA
M
Single Site P CV
N
Evoked Site Density (Sites/µm²)
O
Brp Density (Puncta/µm²)
P
0.25 ΔF/F
1 s
Q
WT
R
GluRIIA
Minimum Distance (µm)
S
Cumulative Probability
****
1.0 mM Ca2+
(25 mM Mg2+)
WT Is
GluRIIA Is
Mean Evoked Site Amplitude (ΔF/F)
T
Mean Quantal Density
U
Mean Pr
V

Figure S5. Additional characterization of GluRIIA properties (Related to Figure 5) (A-B) Baseline SynapGCaMP6f fluorescence along with maximum intensity for Hrp (green), GluRIIA (magenta), and the merged image for WT SynapGCaMP6f (A) and GluRIIA SynapGCaMP6f (B) animals. Type II axons (yellow) are also indicated but are not labeled with either SynapGCaMP6f or the GluRIIA antibody (A). Insets to right in (A) show a higher resolution view of the GluRIIA clusters at Ib (blue) and Is (orange) NMJs. (C) GluRIIA SynapGCaMP6f mean baseline SynapGCaMP6f fluorescence. (GluRIIA Ib n = 24 NMJs; GluRIIA Is n = 24 NMJs; 24 NMJ pairs) (D-H) Electrophysiological analysis shows normal homeostatic compensation of the compound quantal content in the presence of SynapGCaMP6f. (D) Representative individual EPSPs in a WT SynapGCaMP6f larva with the inset being a representative trace showing mEPSPs. (E) Representative individual EPSP in a GluRIIA SynapGCaMP6f larva with the inset being a representative trace showing mEPSPs. (F) Mean EPSP amplitude for WT SynapGCaMP6f and GluRIIA SynapGCaMP6f NMJs. (G) Mean mEPSP amplitude for multiple NMJs. (H) Mean quantal content for each NMJ. Calculated as the mean EPSP/mEPSP amplitude for each NMJ. All measurements were performed in segment A3 (WT n = 11 NMJs; GluRIIA n = 10 NMJs) (I-L) Example of optical quantal analysis on a GluRIIA SynapGCaMP6f muscle 4 NMJ including the baseline SynapGCaMP6f fluorescence (I) with Ib (blue) and Is (orange) NMJ borders highlighted, cumulative AP-evoked quantal release location heatmap (J) (200 trials at 0.1 Hz; green), as well as the corresponding maximum intensity projection for Hrp (green) and GluRIIA (magenta) (K) and the maximum intensity projection for GluRIIA alone (magenta) confirming the GluRIIA genotype (L). (M) GluRIIA SynapGCaMP6f coefficient of variation for individual NMJ Pr distributions. (Ib n = 12 NMJs; Is n = 12 NMJs; 12 NMJ pairs). (N) GluRIIA SynapGCaMP6f mean MN-evoked active site density by NMJ. Active sites were defined as described previously (see Figure S4F) (Ib n = 12 NMJs; Is n = 12 NMJs; 12 NMJ pairs). (O) Mean Brp puncta density by NMJ. Areas were calculated using the corresponding Hrp motor neuron area. (WT Ib n = 16 NMJs and WT Is n = 16 NMJs from 5 larvae; GluRIIA Ib n = 17 NMJs and GluRIIA Is n = 17 NMJs from 5 larvae). (P) Mean single synapse $\Delta F/F$ traces for examples of single spontaneous release events at GluRIIA Ib (blue) and GluRIIA Is (red) NMJs showing the relationship between the signal and the background noise. (Q-R) Comparison between the mean evoked Pr at each synapse and the minimum distance to the nearest neighboring synapse in the corresponding axon for both WT SynapGCaMP6f (Q) and GluRIIA SynapGCaMP6f (R). Linear regressions are indicated (WT Ib r = 0.017, NS; WT Is r = -0.19, ***; GluRIIA Ib r = -0.023, NS; GluRIIA Is r = -0.023, NS) (S-V) Optical quantal analysis of Is NMJ evoked transmission properties in lower Ca^{2+} saline shows no presynaptic compensation (HL3 with 1.0 mM Ca^{2+}, 25 mM Mg^{2+}). Analysis of Ib transmission is not possible as the reduced Ca^{2+} concentration and GluRIIA mutation reduces the amplitude of the optical quantal events to our detection threshold. However, low Ca^{2+} GluRIIA responses at the Is NMJs are still detectable. (S) Pooled mean optical evoked amplitudes for WT Is and GluRIIA Is sites show a significant reduction in GluRIIA animals. (T) Mean quantal density for multiple NMJs shows no difference in the normalized quantal output of the Is NMJs in these genotypes. (U) Mean NMJ Pr shows no difference at Is synapses. In both cases Pr has been reduced to a level comparable to WT Ib Pr in 1.5 mM Ca^{2+} (see Figure 4L) (V) Cumulative probability for single synapse Pr at all pooled WT and GluRIIA Is synapses in low Ca^{2+} also shows no difference in synaptic strength. (1.0 mM Ca^{2+} WT n = 5 NMJs and 339 pooled sites; 1.0 mM Ca^{2+} GluRIIA n = 5 NMJs and 328 pooled sites) Mean ± SEM indicated in relevant panels. Additionally, in relevant plots (C, M, N), data for WT Ib (blue dashed line) or WT Is (orange dashed line) are presented for comparisons and correspond to the same mean data presented in Figure S3A, 4 and S4). Comparisons made with Pearsons's test (Q, R), Student's t-test (F, G, H, T, U), Kolmogorov-Smirnov test (S, V), one-way ANOVA with Tukey's post hoc test (C, M, N, O) or Pearson's test (LM). * $p < 0.05$, ** $p < 0.01$, *** $p < 0.001$, **** $p < 0.001$ or NS not significant.

Figure S6

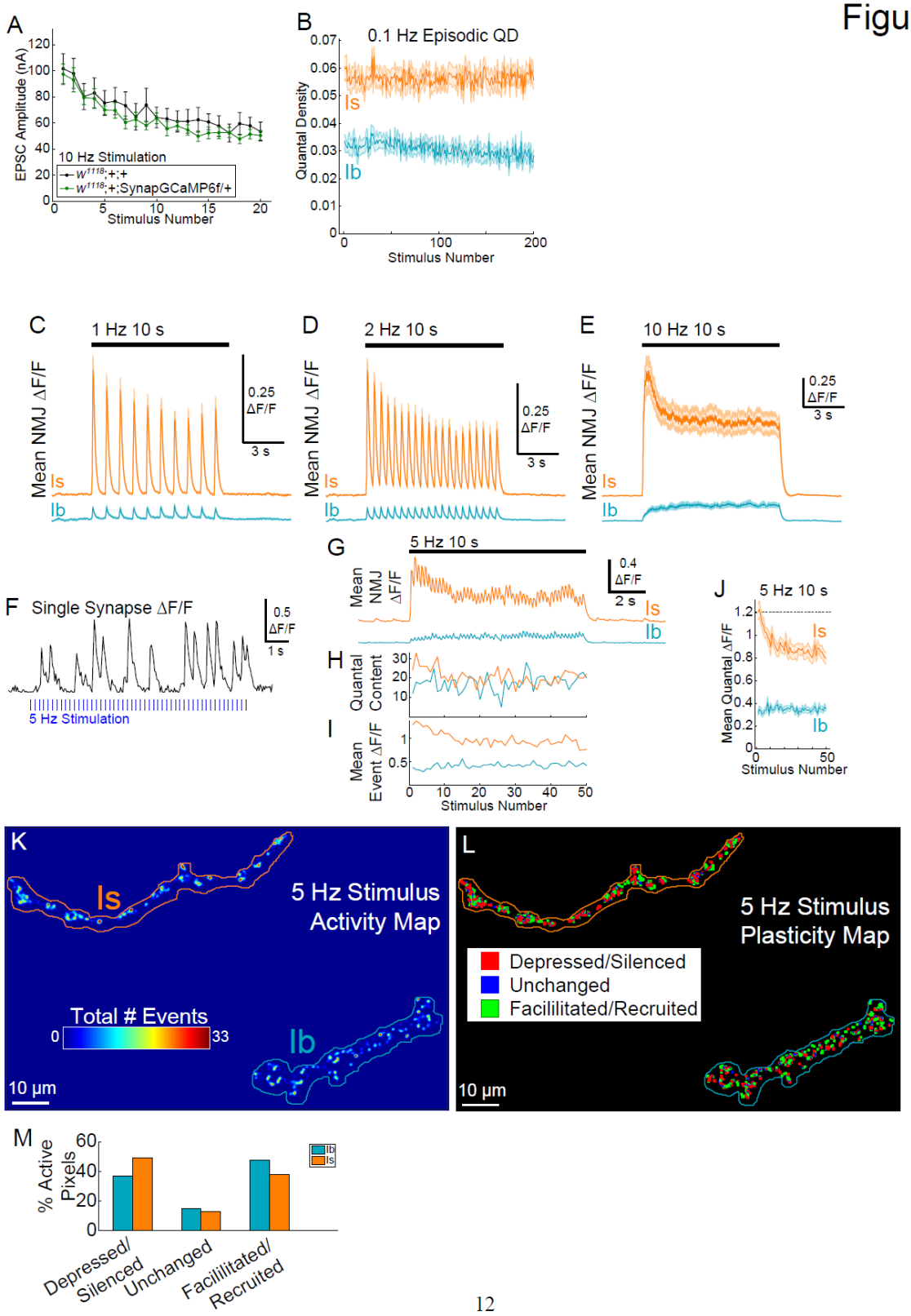
A
EPSC Amplitude (nA)
Stimulus Number
10 Hz Stimulation
w1118;+;+
w1118;+;SynapGCaMP6f/+
B
0.1 Hz Episodic QD
Quantal Density
Is
Ib
Stimulus Number
C
1 Hz 10 s
Mean NMJ ΔF/F
0.25 ΔF/F
3 s
D
2 Hz 10 s
E
10 Hz 10 s
F
Single Synapse ΔF/F
0.5 ΔF/F
1 s
5 Hz Stimulation
G
5 Hz 10 s
0.4 ΔF/F
2 s
H
Quantal Content
I
Mean Event ΔF/F
J
Mean Quantal ΔF/F
K
5 Hz Stimulus Activity Map
Total # Events
0
33
10 µm
L
5 Hz Stimulus Plasticity Map
Depressed/Silenced
Unchanged
Facililitated/Recruited
M
% Active Pixels
Depressed/ Silenced
Unchanged
Facililitated/ Recruited

Figure S6. Additional optical quantal analysis during different stimulation frequencies (Related to Figure 6) (A) Short-term depression in compound EPSC amplitudes during a 10 Hz stimulation shows no difference with or without the expression of SynapGCaMP6f. (w1118;+;+ n = 4 NMJs; w1118:+/+;SynapGCaMP6f/+ n = 5 NMJs) (B) Quantal density versus stimulation trial during 0.1 Hz episodic stimulation shows stable responses for > 30 min (0.1 Hz Ib n = 12 NMJs; 0.1 Hz Is n = 11 NMJ) (C-E) Mean NMJ ΔF/F traces for 10 s stimuli at (C) 1 Hz, (D) 2 Hz, and (E) 10 Hz. (1 Hz 10s Ib n = 11 NMJs; 1 Hz 10s Is n = 11 NMJs; 2 Hz 10s Ib n = 13 NMJs; 2 Hz 10s Is n = 13 NMJs; 10 Hz 10s Ib n = 7 NMJs; 10 Hz 10s Is n = 7 NMJs) (F) An example of a single Ib synapse ΔF/F trace during a 5 Hz nerve stimulation. Quantal responses are relatively uniform in both size and kinetics, with individual peaks being identifiable during the stimulus period as they are able to decay before another vesicle is released. Blue hash marks indicate when action potentials were initiated. (G-I) An example of high frequency optical quantal analysis corresponding to Supplemental Movie 7. (G) Mean ΔF/F for the whole imaged Ib and Is region during a 10s, 5 Hz stimulus. (H) Total quantal content per stimulus during the stimulus train. (I) The mean event amplitude per stimulus during the stimulus train. (J) Mean quantal response amplitudes during 5 Hz stimulus. Data corresponds to the quantal response in Figure 6C and 6D. The declining amplitudes in the Is NMJs during this stimulus period are due to the decrease in quantal density reducing the overlap of quantal spots (See Methods for a more detailed explanation). No change in the amplitudes were noted at Ib NMJs. (Ib n = 13 and Is n = 13 NMJs). (K) A quantal activity heatmap during a 5 Hz stimulus scaled to the total number of events at each synapse during the 50 stimulus trials. Ib (blue) and Is (orange) NMJ borders highlighted. Data corresponds to Supplemental Movie 7 and (G-I), (L-M) Single pixel quantal plasticity analysis during the same 5 Hz 10s stimulus example in (G-I and K), including the locations of pixels that were either depressed/silenced (red), unchanged (blue), or facilitated/recruited (green) and (M) the corresponding percent of active pixel breakdown of these categories for both the Ib and Is NMJ. Data are mean ± SEM (A) and all lines for multiple NMJs (B-E and J) are mean ± SEM.

Chapter III: Circuit homeostasis in response to synaptic perturbation ensures robust behavior

Abstract

At the *Drosophila* larval neuromuscular junction, reduction in postsynaptic sensitivity triggers presynaptic homeostatic plasticity (PHP), which compensates by increasing transmitter release and preserves locomotion. Remarkably, locomotion is also preserved with knockdown of presynaptic proteins that reduces transmitter release by up to 90%, even without postsynaptic compensation. We find that reduction of either postsynaptic sensitivity or presynaptic release elicits another form of compensation: *increased* activity in motor neurons (MNs) that innervate dorso-longitudinal (DL) muscles. This compensation occurs in type Ib MNs but not in the Is MN that innervates the same muscles. Increased MN activity is accompanied by *decreased* activity in a group of inhibitory premotor neurons that synapse onto Ib MNs but not the Is MN and prolongs Ib MN bursts. Acute disruption of MN transmitter release shows that increased MN activity occurs after 1-1.5 hrs, i.e. delayed compared to the minute time-scale of PHP. Thus, weakening of locomotory output reduces central inhibition of MNs and raises their activity to preserve behavior.

Introduction

A fundamental property of the nervous system is its ability to support behavior across a large set of changing conditions. This robustness emerges partly from mechanisms that stabilize circuit function as connections are formed and eliminated, that change synaptic strength due to activity-dependent plasticity, and that are caused by other physiological or pathological perturbations (Marder 2006). These compensatory responses ensure a reliable circuit output, as discovered originally in the lobster somatogastric ganglion (Marder 2007). Homeostatic mechanisms rebalance the system by adjusting synaptic strength via a scaling process that preserves both the relative strength of synapses and the ratio between excitatory and inhibitory drive, or by adjusting excitability (Turrigiano 2012). One homeostatic mechanism is presynaptic homeostatic plasticity (PHP), which has been studied at the glutamatergic neuromuscular junction (NMJ) of larval Drosophila (Peterson 1997; Davis 2015). In PHP, postsynaptic reduction in sensitivity to transmitter (amplitude of the quantal response), due either to loss of a subunit of the postsynaptic muscle ionotropic glutamate receptor ($GluRIIA^{-/-}$) or block of the glutamate receptor pore, triggers a compensatory increase in transmitter release (Frank 2006). Of the two classes of motor neuron (MN) input to muscle, the synapses of the type Ib MN undergo PHP, boosting the probability of action potential evoked transmission (P_r), but those of the type Is MN do not adjust (Newman, 2017; Aponte-Santiago 2020). The lack of compensation at Is synapses, suggests that there could be a defect circuit output, and therefore in locomotion. However, we find that locomotion in $GluRIIA^{-/-}$ larvae is normal.

To understand how locomotion could be normal without restoration of Is synaptic transmission, we examined locomotion in larvae using another class of synaptic perturbation: a severe presynaptic perturbation due to knockdown of one of three key components of the MN presynaptic release machinery. We used RNAi to knock down the MN voltage-gated Ca^{2+} channel, *cac*, the vesicle priming protein Unc-13, and Rim binding protein (RBP). These knockdowns reduced P_r by up to 90% and did not elicit postsynaptic compensation, leading us to expect a major disruption in locomotion. However, locomotion was near normal. This suggested that another form of homeostatic adjustment may compensate for reduced per action potential transmission. Indeed, activity imaging in the intact restrained larva of either postsynaptic bouts of Ca^{2+} influx through glutamate receptors or in MNs showed that animals with synapses that were weakened at either the presynaptic or postsynaptic side *increased* MN activity. In dorso-lateral muscles 1, 2, 9 and 10, this *increased* activity occurred only in type Ib MNs (MNs 1, 2, 9 and 10), but not in the common Is MN (MSNISN) that innervates each of these muscles. We wondered if this adjustment also involves changes to the activity of central neurons that lie upstream in the motor circuit. Ca^{2+} imaging in pre-motor neurons (PMNs) that innervate the MNs showed that these perturbations of synaptic transmission at the MN-muscle synapse also *decrease* activity in the period-positive median segmental interneurons (PMSIs), a class of inhibitory PMN. The PMSIs synapse onto MN-Ibs 1, 2, 9 and 10 but not the Is MSNISN, suggesting why firing compensation occurs selectively in the Ib MNs.

Earlier work (Kohsaka 2014) showed that optogenetic inhibition of PMSIs prolongs the bursts of MNs, as observed here, and also increases the intersegmental delay in propagation of the locomotor activity wave. Consistent with this, we also observed slowed propagation of activity waves in animals with compromised MN-muscle transmission whose PMSI activity is reduced. We wondered how rapidly circuit homeostasis would occur following downstream synaptic perturbation. Acute disruption of MN transmitter release with the temperature-sensitive dynamin Shibire showed that increased MN activity occurs within 1-1.5 hrs, considerably longer than the minute timescale demonstrated earlier for PHP (Frank 2006). We conclude that when synaptic transmission at the NMJ is weakened, PHP compensates rapidly by boosting the number of vesicles released by Ib MNs in response to each action potential, and that additional compensation occurs after a delay via a second mechanism in which central inhibitory drive to MNs is reduced, thereby increasing the number of action potentials fired by the MNs. Together, PHP and circuit homeostasis ensure adequate locomotor circuit drive and preserve behavior.

Results

Screen to Identify Deficiencies in Neurotransmission at Ib and Is Synapses

Synaptic homeostasis at the fly NMJ seeks to maintain drive to the muscles in response to the animals ever changing physiological needs. In the GluRIIA model of homeostasis, a genetically or pharmacologically induced perturbation reduces the sensitivity of postsynaptic glutamate receptors (Davis and Müller, 2015). The deletion of the GluRIIA subunit reduces mEPSP amplitudes (quantal size), but EPSP amplitudes remain unchanged. This suggests the presence of a homeostatic adjustment where an increased number of presynaptic vesicles (quantal content) compensates for the decreased postsynaptic sensitivity to glutamate (Peterson 1997).

Our previous study found that GluRIIA homeostasis happens exclusively at the Ib terminals yet fails to compensate at the Is axons (Newman 2017) (Figure 1G). In order reach this conclusion, we performed Optical Quantal Analysis, where both the brain and ventral nerve cord (VNC) are removed and nerve bundles containing both the Ib and Is are artificially stimulated.
Using our genetically-encoded Ca^{2+} reporter, SynapGCaMP6f, which is localized to the glutamate receptors in the postsynaptic density, we are able to image Ca^{2+} influx through the channels to detect quantal vesicular release events during both evoked and spontaneous transmission. By aligning the SynapGCaMP6f activity maps with presynaptic Brp puncta from post hoc immunostaining, P_r at induvial active zones can be counted by measuring the number of release events and dividing it by the number of motor nerve stimuli (Figure 1B).

Yet despite the restoration of the EPSP at Ib terminals in the dissected preparation, we wondered if there remained a deficit in transmission due to the failure of the Is to compensate, which still needed to be accounted for in the behaving animal. Moreover, are there additional mechanisms of compensation for deficiencies in transmission when synaptic homeostasis fails to restore EPSP amplitude at *both* the Ib and Is terminals? To explore these questions, we screened candidate presynaptic perturbations to find cases where PHP failed to restore normal Ib and Is EPSP amplitudes.

We utilized the MN-specific Gal4 driver, OK6 (Aberle 2002), to conditionally drive RNAi expression in the Ib and Is neurons to knockdown a candidate list of proteins integral to the presynaptic release machinery. Three candidates that fit our criteria were the voltage-gated Ca^{2+} channel, *cacophony* (*cac*), RIM-binding protein (*RBP*), and *Unc-13*. At the Ib terminals, the candidates had at least a 2-fold decrease in P_r and a ~9-fold decrease in quantal density (Figure 1C and 1E). The Is terminals displayed an even more drastic decrease in release, where *cac*, *RBP,* and *Unc-13* knock-downs led to reductions in P_r from ~9 to 10-fold while reducing quantal density from ~12 to 15-fold (Figure 1D and 1F).

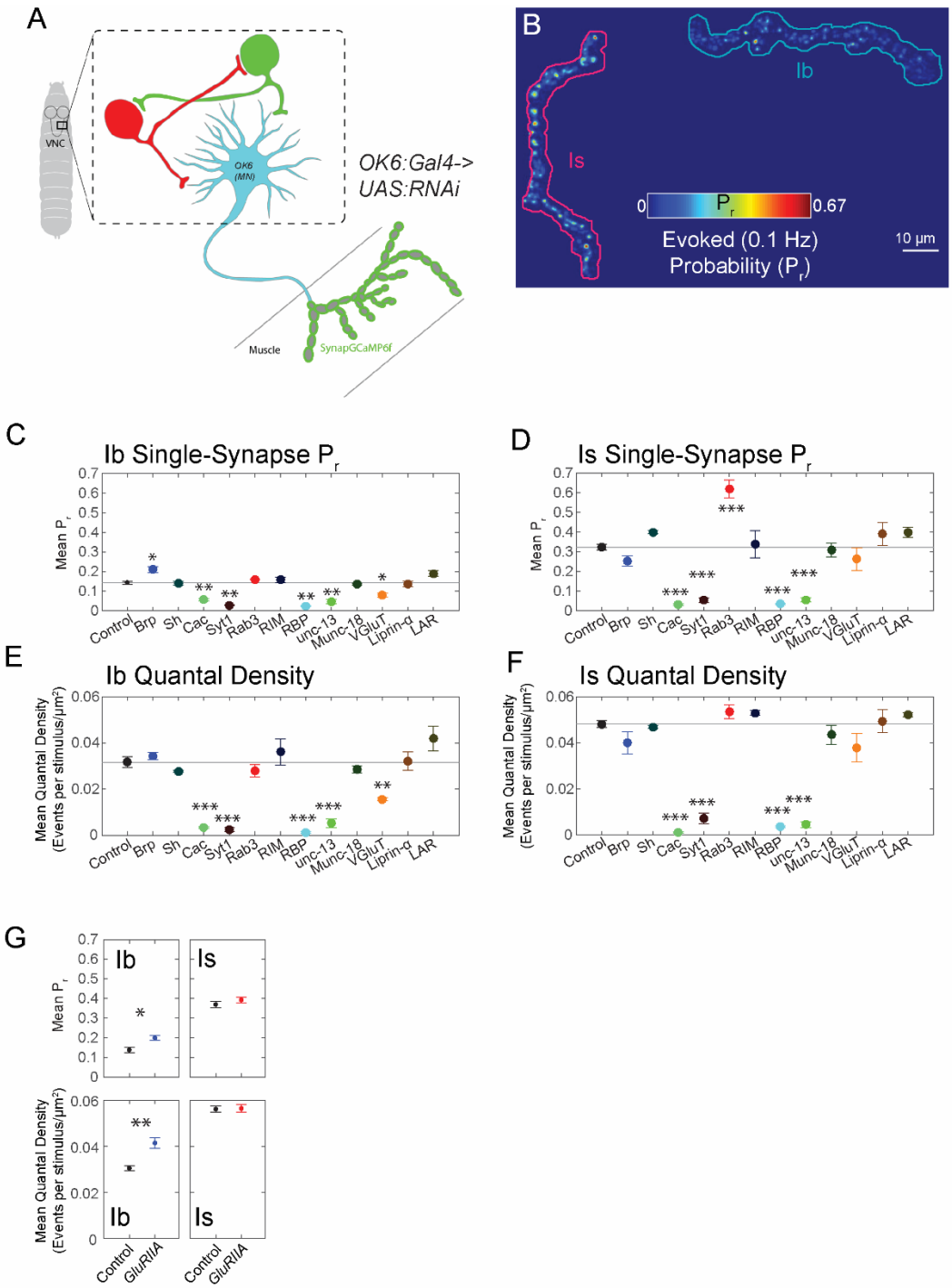

Figure 1: RNAi Screen in MNs Identifies Candidates for Vesicular Release Deficiencies in both Ib and Is (A) Overview of RNAi screen. OK6 Gal4 conditionally drives RNAi in MNs. (B) Representative evoked Pr heatmap (C and D) Mean 0.1Hz evoked single-synapse Pr for Ib and Is synapses for RNAi screen (E and F) Mean quantal density (quantal content normalized to imaged NMJ area) for RNAi candidates (G) Pr and quantal densities for Ib and Is axons for GluRIIA null mutant

Our screen identified knockdowns of proteins, *cac*, *RBP,* and *Unc-13,* where PHP failed to restore normal levels of transmission at both the Ib and Is terminals. Combined with the GluRIIA mutant, we now had models where PHP failed at both the Ib and Is terminals and the Is terminal alone.

Behavior of RNAi and Mutant Animals

Given the knockdown and mutant larvae's apparent ability to survive to third-instar in the medium on which they were raised, we next sought to quantify exactly how much the crawling behavior was compromised by their deficiencies in neurotransmission. To achieve this, we monitored crawling activity of third-instar larvae on an agarose medium in a behavioral arena using an analysis method inspired by previous reports. The larvae behavior fell into two distinct modes of active crawling and reorientation: the active crawling phase is characterized by peristaltic crawling following a relatively straight and persistent trajectory (Figure 2E). These periods are punctuated by reorientation phases, where the larvae ceases crawling, sweep their head from side to side, and chooses a new direction for forward movement (Günther et al., 2016; Lahiri et al., 2011; Loveless et al., 2019).

To our surprise – despite the severe decrease in vesicular release – the knockdown and *GluRIIA* larvae were capable of crawling remarkably similar to the controls. Measurements related to displacement, specifically the overall velocity and stride length, were not significantly compromised (Figure 2A-B and S2). It could be the case that the knockdown and mutant larvae maintain the same overall velocity by spending less time in the reorientation phase and more time traveling along persistent trajectories. However, when analyzing the two different crawling phases separately, the reorientation durations and the velocity during the persistent trajectories showed no significant decreases relative to controls (Figure 2C and S2C). In fact, the *RBP* RNAi spent even less time traveling on the continuous trajectories (Figure 2D).

Only when quantifying metrics related to the larvae's agility did were any defects in behavior statistically significant. The distributions of turning angles, or angle between continuous trajectories (Figure S2E), were zero-shifted in the cases of *Unc-13* and *cac* RNAi and *GluRIIA* null animals (Figure S2A). By fitting a spline down the midline of the larva we were able to calculate the body curvature of the larvae throughout the recordings (Figure S2D). The curvature distributions also proved to be significantly less in the cases of *cac*, *Unc-13*, *RBP¸and GluRIIA* animals (Figure S2B).

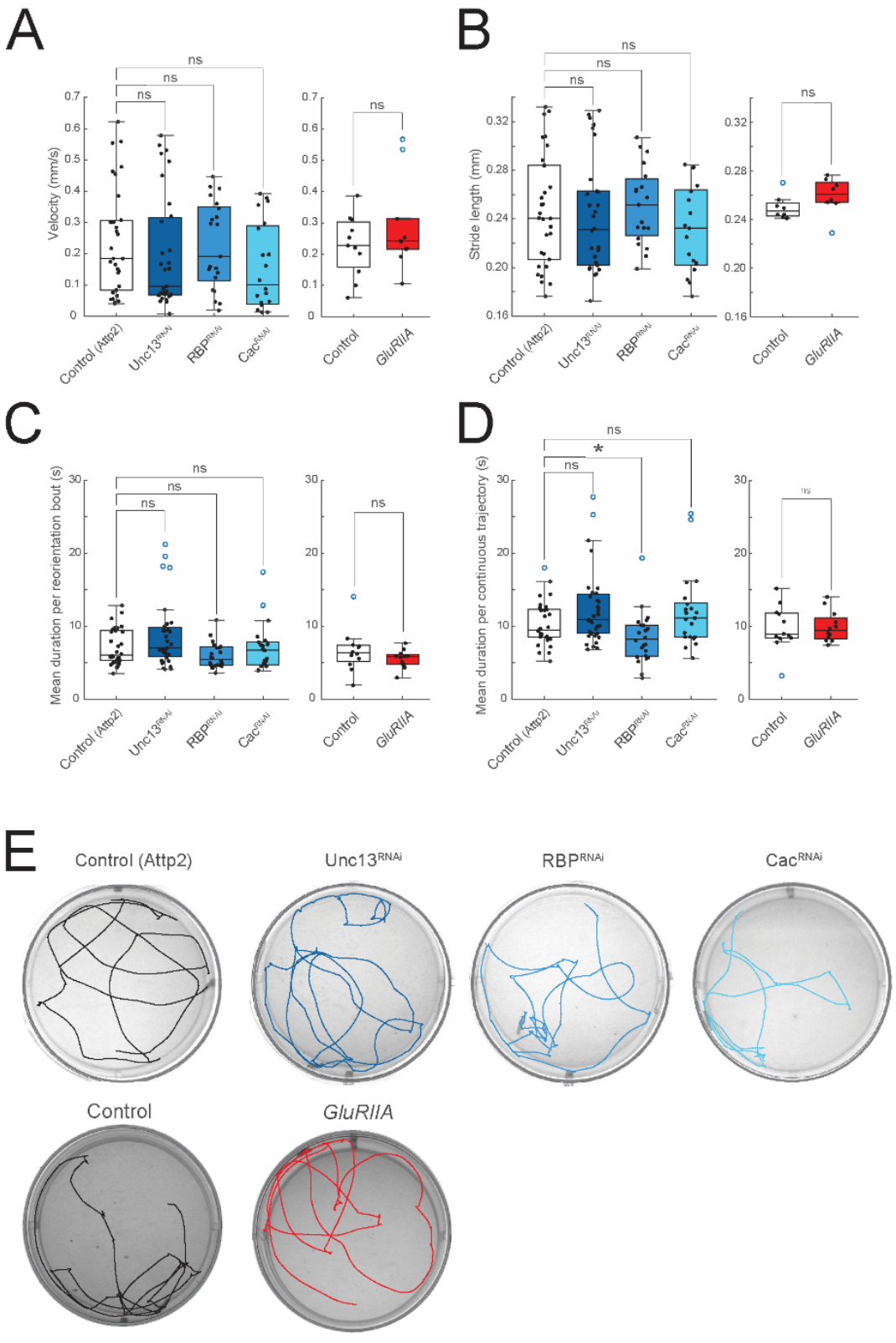
A
B
C
D
E
Velocity (mm/s)
Stride length (mm)
Mean duration per reorientation bout (s)
Mean duration per continuous trajectory (s)
ns
*
Control (Attp2)
Unc13RNAi
RBPRNAi
CacRNAi
Control
GluRIIA

Figure 2: Normal Crawling Displacement is Preserved Despite Impaired Release (A) Overall mean velocity for entirety of recording (B) Mean stride length (C) Mean duration spent during the reorienting phase (D) Mean duration spent during the active crawling phase (E) Representative crawling tracks in 50mm wells
Comparisons made with Mann-Whitney test (A-E) $*p < 0.05$; $**p < 0.01$; $***p < 0.001$;

Despite the RNAi's having such a severe deficiency in vesicular transmission at both Ib and Is NMJs and the GluRIIA null mutant having uncompensated release at the Is terminals, the larvae exhibited remarkably normal crawling behavior, particularly during the active crawling phases. Since no forms of synaptic compensation manifested themselves in the dissected preparation to account for these strikingly normal behavioral results, we were then motivated to examine the NMJ in the intact, behaving animal.

Peristaltic Waves During Restrained Crawling

The *Drosophila* larva consists of 3 thoracic (T1-T3) and nine abdominal segments (A1-A9), where most are composed of 30 bilateral body wall muscles. 26 pair of type Ib MNs innervate one muscle, whereas two pair of Is muscles innervate large groups of dorsal or ventral muscles (Hoang and Chiba, 2001). Posterior-to-anterior (P-to-A) propagation of peristaltic muscle contraction simultaneously contracts both left and right side of each segment to propel the larva in the forward direction (Gjorgjjeva 2013). In order to measure motor neuron input to the muscles while simultaneously observing forward-crawling peristaltic behavior, we turned to our restrained crawling setup. As described in our recent work, we designed linear PDMS chambers that enabled restrained crawling while simultaneously being able to record multiple muscle segments in the larvae (Newman 2017). Our SynapGCamP6f sensor gave reliable postsynaptic proxy for presynaptic signal, where clear off-and-on periods of MN-evoked activity were apparent (Figure 3G-H).

In order to simultaneously record SynapGCaMP6f activity and peristaltic wave behavior, we chose a magnification level where we could identify 3 abdominal segments (A4-A2) while still being able to clear SyanpGCaMP6f signal at the NMJ. From larger field-of-view recordings, we verified that when 3 segments resulted in a peristaltic wave, about 95% of the time this resulted in a peristaltic wave that traveled along the length of the larva, from posterior-to-anterior end. As in previous reports, all the dorsal muscle cells contracted during forward-crawling peristalsis (Zarin 2019). Despite the general coordination of all muscle cells contraction together, it has been previously reported that the muscle cells could be clustered into four co-activated muscle groups. For this reason, we chose to focus on Ib MNs innervating muscles 2 and 10, which both belong to the same initial group during peristaltic contraction in the forward crawling direction (Zarin 2019).

While the larvae were semi-restrained, the coordinated propagation of P-to-A waves nevertheless generated a degree of segmental displacement. In fact, most genotypes, aside from the *cac* RNAi, generated segmental displacement similar to controls (Figure 3D). Yet what was most strikingly

apparent from the SynapGCaMP6f traces during peristalsis was the roughly ~2 fold increase in the duration of evoked activity in both the RNAi and *GluRIIA* cases (Figure 3A). Furthermore, the contraction bouts took longer in achieving their maximum ΔF/F, which was significantly lower in the case of *Unc-13* and *cac* RNAis (Figures 3E-F and S3A-C). As a result of the longer contraction durations yet normal delays between the onsets of bouts, the RNAi and mutant larvae exhibited increased durations of simultaneously contracting adjacent segments (Figures 3B and 3C).

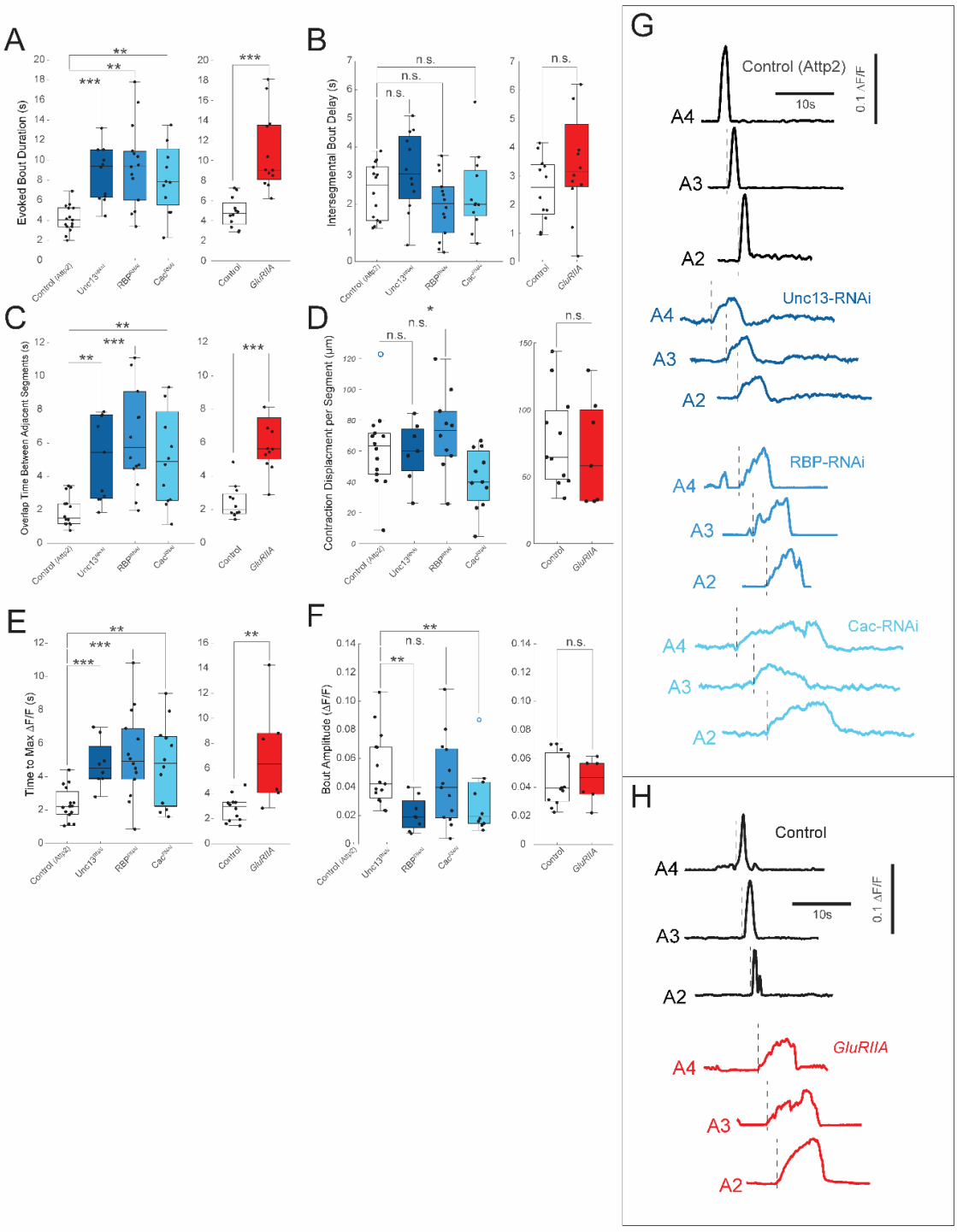

Figure 3: Increased MN burst activity during restrained crawling (A) Evoked MN burst duration (B) Intersegmental bout delay (C) Overlap time between adjacent segments (D) Contraction displacement per segment (E) Time to reach max ΔF/F signal (F) Mean ΔF/F bout amplitudes (G) Representative ΔF/F traces for RNAis and their control (H) ΔF/F traces for GlurIIA and its control
Comparisons made with Mann-Whitney test (A-F) $*p < 0.05$; $**p < 0.01$; $***p < 0.001$;

These results led us to hypothesize that the increased duration of evoked Ib activity during forward-crawling peristalsis could be the missing compensatory mechanism that was of course absent in the dissected preparation.

Increased Evoked MN Activity is Specific to the Ib Input

We next wondered whether this increase in MN-firing duration occurred exclusively in the Ib axons and not the Is, as was the case with PHP in our earlier study (2017 Newman). To resolve the Is NMJs, which are smaller and lower in signal than the Ibs, it was necessary to increase our imaging magnification and restrict our field of view to the A1 segment – a region that suffered from the least background fluorescence contamination from the larva's digestive system. This increase in light intensity due to the higher magnification, combined with its positioning nearer to the anterior end of the larva induced longer, synchronous contractions amongst neighboring segments closest to the head (A1-T1). We conjecture that this pattern of muscle contraction underlies the onset of a head sweep during the light avoidance or negative phototaxis behavior if the larva were able to move freely (Sawin-McCormack 1995; Humberg 2017). Imaging under these conditions not only allowed us to examine whether the Is MNs also increased in firing duration, yet further enabled us to study whether the increase Ib firing duration extended more generally to muscle contractions component to behaviors beyond forward-crawling movement (Figures 4G-H).

Indeed, the occurrence of increased Ib firing duration extended to this magnification as well, as we observed a roughly 2-fold increase in bout duration for *Unc-13*, *cac*, and *RBP* RNAis, as well as a roughly 2-fold for the *GluRIIA* mutant (Figures 4A-B). In some RNAi cases, we observed sustained evoked Ib activity for the entirety of the recording period, thereby likely underestimating our fold-increase in firing duration. As expected, the mean ΔF/F amplitudes of the Ib NMJ were decreased in the RNAis and unexpectedly in the GluRIIA case, since PHP should compensate for reduced EPSP amplitude, whereas the Is showed no significant decreased in Δ F/F amplitudes (Figures 4C and 4F). The degree of local muscle contraction was also maintained in all the cases (Figure S4C). However, we did not observe a significant change in Is MN firing duration for either the RNAis or *GluRIIA* mutant (Figures 4D-E).

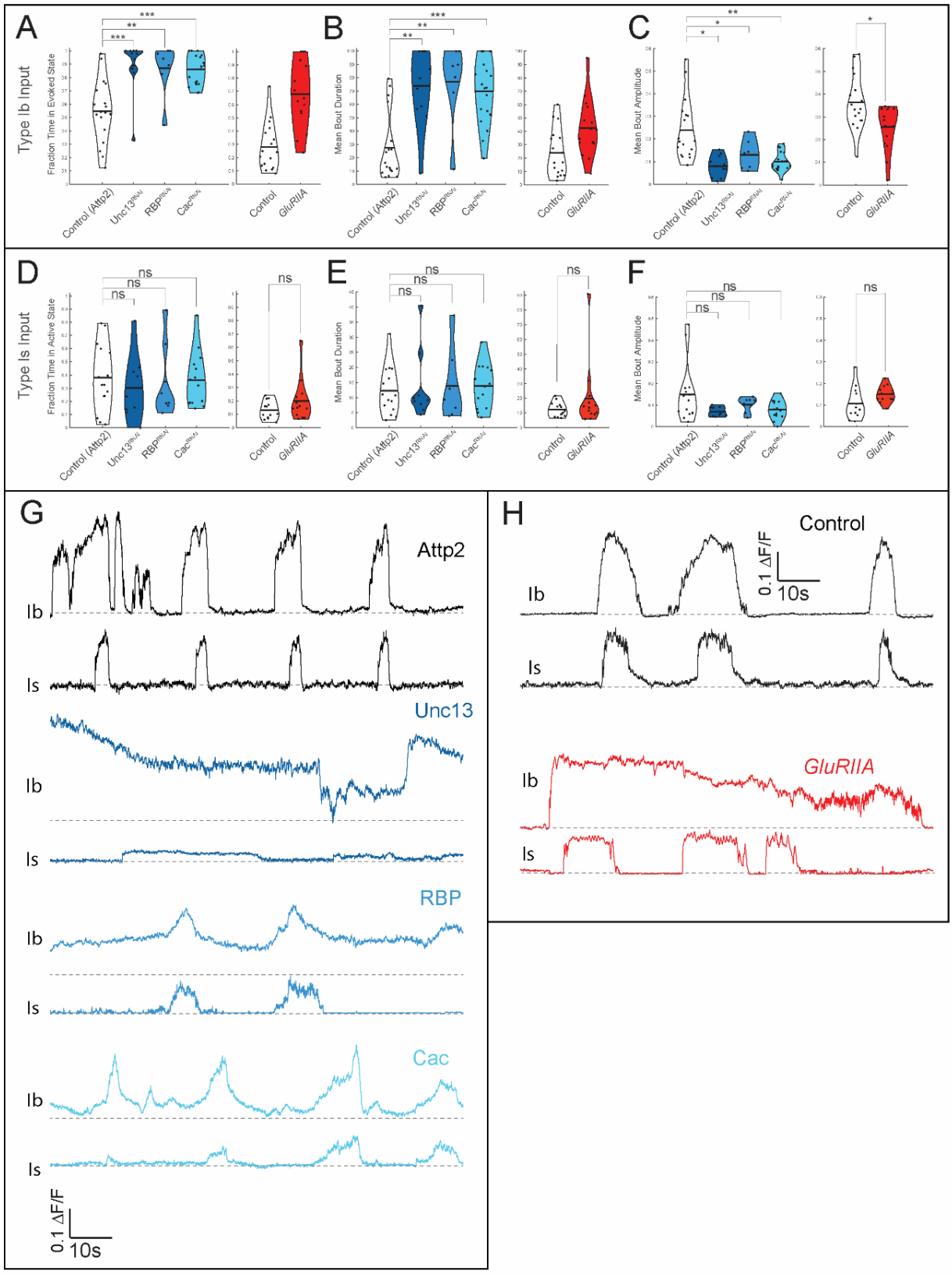
A
Type Ib Input
Fraction Time in Evoked State
B
Mean Bout Duration
C
Mean Bout Amplitude
D
Type Is Input
Fraction Time in Active State
E
Mean Bout Duration
F
Mean Bout Amplitude
Control (Attp2)
Unc13
RBP
Cac
Control
GluRIIA
ns
G
Attp2
Ib
Is
Unc13
RBP
Cac
0.1 ΔF/F
10s
H
Control
GluRIIA
0.1 ΔF/F
10s

Figure 4: Increased MN burst activity is specific to Ib inputs (A) Fraction time in evoked state for Ib (B) Mean bout duration for Ib (C) Mean ΔF/F bout amplitudes for Ib (D) Fraction time in evoked state for Is (E) Mean bout duration for Ib (F) Mean ΔF/F bout amplitudes for Is (G) Representative ΔF/F traces for RNAis and their control (H) ΔF/F traces for GlurIIA and its control
Comparisons made with Mann-Whitney test (A-F) $*p < 0.05$; $**p < 0.01$; $***p < 0.001$;

These results suggest that the increase in Ib MN firing duration is a compensatory mechanism that extends to muscle contraction in general, as it is employed in both forward-crawling and negative-phototaxis behaviors. Moreoever – as we observed in the case of PHP – the MN firing homeostasis appears to be specific to the Ib inputs and not the Is.

Timescale of Ib Firing Homeostatic Adjustment

Synaptic homeostasis at the NMJ has been shown to occur over the minute-timescale (Frank 2006), leading us to ask how fast the MNs can increase firing to compensate for perturbations at the NMJ. To test this, we turned to the temperature-sensitive Drosophila dynamin mutant, *shibire*^{ts1} (*shi*^{ts1}), which reduces quantal content at the restrictive temperature within several minutes (>29ºC) (Koenig 1989). After initially driving UAS-*shi*^{ts1} under our MN-Gal4 and incubating at 29C for 1.5hrs, we observed constitutive MN activity across all NMJs over all muscle segments, yet the larvae were unable to crawl within several minutes of applying heat-shock (Figures 5D-F).

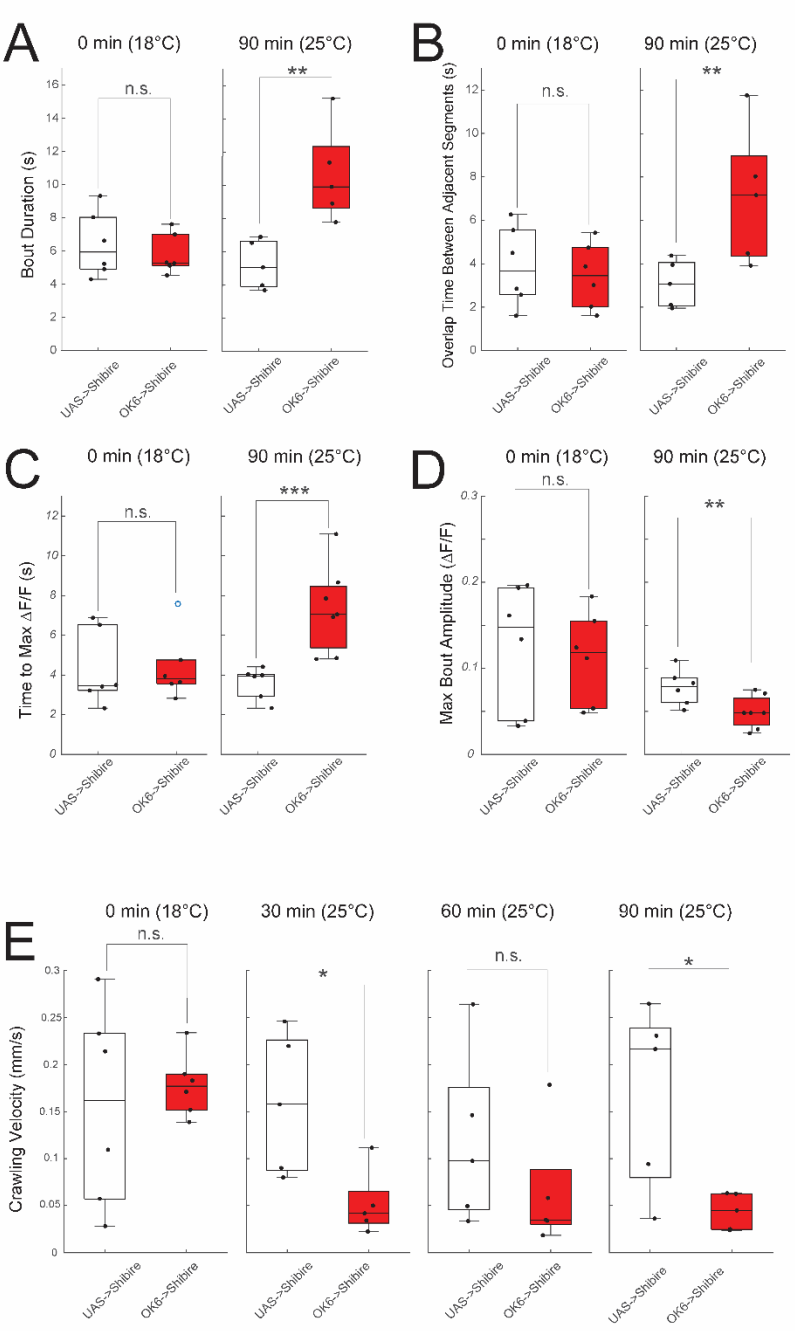

Figure 5: Shibire-induced MN homeostasis (A) Mean bout durations for UAS->Shibire and Ok6->Shibire at 0 min and 90 min (B) Overlap time between adjacent segments for UAS->Shibire and Ok6->Shibire at 0 min and 90 min (C) Time to max ΔF/F at 0 min and 90 min (D) Max ΔF/F bout amplitudes for at 0 and 90 min (E) Crawling velocities for 0, 30, 60, and 90 min timepoints
Comparisons made with Mann-Whitney test (A-E) $*p < 0.05$; $**p < 0.01$; $***p < 0.001$;

In theory, the lack of vesicular recycling for 1.5hrs and – as our model suggests – a corresponding increase in firing could reduce transmission enough to where the muscle contraction required for peristalsis may never be achieved. For this reason, we incubated the larvae at an intermediate temperature (25 ºC) for 1.5hrs, which caused a significant reduction in mean ΔF/F amplitudes while still preserving crawling behavior (Figures 5D-E). Despite crawling not being able to be fully restored, the *shibire*^{ts1}-induced decrease in transmission was accompanied by a nearly 2-fold increase in bout firing duration during peristaltic waves (Figure 5A), similar to what we observed in the case of the RNAi and GluRIIA mutant larvae. Additionally, we saw a similar increase in bout overlap time, indicating an increased amount of simultaneous contraction between two neighboring segments (Figure 5B).

Thus, the induction MN firing homeostasis can occur as fast as 1.5hrs after delivering an acute reduction in neurotransmitter release at the NMJ. Moreover, *shibire*^{ts1} demonstrates yet another mode where such homeostatic response can be generated by decreasing presynaptic vesicular release.

Inhibitory Premotor Inputs Regulate MN Firing Homeostasis

A homeostatic increase in MN firing could be due to cell-autonomous adjustments in its excitability, the calibration of excitatory and inhibitory drive from the premotor neurons (PMNs), or some combination of the two. Since our observed ~2-fold increase in MN firing duration could likely not be accounted for by changes in MN excitability alone, the PMNs appeared as a more promising first direction to investigate. We choose to focus on a relatively well characterized group of inhibitory PMNs, the *period*-positive median segmental interneurons, or PMSIs. The PMSIs are bilaterally located within the segments of the VNC that correspond to the segments of the body wall muscles. The PMSIs were an attractive candidate since optogenetically silencing them increases MN-burst duration and they synapse onto the Ib MNs and not the Is MNs (Kohsaka 2014; Zarin 2019).

By driving GCaMP6m expression in the PMSIs using LexA-LexAop while simultaneously knocking down presynaptic proteins using our OK6-Gal4 and UAS-RNAis, we were able to measure fluorescent activity in the PMSI processes within clearly demarcated segments of the VNC (Figures 6F). We observed fluorescence activity bouts that both belonged to peristaltic waves and existed independently of a wave (Figure 6G). While the ΔF/F kinetics and amplitudes of the individual activity bouts were similar between the control and RNAis (Figures S6A-C), the frequency of bouts both occurring independently and within peristaltic waves was significantly less in the case of the RNAis (Figures 6A-C). Furthermore, the intersegmental delay between the onset of bouts occurring in peristaltic waves trended upward in the RNAi animals (Figure 6D).

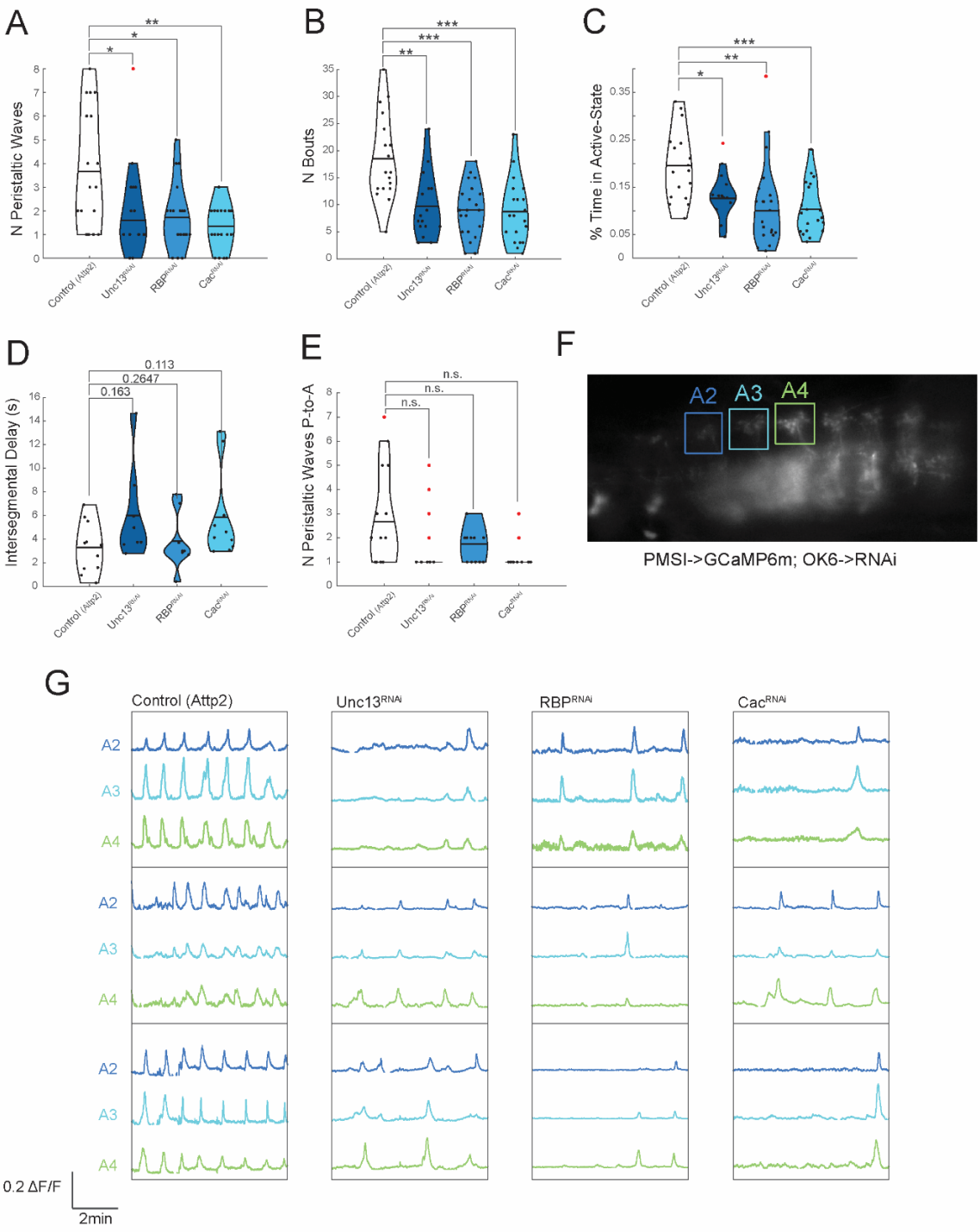
A
N Peristaltic Waves
B
N Bouts
C
% Time in Active-State
Control (Attp2)
Unc13RNAi
RBPRNAi
CacRNAi
D
Intersegmental Delay (s)
0.113
0.2647
0.163
E
N Peristaltic Waves P-to-A
n.s.
F
A2
A3
A4
PMSI->GCaMP6m; OK6->RNAi
G
Control (Attp2)
Unc13RNAi
RBPRNAi
CacRNAi
0.2 ΔF/F
2min

Figure 6: PMSIs reduce inhibitory drive to MNs (A) Mean number of ΔF/F bouts within peristaltic waves per each segment of the VNC (B) Mean number of ΔF/F bouts in both peristaltic waves and independently occurring per each segment of the VNC (C) Time in active state (D) Intersegmental delays between the onset of bouts occurring in peristaltic waves (E) Number of peristaltic waves propogating from the posterior-to-anterior (P-to-A) direction (F) Representative image of GC6m in the PMSI neurons within the VNC (G) Representative traces of 3 of the 5 segments recording from Comparisons made with Mann-Whitney test (A-E) $^{*}p < 0.05$; $^{**}p < 0.01$; $^{***}p < 0.001$;

Taken together, these results demonstrate a decrease in inhibitory PMN input to the Ib MNs and perhaps a prolonged intersegmental delay, which could result in the extension of Ib evoked activity bouts during peristalsis.

Discussion

The fundamental properties of circuit homeostasis remain unclear, particularly in an intact behaving animal. To understand the mechanisms that compensate for decreased vesicular release at the larval NMJ, we turned to our *in vivo* recording setup to record physiologically relevant MN activity.

As a form of compensation, we observed increased bursts of MN activity during restrained crawling and avoidance behaviors. If synaptic release were compromised, it may take longer to reach maximum ΔF/F signal thereby resulting in increased burst duration. We also observed an increase in the amount of time neighboring segments underwent simultaneous contraction because of the increased bout duration. It is possible that the simultaneous contraction of neighboring segments in the RNAis and mutant cases generates the same contractile displacement as one segment in the case of the controls.

It has also been shown that crawling velocity is regulated by peristaltic wave frequency rather than stride length (Heckscher 2012). Peristalsis wave speed and frequency was preserved in the cases of the RNAis and mutant larvae. Combined with longer bout duration, which may generate contractile force similar to controls, the preserved frequency of peristalsis would generate relatively normal forward crawling behavior.

We observed that the increase in firing duration occurred only in the Ib inputs and not Is. In our previous findings, we showed that the Ib input generates most of the contractile force (Newman 2017). Thus, the Ib input maybe provide more of a role in compensating for a decrease in transmission. Furthermore, PHP occurs exclusively at the Ib through an input-specific retrograde signal. This is intriguing because it raises the possibility of a shared homeostatic signaling pathway between PHP and increased MN burst duration occurring within the Ib terminals.

Our *shibire* experiments revealed that the circuit level adjustment in firing can occur within at least 1.5hr of a synaptic perturbation. PHP, on the other hand, occurs more rapidly within 10mins of induction. It could be the case that circuit homeostasis is a delayed, second line of

defense when PHP fails to restore adequate transmission. More experiments are needed to determine which forms of homeostatic compensation are recruited in what sequence, and if there is a hierarchical order in recruitment.

We witnessed a decrease amount of activity in the inhibitory PMSI inputs to the MNs in the case of the RNAis and mutant. Furthermore, we observed an increasing trend in the inter-segmental delay during peristaltic waves of fluorescence. Since the PMSIs are partly responsible for terminating MN burst firing, longer inter-segmental delays would result in longer MN bursts. Furthermore, the PMSIs only innervate the Ib MNs, which agrees with the homeostasis only occurring in the Ib and not Is axons.

Since the GluRIIA mutant fly has incomplete compensation at the Is, but exhibits PHP at the Ib, we wondered why there still existed an increase in firing duration on the same magnitude as that of the RNAis. Since Ibs in GluRII nulls facilitate at a slower rate than controls (2017 Newman), it may take longer for them to reach the same degree of muscle depolarization as the controls, thereby requiring increased burst duration of the motor neurons. These differences in rates of facilitation could be much more pronounced at the higher endogenous levels of firing than compared with our 5Hz experiment. Furthermore, the Is still fails to compensate, which could also account for the increase in Ib firing.

Further experiments are needed to address several key questions. First, previous work has demonstrated that by completely blocking synaptic transmission at the NMJ using tetanus toxin light chain, the motor neurons experience a compensatory increase in both voltage-gated inward Na+ and outward K+ currents accompanied by an increase in excitability (Baines 2001). Thus, it possible that there could be cell-autonomous forms of compensation that occur in parallel with the non-cell-autonomous decrease in premotor neuron activity. If this were true, the GluRIIA mutant larvae may exhibit at least three forms of homeostatic compensation: increasing synaptic release from the motor neuron terminals, lowering the action potential threshold in the motor neurons, and decreasing the inhibitory input of premotor neurons.

It remains unclear whether there are other changes in upstream inputs to the motor neurons to compensate for decreased transmission. It has been shown that there are 118 premotor neurons that synapse onto the 31 motor neurons per hemisegment, with individual motor neurons receiving up to 30 different types of input (Zarin 2019). These premotor neurons can be excitatory, inhibitory, or neuromodulatory and synapse onto multiple motor neurons per hemisegment. Thus, the PMSI neurons we choose to focus on could be one of the many players in modulating motor neuron activity.

Like most forms of compensation in the nervous system, the homeostat responsible for establishing the normal “set point” of transmission and modulating motor neuron firing remains unknown. In presynaptic homeostasis at the NMJ, the myriad of molecules at both the pre- and postsynapse that have been found to play a role in regulating homeostasis point to the homeostat being some sort of signaling molecule in the vicinity of the NMJ (Frank 2020). However, it is possible that proprioceptive neurons responsible for detecting proper crawling movement feedback onto the premotor neurons (Pehlevan 2016). When there is a deficit in

neurotransmission at the NMJ, the proprioceptive neurons could in theory act as a homeostat, sending feedback to the VNC, and boost firing of the motor neurons. Of course, there could be several levels of homeostatic regulation throughout the circuit, and the level at which it occurs could depend on the type of perturbation at the NMJ. For instance, the relatively fast timescale over which we observe the homeostatic increase in firing in the shibire larvae suggests that the homeostatic pathway lies within the proprioceptive feedback mechanisms, which could in theory deliver feedback to the premotor neurons much faster than a retrograde signal traveling from the muscle to the motor neuron, then to the premotor neurons. Our chronic perturbations we made at the NMJ, on the other hand, could regulate homeostasis through such a retrograde, transsynaptic signaling pathway. Thus, it remains to be determined if it is the overall decrease in locomotory output or imbalances in synaptic molecular signals that are responsible for compensating decreased transmission at the NMJ.

This study highlights the notion that homeostatic regulation of transmission at the NMJ is not solely confined to the level of its synapses. Our novel in vivo approach has shown that deficiencies at a single type of synapse within a circuit can elicit a complex compensatory interplay between several forms of excitatory, inhibitory, and intrinsic mechanisms occurring at many levels throughout the network. Understanding the complete picture of homeostatic plasticity in the Drosophila larva will likely require an integrated analysis of how these various forms of compensation cooperate to regulate normal crawling behavior. The existence of redundant forms of homeostasis may ensure that the system can respond to a wide range of perturbations at the NMJ.

Supplementary Figures

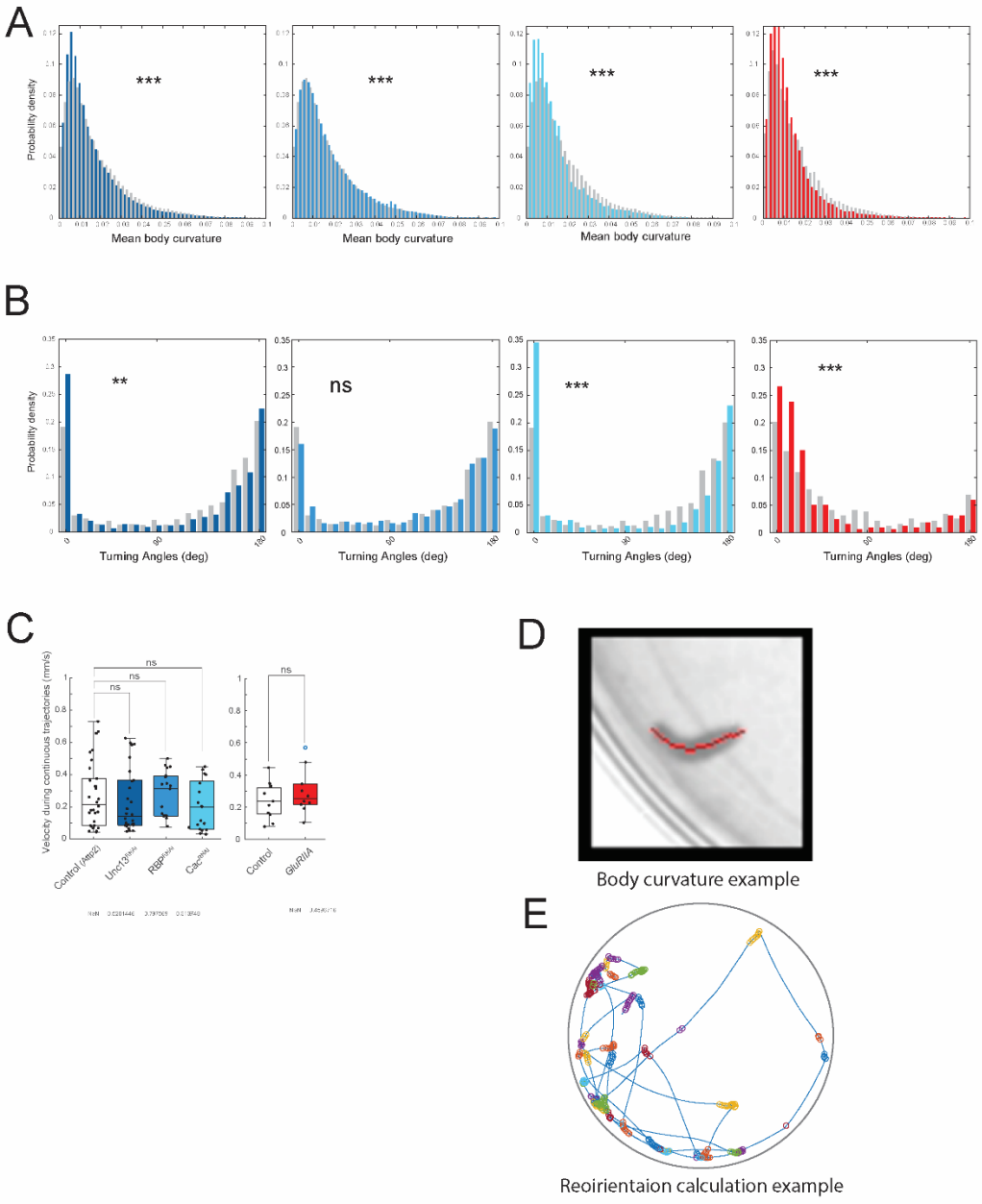

Supp. Figure 2 (related to Figure 2) Larva crawling agility (A) Probability densities of mean body curvatures for RNAis and *GluRIIA* mutant (B) Distributions of turning angles from 0 to 180 degrees (C) Velocity during the active crawling phases (D) Representative spline (red) fit along the body axis of the larva (E) Example of active crawling phases (blue lines) punctuated by reorientation phases (circles) Comparisons made with Mann-Whitney test (A-C) $^{*}p < 0.05$; $^{**}p < 0.01$; $^{***}p < 0.001$;

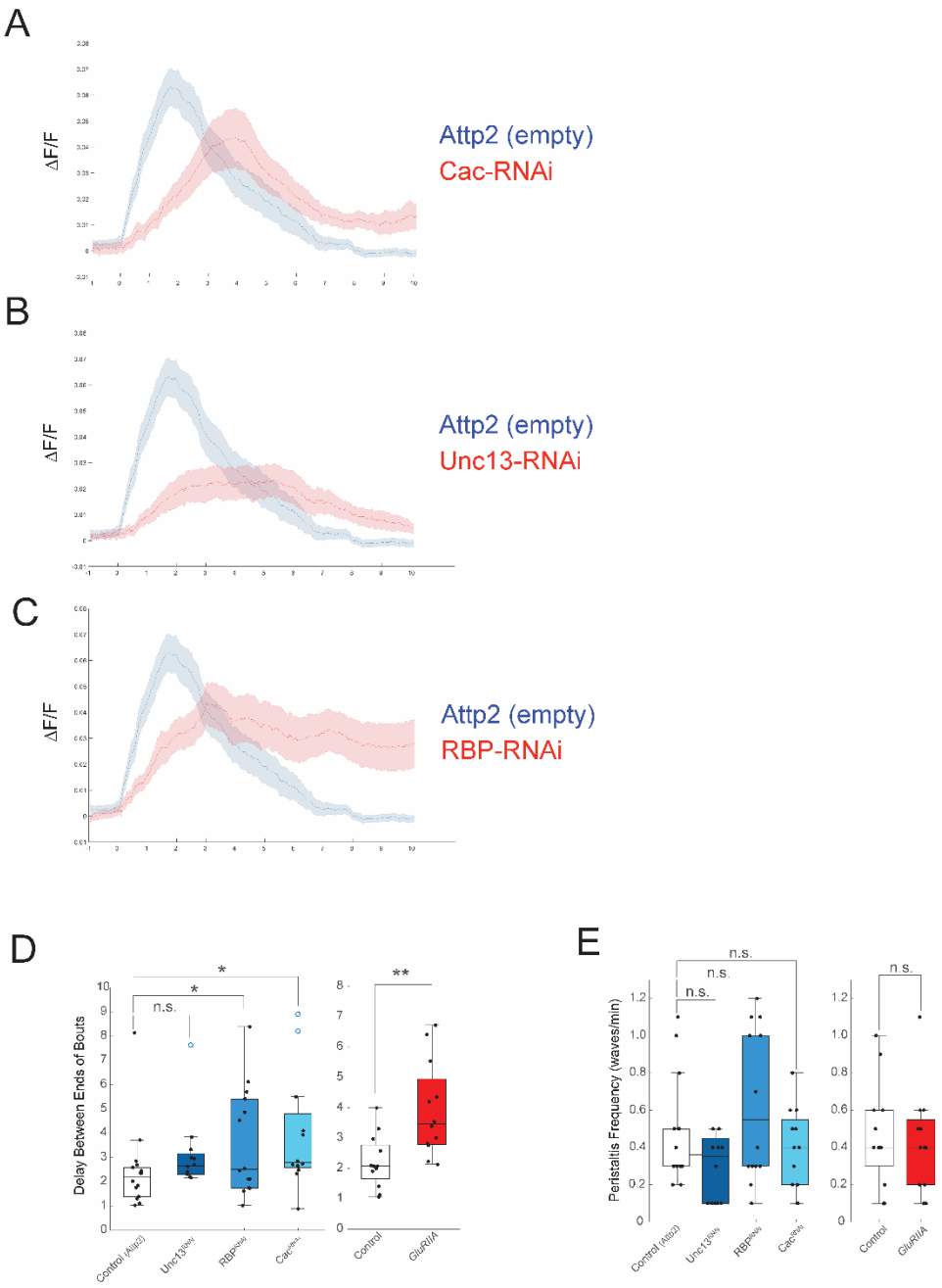

Supp. Figure 3 (related to Figure 3) Extended properties of peristaltic bouts (A) Mean time course of Cac activity bout (B) Mean time course of Unc13 activity bout (C) Mean time course of RBP activity bout (D) Delays between ends of bouts in peristaltic waves (E) Peristaltic wave frequencies (A-C) Means with SEM. Comparisons made with Mann-Whitney test (D-E) $^{*}p < 0.05$; $^{**}p < 0.01$; $^{***}p < 0.001$;

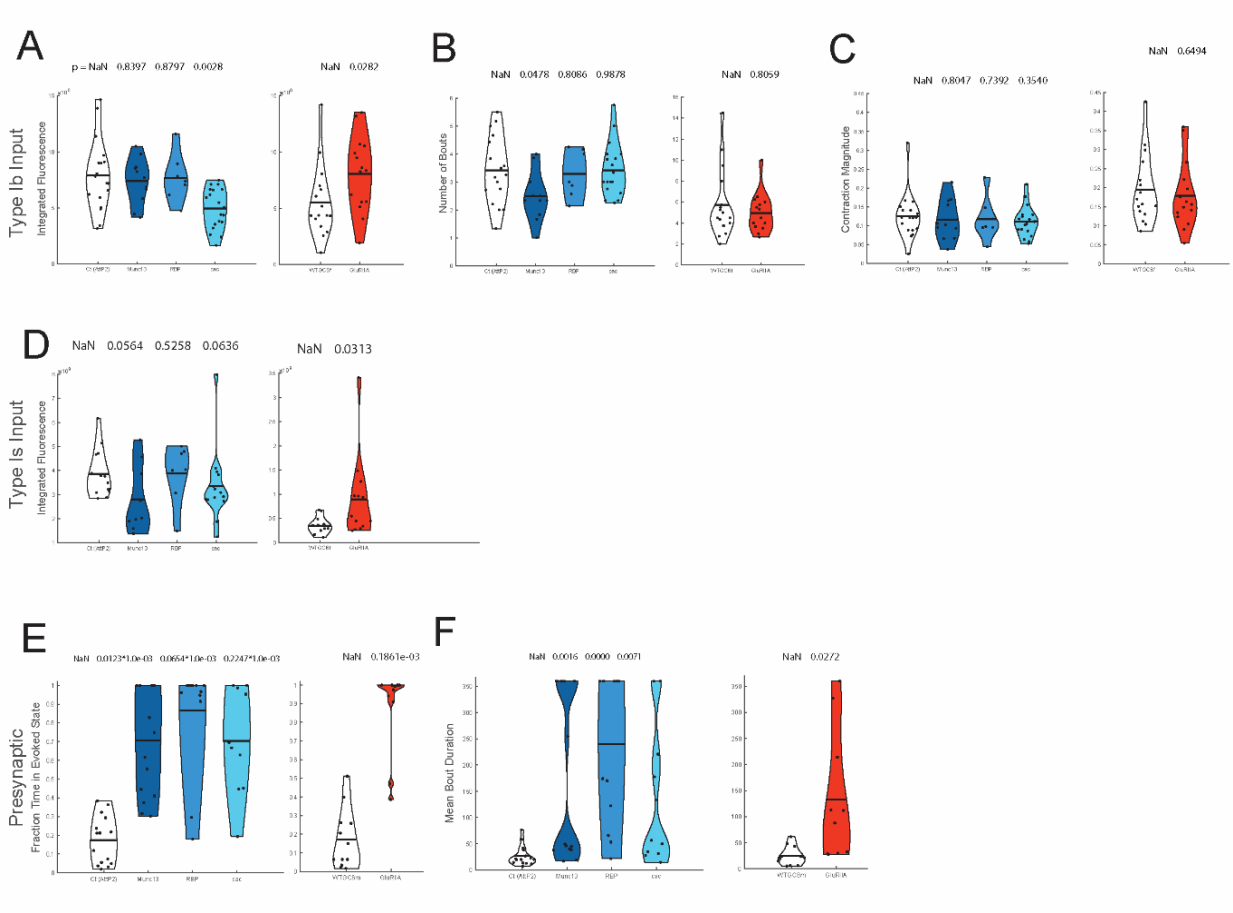

Supp. Figure 4 (related to Figure 4) Extended properties Ib and Is comparisons (A) Integrated fluorescence in type Ib (B) Number of bouts in type Ib (C) Contraction magnitude of bouts (D) Integrated fluorescence in type Is (E) Fraction time in active state using presynaptic MN GC6f (F) Mean bout duration using presynaptic MN GC6f
Comparisons made with Mann-Whitney test (A-F) $^{*}p < 0.05$; $^{**}p < 0.01$; $^{***}p < 0.001$;

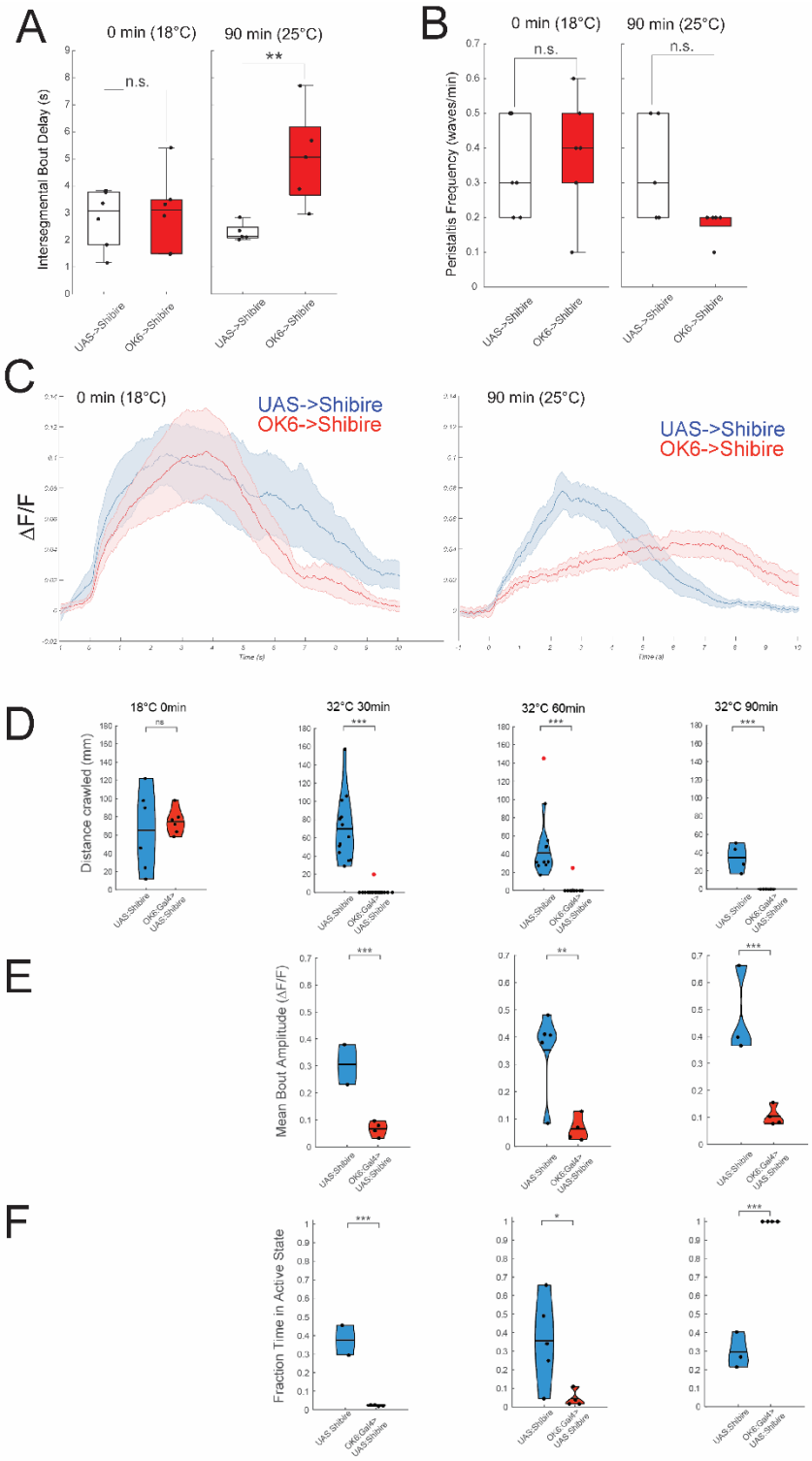

Supp. Figure 5 (related to Figure 5) Extended Shibire Results (A) Intersegmental bout delay (B) Peristalsis wave frequency (C) Time courses before and after 90 min of heat-shock (D) Distance crawled when incubated at a higher temperature (32C) for 90min (E) Bout amplitudes at 32C (F) Fraction time in active state at 32C
Comparisons made with Mann-Whitney test (A-F) *$p < 0.05$; **$p < 0.01$; ***$p < 0.001$;

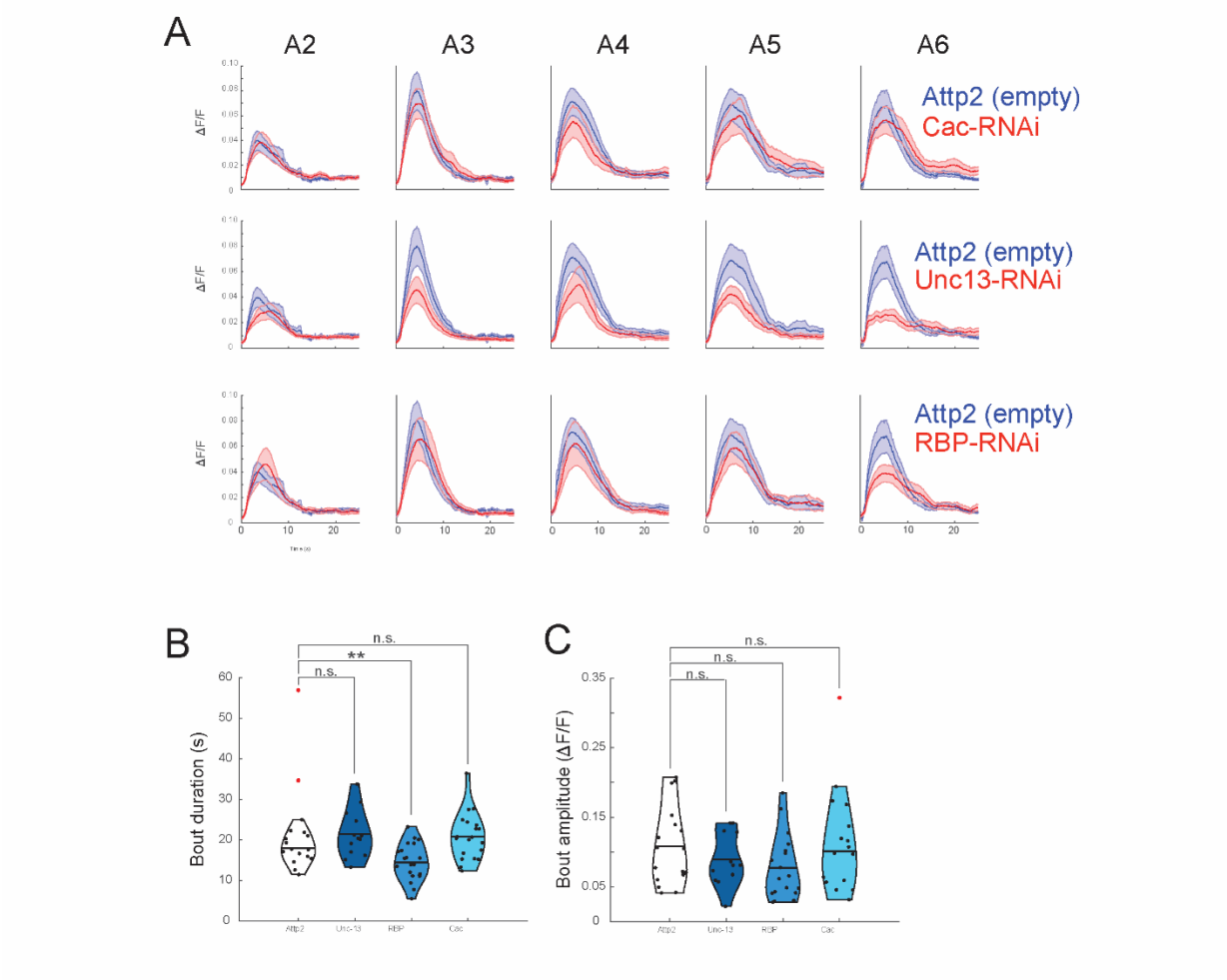

Supp. Figure 6 (related to Figure 6) Extended PMSI Results (A) Mean fluorescence traces from segments A1-A5 (B) PMSI bout durations (C) PMSI bout amplitudes
Comparisons made with Mann-Whitney test (A-F) $^{*}p < 0.05$; $^{**}p < 0.01$; $^{***}p < 0.001$;

Summary

My thesis work has explored the complex interplay between generating diversity and maintaining stability in the nervous system. In our study on the neuromodulatory control of behavior variability in zebrafish, our high throughput behavioral analysis revealed a large diversity in the rate of ASR habituation. Where most variation among individuals is often ignored when behavior is quantified as averages (Geiler-Samerotte 2013), our large sample revealed a spectrum of inter-individual variation. We found that differences in habituation are maintained over days and are heritable, indicating that ASR habituation has a genetic and / or epigenetic component. Zebrafish in which a larger number of DRN neurons responded to the sound stimulus habituated more slowly. Consistent with this, ASR habituation was decreased by either the application of a serotonin agonist or optogenetic stimulation of DRN neurons. And lastly, a genetic manipulation that reduced the serotonin content of the DRN neurons had the opposing effect by increasing the rate of habituation. Taken together, these results suggest that serotonin released from the DRN can generate behavioral diversity within a population.

Yet there remain several questions still unanswered. In particular, the exact identity of the neuronal populations that are the targets of serotonin release from the DRN remain unknown. We speculate that elements of the ASR circuit in the hindbrain receive such signals, due to the observed differential drop-off of Mauthner cell activity between individuals during ASR habituation. Serotonin also modulates Mautherner cells and the inhibitory glycinergic neurons that control ASR circuit gain. Moreover, the DRN sends projections that traverse the hindbrain. These results suggest that the DRN modulates the hindbrain circuitry integral to the ASR, yet the exact cell-types that serotonin act upon remain yet to be determined. Furthermore, the cause of variability in DRN responses between individuals is unclear, whether it is cell autonomous or due to differences in synaptic input to the DRN neurons. And finally, it remains to be determined if and how the genetic component we measured is linked to the degree of DRN activity.

Our research surrounding the *Drosophila* larva NMJ has gained insight into the diversity of inputs onto a convergent postsynaptic cell. We have shown that the regulation of basal synaptic strength, short-term plasticity, and homeostasis are shaped in an input-specific manner. The Ib input has higher levels of *in vivo* activity, synapses with lower P_r, and a propensity to facilitate during spike trains. Moreover, presynaptic homeostatic plasticity occurs exclusively as the Ib input. These results demonstrate how synaptic activity at the *Drosophila* NMJ is differentially regulated to ensure functional diversity and stability.

Several questions from our analysis remain. It has been shown that spontaneous vesicle release is required for the normal structural maturation of the NMJ, where increasing spontaneous release activity increases synaptic terminal growth (Choi 2014). However, we found that spontaneous release *in vivo* only represents about ~1% of total release, suggesting that evoked release would drown out any influence of spontaneous release. There are two possible explanations to this. First, the minute fraction of total release due to spontaneous activity could only be observed at the developmental stage at which we performed our experiments, where spontaneous activity could be much more significant earlier on in the larva's development. Yet perhaps more interestingly, we found that at both Ib and Is inputs there exist synapses that participate in either

evoked or spontaneous release. It could be the case that developmental signals could occur at a subset of synapses that are dominated by spontaneous release. Furthermore, a number of molecules have been demonstrated to play a role in mediating presynaptic homeostatic compensation (Davis and Müller, 2015). It remains to be determined how these molecular players compartmentalize to differentially regulate homeostasis exclusively at the Ib terminals.

In my final project, our investigation using the intact *Drosophila* larva enabled us to discover a new form of upstream, circuit-level homeostatic compensation in response to deficiencies at the NMJ. We chose to not only examine how the firing dynamics may change in the *GluRIIA* mutant background, which only has PHP occur at the Ib synapses, but in cases where PHP failed to occur at both Ib and Is terminals. Using an RNAi screen where we knocked-down presynaptic proteins, we identified cases where neurotransmitter release was reduced by up to 90% without any presynaptic compensation. Remarkably, both the RNAi and *GluRIIA* larvae exhibited relatively normal crawling behavior despite the severe deficiencies in neurotransmission. To accomplish this, we found that the motor neurons were in fact increasing their burst durations roughly 2-fold. This compensation occurs in type Ib MNs but not in the Is, and results from less inhibitory drive from upstream premotor neurons. Acute disruption of MN transmitter release shows that increased MN activity occurs after 1-1.5 hrs, i.e. delayed compared to the minute time-scale of PHP (2006 Frank).

Further experiments are needed to address several key questions. First, previous work has demonstrated that by completely blocking synaptic transmission at the NMJ using tetanus toxin light chain, the motor neurons experience a compensatory increase in both voltage-gated inward Na^+ and outward K^+ currents accompanied by an increase in excitability (Baines 2001). Thus, it possible that there could be cell-autonomous forms of compensation that occur in parallel with the non-cell-autonomous decrease in premotor neuron activity. If this were true, the *GluRIIA* mutant larvae may exhibit at least three forms of homeostatic compensation: increasing synaptic release from the motor neuron terminals, lowering the action potential threshold in the motor neurons, and decreasing the inhibitory input of premotor neurons.

It remains unclear whether there are other changes in upstream inputs to the motor neurons to compensate for decreased transmission. It has been shown that there are 118 premotor neurons that synapse onto the 31 motor neurons per hemisegment, with individual motor neurons receiving up to 30 different types of input (Zarin 2019). These premotor neurons can be excitatory, inhibitory, or neuromodulatory and synapse onto multiple motor neurons per hemisegment. Thus, the PMSI neurons we choose to focus on could be one of the many players in modulating motor neuron activity.

Like most forms of compensation in the nervous system, the homeostat responsible for establishing the normal “set point” of transmission and modulating motor neuron firing remains unknown. In presynaptic homeostasis at the NMJ, the myriad of molecules at both the pre- and postsynapse that have been found to play a role in regulating homeostasis point to the homeostat being some sort of signaling molecule in the vicinity of the NMJ (Frank 2020). However, it is possible that proprioceptive neurons responsible for detecting proper crawling movement feedback onto the premotor neurons (Pehlevan 2016). When there is a deficit in neurotransmission at the NMJ, the proprioceptive neurons could in theory act as a homeostat,

sending feedback to the VNC, and boost firing of the motor neurons. Of course, there could be several levels of homeostatic regulation throughout the circuit, and the level at which it occurs could depend on the type of perturbation at the NMJ. For instance, the relatively fast timescale over which we observe the homeostatic increase in firing in the *shibire* larvae suggests that the homeostatic pathway lies within the proprioceptive feedback mechanisms, which could in theory deliver feedback to the premotor neurons much faster than a retrograde signal traveling from the muscle to the motor neuron, then to the premotor neurons. Our chronic perturbations we made at the NMJ, on the other hand, could regulate homeostasis through such a retrograde, transsynaptic signaling pathway. Thus, it remains to be determined if it is the overall decrease in locomotory output or imbalances in synaptic molecular signals that are responsible for compensating decreased transmission at the NMJ.

This study highlights the notion that homeostatic regulation of transmission at the NMJ is not solely confined to the level of its synapses. Our novel *in vivo* approach has shown that deficiencies at a single type of synapse within a circuit can elicit a complex compensatory interplay between several forms of excitatory, inhibitory, and intrinsic mechanisms occurring at many levels throughout the network. Understanding the complete picture of homeostatic plasticity in the *Drosophila* larva will likely require an integrated analysis of how these various forms of compensation cooperate to regulate normal crawling behavior. The existence of redundant forms of homeostasis may ensure that the system can respond to a wide range of perturbations at the NMJ.

References

Aberle, H. et al. wishful thinking encodes a BMP type II receptor that regulates synaptic growth in 1067 Drosophila. Neuron 33, 545–58 (2002).

Agetsuma M, Aizawa H, Aoki T, Nakayama R, Takahoko M, Goto M, Sassa T, Amo R, Shiraki T, Kawakami K, et al. The habenula is crucial for experience-dependent modification of fear responses in zebrafish. *Nat. Neurosci.* 2010;13:1354–1356.

Akerboom J, Chen T-W, Wardill TJ, Tian L, Marvin JS, Mutlu S, Calderon NC, Esposti F, Borghuis BG, Sun XR, et al. Optimization of a GCaMP Calcium Indicator for Neural Activity Imaging. *J. Neurosci.* 2012;32:13819–13840.

Aponte-Santiago, N. A., Ormerod, K. G., Akbergenova, Y., & Littleton, J. T. (2020). Synaptic plasticity induced by differential manipulation of tonic and phasic motoneurons in Drosophila. Journal of Neuroscience, 40(33), 6270-6288.

Arnsten A. F. T., Wang M. J., Paspalas C. D. (2012). Neuromodulation of thought: flexibilities and vulnerabilities in prefrontal cortical network synapses. *Neuron* 76 223–239. 10.1016/j.neuron.2012.08.038

Atwood HL, Govind CK, Wu CF. Differential ultrastructure of synaptic terminals on ventral longitudinal abdominal muscles in Drosophila larvae. *J Neurobiol.* 1993;24:1008–1024.

Atwood HL, Karunanithi S. Diversification of Synaptic Strength: Presynaptic Elements. *Nat Rev Neurosci.* 2002;3:497–516.

Ayroles J. F., Buchanan S. M., O'Leary C., Skutt-Kakaria K., Grenier J. K., Clark A. G., et al. (2015). Behavioral idiosyncrasy reveals genetic control of phenotypic variability. *Proc. Natl. Acad. Sci. U. S. A.* 112 6706–6711. 10.1073/pnas.1503830112

Ayroles JF, Buchanan SM, O'Leary C, Skutt-Kakaria K, Grenier JK, Clark AG, HartlDL, de Bivort BL. Behavioral idiosyncrasy reveals genetic control of phenotypic variability. *Proc. Natl. Acad. Sci. U. S. A.* 2015;112:6706–6711.

Baines, R. A., Uhler, J. P., Thompson, A., Sweeney, S. T., & Bate, M. (2001). Altered electrical properties in drosophilaneurons developing without synaptic transmission. *Journal of Neuroscience*, *21*(5), 1523-1531.

Bargmann C. I., Marder E. (2013). From the connectome to brain function. *Nat. Methods* 10 483–490. 10.1038/nmeth.2451

Bianco IH, Kampff AR, Engert F. Prey Capture Behavior Evoked by Simple Visual Stimuli in Larval Zebrafish. *Front. Syst. Neurosci.* 2011:5.

Blanch A, Balada F, Aluja A. Habituation in acoustic startle reflex: Individual differences in personality. *Int. J. Psychophysiol. Off. J. Int. Organ. Psychophysiol.* 2014

Boureau Y-L, Dayan P. Opponency Revisited: Competition and Cooperation Between Dopamine and Serotonin. *Neuropsychopharmacology.* 2010;36:74–97.

Braff DL. Gating and Habituation of the Startle Reflex in Schizophrenic Patients. *Arch. Gen. Psychiatry.* 1992;49:206.

Branco T, Staras K, Darcy KJ, Goda Y. Local dendritic activity sets release probability at hippocampal synapses. *Neuron.* 2008;59:475–485.

Branco T, Staras K. The probability of neurotransmitter release: variability and feedback control at single synapses. *Nat Rev Neurosci.* 2009;10:373–383.

Brown KH, Dobrinski KP, Lee AS, Gokcumen O, Mills RE, Shi X, Chong WWS, Chen JYH, Yoo P, David S, et al. Extensive genetic diversity and substructuring among zebrafish strains revealed through copy number variant analysis. *Proc. Natl. Acad. Sci.* 2012;109:529–534.

Bruijning M., Metcalf C. J. E., Jongejans E., Ayroles J. F. (2020). The evolution of variance control. *Trends Ecol. Evol.* 35 22–33. 10.1016/j.tree.2019.08.005

Brustein E, Chong M, Holmqvist B, Drapeau P. Serotonin patterns locomotor network activity in the developing zebrafish by modulating quiescent periods. *J. Neurobiol.* 2003;57:303–322.

Budnik V, Ruiz-Cañada C. *The Fly Neuromuscular Junction: Structure and Function.* San Diego: Elsevier Academic Press; 2006.

Burgess HA, Granato M. Sensorimotor gating in larval zebrafish. *J. Neurosci. Off. J. Soc. Neurosci.* 2007;27:4984–4994.

Burrone J, O'Byrne M, Murthy VN. Multiple forms of synaptic plasticity triggered by selective suppression of activity in individual neurons. *Nature.* 2002;420:414–418.

Chadderton P, Margrie TW, Häusser M. Integration of quanta in cerebellar granule cells during sensory processing. *Nature.* 2004;428:856–860.

Chen TW, Wardill TJ, Sun Y, Pulver SR, Renninger SL, Baohan A, Schreiter ER, Kerr RA, Orger MB, Jayaraman V, et al. Ultrasensitive fluorescent proteins for imaging neuronal activity. *Nature.* 2013;499:295–300.

Cheng R-K, Krishnan S, Jesuthasan S. Activation and inhibition of tph2 serotonergic neurons operate in tandem to influence larval zebrafish preference for light over darkness. *Sci. Rep.* 2016;6:20788.

Cho RW, Buhl LK, Volfson D, Tran A, Li F, Akbergenova Y, Littleton JT. Phosphorylation of Complexin by PKA Regulates Activity-Dependent Spontaneous Neurotransmitter Release and Structural Synaptic Plasticity. *Neuron.* 2015;88:749–761.

Choi BJ, Imlach WL, Jiao W, Wolfram V, Wu Y, Grbic M, Cela C, Baines RA, Nitabach MN, McCabe BD. Miniature neurotransmission regulates Drosophila synaptic structural maturation. *Neuron.* 2014;82:618–634.

Choi JC, Park D, Griffith LC. Electrophysiological and morphological characterization of identified motor neurons in the Drosophila third instar larva central nervous system. *J Neurophysiol.* 2004;91:2353–2365.

Cingolani LA, Thalhammer A, Yu LM, Catalano M, Ramos T, Colicos MA, Goda Y. Activity-dependent regulation of synaptic AMPA receptor composition and abundance by beta3 integrins. *Neuron.* 2008;58:749–762.

Colwill RM, Creton R. Imaging escape and avoidance behavior in zebrafish larvae. *Rev. Neurosci.* 2011;22:63–73.

Cullins MJ, Gill JP, McManus JM, Lu H, Shaw KM, Chiel HJ. Sensory Feedback Reduces Individuality by Increasing Variability within Subjects. *Curr. Biol. CB.* 2015;25:2672–2676.

Curtin PCP, Medan V, Neumeister H, Bronson DR, Preuss T. The 5-HT5A Receptor Regulates Excitability in the Auditory Startle Circuit: Functional Implications for Sensorimotor Gating. *J. Neurosci.* 2013;33:10011–10020.

Daur N., Bryan A. S., Garcia V. J., Bucher D. (2012). Short-term synaptic plasticity compensates for variability in number of motor neurons at a neuromuscular junction. *J. Neurosci.* 32 16007–16017. 10.1523/jneurosci.2584-12.2012.

Davis GW, Bezprozvanny I 2001. Maintaining the stability of neural function: A homeostatic hypothesis. *Annu Rev Physiol* 63: 847–869

Davis GW, Müller M. Homeostatic Control of Presynaptic Neurotransmitter Release. *Annu Rev Physiol.* 2015;77:251–270.

Davis GW. Homeostatic signaling and the stabilization of neural function. Neuron. 2013;80(3):718–28.

Davis, G. W., & Müller, M. (2015). Homeostatic control of presynaptic neurotransmitter release. Annual review of physiology, 77, 251-270.

Dell AL, Fried-Cassorla E, Xu H, Raper JA. cAMP-induced expression of neuropilin1 promotes retinal axon crossing in the zebrafish optic chiasm. *J. Neurosci. Off. J. Soc. Neurosci.* 2013;33:11076–11088.

Desai NS, Cudmore RH, Nelson SB, Turrigiano GG. Critical periods for experience-dependent synaptic scaling in visual cortex. *Nat Neurosci.* 2002;5:783–789.

Dittman JS, Kreitzer AC, Regehr WG. Interplay between facilitation, depression, and residual calcium at three presynaptic terminals. *J Neurosci.* 2000;20:1374–1385.

Ehmann N, van de Linde S, Alon A, Ljaschenko D, Keung XZ, Holm T, Rings A, DiAntonio A, Hallermann S, Ashery U, et al. Quantitative super-resolution imaging of Bruchpilot distinguishes active zone states. *Nat Commun.* 2014;5:ncomms5650.

Filosa A, Barker AJ, Dal Maschio M, Baier H. Feeding State Modulates Behavioral Choice and Processing of Prey Stimuli in the Zebrafish Tectum. *Neuron.* 2016

Flavell SW, Pokala N, Macosko EZ, Albrecht DR, Larsch J, Bargmann CI. Serotonin and the neuropeptide PDF initiate and extend opposing behavioral states in C. elegans. *Cell.* 2013;154:1023–1035.

Frank CA, Kennedy MJ, Goold CP, Marek KW, Davis GW. Mechanisms underlying the rapid induction and sustained expression of synaptic homeostasis. *Neuron.* 2006;52:663–677.

Frank, C. A., James, T. D., & Müller, M. (2020). Homeostatic control of Drosophila neuromuscular junction function. Synapse, 74(1), e22133.

Frank, C. A., Kennedy, M. J., Goold, C. P., Marek, K. W., & Davis, G. W. (2006). Mechanisms underlying the rapid induction and sustained expression of synaptic homeostasis. Neuron, 52(4), 663-677.

Fujioka M, Lear BC, Landgraf M, Yusibova GL, Zhou J, Riley KM, Patel NH, Jaynes JB. Even-skipped, acting as a repressor, regulates axonal projections in Drosophila. *Development.* 2003;130:5385–5400.

Geiler-Samerotte KA, Bauer CR, Li S, Ziv N, Gresham D, Siegal ML. The details in the distributions: why and how to study phenotypic variability. *Curr. Opin. Biotechnol.* 2013;24:752–759.

Gjorgjieva, Julijana, et al. "Neural circuits for peristaltic wave propagation in crawling Drosophila larvae: analysis and modeling." Frontiers in computational ne uroscience 7 (2013): 24.

Glanzman DL, Mackey SL, Hawkins RD, Dyke AM, Lloyd PE, Kandel ER. Depletion of serotonin in the nervous system of Aplysia reduces the behavioral enhancement of gill withdrawal as well as the heterosynaptic facilitation produced by tail shock. *J. Neurosci. Off. J. Soc. Neurosci.* 1989;9:4200–4213.

Goaillard J.-M., Marder E. (2021). Ion channel degeneracy, variability, and covariation in neuron and circuit resilience. *Annu. Rev. Neurosci.* 44 335–357. 10.1146/annurev-neuro-092920-121538

Goddard CA, Butts DA, Shatz CJ. Regulation of CNS synapses by neuronal MHC class I. *Proc Natl Acad Sci U S A.* 2007;104:6828–6833.

Gordus A, Pokala N, Levy S, Flavell SW, Bargmann CI. Feedback from Network States Generates Variability in a Probabilistic Olfactory Circuit. *Cell.* 2015;161:215–227.

Griffith LC, Verselis LM, Aitken KM, Kyriacou CP, Danho W, Greenspan RJ. Inhibition of calcium/calmodulin-dependent protein kinase in Drosophila disrupts behavioral plasticity. *Neuron.* 1993;10:501–509.

Guerrero G, Reiff DF, Rieff DF, Agarwal G, Ball RW, Borst A, Goodman CS, Isacoff EY. Heterogeneity in synaptic transmission along a Drosophila larval motor axon. *Nat Neurosci.* 2005;8:1188–1196.

Guizar-Sicairos M, Thurman ST, Fienup JR. Efficient subpixel image registration algorithms. *Opt Lett.* 2008;33:156–158.

Günther, M. N., Nettesheim, G., & Shubeita, G. T. (2016). Quantifying and predicting Drosophila larvae crawling phenotypes. Scientific Reports, 6(1), 27972.

Gupta A, Wang Y, Markram H. Organizing Principles for a Diversity of GABAergic Interneurons and Synapses in the Neocortex. *Science.* 2000;287:273–278.

Guptaroy B, Marwaha N, Pla M, Wang Z, Nelson HB, Beckingham K, Griffith LC. Alternative splicing of Drosophila calcium/calmodulin-dependent protein kinase II regulates substrate specificity and activation. *Mol Brain Res.* 2000;80:26–34.

Haghighi AP, McCabe BD, Fetter RD, Palmer JE, Hom S, Goodman CS. Retrograde control of synaptic transmission by postsynaptic CaMKII at the Drosophila neuromuscular junction. *Neuron.* 2003;39:255–267.

Heckscher ES, Lockery SR, Doe CQ. Characterization of Drosophila larval crawling at the level of organism, segment, and somatic body wall musculature. *J Neurosci.* 2012;32:12460–12471.

Heckscher ES, Zarin AA, Faumont S, Clark MQ, Manning L, Fushiki A, Schneider-Mizell CM, Fetter RD, Truman JW, Zwart MF, et al. Even-Skipped+ Interneurons Are Core Components of a Sensorimotor Circuit that Maintains Left-Right Symmetric Muscle Contraction Amplitude. *Neuron.* 2015;88:314–329.

Heckscher, E. S., Lockery, S. R., & Doe, C. Q. (2012). Characterization of Drosophila larval crawling at the level of organism, segment, and somatic body wall musculature. Journal of Neuroscience, 32(36), 12460-12471.

Hoang B, Chiba A. Single-cell analysis of Drosophila larval neuromuscular synapses. *Dev Biol.* 2001;229:55–70.

Hoang, B., & Chiba, A. (2001). Single-cell analysis of Drosophila larval neuromuscular synapses. Developmental biology, 229(1), 55-70.

Howe K, Clark MD, Torroja CF, Torrance J, Berthelot C, Muffato M, Collins JE, Humphray S, McLaren K, Matthews L, et al. The zebrafish reference genome sequence and its relationship to the human genome. *Nature.* 2013;496:498–503.

Ibata K, Sun Q, Turrigiano GG. Rapid synaptic scaling induced by changes in postsynaptic firing. *Neuron.* 2008;57:819–826.

Jakawich SK, Nasser HB, Strong MJ, McCartney AJ, Perez AS, Rakesh N, Carruthers CJL, Sutton MA. Local Presynaptic Activity Gates Homeostatic Changes in Presynaptic Function Driven by Dendritic BDNF Synthesis. *Neuron.* 2010;68:1143–1158.

Jia XX, Gorczyca M, Budnik V. Ultrastructure of neuromuscular junctions in Drosophila: Comparison of wild type and mutants with increased excitability. *J Neurobiol.* 1993;24:1025–1044.

Johnston R. J., Jr., Desplan C. (2010). Stochastic mechanisms of cell fate specification that yield random or robust outcomes. *Annu. Rev. Cell Dev. Biol.* 26 689–719. 10.1146/annurev-cellbio-100109-104113

Kain J. S., Zhang S., Akhund-Zade J., Samuel A. D. T., Klein M., de Bivort B. L. (2015). Variability in thermal and phototactic preferences in Drosophila may reflect an adaptive bet-hedging strategy. *Evolution* 69 3171–3185. 10.1111/evo.12813

Kain JS, Stokes C, de Bivort BL. Phototactic personality in fruit flies and its suppression by serotonin and white. *Proc. Natl. Acad. Sci. U. S. A.* 2012;109:19834–19839.

Kaneko M, Stellwagen D, Malenka RC, Stryker MP. Tumor necrosis factor-alpha mediates one component of competitive, experience-dependent plasticity in developing visual cortex. *Neuron.* 2008;58:673–680.

Kappeler PM, Anthes N. *Animal behaviour evolution and mechanisms.* Berlin; London; New York: Springer; 2010.

Karunanithi S, Marin L, Wong K, Atwood HL. Quantal size and variation determined by vesicle size in normal and mutant Drosophila glutamatergic synapses. *J Neurosci.* 2002;22:10267–10276.

Katz P. S., Lillvis J. L. (2014). Reconciling the deep homology of neuromodulation with the evolution of behavior. *Curr. Opin. Neurobiol.* 29 39–47. 10.1016/j.conb.2014.05.002

Kavalali ET. The mechanisms and functions of spontaneous neurotransmitter release. *Nat Rev Neurosci.* 2015;16:5–16.

Kishi T, Yoshimura R, Fukuo Y, Okochi T, Matsunaga S, Umene-Nakano W, Nakamura J, Serretti A, Correll CU, Kane JM, et al. The serotonin 1A receptor gene confer susceptibility to mood disorders: results from an extended meta-analysis of patients with major depression and bipolar disorder. *Eur. Arch. Psychiatry Clin. Neurosci.* 2013;263:105–118.

Kittel RJ, Wichmann C, Rasse TM, Fouquet W, Schmidt M, Schmid A, Wagh DA, Pawlu C, Kellner RR, Willig KI, et al. Bruchpilot promotes active zone assembly, Ca2+ channel clustering, and vesicle release. *Science.* 2006;312:1051–1054.

Knodel MM, Geiger R, Ge L, Bucher D, Grillo A, Wittum G, Schuster CM, Queisser G. Synaptic bouton properties are tuned to best fit the prevailing firing pattern. *Front Comput Neurosci.* 2014;8 doi: 10.3389/fncom.2014.00101.

Koenig, J. H., Toshio Kosaka, and K. Ikeda. "The relationship between the number of synaptic vesicles and the amount of transmitter released." Journal of Neuroscience 9.6 (1989): 1937-1942.

Koh YH, Popova E, Thomas U, Griffith LC, Budnik V. Regulation of DLG localization at synapses by CaMKII-dependent phosphorylation. *Cell.* 1999;98:353–363.

Kohsaka, H., Takasu, E., Morimoto, T., & Nose, A. (2014). A group of segmental premotor interneurons regulates the speed of axial locomotion in Drosophila larvae. Current Biology, 24(22), 2632-2642.

Korn H, Faber DS. The Mauthner cell half a century later: a neurobiological model for decision-making? *Neuron.* 2005;47:13–28.

Kurdyak P, Atwood HL, Stewart BA, Wu CF. Differential physiology and morphology of motor axons to ventral longitudinal muscles in larval Drosophila. *J Comp Neurol.* 1994;350:463–472.

Lacoste AMB, Schoppik D, Robson DN, Haesemeyer M, Portugues R, Li JM, Randlett O, Wee CL, Engert F, Schier AF. A convergent and essential interneuron pathway for Mauthner-cell-mediated escapes. *Curr. Biol. CB.* 2015;25:1526–1534.

Lahey T, Gorczyca M, Jia XX, Budnik V. The Drosophila tumor suppressor gene dlg is required for normal synaptic bouton structure. *Neuron.* 1994;13:823–835.

Lahiri, S., Shen, K., Klein, M., Tang, A., Kane, E., Gershow, M., Garrity, P., & Samuel, A. D. T. (2011). Two Alternating Motor Programs Drive Navigation in Drosophila Larva. PLoS ONE, 6(8), e23180.

Lambert AM, Bonkowsky JL, Masino MA. The conserved dopaminergic diencephalospinal tract mediates vertebrate locomotor development in zebrafish larvae. *J. Neurosci. Off. J. Soc. Neurosci.* 2012;32:13488–13500.

Laskowski KL, Bell AM. Strong personalities, not social niches, drive individual differences in social behaviours in sticklebacks. *Anim. Behav.* 2014;90:287–295.

Laurila A, Lindgren B, Laugen AT. Antipredator defenses along a latitudinal gradient in Rana temporaria. *Ecology.* 2008;89:1399–1413.

Lee S.-H., Dan Y. (2012). Neuromodulation of brain states. *Neuron* 76 209–222. 10.1016/j.neuron.2012.09.012

Lee S-H, Dan Y. Neuromodulation of Brain States. *Neuron.* 2012;76:209–222.

Lee, H. K., & Kirkwood, A. (2019). Mechanisms of homeostatic synaptic plasticity in vivo. Frontiers in cellular neuroscience, 13, 520.

Levitz J, Pantoja C, Isacoff EY, Gaub B, Reiner A, Trauner D. Optical Control of Metabotropic Glutamate Receptors. *Nat. Neurosci.* 2013

Lillesaar C, Stigloher C, Tannhäuser B, Wullimann MF, Bally-Cuif L. Axonal projections originating from raphe serotonergic neurons in the developing and adult zebrafish, Danio rerio, using transgenics to visualize raphe-specific pet1 expression. *J. Comp. Neurol.* 2009;512:158–182.

Lillvis JL, Katz PS. Parallel evolution of serotonergic neuromodulation underlies independent evolution of rhythmic motor behavior. J. Neurosci. *Off. J. Soc. Neurosci.* 2013;33:2709–2717.

Lin MZ, Schnitzer MJ. Genetically encoded indicators of neuronal activity. *Nat Neurosci.* 2016;19:1142–1153.

Linkert M, Rueden CT, Allan C, Burel JM, Moore W, Patterson A, Loranger B, Moore J, Neves C, MacDonald D, et al. Metadata matters: Access to image data in the real world. *J Cell Biol.* 2010;189:777–782.

Lnenicka GA, Keshishian H. Identified motor terminals in Drosophila larvae show distinct differences in morphology and physiology. *J Neurobiol.* 2000;43:186–197.

Loveless, J., Lagogiannis, K., & Webb, B. (2019). Modelling the mechanics of exploration in larval Drosophila. PLOS Computational Biology, 15(7), e1006635.

Lu Z, Chouhan AK, Borycz JA, Lu Z, Rossano AJ, Brain KL, Zhou Y, Meinertzhagen IA, Macleod GT. High-Probability Neurotransmitter Release Sites Represent an Energy-Efficient Design. *Curr Biol.* 2016;26:2562–2571.

Luo L, Liao YJ, Jan LY, Jan YN. Distinct morphogenetic functions of similar small GTPases: Drosophila Drac1 is involved in axonal outgrowth and myoblast fusion. *Genes Dev.* 1994;8:1787–1802.

Maffei A, Fontanini A. Network homeostasis: a matter of coordination. Curr Opin Neurobiol. 2009;19(2):168–73.

Maloney, R. T. (2021). Neuromodulation and Individuality. *Frontiers in Behavioral Neuroscience*, 15.

Mapelli L, Pagani M, Garrido JA, D'Angelo E. Integrated plasticity at inhibitory and excitatory synapses in the cerebellar circuit. *Front Cell Neurosci.* 2015;9:1–17.

Marder E. Neuromodulation of neuronal circuits: back to the future. *Neuron.* 2012;76:1–11.

Marder, E., & Bucher, D. (2007). Understanding circuit dynamics using the stomatogastric nervous system of lobsters and crabs. Annu. Rev. Physiol., 69, 291-316.

Marder, E., & Goaillard, J. M. (2006). Variability, compensation and homeostasis in neuron and network function. Nature Reviews Neuroscience, 7(7), 563-574.

Marella S., Mann K., Scott K. (2012). Dopaminergic modulation of sucrose acceptance behavior in Drosophila. *Neuron* 73 941–950. 10.1016/j.neuron.2011.12.032

Marrus SB, Portman SL, Allen MJ, Moffat KG, DiAntonio A. Differential localization of glutamate receptor subunits at the Drosophila neuromuscular junction. *J Neurosci.* 2004;24:1406–1415.

Marsden KC, Granato M. In Vivo Ca2+ Imaging Reveals that Decreased Dendritic Excitability Drives Startle Habituation. *Cell Rep.* 2015

Martin A. A further study of the statistical composition on the end-plate potential. *J Physiol.* 1955;130:114–122.

McLean DL, Fetcho JR. Ontogeny and innervation patterns of dopaminergic, noradrenergic, and serotonergic neurons in larval zebrafish. *J. Comp. Neurol.* 2004b;480:38–56.

McLean DL, Fetcho JR. Relationship of tyrosine hydroxylase and serotonin immunoreactivity to sensorimotor circuitry in larval zebrafish. *J. Comp. Neurol.* 2004a;480:57–71.

Melom JE, Akbergenova Y, Gavornik JP, Littleton JT. Spontaneous and Evoked Release Are Independently Regulated at Individual Active Zones. *J Neurosci.* 2013;33:17253–17263.

Mersha M, Formisano R, McDonald R, Pandey P, Tavernarakis N, Harbinder S. GPA-14, a Gα(i) subunit mediates dopaminergic behavioral plasticity in C. elegans. *Behav. Brain Funct. BBF.* 2013;9:16.

Miller KD, MacKay DJC 1994. The role of constraints in Hebbian learning. *Neural Computation* 6: 100–124

Mintz I, Korn H. Serotonergic facilitation of quantal release at central inhibitory synapses. *J. Neurosci. Off. J. Soc. Neurosci.* 1991;11:3359–3370.

Miyazaki KW, Miyazaki K, Tanaka KF, Yamanaka A, Takahashi A, Tabuchi S, Doya K. Optogenetic activation of dorsal raphe serotonin neurons enhances patience for future rewards. *Curr. Biol. CB.* 2014;24:2033–2040.

Mu Y, Li X-Q, Zhang B, Du J-L. Visual Input Modulates Audiomotor Function via Hypothalamic Dopaminergic Neurons through a Cooperative Mechanism. *Neuron.* 2012;75:688–699.

Muhammad K, Reddy-Alla S, Driller JH, Schreiner D, Rey U, Böhme MA, Hollmann C, Ramesh N, Depner H, Lützkendorf J, et al. Presynaptic spinophilin tunes neurexin signalling to control active zone architecture and function. *Nat Commun.* 2015;6:ncomms9362.

Müller M, Davis GW. Transsynaptic control of presynaptic Ca^{2+} influx achieves homeostatic potentiation of neurotransmitter release. *Curr Biol.* 2012;22:1102–1108. [PMC free article] [PubMed] [Google Scholar]

Müller U, Hildebrandt H. Nitric oxide/cGMP-mediated protein kinase A activation in the antennal lobes plays an important role in appetitive reflex habituation in the honeybee. *J. Neurosci. Off. J. Soc. Neurosci.* 2002;22:8739–8747.

Nesler KR, Starke EL, Boin NG, Ritz M, Barbee SA. Presynaptic CamKII regulates activity-dependent axon terminal growth. *Mol Cell Neurosci.* 2016;76:33–41.

Neuromodulatory Control of Long-Term Behavioral Patterns and Individuality across Development. Stern S, Kirst C, Bargmann CI. *Cell*. 2017 Dec 14; 171(7):1649-1662.e10.

Nguyen CT, Stewart BA. The influence of postsynaptic structure on missing quanta at the Drosophila neuromuscular junction. *BMC Neurosci.* 2016;17:53.

O'Rourke NA, Weiler NC, Micheva KD, Smith SJ. Deep molecular diversity of mammalian synapses: why it matters and how to measure it. *Nat Rev Neurosci.* 2012;13:365–379.

Paradis S, Sweeney ST, Davis GW 2001. Homeostatic control of presynaptic release is triggered by postsynaptic membrane depolarization. *Neuron* 30: 737–749

Paradis S, Sweeney ST, Davis GW. Homeostatic control of presynaptic release is triggered by postsynaptic membrane depolarization. *Neuron.* 2001;30:737–749.

Paul MM, Pauli M, Ehmann N, Hallermann S, Sauer M, Kittel RJ, Heckmann M. Bruchpilot and Synaptotagmin collaborate to drive rapid glutamate release and active zone differentiation. *Front Cell Neurosci.* 2015;9 doi: 10.3389/fncel.2015.00029.

Pehlevan, C., Paoletti, P., & Mahadevan, L. (2016). Integrative neuromechanics of crawling in D. melanogaster larvae. *Elife*, *5*, e11031.

Peled ES, Isacoff EY. Optical quantal analysis of synaptic transmission in wild-type and rab3-mutant Drosophila motor axons. *Nat Neurosci.* 2011;14:519–526.

Peled ES, Newman ZL, Isacoff EY. Evoked and spontaneous transmission favored by distinct sets of synapses. *Curr Biol.* 2014;24:484–493.

Pelkey KA, McBain CJ. Differential regulation at functionally divergent release sites along a common axon. *Curr Opin Neurobiol.* 2007;17:366–373.

Pereda A, Triller A, Korn H, Faber DS. Dopamine enhances both electrotonic coupling and chemical excitatory postsynaptic potentials at mixed synapses. *Proc. Natl. Acad. Sci. U. S. A.* 1992;89:12088–12092.

Petersen SA, Fetter RD, Noordermeer JN, Goodman CS, DiAntonio A. Genetic analysis of glutamate receptors in Drosophila reveals a retrograde signal regulating presynaptic transmitter release. *Neuron.* 1997;19:1237–1248.

Petersen, S. A., Fetter, R. D., Noordermeer, J. N., Goodman, C. S., & DiAntonio, A. (1997). Genetic analysis of glutamate receptors in Drosophila reveals a retrograde signal regulating presynaptic transmitter release. Neuron, 19(6), 1237-1248.

Pollak Dorocic I, Fürth D, Xuan Y, Johansson Y, Pozzi L, Silberberg G, Carlén M, Meletis K. A whole-brain atlas of inputs to serotonergic neurons of the dorsal and median raphe nuclei. *Neuron.* 2014;83:663–678.

Prinz, A. A., Bucher, D. & Marder, E. Similar network activity from disparate circuit parameters. Nature Neurosci. 7, 1345–1352 (2004).

Ptacek R, Kuzelova H, Stefano GB. Dopamine D4 receptor gene DRD4 and its association with psychiatric disorders. *Med. Sci. Monit.* 2011;17:RA215–RA220.

Ramaswami M. Network Plasticity in Adaptive Filtering and Behavioral Habituation. *Neuron.* 2014;82:1216–1229.

Ranade SP, Mainen ZF. Transient Firing of Dorsal Raphe Neurons Encodes Diverse and Specific Sensory, Motor, and Reward Events. *J. Neurophysiol.* 2009;102:3026–3037.

Rankin CH, Abrams T, Barry RJ, Bhatnagar S, Clayton DF, Colombo J, Coppola G, Geyer MA, Glanzman DL, Marsland S, et al. Habituation revisited: an updated and revised description of the behavioral characteristics of habituation. *Neurobiol. Learn. Mem.* 2009;92:135–138.

Reese AL, Kavalali ET. Single synapse evaluation of the postsynaptic NMDA receptors targeted by evoked and spontaneous neurotransmission. *Elife.* 2016;5:e21170.

Reese AL, Kavalali ET. Spontaneous neurotransmission signals through store-driven Ca(2+) transients to maintain synaptic homeostasis. *Elife.* 2015;4:e09262.

Rittschof C. C., Bukhari S. A., Sloofman L. G., Troy J. M., Caetano-Anollés D., Cash-Ahmed A., et al. (2014). Neuromolecular responses to social challenge: common mechanisms across mouse, stickleback fish, and honey bee. *Proc. Natl. Acad. Sci. U. S. A.* 111 17929–17934. 10.1073/pnas.1420369111

Robertson, F. W. (1963). The ecological genetics of growth in Drosophila 6. The genetic correlation between the duration of the larval period and body size in relation to larval diet. Genetics Research, 4(1), 74-92.

Rodrigues S. M., LeDoux J. E., Sapolsky R. M. (2009). The influence of stress hormones on fear circuitry. *Annu. Rev. Neurosci.* 32 289–313. 10.1146/annurev.neuro.051508.135620

Rumajogee P, Vergé D, Darmon M, Brisorgueil M-J, Hamon M, Miquel M-C. Rapid up-regulation of the neuronal serotoninergic phenotype by brain-derived neurotrophic factor and cyclic adenosine monophosphate: relations with raphe astrocytes. *J. Neurosci. Res.* 2005;81:481–487.

Rutherford LC, Nelson SB, Turrigiano GG. BDNF has opposite effects on the quantal amplitude of pyramidal neuron and interneuron excitatory synapses. *Neuron.* 1998;21:521–530.

Saitoe M, Schwarz TL, Umbach JA, Gundersen CB, Kidokoro Y. Absence of junctional glutamate receptor clusters in Drosophila mutants lacking spontaneous transmitter release. *Science.* 2001;293:514–517.

Sanchez-Roige S., Gray J. C., MacKillop J., Chen C. -H., Palmer A. A. (2018). The genetics of human personality. *Genes Brain Behav.* 17:e12439. 10.1111/gbb.12439

Satou C, Kimura Y, Kohashi T, Horikawa K, Takeda H, Oda Y, Higashijima S. Functional role of a specialized class of spinal commissural inhibitory neurons during fast escapes in zebrafish. *J. Neurosci. Off. J. Soc. Neurosci.* 2009;29:6780–6793.

Sawin-McCormack, Elena P., Marla B. Sokolowski, and Ana Regina Campos. "Characterization and genetic analysis of Drosophila melanogaster photobehavior during larval development." Journal of neurogenetics 10.2 (1995): 119-135.

Schaefer JE, Worrell JW, Levine RB. Role of intrinsic properties in Drosophila motoneuron recruitment during fictive crawling. *J Neurophysiol.* 2010;104:1257–1266.

Schulz, D. J., Goaillard, J. M. & Marder, E. Variable channel expression in identified single and electrically coupled neurons in different animals. *Nature Neurosci*. 9, 356–362 (2006).

Scott EK, Mason L, Arrenberg AB, Ziv L, Gosse NJ, Xiao T, Chi NC, Asakawa K, Kawakami K, Baier H. Targeting neural circuitry in zebrafish using GAL4 enhancer trapping. *Nat. Methods.* 2007;4:323–326.

Siegel F, Lohmann C. Probing synaptic function in dendrites with calcium imaging. *Exp Neurol.* 2013;242:27–32.

Stewart BA, Atwood HL, Renger JJ, Wang J, Wu CF. Improved stability of Drosophila larval neuromuscular preparations in haemolymph-like physiological solutions. *J Comp Physiol A.* 1994;175:179–191.

Stratton MM, Chao LH, Schulman H, Kuriyan J. Structural studies on the regulation of Ca2+/calmodulin dependent protein kinase II. *Curr Opin Struct Biol.* 2013;23:292–301.

Suster ML, Martin JR, Sung C, Robinow S. Targeted expression of tetanus toxin reveals sets of neurons involved in larval locomotion in Drosophila. *J Neurobiol.* 2003;55:233–246.

Sweeney ST, Broadie K, Keane J, Niemann H, O'Kane CJ. Targeted expression of tetanus toxin light chain in Drosophila specifically eliminates synaptic transmission and causes behavioral defects. *Neuron.* 1995;14:341–351.

Swensen, A. M. & Bean, B. P. Robustness of burst firing in dissociated purkinje neurons with acute or long-term reductions in sodium conductance. J. Neurosci. 25, 3509–3520 (2005). Taghert P. H., Nitabach M. N. (2012). Peptide neuromodulation in invertebrate model systems. *Neuron* 76 82–97. 10.1016/j.neuron.2012.08.035

Takahashi H. Juvenile hermaphroditism in the zebrafish, Brachydanio rerio. *Bull. Fac. Fish. HOKKAIDO Univ.* 1977;28:57–65.

Takizawa E, Komatsu A, Tsujimura H. Identification of common excitatory motoneurons in Drosophila melanogaster larvae. *Zoolog Sci.* 2007;24:504–513.

Tereshchenko Y, Brandewiede J, Schachner M, Irintchev A, Morellini F. Novelty-induced behavioral traits correlate with numbers of brainstem noradrenergic neurons and septal cholinergic neurons in C57BL/6J mice. *Behav. Brain Res.* 2008;191:280–284.

Thiagarajan TC, Lindskog M, Tsien RW. Adaptation to synaptic inactivity in hippocampal neurons. *Neuron.* 2005;47:725–737.

Thirumalai V, Cline HT. Endogenous dopamine suppresses initiation of swimming in prefeeding zebrafish larvae. *J. Neurophysiol.* 2008;100:1635–1648.

Toro C, Trapani JG, Pacentine I, Maeda R, Sheets L, Mo W, Nicolson T. Dopamine Modulates the Activity of Sensory Hair Cells. *J. Neurosci.* 2015;35:16494–16503.

Tran S, Gerlai R. Individual differences in activity levels in zebrafish (Danio rerio) *Behav. Brain Res.* 2013;257:224–229.

Turrigiano G. Homeostatic synaptic plasticity: local and global mechanisms for stabilizing neuronal function. *Cold Spring Harb Perspect Biol.* 2012;4:a005736.

Turrigiano GG, Leslie KR, Desai NS, Rutherford LC, Nelson SB. Activity-dependent scaling of quantal amplitude in neocortical neurons. *Nature.* 1998;391:892–896.
Turrigiano GG, Nelson SB. Homeostatic plasticity in the developing nervous system. Nat Rev Neurosci. 2004;5(2):97–107.
Turrigiano, G. (2012). Homeostatic synaptic plasticity: local and global mechanisms for stabilizing neuronal function. Cold Spring Harbor perspectives in biology, 4(1), a005736.

Weissbourd B, Ren J, DeLoach KE, Guenthner CJ, Miyamichi K, Luo L. Presynaptic partners of dorsal raphe serotonergic and GABAergic neurons. *Neuron.* 2014;83:645–662.

Whitaker KW, Neumeister H, Huffman LS, Kidd CE, Preuss T, Hofmann HA. Serotonergic modulation of startle-escape plasticity in an African cichlid fish: a single-cell molecular and physiological analysis of a vital neural circuit. *J. Neurophysiol.* 2011;106:127–137.

Witvliet D., Mulcahy B., Mitchell J. K., Meirovitch Y., Berger D. R., Wu Y., et al. (2021). Connectomes across development reveal principles of brain maturation. *Nature* 596 257–261. 10.1038/s41586-021-03778-8

Wolf E, Zhao FY, Roberts A. Non-linear summation of excitatory synaptic inputs to small neurones: a case study in spinal motoneurones of the young Xenopus tadpole. *J Physiol.* 1998;511:871–886.

Wolf M, Weissing FJ. Animal personalities: consequences for ecology and evolution. *Trends Ecol. Evol.* 2012;27:452–461.

Wolman MA, Jain RA, Liss L, Granato M. Chemical modulation of memory formation in larval zebrafish. *Proc. Natl. Acad. Sci. U. S. A.* 2011;108:15468–15473.

Wolman MA, Jain RA, Marsden KC, Bell H, Skinner J, Hayer KE, Hogenesch JB, Granato M. A genome-wide screen identifies PAPP-AA-mediated IGFR signaling as a novel regulator of habituation learning. *Neuron.* 2015;85:1200–1211.

Woods IG, Schoppik D, Shi VJ, Zimmerman S, Coleman HA, Greenwood J, Soucy ER, Schier AF. Neuropeptidergic signaling partitions arousal behaviors in zebrafish. *J. Neurosci. Off. J. Soc. Neurosci.* 2014;34:3142–3160.

Yokogawa T, Hannan MC, Burgess HA. The dorsal raphe modulates sensory responsiveness during arousal in zebrafish. *J. Neurosci. Off. J. Soc. Neurosci.* 2012;32:15205–15215.

Zalocusky KA, Ramakrishnan C, Lerner TN, Davidson TJ, Knutson B, Deisseroth K. Nucleus accumbens D2R cells signal prior outcomes and control risky decision-making. *Nature.* 2016;531:642–646.

Zarin, Aref Arzan, et al. "A multilayer circuit architecture for the generation of distinct locomotor behaviors in Drosophila." Elife 8 (2019): e51781.

Zucker RS, Regehr WG. Short-Term Synaptic Plasticity. *Annu Rev Physiol.* 2002;64:355–405.

Zwart MF, Pulver SR, Truman JW, Fushiki A, Cardona A, Landgraf M. Selective Inhibition Mediates the Sequential Recruitment of Motor Pools. *Neuron.* 2016;91:615–628.